Monotonic and Cyclic Behaviour of Reinforced Concrete-Masonry Shear Wall Boundary Elements

BELAL ALI ABDELHAFEEZ ABDELRAHMAN

A Thesis

In the Department of

Building, Civil, and Environmental Engineering

Presented in Partial Fulfillment of the Requirements for the Degree of

Doctor of Philosophy (Civil Engineering) at

Concordia University

Montréal, Québec, Canada

January 2021

CONCORDIA UNIVERSITY

School of Graduate Studies

This is to certify that the thesis prepared

By: Belal Ali AbdelHafeez AbdelRahman

Entitled: Monotonic and Cyclic Behaviour of Reinforced Concrete-Masonry Shear Wall Boundary Elements

and submitted in partial fulfillment of the requirements for the degree of

Doctor of Philosophy (Civil Engineering)

complies with the regulations of the University and meets the accepted standards with respect to originality and quality.

Signed by the final examining committee:

_____ Dr. John Xiupu Zhang	Chair
_____ Dr. Mohamed ElGawady	External examiner
_____ Dr. Ramin Sedaghati	External to program
_____ Dr. Ashutosh Bagchi	Examiner
_____ Dr. Emre Erkmen	Examiner
_____ Dr. Khaled Galal	Thesis supervisor

Approved by   _____
Dr. Michelle Nokken, Graduate Program Director

_____
Dr. Mourad Debbabi, Dean
Gina Cody School of Engineering and Computer Science

Date of Defence: 2021-04-08

ABSTRACT

Monotonic and Cyclic Behaviour of Reinforced Concrete-Masonry Shear Wall Boundary Elements

Belal Ali AbdelHafeez AbdelRahman, Ph.D.

Concordia University, 2021

As a seismic force-resisting system (SFRS), reinforced masonry shear walls with masonry boundary elements (RMSW+BEs) were found to achieve enhanced strength, stability, and ductility levels compared to rectangular RMSWs. The seismic design of RMSW+BEs necessitates reliable experimental and analytical investigations of their reinforced masonry boundary elements (RMBEs). The axial monotonic and cyclic stress-strain curves of RMBEs are essential to predict the lateral cyclic response of RMSW+BEs. This research aims to investigate, experimentally and analytically, the axial monotonic and cyclic behaviour of RMBEs built with C-shape masonry blocks. Moreover, this research proposes monotonic and cyclic stress-strain models for unconfined and confined RMBEs subjected to axial compression loading. Furthermore, a numerical study was performed to assess the sensitivity of the nonlinear seismic response of RMSW+BEs to various wall configurations and design parameters.

This research's experimental work involved investigating various parameters affecting the compressive strength of fully grouted concrete masonry prisms and the axial monotonic and cyclic behaviour of RMBEs. Forty-two masonry prisms and 69 RMBEs were tested. The studied parameters were the vertical reinforcement ratio, the confinement ratio, the cross-section geometry (i.e., square vs. rectangular RMBEs), the masonry bonding pattern, pre-wetting of dry RMBEs, various grout types, and the grout compressive strength. The results showed that RMBEs built with rectangular sections exhibited enhanced strain ductility and post-peak behaviour than square RMBEs. Besides, using low grout compressive strength significantly reduced the strain ductility and yielded sharp strength degradation of the RMBEs.

The RMBEs′ experimental results revealed that the monotonic stress-strain curves form envelope curves to their cyclically tested counterparts. The proposed monotonic and cyclic stress-

strain models showed good-to-excellent agreement with the experimental results, predicting the envelope and cyclic stress-strain curves′ major characteristics.

The numerical study's results showed that the seismic design of RMSW+BEs can be optimized through careful choice of their design parameters. Enhancing the RMSW+BEs lateral yield and ultimate capacities and the lateral effective stiffness can be achieved by increasing the vertical reinforcement ratio of the RMBEs and the masonry compressive strength. Contrarily, reducing the masonry strain at peak stress and/or the masonry modulus of elasticity greatly hinders the walls′ displacement ductility.

Dedications

To my beloved parents, Samia and Ali,
To my lovely son, Ahmed, and my pretty daughter, Hana,
To my dear wife, Lobna,
To my brother, Hamza

Acknowledgments

All thanks and praises are due to Allah the Most Gracious, the Most Compassionate, and the Most Merciful with the blessings of Whom the good deeds are fulfilled

I would like to express my deepest thanks to my supervisor, Dr. Khaled Galal, who has saved no effort to help me during my Ph.D. journey. Dr. Khaled Galal is a supportive, helpful, and smart supervisor, where he spends tons of his time guiding, supervising, and facilitating the way for his students during their studies; his supportive and positive discussions are really appreciated. Also, I would like to thank my committee members, Dr. Ashutosh Bagchi, Dr. Emre Erkmen, and Dr. Ramin Sedaghati for their valuable and constructive comments. Finally, I want to thank Dr. Mohamed ElGawady for his review of my thesis and his expected constructive comments.

I would like to sincerely thank my friend, colleague, and former postdoc fellow Dr. Ahmed Ashour for his appreciated help to have the opportunity to pursue my Ph.D. studies at Concordia University. His valuable pieces of advice during my first steps in the Ph.D. are acknowledged. I also want to send my thanks to my colleagues and friends Dr. Ala' Obaidat, Dr. Khalid Al-Otaibi, Mohamed Albutainy, Dr. Nader Aly, Mohamed Yosry, Dr. Shadman Hosseinzadeh, Omar Yagob, Layane Hamzeh, Omar Gouda, Omar Elmeligy, AbdulElah Al-Ahdal, Islam Elsayed, and Mostafa Ibrahim. Our discussions, their comments, and help are really appreciated. Special and sincere thanks to my friend and colleague, Islam Elsayed, for his support, dedication, and help during phase 2 and phase 3's experimental testing. Besides, I want to thank the technical staff at Concordia University's Structures Laboratory, Andy Shin-Pong, Alexis Gosselin, and Ricky Gioia, for their support during my experimental work. I also would like to thank the graduate students, Olanrewaju Ibrahim, Richard Aidoo, Saif Ahmed, Faizaan Shaikh, and Birinder Singh; the undergraduate students, Faris Khader, Qusay Alsahaf, Shaker Madi, and Lizhu Chen, without them my experimental work would not have been accomplished. Special thanks to my friend and graduate student Osama Meloud, his help in the experimental work is appreciated.

Co-Authorship

This thesis has been prepared in accordance with the regulations of a sandwich (manuscript-based) thesis format. This research presents experimental, analytical, and numerical work carried out solely by Belal AbdelRahman. Advice and guidance provided for the whole thesis by the academic supervisor Dr. Khaled Galal. This thesis consists of the following chapters:

Chapter 3

AbdelRahman, B., and Galal, K. (2020). Influence of pre-wetting, non-shrink grout, and scaling on the compressive strength of grouted concrete masonry prisms. *Construction and Building Materials Journal*, Elsevier; 241, 117985.

Chapter 4

AbdelRahman, B., and Galal, K. (2020). Experimental Investigation of Axial Compressive Behaviour of Square and Rectangular Confined Concrete-Masonry Structural Wall Boundary Elements. *Engineering Structures Journal*, Elsevier; submitted for publication in December 2020.

Chapter 5

AbdelRahman, B., and Galal, K. (2021). Monotonic and Cyclic Stress-Strain Models for Confined Concrete-Masonry Shear Wall Boundary Elements. *Engineering Structures Journal*, Elsevier; submitted for publication in January 2021.

Chapter 6

AbdelRahman, B., and Galal, K. (2020). Sensitivity of the Seismic Response of Fully Grouted Reinforced Masonry Shear Walls with Boundary Elements to its Design Parameters. *Journal of Structural Engineering*, ASCE; submitted for publication in November 2020.

Table of Contents

List of Figures

List of Tables

List of Acronyms

BE	Boundary Element
LVDT	Linear Variable Displacement Transducer
MBE	Masonry Boundary Element
RC	Reinforced Concrete
RM	Reinforced Masonry
RMSW	Reinforced Masonry Shear Walls
RMBE	Reinforced Masonry Boundary element
RMSW+BEs	Reinforced Masonry Shear Walls with Boundary Elements
SFRS	Seismic Force Resisting System

Nomenclature

A_b	Area of reinforcement bar (mm^2)
A_{cm}	Sectional area of confined masonry (mm^2)
A_s	Area of vertical reinforcement (mm^2)
A_t	Total cross-sectional area of a masonry boundary element (mm^2)
A_{um}	Sectional area of unconfined masonry (mm^2)
AR	Aspect ratio of masonry boundary element
b_c	Confined masonry core dimension in x-direction between centerlines of hoops (mm)
d_b	Diameter of reinforcement bar (mm)
d_c	Confined masonry core dimension in y-direction between centerlines of hoops (mm)
E_m	Initial modulus of elasticity of masonry (MPa)
E_r	Reloading branch modulus of elasticity (MPa)
E_{sec}	Secant modulus of confined masonry at its peak stress (MPa)
E_{sec-un}	Unloading secant modulus of elasticity (MPa)
E_u	Tangent modulus of elasticity to the unloading curve corresponding to ε_{un} (MPa)
f_b	Masonry block compressive strength (MPa)
f'_c	Concrete compressive strength of top cap and bottom footing (MPa)
f_{cm}	Confined masonry compressive stress (MPa)
f_{cm-max}	Peak stress of confined masonry core (MPa)
f_g	Grout compressive strength (MPa)
f'_l	Effective lateral confining stress (MPa)
f_{m-max}	Peak stress of tested RMBE (MPa)
f_m	Masonry compressive stress at given strain (MPa)
f_{mor}	Mortar compressive strength (MPa)
f_{new}	Masonry compressive stress on reloading branch corresponding to ε_{un} (MPa)
f_p	Compressive strength of masonry boundary element prism (MPa)
f_{ro}	Compressive stress at the point of reloading (MPa)
f_{re}	Compressive stress at return point on envelope stress-strain curve (MPa)
f_s	Compressive stress in vertical reinforcement (MPa)

f_{um}	Unconfined masonry compressive stress (MPa)
f'_{um}	Unconfined masonry peak stress (MPa)
f_{un}	Unloading (reversal) stress in the proposed masonry model (MPa)
f_{yh}	Yield strength of the transverse confinement steel (MPa)
k_e	Confinement effectiveness coefficient
P_t	Total axial compression resisted by RMBE section at given axial displacement (N)
R_{BE}	Cross-section rectangularity ratio (%)
s'	Vertical clear spacing between adjacent confinement hoops (mm)
w'_i	Clear distance between adjacent vertical steel bars (mm)
ε_a	Common strain at which initial modulus of elasticity and unloading modules intersect
$\varepsilon_{cm\text{-}max}$	Strain corresponding to peak stress of confined masonry core
$\varepsilon_{m\text{-}max}$	Strain corresponding to peak stress of tested RMBE
ε_{mo}	Strain corresponding to peak stress of unconfined masonry
ε_p	Plastic (residual) strain of masonry
ε_{re}	strain coordinate at return point on envelope stress-train curve
ε_{ro}	strain at reloading point of the proposed model
ε_{sp}	Spalling strain of unconfined masonry
ε_{um}	unconfined masonry strain in the proposed model
ε_{un}	Unloading (reversal) strain in the proposed model
ε_{50}	Masonry strain at 50% strength degradation
$\mu_{\varepsilon50}$	Strain ductility at 50% strength degradation
ρ_{cc}	vertical reinforcement to confined core area ratio (%)
ρ_h	Volumetric ratio of confinement reinforcement (%)
ρ_v	Vertical reinforcement ratio (%)
ρ_x	Volumetric ratio of confinement hoops to confined masonry core in x-direction (%)
ρ_y	Volumetric ratio of confinement hoops to confined masonry core in y-direction (%)
AR	Aspect ratio of wall (h_w/l_w);
AS	Axial compressive stress on wall (MPa);
c	Compression zone depth (mm);
E_m	Modulus of elasticity of masonry (MPa);
E_s	Modulus of elasticity of steel reinforcement (MPa);
f'_m	Compressive strength of masonry (MPa);
f_{tm}	Tensile strength of masonry (MPa);
f_y	Yield strength of steel reinforcement (MPa);
h_w	Height of wall (mm);
K_{eff}	Effective lateral stiffness of wall (kN/mm);
$K_{eff,ref}$	Effective lateral stiffness of the reference wall (kN/mm);
$K_{2.5\%}$	Secant stiffness of wall at 2.5% drift (kN/mm);
$K_{2.5\%,ref}$	Secant stiffness of the reference wall at 2.5% drift (kN/mm);
l_p	Plastic hinge length of wall (mm);
l_w	Length of wall (mm);
Q_u	Wall's ultimate lateral capacity (kN);
$Q_{u,ref}$	Reference wall's ultimate lateral capacity (kN);

$Q_{2.5\%drift}$	Wall's lateral capacity at 2.5% drift (kN);
Q_y	Wall's lateral yield capacity (kN);
$Q_{y,ref}$	Reference wall's lateral yield capacity (kN);
ε_{mu}	Masonry compressive strain at peak stress (mm/mm);
Δ_u	Lateral ultimate displacement at top of wall (mm);
Δ_y	Lateral yield displacement at top of wall (mm);
$\Delta_{2.5\%drift}$	Lateral displacement at 2.5% drift at top of wall (mm);
$\Delta_{0.8Qu}$	Lateral displacement at top of wall at 20% strength degradation (mm);
$\mu_{\Delta0.8Qu}$	Displacement ductility of wall at 20% strength degradation;
$\mu_{\Delta0.8Qu,ref}$	Displacement ductility of the reference wall at 20% strength degradation;
$\mu_{\Delta,id}$	Idealized displacement ductility of wall; and
ρ_{vBE}	Vertical reinforcement ratio of the masonry boundary elements (%)

Chapter 1

Introduction

1.1 Background

As an ancient construction material, masonry has been a critical pillar in building various impressive existing and new, residential and commercial, infra- and super-structures worldwide because of its aesthetics and construction readiness. Unreinforced concrete-masonry (URM) and reinforced concrete-masonry (RCM) are high-competitive structural materials. The URM material is typically employed as load-bearing walls, curtain walls, or infill walls. Unreinforced masonry buildings and URM walls exhibited an unfavorable failure mode when subjected to earthquake ground motions. As a result, a mistaken perception of poor ductile behaviour and underestimated energy dissipation levels are associated with the concrete-masonry as a structural material. However, this perception is mainly drawn because of the undesired disastrous brittle behaviour of unreinforced and non-engineered masonry structures under seismic excitations (Banting 2013).

Tomaževič and Weiss (1994) tested two three-story unreinforced and reinforced masonry buildings constructed with similar structural configurations. The two model buildings were tested under simulated earthquake motions on a shaking table. The unreinforced masonry building experienced a soft-story failure mechanism with a dramatically low flexural capacity and a brittle failure. On the contrary, the reinforced building (i.e., reinforcing its masonry structural walls) exhibited a substantial enhancement of the lateral capacity, energy dissipation, and ductility levels. Furthermore, in experimental studies by Seible et al. (1994a; b), where they tested a full-scale five-story RCM building under simulated earthquake ground motions, the tested building showed considerable displacement ductility levels. These research efforts ensured that RCM structural wall buildings were capable of mitigating the seismic effects without catastrophic failure mechanisms (El-Dakhakhni and Ashour 2017). Therefore, URM buildings should be avoided in moderate and high seismicity zones (Seible et al. 1994a; b).

The growing masonry industry necessitates reliable, innovative, and ductile masonry systems to be integrated into mid- and high-rise RCM buildings to ensure high load-carrying capacity and meet ductility demands. This is associated with evolving and continuous advancement towards masonry building codes and standards that strived to ensure the safety, applicability, and

conformity of RCM structural walls (commonly referred to as shear walls) as seismic force-resisting systems (SFRS). However, most concrete-masonry structures built with reinforced masonry shear walls (RMSWs) are in low seismicity zones and classified as low-rise buildings. This could be attributed to the limited strength and ductility offered by the rectangular RMSWs as a SFRS.

Extensive research work that was conducted on rectangular RMSWs exhibited their ductility, stability, and strength limitations (El-Dakhakhni and Ashour 2017). Unlike reinforced concrete (RC) shear walls, rectangular RMSWs have restricted arrangement of one row of vertical reinforcement with no means of confinement due to the concrete-masonry blocks′ configuration. Moreover, fully grouted concrete-masonry material is assigned specified low compressive strengths in the North American standards, CSA S304-14 (2014) and TMS 402/602-16 (2016). These limitations make it challenging to use masonry in mid- and high-rise buildings. The seismic design of RMSWs requires ensuring adequate ductility and energy dissipation levels that can meet the ductility demands without significant loss of their lateral flexural capacity. This can be achieved by introducing a confined masonry core (i.e., masonry boundary elements, MBEs) to the end zones of a rectangular RMSW. Figure 1.1 shows schematic diagrams of reinforced masonry shear walls with boundary elements (RMSW+BEs) and their reinforced masonry boundary elements (RMBEs).

Reinforced masonry boundary element (RMBE)

Reinforced masonry shear wall with boundary elements (RMSW+BEs)
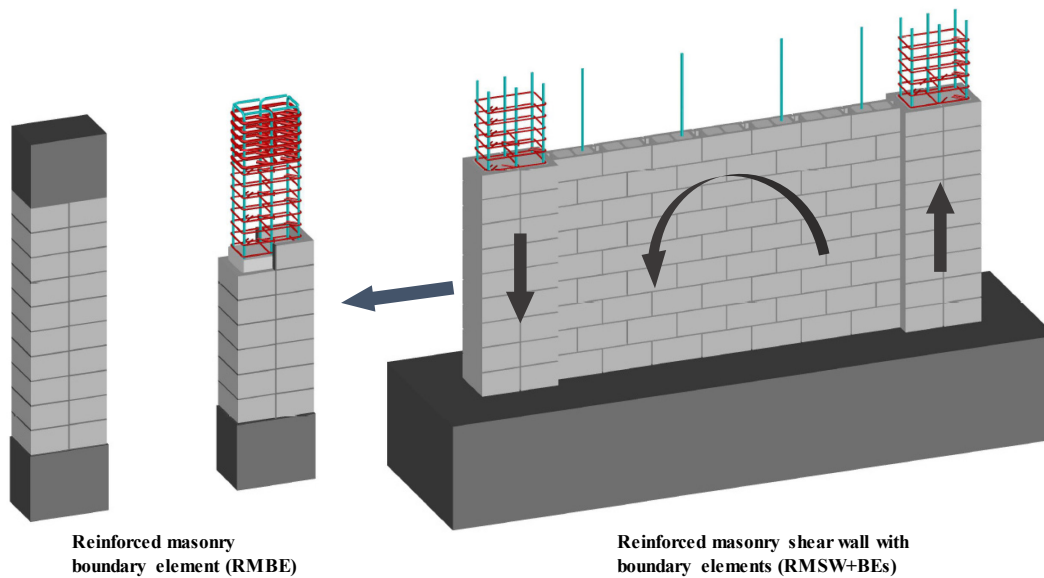
Figure 1.1 Schematic diagram of RMSW with boundary elements and reinforced masonry boundary element (RMBE)

2

These RMBEs enhance the stability and ductility of RMSW+BEs through the introduced reinforcement steel cages with the confinement hoops that reduce the walls′ compression zone depth yielding a significant boost in their curvature ductility. Proper confinement of the shear walls′ MBEs alleviates the reinforcement's buckling under high displacement levels, enhances their stability, boost their displacement ductility, and improves their overall seismic response.

The seismic design of RMSW+BEs necessitates reliable experimental and analytical investigations of their RMBEs. The RMBEs′ monotonic and cyclic behaviours are critical components in predicting the lateral cyclic response of RMSW+BEs. Therefore, there is a need to investigate, experimentally and analytically, the axial and cyclic compressive behaviour of RMBEs with different steel arrangements, various cross-sections, and multiple confinement configurations.

1.2 Motivation and Research Significance

High-performance masonry is essential to promote mid- and high-rise RCM structures. High strength masonry and proper ductility behaviour enable RCM systems to efficiently sustain high compressive loads and lateral cyclic loads. High-performance masonry can be achieved in fully grouted RMSWs′ boundary elements and RCM columns subjected to lateral loads. It is still questionable why most fully grouted concrete-masonry prisms show less compressive strength than their ungrouted counterparts, which in turn can impair the lateral flexural capacity and the ductility of fully grouted RMSW+BEs. Therefore, there is an urgent need to further investigate the compressive stress-strain behaviour of ungrouted and fully grouted concrete-masonry with different constituent materials and test parameters.

Research efforts (e.g., Abo El Ezz et al. 2015; and Obaidat et al. 2018, 2019) have been initiated to investigate the axial compressive behaviour of confined RMBEs. Previous researchers (e.g., Banting 2013, Aly 2019) recommended more investigation and quantification of the concrete-masonry material behaviour with various confinement configurations is beneficial for interpreting the seismic response of RMSW+BEs. Besides, the CSA S304-14 stipulated special requirements for the geometrical and detailing of RMSWs′ boundary elements; however, further investigations are needed for a reliable application to ensure conformity of RMBEs to RMSW+BEs. The literature has also a substantial lack of experimental results of confined RMBEs tested under axial cyclic compression loading. Therefore, more investigations and experimental

tests should be conducted on the axial compressive stress-strain behaviour of RMBEs with different cross-section configuration, various vertical reinforcement arrangements, and different confinement configurations (see Figure 1.2). This complements the literature gap and establishes a reliable axial and cyclic stress-strain model for unconfined and confined RMBEs. Enhancing the masonry axial compressive strength and the ductility of the RMBEs contributes to the resilience and sustainability of the RCM structures when subjected to severe seismic motions.
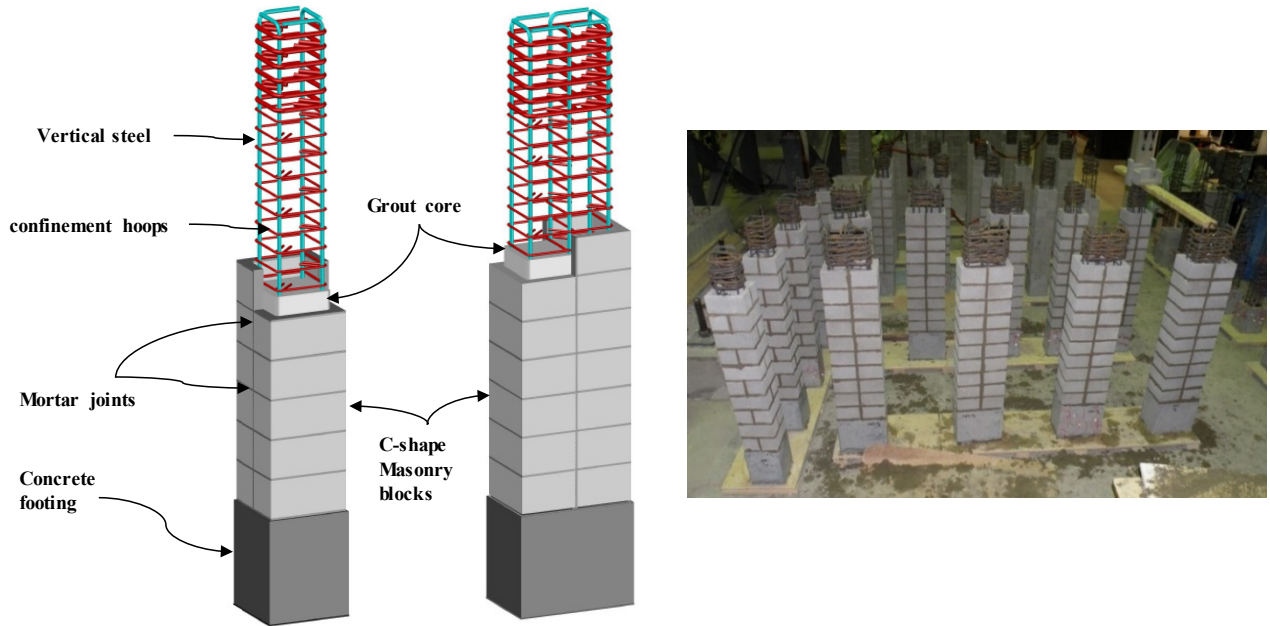
Figure 1.2 Square and rectangular RMBEs

Unlike confined RC columns, very limited experimental and numerical research was conducted on the axial cyclic behaviour of RMBEs. Enormous research studies focused on the axial compressive behaviour of unconfined and confined RC columns tested under slow and dynamic strain rates. Besides, many researchers initiated, developed, and refined axial and cyclic constitutive models for the confined concrete to simulate the lateral seismic response of RC structural walls. Unfortunately, this is not the case for confined and unconfined masonry boundary elements, where minimal research efforts were focused on their axial monotonic and cyclic behaviour. The anticipated stress-strain curves of confined RMBEs using the literature models were found not applicable to RMBEs tested under axial monotonic compression loading (Obaidat et al., 2018). Moreover, the majority of numerical software tools have a substantial lack of an axial and cyclic stress-strain material model for confined RMBEs. Therefore, refined stress-strain

models are required to predict the envelope and cyclic stress-strain responses of confined RMBEs built with different sections and confinement configurations. These models can be utilized to predict the lateral cyclic response of RMSW+BEs considering the stored ductility at the end-confined zones of the shear walls.

Unlike RC shear walls, limited experimental and numerical research was conducted on the lateral cyclic behaviour of RMSW+BEs. Based on the literature studies performed on the RCM components (i.e., shear walls) or the system level (i.e., multistory buildings), it can be inferred that the RMSW+BEs is still a point of interest where more studies, in-depth investigations, and quantifications are yet to come. Therefore, there is a need to study the sensitivity of the seismic response of RMSW+BEs to critical design parameters that also affect their RMBEs behaviour, such as the masonry compressive strength, the masonry strain at peak stress, and the vertical steel ratio of the RMBEs. Various wall configurations can also be investigated to determine which design parameters and wall configurations critically influence the RMSW+BEs′ lateral cyclic behaviour.

1.3 Objectives and Scope of Work

The objectives of this research are to investigate the axial monotonic and cyclic stress-strain behaviour of unconfined and confined RMBEs, to develop stress-strain monotonic and cyclic models for confined RMBEs, and to quantify the influence of different design parameters and various wall configurations on the seismic response of RMSWs built with RMBEs. The proposed stress-strain models of the RMBEs and the numerical model of the RMSW+BEs aim to enhance the design tools and mitigate the challenging seismic design of RCM shear wall buildings.

In order to achieve the objectives of this thesis, the following is the scope of work:

1. Constructing and testing forty-two ungrouted and fully grouted concrete-masonry prisms under concentric axial compression loading. Three main test parameters affecting the axial compressive stress-strain behaviour of fully grouted half-scale and full-scale concrete-masonry prisms will be investigated, namely, pre-wetting of dry masonry prisms, non-shrink grout, and grout strength.

2. Constructing and testing forty-three scaled unconfined and confined RMBEs built with C-shape concrete-masonry units. The influence of various design parameters and

construction procedures on the axial compressive behaviour of fully grouted RMBEs will be examined. The RMBEs will be tested under concentric axial compression loading till failure. The effect of five parameters, namely, the vertical reinforcement ratio, the volumetric ratio of confinement steel, the cross-section configuration, stack pattern and running-bond, and pre-wetting of dry masonry shell before grouting, will be investigated.

3. Constructing and testing twenty-six RMBEs under axial cyclic compression loading to assess the cyclic response of confined RMBEs whose counterparts were tested under axial monotonic compression.

4. Developing axial and cyclic stress-strain models for confined RMBEs subjected to axial compression loading to enable better prediction of the seismic performance of RMSW+BEs.

5. Developing a simplified 2D macro-model to predict the lateral cyclic response of RMSW+BEs.

6. Examining and quantifying the sensitivity of the RMSW+BEs′ seismic response to various design parameters and different wall configurations. The design parameters are the vertical reinforcement ratio of the RMBEs, the masonry strain at peak stress, the masonry modulus of elasticity, and the masonry compressive strength. Four wall configurations, namely, the wall's aspect ratio, the axial stress level, the masonry boundary element (MBE) size, and the wall's length, will be investigated.

1.4 Thesis layout

This thesis contains seven chapters that present an in-depth concise review of the literature and the current state of the art, the experimental research performed on fully grouted concrete-masonry prisms and RMBEs, and the numerical study focused on the sensitivity of the seismic response of RMSW+BEs to critical design parameters and wall configurations. The chapters of this dissertation are organized as follows:

- Chapter 2 presents a detailed literature review of the current state of the art of the unconfined and confined concrete-masonry prisms and boundary elements. It contains six sections: section 2.2 presents a summary of literature studies focused on the behaviour of fully grouted concrete-masonry prisms under axial compression loading,

section 2.3 discusses the confined concrete-masonry prisms and boundary elements tested under axial compression loading and illustrates previous stress-strain models proposed for confined masonry, section 2.4 presents previously developed stress-strain models for confined RC columns, section 2.5 discusses the experimental and numerical studies focused on the seismic response of RMSW+BEs, and section 2.6 summarize the conclusions drawn from the literature review.

- Chapter 3 experimentally investigates the influence of pre-wetting of dry masonry prisms, non-shrink grout, and grout strength on the axial compressive stress-strain response of grouted masonry prisms. A total of forty-two ungrouted and grouted concrete-masonry prisms were built and tested. It presents the comparisons of stress-strain responses of the tested specimens. It examines previously developed literature equations against the test results to study these equations' effectiveness in predicting the masonry prism compressive strength. This chapter highlights the most critical parameters affecting the compressive strength of fully grouted concrete-masonry and recommends construction procedures to enhance their compressive strength.

- Chapter 4 presents an in-depth experimental study focused on the axial compressive stress-strain response of unreinforced MBEs and confined RMBEs. It also illustrates the test matrix's choice, the construction procedures, the material properties, the test setup, and the tested specimens' instrumentation. Thirty-eight unreinforced and RMBEs were constructed and tested under concentric axial compression loading. The effect of critical design parameters such as the vertical reinforcement ratio, the volumetric ratio of confinement reinforcement, cross-section configuration, and the construction pattern was investigated. It presents the comparisons of the test results in terms of stress-strain curves as well as correlations of the test parameters and their influence on the peak stress and ductility of confined RMBEs.

- Chapter 5 reports the experimental test results of thirteen unreinforced MBEs tested under axial monotonic compression and twenty-six confined RMBEs were tested under axial cyclic compression loading. Moreover, it investigates the influence of various parameters on the axial cyclic stress-strain response of confined RMBEs, such as the grout compressive strength, the cross-section configuration, and the vertical and transverse confinement steel configurations. It also provides a concise comparison of

7

the test results of confined RMBEs that were tested under monotonic and cyclic compression loading to ensure a concept validity; that is, the monotonic curve forms an envelope curve to its cyclic counterpart. Furthermore, this chapter proposes monotonic and cyclic stress-strain models for unconfined and confined RMBEs.

- Chapter 6 performs a numerical study to investigate the sensitivity of the seismic response of RMSW+BEs against various wall configurations, namely, the wall's aspect ratio, the axial compressive stress level, the masonry boundary element (MBE) size, and the wall's length. Different design parameters such as the masonry maximum compressive strength, the masonry strain at peak stress, and the MBE vertical reinforcement ratio were studied. It illustrates the numerical modelling approach, the material models, and the model validation. Furthermore, it proposes efficient, yet straightforward recommendations to optimize the seismic design of RMSW+BEs through the careful choice of the design parameters and their influence on the flexural yield strength and ultimate capacity, the displacement ductility, and effective stiffness of the RMSW+BEs.

- Chapter 7 summarizes the significant findings of this thesis. It also presents valuable conclusions of the detailed and comprehensive experimental and analytical investigations of RMBEs outlined in this dissertation. Furthermore, it presents the conclusions of the numerical study and simple recommendations for the seismic design of RMSW+BEs through the studied design parameters. Finally, it outlines future research work recommendations that are necessary for the continuous development, evolution, and innovation of the masonry industry.

It should be noted that there might be some overlap between the content of the thesis's chapters. This is mainly to ensure the comprehensiveness of each chapter. It should be also mentioned that some of the test results of the RMBEs that are reported in chapter 4 are utilized in chapter 5 as references.

Chapter 2

Literature Review

2.1 Introduction

This chapter presents a literature review for fully grouted unconfined and confined concrete-masonry prisms, boundary elements, and shear walls. It consists of six sections, where each section provides a summarized review of the available studies in the literature, including the studied parameters, the results, and the conclusions. Section 2.2 presents a summary of literature studies focused on the behaviour of fully grouted concrete-masonry prisms under axial compression loading with different interacting parameters. Section 2.3 discusses the confined concrete-masonry prisms and boundary elements tested under axial compression loading and illustrates previous stress-strain models proposed for confined masonry. Section 2.4 presents confined-concrete stress-strain models being utilized for modelling the lateral cyclic response of RMSW+BEs. Furthermore, section 2.5 reports a summarized discussion of the experimental and numerical studies focused on the seismic response of RMSW+BEs. In conclusion, section 2.6 shows summary and remarkable conclusions drawn from the literature review to outline the literature gap and the significance of the proposed research presented hereinafter.

2.2 Behaviour of Fully Grouted Concrete-Masonry Prisms under Axial Compression

High strength masonry was expected to be achieved by increasing the grout strength and the masonry block strength. However, for grouted masonry, the literature (e.g., Drysdale and Hamid 1979; Fortes et al. 2014; Long et al. 2005; Obaidat et al. 2018; Romagna and Roman 2002) showed that increasing the grout strength for a specific block strength does not result in a significant increase in the corresponding masonry prism compressive strength. Moreover, only a small portion of the grout capacity contributes to that of the masonry prism. The literature (e.g., Drysdale and Hamid 1979; Hamid et al. 1978; Mohamed 2018) indicated that the strength superposition of the masonry assemblage components (i.e., masonry shell and grout) was invalid. This was attributed to the fact that the two components′ peak stresses were reached at different strain levels. Moreover, the inefficiency and reduction of compressive strength of grouted masonry compared to that of their ungrouted counterparts were attributed to four main reasons, namely insufficient grout

compaction, plastic and drying shrinkage of the grout, stress-strain material incompatibility of masonry assemblage (i.e., masonry block and mortar) and the grout core, and the effect of block geometry and bond pattern (Drysdale and Hamid 2005).

Numerous studies have been conducted to investigate the grout strength and grouting effect on masonry prisms′ compressive strength. Drysdale and Hamid (1979) aimed to investigate the grout strength's effect on grouted masonry's compressive strength. Drysdale and Hamid (1979) tested 146 concrete block masonry prisms. These prisms were divided into series of ungrouted, grouted, half block, full block, and zero joint specimens. It aimed to investigate the effect of the grout strength on the compressive strength of the grouted masonry. Five different grout mixes were used to construct the required prisms. Although grout cylinders were sampled to assess the grout compressive strength, grout prisms were moulded between the masonry units′ cells to eliminate the grout water absorption by the masonry blocks. It was observed that increasing the grout strength increased the compressive strength of grouted masonry prisms slightly. Figure 2.1 shows the effect of the compressive strength of grout on the compressive strength of grouted masonry.
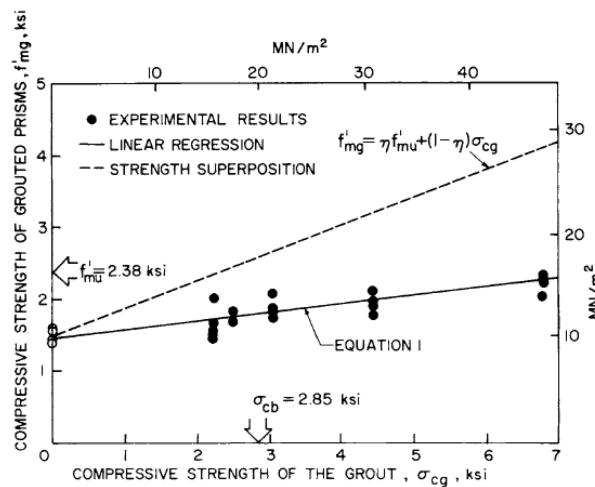
Figure 2.1 Grouted prism strength versus grout strength (Drysdale and Hamid 1979)

It was also indicated that the ungrouted masonry demonstrated a higher compressive strength than its grouted counterpart. Furthermore, the superposition of the masonry shell strength and the grout strength was found to overestimate grouted masonry's compressive strength. This was mainly attributed to the incompatibility of deformational characteristics of the grout and the masonry block. Besides, it was suggested that the excessive lateral tensile strains exerted by the

10

grout core, due to the vertical compression strains, on the masonry block, resulted in premature failure of the masonry shell characterized by the tensile splitting failure of the masonry shell. This supported the observation of the intact grout core after the failure of the masonry prism. The researchers recommended that matching the deformation characteristics would effectively enhance grouted masonry's compressive strength rather than increase the grout strength.

Baba and Senbu (1986) examined the grout strength effect on masonry prisms' compressive strength using different shapes of masonry blocks. Various combinations of the components were used to represent the traditional construction in Japan. All the prisms were either 3 or 5 courses high. It was concluded that the influence of the grout strength on the compressive strength of masonry prisms was dependent on the shape and the characteristics of the masonry blocks.

Khalaf et al. (1994) studied the effect of changing the concrete infill strength (i.e., grout strength) on masonry prisms' compressive behaviour. A total of 57 full-block and 39 half-block 3-course-high masonry prisms were tested under axial compression to derive an empirical equation for the compressive strength (f'_m) of the block masonry work. Three different concrete infill strengths were used to construct the filled prisms: low strength, medium strength, and high strength. It was found that for 3-course-high masonry prisms that had different mortar joint strengths and types, the presence of concrete infill (i.e., grout) for both full- and half-block masonry prisms dramatically reduced the compressive strength of the tested prisms compared to their unfilled counterparts, as shown in Figure 2.2.
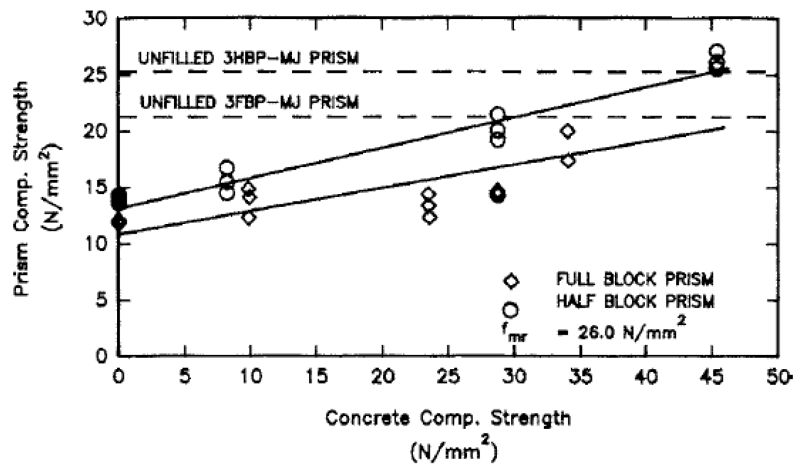
Figure 2.2 Effect of concrete infill strength on filled 3FBP-MJ and 3HBP-MJ prism strength, with similar mortar strength (Khalaf et al. 1994)

11

Except for the previously mentioned result, only when the concrete infill's deformational characteristics matched those of the concrete block, the highest compressive strength was gained. This gain was achieved by a cube compressive strength of the concrete infill 45-50% greater than that of the surrounding concrete masonry block.

Steadman et al. (1995) studied the effect of fine and coarse grout varied between standard and high strength grout mixes on masonry prisms' compressive strength. They tested four-blocks high by one-block long prisms constructed in a running bond pattern under axial compressive loading. Steadman et al. (1995) addressed the strong coarse grout's contribution to the highest achieved compressive strength of the tested prisms that exceeded the ungrouted masonry prisms. However, in general, increasing the grout compressive strength was found to increase the masonry prisms' capacity but not the compressive strength compared to their ungrouted counterparts. That means the strength of hollow concrete masonry prisms was considerably higher than its fully grouted counterparts.

Romagna and Roman (2002) studied the influences of the components of grouted masonry on the compressive behaviour and the mode of failure of ungrouted and grouted masonry prisms. The prisms were built using three different concrete block compressive strengths, two mortar strengths, two types of bedding joints (i.e., face shell and full bedding), and four different grout mixes of low, medium, and high strengths. All the prisms were three units high constructed with a stack bonded pattern. The results showed that for a specific block strength and mortar strength (full bedded prisms), increasing the grout strength resulted in a slight gain in the masonry prisms' compressive strength. The best results were recorded when the compressive strength of the grouts and the blocks were almost matched.

Fortes et al. (2014) examined the relationship between the ungrouted and grouted masonry compressive strength and the strength of the masonry block using four different grout mixtures. This was conducted by testing 192 two-course high masonry prisms having eight different block strengths, five mortar mixes, and four grout compressive strengths. It was concluded that ungrouted masonry's compressive strength was highly efficient than its grouted masonry counterpart.

12

Mohamed (2018) studied the effect of changing the grout compressive strength on the C-shape boundary element prisms′ compressive response. The masonry prisms were either four courses or ten courses high built in a stacked pattern representing aspect ratios of 2 and 5. Grout cores and ungrouted prisms (i.e., masonry shell) were also constructed with the same height as the grouted masonry prisms to validate the concept of the superposition of the masonry shell and the grout core. The researcher reported that increasing the grout compressive strength from 15 MPa to 45 MPa resulted in an increase of approximately 50% in the peak stress. It was found that the simple superposition concept of the masonry shell capacity and the grout core capacity was invalid, as illustrated in Figure 2.3. This was mainly attributed to the grout shrinkage, which resulted in bilateral tensile cracks and breaking the bond at the masonry shell-grout core interface leading to a much lower compressive strength contribution to the masonry prism.
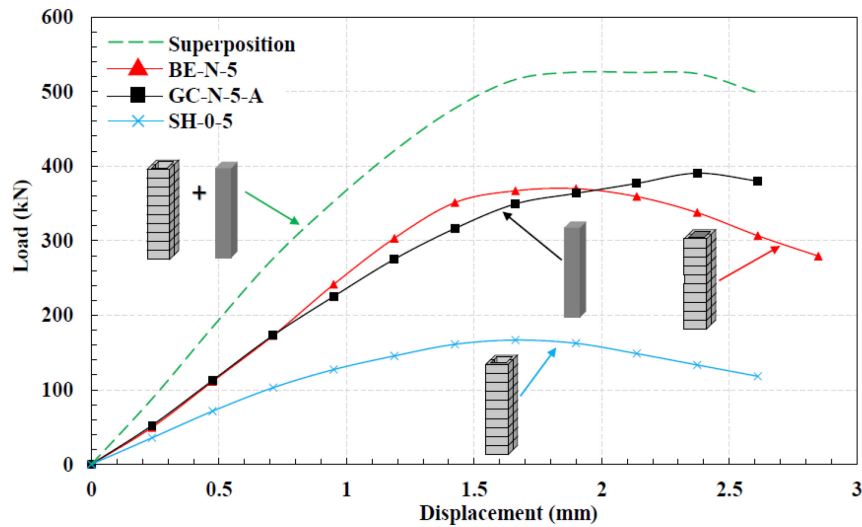
Figure 2.3 Superposition of the masonry shell and the grout core strengths (Mohammed 2018)

Limited studies have been conducted on the effect of scaling on the behaviour of masonry structures. Due to the laboratory testing facilities′ physical and cost limitations, testing full-scale masonry assemblages, components, and systems could be unfeasible. Abboud et al. (1990) examined the feasibility of using a one-quarter scale model masonry unit in predicting the response of concrete block masonry. Three different models duplicate the standard 6 and 8 in. prototype available in North America were studied. Moreover, the behaviour of modeled masonry materials, namely the mortar, the grout, and the reinforcement, was also reported. The concrete block masonry behaviour under axial compression, joint shear, and diagonal tension was compared and

13

correlated to the prototype. This was conducted on three courses masonry prisms and four courses masonry wallets, respectively. Besides, model slender wall panels were tested under monotonic and cyclic out of plane loading either with axial or without axial loading. The researchers indicated that the model units confidentially behaved like the prototype for the material and the assemblage levels. Although minimal deviations arose, good-to-excellent correlations of the model and the prototype were reported. In other words, it was concluded that direct modelling of the prototype concrete block masonry is a feasible and economical technique to investigate with a better understanding of complex masonry systems′ behaviour.

Half-scale masonry units were first proposed in a research program to model and investigate the in-plane behaviour of reinforced masonry shear walls at McMaster University in 2005. In this regard, Long et al. (2005) investigated the behaviour of half-scale, full-scale, hollow, and grouted concrete block masonry assemblages under axial compression and diagonal tension. The material properties, the masonry units, and the masonry assemblages (i.e., 4-course masonry prisms in compression and wallets in tension) were also examined. Figure 2.4 shows the half-scale and full-scale masonry prisms tested by Long et al. (2005).
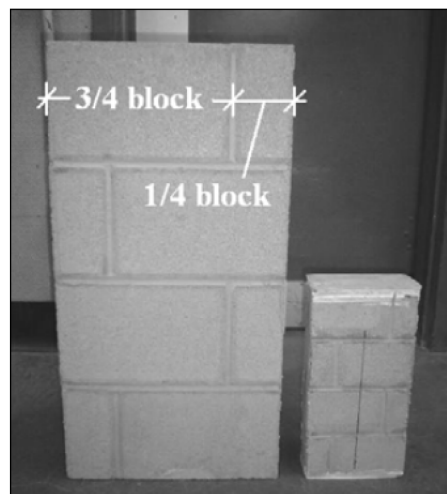
Figure 2.4 Full-scale and half-scale masonry prisms (Long et al. 2005)

It was found that the stress-strain behaviour of both half-scale and full-scale masonry are comparable, especially for the grouted masonry. Also, the half-scale masonry exhibited similar strength and failure modes as the full-scale prototype. It was concluded that the half-scale masonry could be used as a suitable model in the behaviour of full-scale grouted masonry shear walls.

14

Various studies have been carried out to assess the influence of the masonry units′ compressive strength on the behaviour and compressive strength of fully grouted masonry. Romagna and Roman (2002) found that, for both face-shell and full-bedding joints in ungrouted masonry prisms, the block strength increase rendered an unproportioned increase in the compressive strength. On the contrary, for grouted masonry prisms, increasing the block strength significantly increased the compressive strength of face-shell bedded joints rather than those with full bedded joints.

Ross (2013) studied the relationship between the concrete masonry unit strength and the grouted masonry prisms′ compressive strength to recalibrate the previously prescribed masonry strength values for type S and N mortars in the Canadian standards CSA S304.1-04. This was conducted on 105 masonry prisms, each three-courses high and built in a running bond pattern. Nominal strengths of the units used ranged from 10 to 40 MPa. It was reported that the tested specified compressive strength values were found to be 9% - 36 % higher than the standard prescribed values for type S mortar, whereas 37 % - 62% higher than that of the prescribed values for the prisms constructed with type N mortars.

Fortes et al. (2014) studied the effect of the compressive strength of 8 different unit strength on the compressive strength of ungrouted and grouted concrete block masonry prisms. This was conducted using five mortar mixtures and four different grout strengths. The block compressive strength ranged between 21.6 MPa to 74.7 MPa. It was concluded that the masonry prisms′ compressive strength was significantly increased by increasing the unit strength. Nonetheless, this increase was not proportional. It was reported that up to a specific limit, the relationship; the masonry prism strength-the masonry unit decreases with increasing the unit strength. For the ungrouted masonry, the masonry compressive strength to the unit strength ratio varied from 0.8 to 0.5 for low and high masonry units, respectively. On the other hand, for the grouted masonry, this ratio ranged from 0.7 to 0.4 for low and high strength masonry blocks, respectively. Increasing the block strength significantly enhanced the ungrouted masonry's compressive strength rather than the grouted masonry blockwork.

Limited studies have been conducted to assess the effect of breaking the bond at the masonry shell-grout core interface to examine its effect on the grout shrinkage and grouted masonry's compressive strength. Sturgeon et al. (1980) tested 47 four blocks high concrete block masonry

prisms constructed with 16 in. pilaster units. Different grout strengths varied from 1500 psi to 6000 psi were used to construct the masonry prisms. It aimed to investigate the masonry shell-grout core relationship and establish a correlation between the small-scale control masonry prisms and full-scale masonry columns. Therefore, eight masonry prisms were previously lined using a paper towel to eliminate the bond between the masonry shell and the grout core and remove the stripped grout core after masonry prisms′ construction. It was reported that the stripped grout cores averaged 74 % of their concrete cylinders′ compressive strengths. Therefore, it was implied that the best representation of the masonry grout core strength is the moist cured grout cylinders, especially for pilaster units with paper towels in cores acting as a moisture barrier to the grout core. It was concluded that the stripped grout cores′ compressive strength was higher than their counterpart's cores engaged in the masonry prism.

There are no specific studies conducted on the effect of grout shrinkage on the compressive behaviour of the masonry prisms. However, the grout shrinkage remarked one of the most affecting parameters for reducing the masonry prisms′ compressive strength. It is also deemed one of the parameters that deactivated the superposition concept between the masonry shell and the grout core, especially in concrete block masonry prisms.

Boult (1979) observed the significant effect of the infill grout's plastic shrinkage on the grouted masonry's lower compressive strength. It was reported that the plastic shrinkage of the grout due to the absorption of the grout free water by the masonry blocks led to shrinkage cracks at the interface of the masonry shell with the grout cores. Given the masonry units′ flared cells and webs to accommodate the mortar joints, it was implied that the widened face shells and webs restricted the shrinkage of the grout cores at each mortar joint along the prism's height. Such a restriction resulted in substantial cracks along the grout core, which reduced the grout core's contribution to the grouted masonry prisms′ compression capacity. This was also in agreement with another research was conducted by Drysdale and Hamid (1979) and Drysdale and Hamid (2005), that is; the geometry of the masonry unit (i.e., flared and tapered face shells and webs) resulted in a wedge in the grout core cross-section that in turn reduced its integration as a significant component of grouted masonry prisms.

Joyal (2014) examined the effectiveness of two types of anti-shrinkage grout in fully grouted concrete masonry prisms. The aim was to eliminate the grout shrinkage's effect on the strength

drop after the self-confined concrete-block grouted masonry prisms′ peak stress. The anti-shrinkage grout was found to have no significant improvement to the stress drop just after the peak stress.

2.3 Behaviour of Confined Concrete-Masonry under Axial Compression

Priestly and Elder (1983) tested twenty-one full-scale five-course high running-bond grouted concrete masonry prisms under axial compression. The researchers aimed at investigating the masonry block width (i.e., 140 mm and 190 mm), longitudinal reinforcement placed in the grouted cells, confining thin steel plates (i.e., Priestly plate) at the mortar joints, and the strain rate were on the compressive stress-strain behaviour of the masonry prisms. Figure 2.5 shows the dimensions of the confining plate as well as the construction of the masonry prisms.
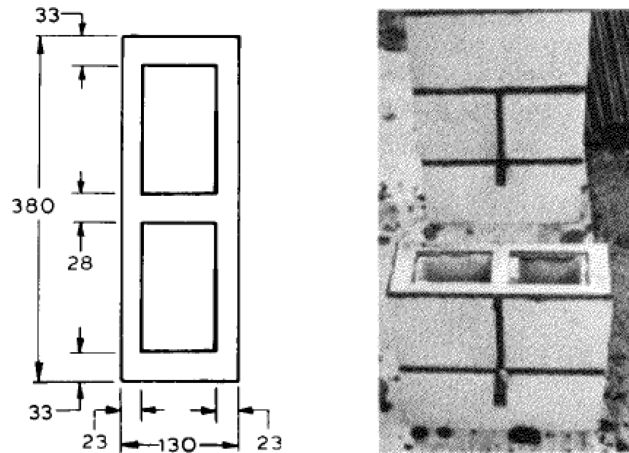
Figure 2.5 Dimensions of the confining plate (left) and construction of the masonry prisms (right) (Priestly and Elder 1983)

The researchers concluded that the unconfined prisms experienced the same mode of failure described by Hamid and Drysdale (1979) in which a premature failure of the masonry shell occurred before crushing the masonry grout core. Also, there was no significant influence for changing the block width on the masonry prisms′ stress-strain behaviour, although the net/gross area ratios were different for both blocks. The steel confining plates placed at the mortar joints enhanced the masonry prisms′ post-peak behaviour generating a more gradual falling branch than unconfined grouted prisms. Moreover, increasing the strain rate from 0.000005 to 0.005 per second

increased the peak stress by 17% and resulted in a more steepening descending branch for the confined grouted concrete masonry prisms.

Priestly and Elder (1983) modified the Kent-Park stress-strain model for reinforced concrete prisms to adequately predict the behaviour of confined and unconfined concrete masonry prisms, as shown in Figure 2.6. The modified model equations are given from Eq. 2.1 – 2.6.
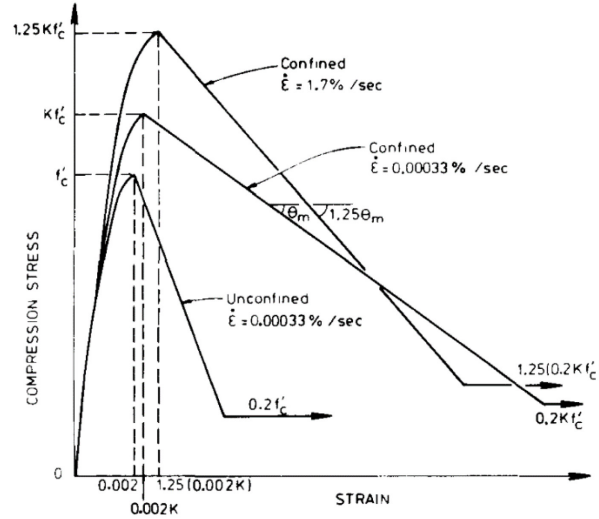
Figure 2.6 Modified Kent-Park curve for confined concrete (Priestly and Elder 1983)

- **Unconfined masonry**

The rising curve masonry stress is given by

$$f_m = 1.067 f'_m \left[\frac{2\,\varepsilon_c}{0.002} - \left(\frac{\varepsilon_c}{0.002} \right)^2 \right] \qquad\qquad \varepsilon_c \leq 0.0015 \tag{2.1}$$

Where ε_c and f_m are the masonry axial strain and corresponding stress, respectively, and f'_m is the masonry compressive strength.

The falling branch masonry stress is given by

$$f_m = f'_m [1 - z_m (\varepsilon_c - 0.0015)] \qquad\qquad \varepsilon_c > 0.0015 \tag{2.2}$$

Horizontal plateau follows the falling branch when f_m is equivalent to $0.2\,f'_m$.

- **Confined masonry**

The proposed confined masonry model consists of three curves as follows:

18

Rising curve

$$f_m = 1.067 kf'_m \left[\frac{2\,\varepsilon_c}{0.002k} - \left(\frac{\varepsilon_c}{0.002k} \right)^2 \right] \qquad \varepsilon_c \leq 0.002k \qquad (2.3)$$

Falling branch

$$f_m = kf'_m [1 - z_m(\varepsilon_c - 0.002k)] \qquad \varepsilon_c > 0.002k \qquad (2.4)$$

$$k_d = 1.17 \left[1 + \rho_s \frac{f_{yh}}{f'_m} \right] \qquad\qquad (2.5)$$

$$z_m = \frac{1.17 \times 0.5}{\left[\frac{3 + 0.29 f'_m}{145 f'_m - 1000} \right] + \frac{3}{4} \rho_s \sqrt{\frac{h''}{s_h}} - 0.002 k_d} \qquad\qquad (2.6)$$

where h'' is the width of the concrete masonry block and s_h is the spacing between the confining plates.

Horizontal plateau following the falling branch

f_m is assumed to be equivalent to $0.2\,f'_m$.

Dhanaseker and Shrive (2002) tested thirty-three three courses high with stack-bonded pattern concrete masonry prisms built from the standard 390x190x190 mm blocks. The prisms were divided into five groups: hollow prisms with face shell bed, hollow prisms, grouted prisms, grouted prisms with fine wire mesh (FWM), and grouted prisms with welded wire mesh (WWM). Figure 2.7 shows the details of the confining reinforcement of the grouted cells.
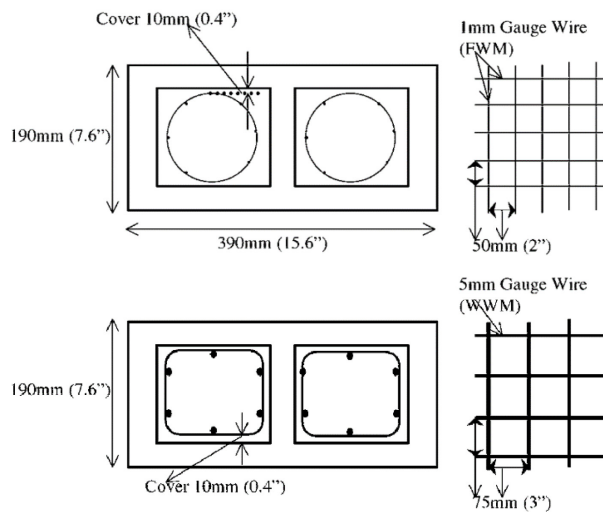
Figure 2.7 Details of the confining reinforcement placed in the grouted cells (Dhanaseker and Shrive 2002)

The mesh was used in the grout core to confine the grout cells such that the compressive strength of grouted masonry may be more than their ungrouted counterparts. At least two prisms from each group were tested monotonically under compression, whereas the remaining prisms were tested under uniaxial cyclic compression loading. All the prisms were tested under a constant rate of straining of 6.67 μm/sec. The researchers concluded that the masonry prisms constructed with FWM and WWM showed an enhanced compressive strength of 29 and 38% compared to their regularly grouted prisms, respectively. Moreover, the strains corresponding to the peak stress exhibited an enhanced 20 and 36% increase compared to the regular grouted prisms.

Dhanaseker and Shrive (2002) developed stress-strain simple and refined equations for the concrete masonry prisms′ cyclic behaviour. The equations were modified based on previously developed mathematical expressions available in the literature. The two equations were opted to obtain the envelope and the common points curve for the masonry prisms′ cyclic stress-strain response.

$$y = y_{max} \left[\frac{u_0 \varepsilon}{1 + x^{u_1}} \right]$$ (2.7)

$$y = y_{max} \left[\frac{(1 + u_0(1 + u_1))x}{u_0(1 + u_1 x) + x^{u_0 + 1}} \right]$$ (2.8)

Where:

x	= Normalized strain ($\varepsilon/\varepsilon_0$)
ε_0	= Mean strain corresponding to the mean peak stress
y	= Normalized stress (σ/σ_0)
σ_0	= Mean peak-stress
u_0, u_1	= Experimental constants for each curve determined separately

The experimental constants (u_0, u_1) for non-dimensional equations are given in Table 2.1.

Table 2.1 Experimental constants (u0, u1) in non-dimensional equations for various types of masonry (Dhanaseker and Shrive (2002))

	Simple equation (Eq. 2.7)		Refined equation (Eq. 2.8)	
Masonry type	u_0	u_1	u_0	u_1
Face-shell bedded (FSP)	1.4	2.6	2.1	0.1
Grouted unconfined (GUP)	2.0	2.0	1.5	1.0
FWM (GMP)	2.0	2.4	2.0	1.2
WWM (GCP)	2.0	2.3	2.3	1.5
Full-bedded (HOP)	2.0	2.2	2.0	1.5

Abo El Ezz et al. (2015) studied the compressive stress-strain behaviour of reinforced masonry boundary elements (RMBE). The researchers aimed at investigating the influence of the confinement reinforcement configuration on the compression behaviour, peak stress, and post-peak behaviour in terms of the strain capacity of RMBE. The intent was to investigate the compression behaviour of RMBE experimentally as a critical component for the seismic design of reinforced masonry shear walls (RMSW). Seventeen full-scale unconfined and confined, reinforced and unreinforced concrete masonry boundary elements were constructed and tested under axial compression loading. All the RMBEs specimens were fully grouted, five-courses high in a running-bond pattern and built using two standards 190x190x390 mm stretcher concrete masonry blocks in each course. The regular blocks′ face shells and webs were cut to accommodate transversal reinforcement's various arrangements (i.e., hoops). The tested specimens had vertical 4 - 20M bars and two different diameters of confinement ties, namely 10M and 15M, and two different spacings, namely 200 mm and 100 mm. Figure 2.8 shows the details of the RMBEs that were tested by the researchers. Unlike a standard masonry block prism, the results showed that unreinforced boundary elements demonstrated enhanced post-peak behaviour with a gradually descending branch with no strength drop was observed. The post-peak strain corresponding to 50% strength degradation was significantly enhanced. The reinforced and confined boundary elements showed an enhanced compressive strength (i.e., peak stress) and a strain capacity compared to the unconfined boundary elements. The confined RMBEs′ peak stress was more than 1.6-2.4 times that of the unconfined BE, whereas the strain at 50% strength degradation ranged from 2.2 to 7 times that of the unconfined RMBEs. It was found that as the confinement ratio increased, the strain ductility increased, and the slope of the falling branch of the stress-strain response decreased (i.e., flattened).

Abo El Ezz et al. (2015) proposed a simplified analytical stress-strain material model for the unconfined and confined concrete masonry RMBEs. They aimed at predicting the inelastic behaviour of RMSW with boundary elements that depends on the complete stress-strain model of its boundary elements. The model incorporated the peak stress, the strain corresponding to the peak stress, the slope of the descending branch of the stress-strain curve, and the ultimate compressive strain. Figure 2.9 shows the proposed stress-strain model for unconfined and confined masonry RMBEs. The proposed unconfined masonry stress train model was based on the Kent and Park model with some modifications.

21
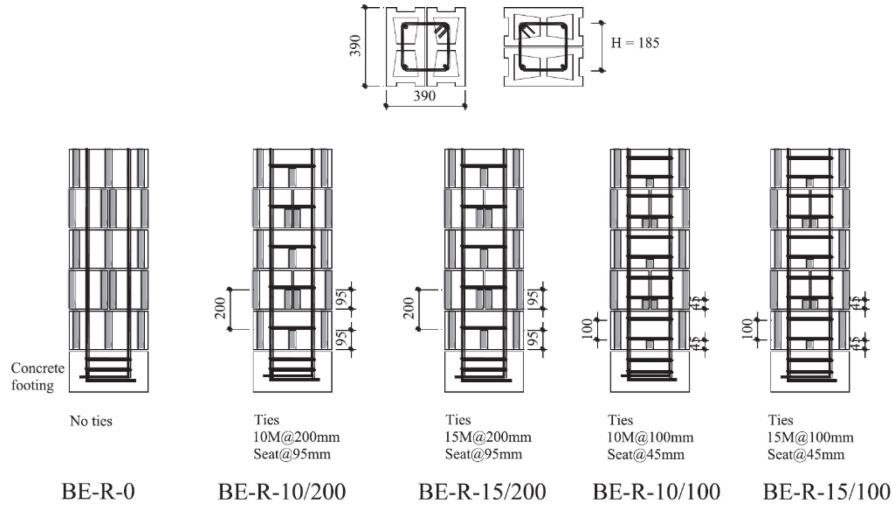
Figure 2.8 Details of reinforced masonry boundary elements tested by Abo El Ezz et al. (2015)

The modified (Kent and Park 1971) model included a plateau portion following the ascending branch and preceding the descending branch based on the observed experimental results. Similarly, the confined stress-strain model was derived based on the Kent and Park model for the ascending branch, including a parabolic curve, and the descending branch was calibrated to the experimental results. The analytical models and the regression equations were a function of the influencing parameters, namely the peak compressive stress of the confined RMBEs, the strain corresponding to the maximum stress, the slope of the falling branch, and the confinement ratio.

(a)   (b)
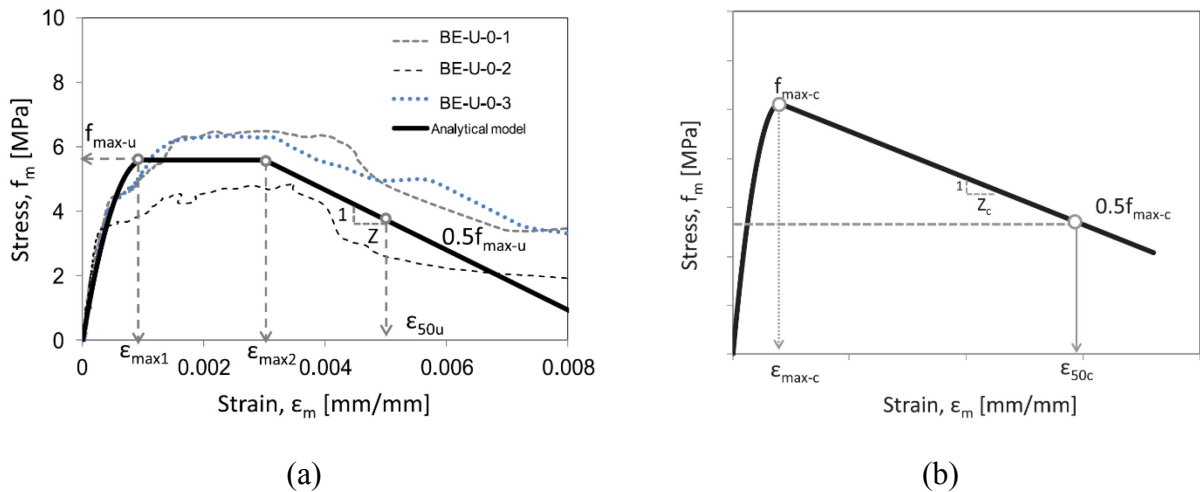
Figure 2.9 Proposed stress-strain curves for (a) unconfined; and (b) confined masonry boundary elements (Abo El Ezz et al. 2015)

- **Unconfined masonry boundary elements (BE)**

  The unconfined masonry stress strain curve is consisted of three branches and described by the following equations:

Parabolic rising curve

$$f_m = f_{max-u} \left[\frac{2\,\varepsilon_m}{\varepsilon_{max1}} - \left(\frac{\varepsilon_m}{\varepsilon_{max1}}\right)^2 \right] \qquad \varepsilon_m \le \varepsilon_{max1} \qquad\qquad (2.9)$$

Horizontal plateau

$$f_m = f_{max-u} \qquad\qquad \varepsilon_{max1} < \varepsilon_m \le \varepsilon_{max2} \qquad\qquad (2.10)$$

Linear falling branch

$$f_m = f_{max-u} \left[1 - z(\varepsilon_m - \varepsilon_{max2}) \right] \qquad \varepsilon_m > \varepsilon_{max2} \qquad\qquad (2.11)$$

$$z = \frac{0.5}{\varepsilon_{50u} - \varepsilon_{max2}} \qquad\qquad (2.12)$$

where f_m is the masonry compressive stress and ε_m is the corresponding axial strain; f_{max-u} is the peak compressive stress for unconfined-unreinforced boundary elements, and ε_{max1} is the corresponding strain averaged 0.001 from the test results; ε_{max2} is the strain at the end of the horizontal plateau region with an average value of 0.003; Z is the slope of the falling branch, and ε_{50u} is the strain corresponding to 50% strength degradation (i.e., on the falling branch) with an average value of 0.005 from the experimental test results.

- **Confined masonry boundary elements (BE)**

  The stress strain curve of the confined masonry core is consisted of two branches and described by the following equations:

Parabolic rising curve

$$f_m = f_{max-c} \left[\frac{2\,\varepsilon_m}{\varepsilon_{max-c}} - \left(\frac{\varepsilon_m}{\varepsilon_{max-c}}\right)^2 \right] \qquad \varepsilon_m < \varepsilon_{max-c} \qquad\qquad (2.13)$$

Linear falling branch

$$f_m = f_{max-c}[1 - z_c (\varepsilon_m - \varepsilon_{max-c})] \qquad\qquad \varepsilon_m > \varepsilon_{max-c} \qquad\qquad (2.14)$$

$$z_c = \frac{0.5}{\varepsilon_{50c} - \varepsilon_{max-c}} \qquad\qquad (2.15)$$

It is worth mentioning that this model has some limitations, such as it did not account for the confined core dimensions and the contribution of the longitudinal reinforcing rebars to the stress-strain behaviour.

To promote a practical construction solution for confined reinforced concrete-masonry boundary elements, Obaidat et al. (2017) proposed C-shaped concrete-block masonry boundary elements. The researchers tested 16 full-scale C-shaped reinforced masonry boundary elements (C-RMBEs) with different confinement reinforcement configurations. Four 20M vertical reinforcement bars were used in the C-RMBE with different volumetric ratios of transverse reinforcement ranging from 0.0089 to 0.0354 %. All the C-RMBE were tested monotonically under uniaxial compressive loading. Figure 2.10 shows the construction and the test setup of the C-RMBE test by the researchers. Obaidat et al. (2017) developed a finite element numerical model to predict the compression stress-strain behaviour of C-RMBEs. It was concluded that increasing the confinement reinforcement ratio significantly enhanced the post-peak behaviour of C-RMBEs in terms of the strain capacity and smoothing the falling branch of the stress-strain curve. Moreover, the numerical model exhibited a satisfying correlation to the experimental results in the pre-peak and the post-peak response of the tested C-RMBE.
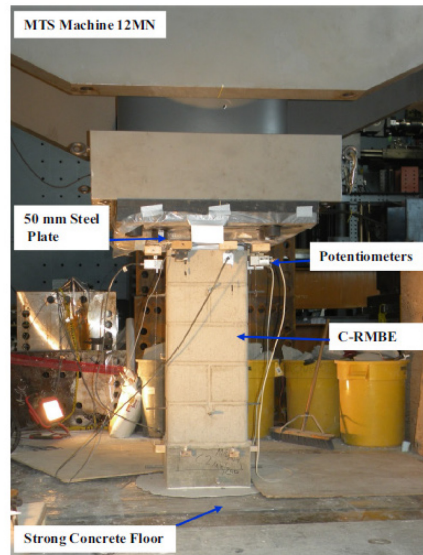
(a)   (b)

Figure 2.10 (a) Construction of C-RMBE; and (b) Test setup of C-RMBE (Obaidat et al. 2017)

Obaidat et al. (2018) tested thirty half-scale fully-grout ten-course high unreinforced and reinforced C-shaped concrete masonry block boundary elements. The reinforced masonry boundary elements represent the end regions of reinforced masonry boundary elements. The influence of the longitudinal reinforcement ratio, the hoop spacing, and the grout strength on the axial compressive stress-strain response was investigated. The test specimens were divided into ten groups; each consists of 3 identical C-shaped reinforced masonry boundary elements (C-RMBE). Two grout strengths were considered, namely 15 and 45 MPa. Two longitudinal reinforcement ratios were investigated, namely 0.8 and 1.4%, whereas three volumetric ratios of confinement reinforcement were studied, namely 0.45, 0.6, and 0.9 % with hoop spacing 60, 45, and 30 mm, respectively. All the test specimens were tested monotonically under uniaxial compressive load under displacement-control of 0.003 mm/sec rate of loading. The test results showed that the stress-strain curve of the confined C-RMBE was characterized by three regions, namely a rising curve to the peak stress, a sudden drop of the observed stress followed by a gradual falling branch. It was found that increasing the grout strength and decreasing the hoops′ spacing (i.e., increasing the transverse confinement ratio) significantly enhanced the peak stress and post-peak behaviour. Increasing the confinement reinforcing ratio from 0.02 to 0.07 resulted in an increase of 28 and 23% for C-RMBE constructed with longitudinal reinforcement ratios of 0.8 and 1.4%, respectively.

Obaidat et al. (2018) compared their test results with three analytical stress-strain models previously developed by literature researchers, namely Priestly and Elder (1983), Mander et al. (1988), and Abo El Ezz et al. (2015) to predict the compressive stress-strain response of unreinforced and confined reinforced concrete concrete-masonry columns. Figure 2.11 illustrates the differences that arose between the predictions and the experimental test results of the researchers. The researchers inferred that compared to the three existing stress-strain models of the above-mentioned researchers for confined concrete and confined masonry was not capable of capturing the stress-strain response of the tested reinforced masonry boundary elements, especially the sudden drop of the stress and the post-peak falling branch.
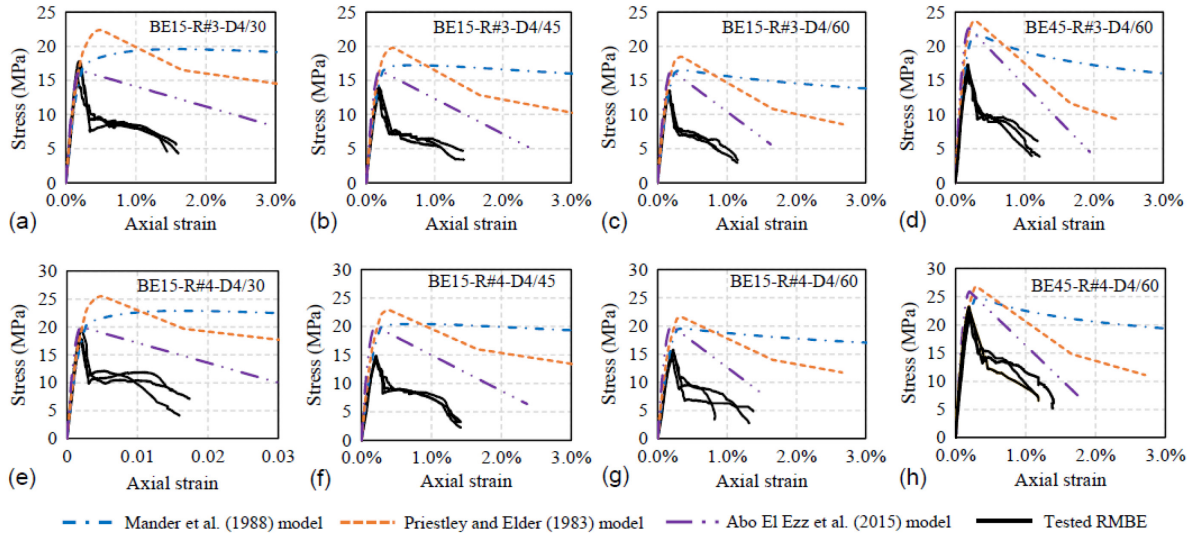
Figure 2.11 Comparison between the observed stress-strain behaviour of the tested C-RMBE and the three predictive models (Obaidat et al. 2018)

To investigate the effect of the aspect ratio and hoop spacing on the compressive stress-strain behaviour of unconfined and confined masonry boundary elements, Obaidat et al. (2019) tested 17 half-scale C-RMBEs with two different aspect ratios, namely 2 and 3, as well as two different hoop spacing namely 30 and 60 mm. The aspect ratio of 2 represents the specimens with 4-course high, whereas the aspect ratio of 3 stands for the C-RMBE constructed with 6-course high all in a stacked-bond pattern. All the C-RMBE tested monotonically under axial compressive load until the failure of the specimens. Moreover, the researchers aimed at developing an empirical compressive stress-strain material model based on the experimental results and the literature, which can predict the compressive stress-strain response of the RMBEs as a vital component of the seismic behaviour of RMSW. The equations of the stress-strain model that was proposed by Obaidat et al. (2019) are summarized as follows:

$$f = f_{mu} \frac{A_{mu}}{A_t} + f_{mc} \frac{A_{mc}}{A_t} + f_s \frac{A_s}{A_t} \tag{2.16}$$

Where f is the compressive stress at a given strain, f_{mu} is the unconfined stress, f_{mc} is the confining stress, f_s is the vertical steel reinforcement stress, A_{mu} is the unconfined zone area, A_{mc} is the confined zone area, A_s is the vertical steel reinforcement area, and A_t is the total cross-section area. Figure 2.12 shows the stress-strain relation of C-RMBE components.
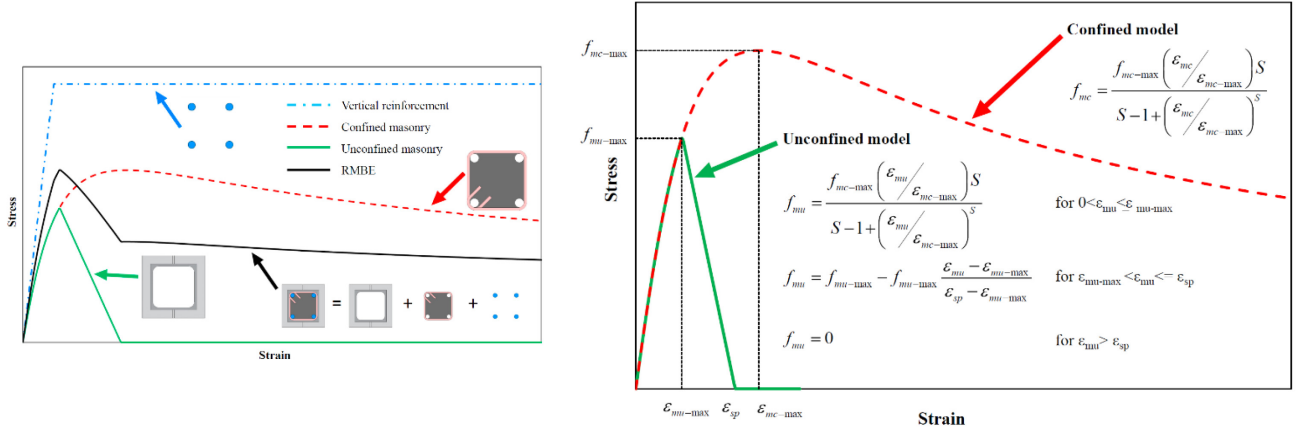
Figure 2.12 RMBEs components (left) Proposed Stress-strain relationships of C-RMBE (right) (Obaidat et al. 2019)

The researchers calibrated their stress-strain model based on an expression previously developed by Mander et al. (1988) to predict the continuous compressive stress-strain behaviour of the unconfined and confined RMBE. The model was calibrated based on the experimental results of 33 specimens having different aspect ratios, vertical reinforcement ratios, horizontal reinforcement ratios, and grout compressive strengths.

- **Unconfined masonry model**

  The following equations describes the rising curve and the falling branch of the unconfined masonry stress-strain behaviour:

$$f_{mu} = \frac{f_{mc\text{-}max}(\frac{\varepsilon_{mu}}{\varepsilon_{mc\text{-}max}})\,s}{s\text{-}1+(\frac{\varepsilon_{mu}}{\varepsilon_{mc\text{-}max}})^{s}} \qquad\qquad 0 < \varepsilon_{mu} \leq \varepsilon_{mu\text{-}max} \qquad\qquad (2.17)$$

$$f_{mu} = f_{mu\text{-}max} - f_{mu\text{-}max}\,\frac{\varepsilon_{mu}\text{-}\varepsilon_{mu\text{-}max}}{\varepsilon_{sp}\text{-}\varepsilon_{mu\text{-}max}} \qquad\qquad \varepsilon_{mu\text{-}max} < \varepsilon_{mu} \leq \varepsilon_{sp} \qquad\qquad (2.18)$$

$$f_{mu} = 0 \qquad\qquad \varepsilon_{mu} > \varepsilon_{sp} \qquad\qquad (2.19)$$

where ε_{mu} is the compressive axial strain of the masonry, $\varepsilon_{mu\text{-}max}$ is the axial strain corresponding to the unconfined peak stress $f_{mu\text{-}max}$, $f_{mc\text{-}max}$ and $\varepsilon_{mu\text{-}max}$ are the confined masonry peak stress and its corresponding strain, respectively, S is the parameter which guides the degradation slope, and ε_{sp} is the spalling strain of unconfined masonry.

- **Confined masonry model**

  The stress-strain response of the confined masonry core is described by the following equation that is function in the parameter s and the peak stress of the confined masonry core and its corresponding strain.

  $$f_{mc} = \frac{f_{mc\text{-}max}(\frac{\varepsilon_{mc}}{\varepsilon_{mc\text{-}max}})\, s}{s\text{-}1+(\frac{\varepsilon_{mc}}{\varepsilon_{mc\text{-}max}})^{s}} \tag{2.20}$$

  where f_{mc} and ε_{mc} are the compressive stress and strain of confined masonry core at any given strain level, respectively. Two sets of empirical equations were proposed to calculate the values of $f_{mc\text{-}max}$, $\varepsilon_{mc\text{-}max}$, and S. The first set of the empirical equations are high-order polynomial equations, whereas the second set is a simple linear regression with lower R^2 values.

  The researchers reported that decreasing the aspect ratio (i.e., height to thickness ratio) and/or increasing the confinement ratio resulted in an increase in the peak stress and the post-peak strain capacity of the C-RMBE. Moreover, it was concluded that the proposed empirical stress-strain model could predict the compressive stress-strain behaviour of RMBEs compared to the experimental results.

2.4 Stress-Strain Models of Confined Concrete

Mander et al. (1988) developed a stress-strain model for the confined concrete columns based on a literature equation and an energy balance approach in which the strain energy stored in the confined concrete core was equated to that of the confinement hoops at yielding. Figure 2.13 illustrates the proposed monotonic stress-strain curve for confined concrete under slow strain rates by Mander et al. (1988).
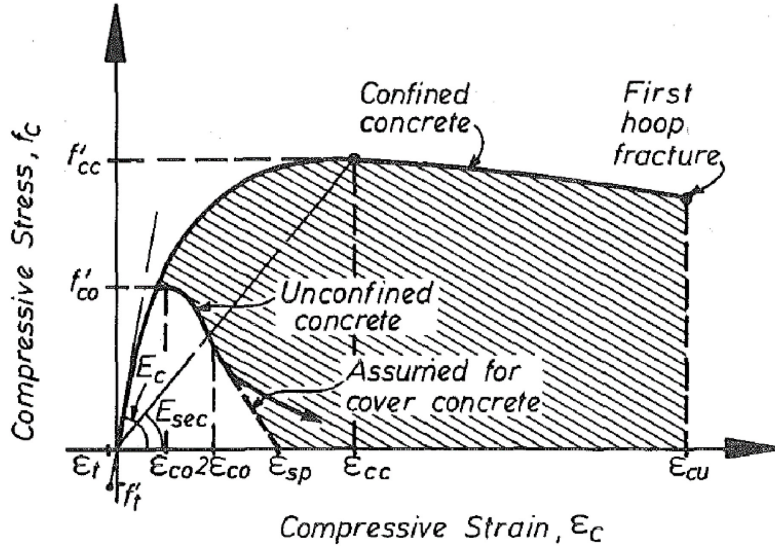
Figure 2.13 Proposed stress-strain model for confined and unconfined concrete under monotonic loading (Mander et al. 1988)

The following equations give the confined concrete compressive stress (f_c) at given concrete strain (ε_c):

$$f_c = \frac{f'_{cc}\, x\, r}{r - 1 + x^r} \tag{2.21}$$

where f'_{cc} is the compressive strength of concrete.

$$x = \frac{\varepsilon_c}{\varepsilon_{cc}} \tag{2.22}$$

where ε_c = longitudinal compressive concrete strain

$$\varepsilon_{cc} = \varepsilon_{co}\left[1 + 5\left(\frac{f'_{cc}}{f'_{co}} - 1\right)\right] \tag{2.23}$$

where f'_{co} *and* ε_{co} = the unconfined concrete strength and corresponding strain, respectively. The strain ε_{co} is assumed to be 0.002.

$$r = \frac{E_c}{E_c - E_{sec}} \tag{2.24}$$

where E_c is the tangent modulus of elasticity of the concrete.

$$E_c = 5000\sqrt{f'_{co}} \tag{2.25}$$

E_{sec} is the secant modulus of the confined core at peak stress and given by

$$E_{sec} = \frac{f'_{cc}}{\varepsilon_{cc}} \tag{2.26}$$

where f'_{cc} is calculated by

29

$$f'_{cc} = -1.254 + 2.254 \sqrt{1 + \frac{7.94\,f'_l}{f'_{co}}} - 2\frac{f'_l}{f'_{co}} \tag{2.27}$$

For circular concrete columns (See Figure 2.14), the effective lateral confining stress (f'_l) is calculated by:

$$f'_l = \frac{1}{2}\,k_e\,\rho_h\,f_{yh} \tag{2.28}$$

where ρ_h is the volumetric ratio of confinement steel to the confined masonry core; f_{yh} is the yield strength of the transverse confinement steel; and k_e is the confinement factor, which is defined by the following equation:

$$k_e = \frac{(1 - \sum_{i=1}^{n} \frac{(w'_i)^2}{6 b_c d_c})(1 - \frac{s'}{2 b_c})(1 - \frac{s'}{2 d_c})}{(1 - \rho_{cc})} \tag{2.29}$$

where w'_i is the ith clear distance between adjacent vertical steel bars; ρ_{cc} is the ratio of vertical steel to the confined core area; s' is the clear vertical spacing between adjacent confinement hoops; b_c and d_c are the confined core dimensions measured between centerlines of confinement hoops in x and y directions, respectively, where $b_c \geq d_c$.
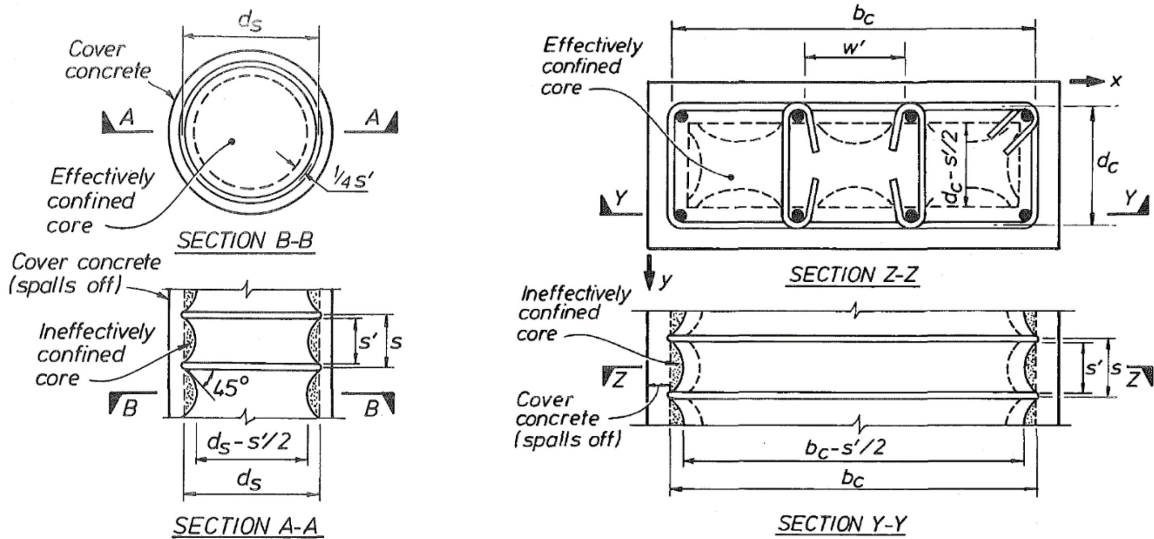
Figure 2.14 Effectively Confined core for circular and rectangular concrete columns

It should be noted that for rectangular RMBEs, the confinement factor k_e is calculated based on the effective lateral confining stresses in x and y directions calculated by

$$f_{lx} = \rho_x\,f_{yh} \tag{2.30}$$

$$f_{ly} = \rho_y\,f_{yh} \tag{2.31}$$

where ρ_x and ρ_y = the volumetric ratio of confinement hoops to the confined core in x and y directions, respectively. Based on the values of f_{lx} and f_{ly}, the k_e can be obtained, as shown in Figure 2.15.
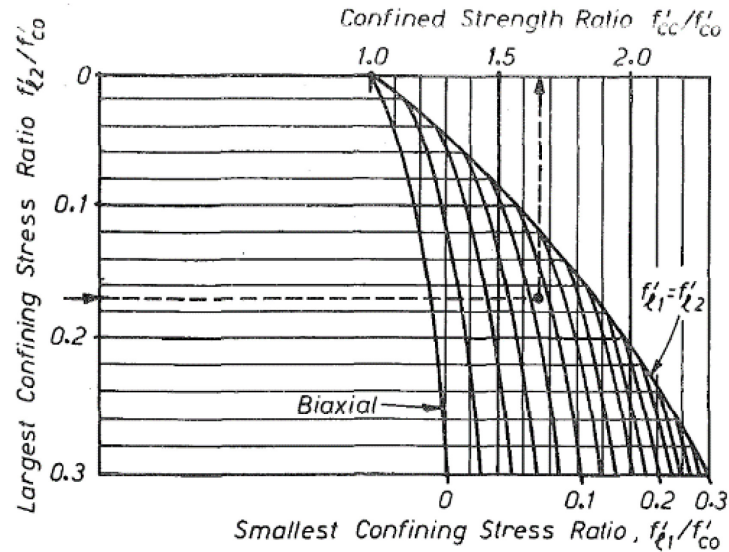
Figure 2.15 Confined strength determination from lateral confining stresses for rectangular concrete columns (Mander et al. 1988)

Mander et al. (1988) developed a stress-strain model for the cyclic loading of confined reinforced concrete columns based on an approach previously developed in the literature. The researchers assumed that the monotonic stress-strain curve is the limiting envelope curve for the cyclic stress-strain curves of reinforced concrete specimens based on their experimental research in 1984. Previous researchers also confirmed this assumption (e.g., Sinha et al. 1964, Karsan and Jirsa 1969) for unconfined concrete. The stress-strain model was derived based on a series of equations that can be summarized as follows:

- **Unloading Branches**

For unloading from the compression loading curve, a plastic strain ε_p based on the coordinates of the reversal point $(\varepsilon_{un}, f_{un})$ shall be computed. Figure 2.16 describes the stress-strain curves for unloading branch and determination of the plastic strain ε_p from a common strain point ε_a.

$$\varepsilon_a = a \sqrt{\varepsilon_{un}\, \varepsilon_{cc}} \tag{2.32}$$

where a is the greater of

31
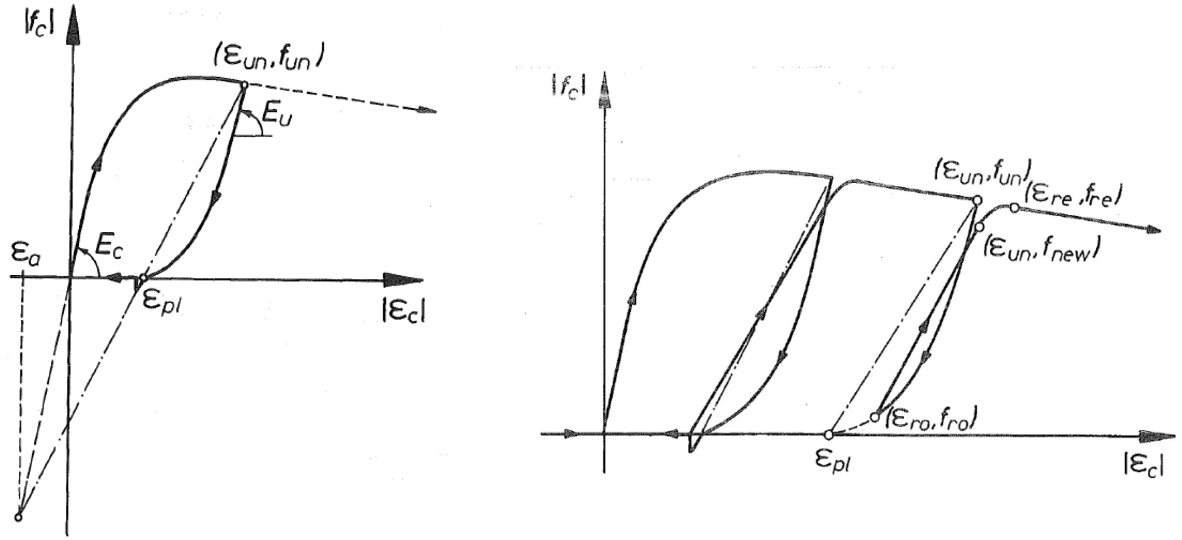
Figure 2.16 Stress-strain cyclic curves for confined concrete proposed by Mander et al. (1988)

$$a = \frac{\varepsilon_{cc}}{\varepsilon_{cc} + \varepsilon_{un}} \quad or \tag{2.33}$$

$$a = \frac{0.09\, \varepsilon_{un}}{\varepsilon_{cc}} \tag{2.34}$$

The plastic strain, ε_p, can be calculated as:

$$\varepsilon_{pl} = \varepsilon_{un} - \frac{(\varepsilon_{un} + \varepsilon_a)\, f_{un}}{(f_{un} + E_c \varepsilon_a)} \tag{2.35}$$

The unloading curve is defined by the longitudinal concrete compressive stress as follows:

$$f_c = f_{un} - \frac{f_{un}\, x r}{r - 1 + x^r} \tag{2.36}$$

in which

$$r = \frac{E_u}{E_u - E_{sec}} \tag{2.37}$$

$$E_{sec} = \frac{f_{un}}{\varepsilon_{un} - \varepsilon_{pl}} \tag{2.38}$$

$$x = \frac{\varepsilon_c - \varepsilon_{un}}{\varepsilon_{pl} - \varepsilon_{un}} \tag{2.39}$$

where E_u = initial modulus of elasticity at the onset of unloading, which is given by

$$E_u = bc E_c \tag{2.40}$$

32

$$b=\frac{f_{un}}{f'_{co}} \geq 1 \tag{2.41}$$

$$c=(\frac{\varepsilon_{cc}}{\varepsilon_{un}})^{0.5} \leq 1 \tag{2.42}$$

- **Reloading Branches**

Figure 2.16 describes the stress-strain curves for unloading and reloading branches in which the coordinates of the point of reloading are (ε_{ro}, f_{ro}).

The new stress point, *f_{new}, is assumed to be given by the following equation*

$$f_{new}=0.92f_{un}+0.08f_{ro} \tag{2.43}$$

The parabolic transition curve is used between the linear relations is given by

$$f_c=f_{ro}+E_r(\varepsilon_c-\varepsilon_{ro}) \tag{2.44}$$

$$E_r=\frac{f_{ro}-f_{new}}{\varepsilon_{ro}-\varepsilon_{un}} \tag{2.45}$$

The monotonic stress-strain curve return coordinates (ε_{re}, f_{re}) can be calculated as follows:

$$\varepsilon_{re}=\varepsilon_{un}+\frac{f_{un}-f_{new}}{E_r(2+\frac{f_{cc}}{f_{co}})} \tag{2.46}$$

Then the parabolic transition curve is given by

$$f_c=f_{re}+E_{re}x+Ax^2 \tag{2.47}$$

$$x=(\varepsilon_c-\varepsilon_{re}) \tag{2.48}$$

$$A=\frac{E_r-E_{re}}{-4[(f_{new}-f_{re})-E_r(\varepsilon_{un}-\varepsilon_{re})]} \tag{2.49}$$

where

E_{re} = the common return point tangent modulus;

f_{re} = the stress determined from the return point, ε_{re}, using the monotonic stress-strain relation.

Martinez-Rueda and Elnashai (1997) developed a uniaxial cyclic model for unconfined and confined reinforced concrete. The researchers developed their stress-strain model based on modifications on the existing Mander et al. (1988) model. The proposed model was then compared with experimental results from the researchers′ tests to ensure the analytical model's applicability

to reinforced concrete members with axial-flexure behaviour characteristics. The researchers′ rectified the rules for cyclic strength degradation, inelastic strain, and the shape of the unloading branches of those previously developed by Mander et al. (1988). Figure 2.17 depicts the stress-strain curves for unloading and reloading branches for the proposed model.

- **Inelastic strain**

The inelastic strain, ε_{pl} is given by Eq. 2.50 – 2.52 based on low, intermediate, and high strain ranges.

$$\varepsilon_{pl}=\varepsilon_{un}-\frac{f_{un}}{E_c}, \qquad\qquad 0\leq\varepsilon_{un}\leq\varepsilon_{35} \qquad\qquad (2.50)$$

$$\varepsilon_{pl}=\varepsilon_{un}-\frac{(\varepsilon_{un}+\varepsilon_a)}{(f_{un}+E_c\varepsilon_a)}, \qquad\qquad \varepsilon_{35}\leq\varepsilon_{un}\leq2.5\varepsilon_{cc} \qquad\qquad (2.51)$$

$$\varepsilon_{pl}=\frac{f_{cr}\,\varepsilon_{un}\,|\varepsilon_f|}{(f_{cr}+f_{un})}, \qquad\qquad 2.5\varepsilon_{cc}\leq\varepsilon_{un} \qquad\qquad (2.52)$$

where ε_{35} is the strain corresponding to a stress of 0.35 f'_c in the ascending branch of the stress-strain curve.
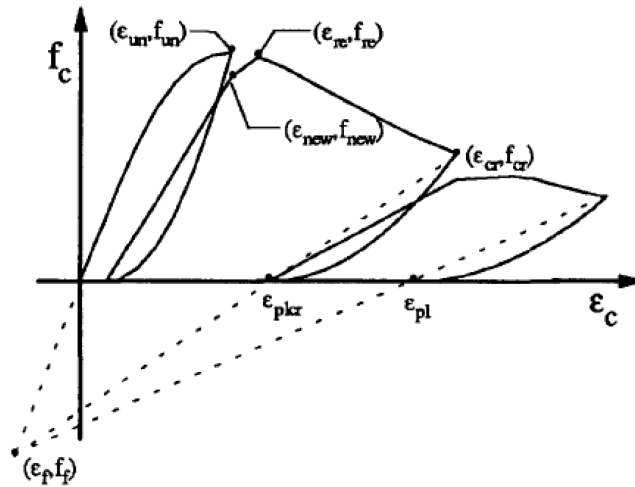
Figure 2.17 Stress-strain cyclic curves proposed by Martinez-Rueda and Elnashai (1997)

The focal point (ε_f, f_f), which is defined based on the upper limit in the intermediate strain range, can be obtained from Eq. 2.53 – 2.55.

$$|\varepsilon_f|=\frac{f_{cr}\,\varepsilon_{plcr}}{E_c(\varepsilon_{cr}\varepsilon_{plcr})-f_{cr}} \qquad\qquad (2.53)$$

$$|f_f| = E_c|\varepsilon_f|$$ (2.54)

$$\varepsilon_{cr} = 2.5\varepsilon_{cc}$$ (2.55)

Where ε_{plcr} is the inelastic strain corresponding to the upper limit of the intermediate strain range ε_{cr}.

- **Unloading branches**

The unloading curves are presented in the form of a second-degree parabola connecting the reversal point (ε_{un}, f_{un}) with the current full-reversal point (ε_{un}, 0) at which a zero slope is considered.

$$f_c = f_{un}\left(\frac{\varepsilon_c - \varepsilon_{pl}}{\varepsilon_{un} - \varepsilon_{pl}}\right)^2$$ (2.56)

- **Loading and reloading branches**

A straight line is fitted between the point of reloading (ε_{ro}, f_{ro}) and the degrading strength point (ε_{un}, f_{new}) when strains are less than the maximum strain ever experienced, ε_{un}. Then, f_{new} is assumed to be located on the curve of common points, which can be given by a modified version of the Popovics (1973) equation through Eq. 2.57 – 2.64.

$$f_{new} = \frac{f'_{cc2}xr}{r-1+x^r}$$ (2.57)

$$f'_{cc2} = 0.9f'_{cc}$$ (2.58)

$$x = \frac{\varepsilon_c}{\varepsilon_{cc2}}$$ (2.59)

$$\varepsilon_{cc2} = 0.9\varepsilon_{cc}$$ (2.60)

For strains greater than ε_{un}, a straight line is fitted between the returning point and the point of strength degradation. The returning point is set to the average between ε_{un} and the returning strain ε'_{re} determined by Karsan and Jirsa (1969) empirical equation.

$$\varepsilon_{re} = \frac{\varepsilon'_{re} + \varepsilon_{un}}{2}$$ (2.61)

$$\varepsilon'_{re} = S_r\varepsilon_{un}$$ (2.62)

$$S_r = 0.00273 + 1.2651S_e$$ (2.63)

$$S_e = \frac{\varepsilon_{un}}{\varepsilon_{cc}}$$ (2.64)

2.5 Seismic Behaviour of RMSW+BEs

Shedid et al. (2010) tested seven reinforced concrete-masonry shear walls under displacement-control quasi-static cyclic loading. The walls were designed to have the same lateral resistance and lateral stiffness while having two aspect ratios of 1.5 and 2.2. Rectangular walls, walls with flanges, and walls with end confined (i.e., stretcher boundary elements and pilaster boundary elements) were investigated, as shown in Figure 2.18. The researchers reported that significant energy dissipation levels were associated with the inelastic response of the flanged walls and walls with boundary elements. Moreover, high ductility levels were achieved with minimal strength degradations for these walls than their rectangular counterparts. It was found that the ductility of the proposed flanged and end confined walls improved at least 39 % and 106% compared to their rectangular walls′ counterparts, respectively. It was concluded that the new proposed construction alternatives of integrating wall boundary elements could be adopted in masonry standards.
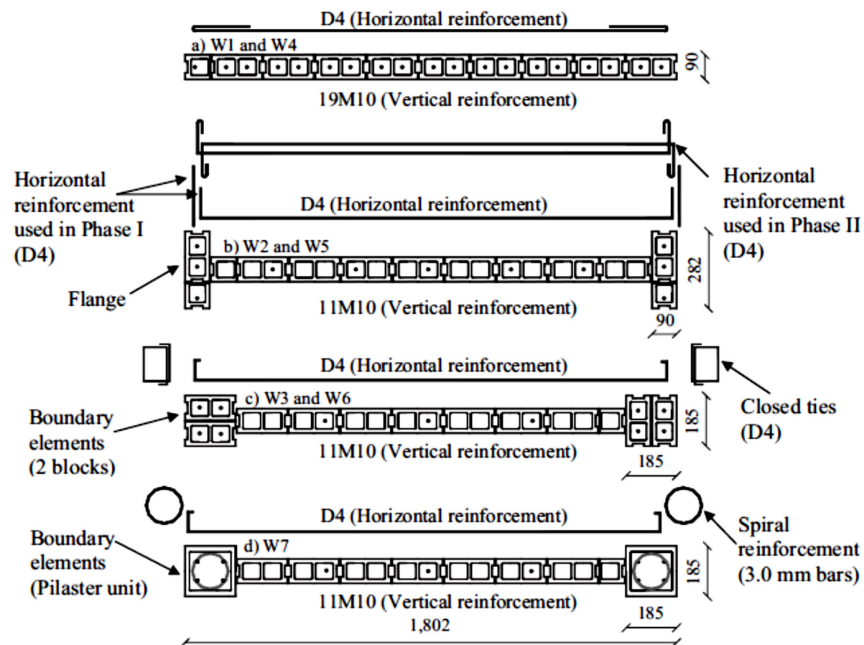
Figure 2.18 RMSW tested by Shedid et al. 2010

Banting and El-Dakhakhni (2014) investigated, experimentally, the seismic performance of nine reinforced masonry shear walls with boundary elements subjected to quasi-static reversed cyclic loading. The researchers studied the aspect ratio's influence and the vertical reinforcement ratio on these walls′ seismic responses. Three different aspect ratios were investigated: 1.5, 2.15, and 3.23, and two vertical reinforcement ratios were studied, namely 0.69% and 1.17%. It was

36

inferred that increasing the aspect ratio increased the plastic hinge length while decreasing the masonry shear walls′ lateral capacity. Moreover, increasing the vertical reinforcement ratio increased the lateral capacity and the top drift, a significant drop in the displacement ductility, and a slight decrease in the tested walls′ curvature ductility. Moreover, the confined masonry boundary elements′ presence resulted in resistance against buckling for the vertical reinforcement, a significant increase in the top drifts up to 3.7%, and the displacement ductility without a sudden drop of the lateral strength of the wall or failure of the boundary elements.

Ezzeldin et al. (2016) studied the seismic behaviour of twenty archetypes of RMSW+BEs designed with different configurations under various gravity loadings. A simplified 2D macro-model tool embedded in the OpenSees (McKenna et al. 2000) was utilized to simulate the flexural behaviour of RMSW+BEs under reversed lateral cyclic loading. It was observed that the RMSW+BE designed with the ASCE7-10 (ASCE/SEI 2010) force modification factors presently assigned to rectangular reinforced masonry shear walls exhibited an enhanced seismic performance, as depicted in Figure 2.19. This boosted performance was sufficient to meet the FEMA P695 (2009) acceptance criteria for the expected seismic collapse risk under the maximum considered earthquake.
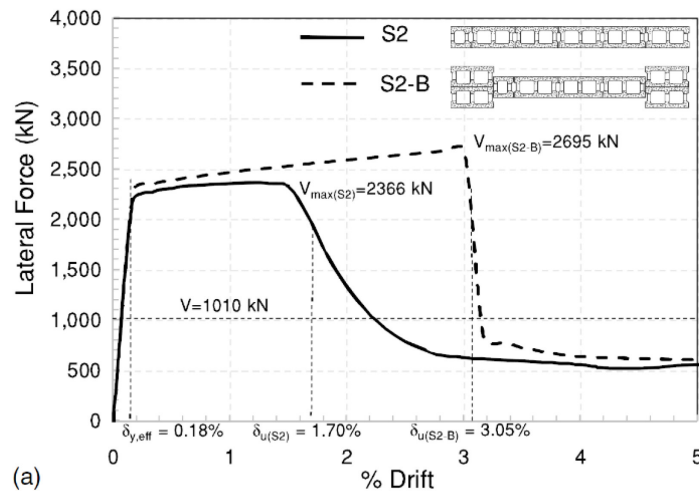
Figure 2.19 Lateral force-drift relationship of RMSW with and without boundary elements
(Ezzeldin et al. 2016)

The seismic performance of ductile reinforced masonry shear wall buildings was investigated by Aly and Galal (2019). Their numerical study investigated the seismic response and the collapse

capacity of six archetype buildings having heights limits exceeding those stipulated in the NBCC (2015) code in two different seismicity regions (i.e., moderate and high). The six buildings have ductile shear walls with boundary elements and were assessed using non-linear static pushover and incremental dynamic analysis following the methodology of the FEMA P695 (2009). Their study highlighted practical design recommendations and enhancement of the system-level performance. The studied buildings were found to have a collapse probability with the acceptance limits of the FEMA P695 (2009). In their findings, the researchers reported that the addition of boundary elements to the wall toes using high strength C-shaped pilaster blocks combined with high strength grout greatly enhanced the overall system ductility and the seismic behaviour. Moreover, the researchers recommended 70 m and 50 m height limits to buildings in the moderate and high seismicity regions. Aly and Galal (2020a, b) studied, experimentally, the influence of different design parameters on the lateral non-linear cyclic response of RMSW+BEs. They investigated the effect of the boundary element configurations (i.e., C-shaped vs. stretcher blocks), the vertical reinforcement lap splice at the plastic hinge region, the shear span-to-depth ratio of the walls, the vertical reinforcement ratio in the MBEs, and the MBE size (i.e., 190x190mm and 190x290mm) on the seismic performance of RMSW+BEs. Figure 2.20 shows the test setup and instrumentation of a sample tested RMSW+BEs by the researchers. The intent was to promote and verify, experimentally, a component-level structural performance of the RMSW+BEs that can be incorporated in mid-to-high rise masonry buildings to ensure ductile behaviour under severe ground motions.
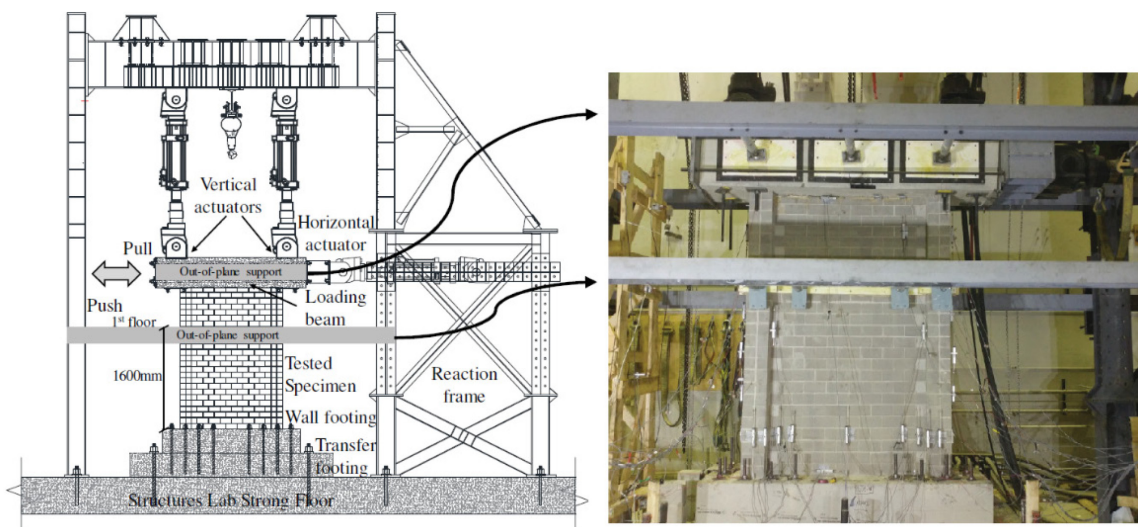
Figure 2.20 Test setup of RMSW+BEs tested by Aly and Galal (2020)

38

The test results showed that using C-shaped MBE blocks enhanced the constructability and the seismic performance of the RMSW+BEs. Moreover, the vertical reinforcement's lap splice at the plastic hinge region was found to enhance the walls′ initial lateral stiffness and increase their strength and stiffness degradation rate. The shear span-to-depth ratio was found to significantly influence the lateral strength and stiffness and the non-linear behaviour of the walls. Increasing the vertical reinforcement ratio in the MBEs was found to significantly enhance the walls′ energy dissipation, whereas increasing the MBE size enhanced the displacement ductility of the tested RMSW+BEs.

2.6 Summary and Conclusions

An in-depth study of the literature revealed that considerable research efforts had been exerted to investigate the axial compressive behaviour of fully grout confined concrete-masonry elements. However, it showed very limited research was performed on the axial compressive behaviour of unconfined and confined RMBEs. The literature also lacked a detailed investigation of the cyclic stress-strain behaviour of confined RMBEs that can be incorporated within reinforced masonry shear walls subjected to earthquake ground motions. Therefore, there is still a need to complement the literature gap and enrich the masonry state of the art with detailed experimental investigations and analytical analysis of the compressive stress-strain behaviour of RMBEs, including various design parameters such as the longitudinal (i.e., vertical) reinforcement steel ratio, the transverse steel confinement configuration, the masonry blocks configuration, the cross-section geometries, the grout's compressive strength, and the construction procedures. Moreover, unlike its concrete counterpart, the grouted masonry's compressive strength and ductility are still interest points. Enhancing the masonry axial compressive stress-strain response will result in high-performance masonry that is essential to promote mid- and high-rise reinforced masonry structures and RMSW+BEs as a seismic force-resisting system in North American buildings. High strength masonry enables reinforced masonry systems to sustain high axial compressive loads and lateral cyclic forces. Additional investigation and quantification of the concrete-masonry material behaviour with various confinement configurations are beneficial for interpreting the overall seismic response of RMSW+BEs. Furthermore, the CSA S304-14 geometrical and detailing requirements for confined boundary elements require further investigations to confirm its conformity with RMSW+BEs.

Most literature studies focused on the monotonic compressive behaviour of confined RMBEs. However, the cyclic compressive stress-strain behaviour of RMBEs is essential to adequately predict the lateral cyclic response of RMSWs built with confined masonry boundary elements under. Predicted stress-strain curves using the above-mentioned literature models were found not applicable to confined RMBEs. Therefore, refined stress-strain models are required to predict the envelope and cyclic stress-strain responses of RMBEs with different sections and various confinement configurations. These models can be integrated into numerical software tools to predict the overall lateral cyclic response of RMSW+BEs, considering the stored ductility at the end-confined zones of the shear walls.

The literature highlighted the possible application of RMSW+BEs as a practical and efficient seismic force-resisting system that can be employed in moderate and high seismicity zones. However, there is still a need to quantify the sensitivity of the seismic response of RMSW+BEs built with different wall configurations to various design parameters such as the masonry compressive strength, the masonry strain at peak stress, and the vertical steel ratio of the confined boundary elements. This would facilitate the seismic design optimization of RMSW+BEs and enhance the overall seismic response of reinforced masonry structures.

Chapter 3

Influence of Pre-Wetting, Non-Shrink Grout, and Scaling on the Compressive Strength of Grouted Concrete Masonry Prisms

3.1 Abstract

This study experimentally investigates the influence of pre-wetting of dry masonry prisms, non-shrink grout, and grout strength on the axial compressive stress-strain response of grouted masonry prisms built using half-scale and full-scale concrete masonry blocks. To achieve the aims of this study, a total of forty-two concrete-masonry prisms were built and tested under concentric axial load. The results showed that grouting of dry masonry prisms rendered a non-proportional increase in the prism compressive strength, whereas grouting of wet masonry prisms exhibited a significant increase in the masonry prism compressive strength. Masonry prisms constructed with non-shrink grout showed, on average, an increase in the compressive strength when compared to masonry prisms constructed with regular grout. Wetting of masonry prisms before grouting was found to enhance the compressive strength of masonry prisms. Half-scale masonry prisms showed a comparable modulus of elasticity and strain at peak strength to their full-scale counterparts. However, some discrepancies in the compressive strength and post-peak behaviour were observed. Superposition of the masonry shell and the grout core strengths was found to highly overestimate dry grouted masonry prism compressive strength, whereas wet masonry prisms demonstrated excellent agreement with superposition values. Wetting of dry masonry prisms is a promising construction procedure that significantly enhanced the compressive strength of grouted masonry; however, further research is needed to determine the proper wetting scheme and to ensure consistent results that can be quantified.

3.2 Introduction

The highest specified compressive strength for a fully grouted concrete masonry prism is 13.5 MPa in table 4 of the Canadian standards CSA S304-14 and 20.69 MPa in table 2 of the US standards TMS 402/602-16. These values are assigned to the highest specified compressive strength of a masonry unit with 30 MPa and 33.10 MPa, respectively. This method (i.e., the unit strength method), however, is deemed as an alternative for the design engineer to use the tabulated values of the masonry compressive strengths avoiding the higher cost of testing masonry prisms. However, these tables do not consider the effect of the grout strength on the specified strength of grouted masonry. Moreover, for the same block strength and the mortar type, the two codes specify higher compressive strength for ungrouted masonry compared to grouted masonry. These values are known to be conservative, particularly, for the grouted masonry prisms (Fortes et al. 2014; Gayed and Korany 2011; Korany 2012; Korany and Glanville 2005; Long et al. 2005). Such low strength levels make it challenging to use reinforced masonry in North American mid- to high-rise buildings.

High strength masonry was expected to be achieved by increasing the grout strength and the masonry block strength. However, for grouted masonry, the literature (e.g., Drysdale and Hamid 1979; Fortes et al. 2014; Long et al. 2005; Obaidat et al. 2018; Romagna and Roman 2002) showed that increasing the grout strength for a specific block strength does not result in a proportionate increase in the corresponding masonry prism compressive strength. Moreover, only a small portion of the grout capacity contributes to that of the masonry prism. The literature (e.g., Drysdale and Hamid 1979; Hamid et al. 1978; Mohamed 2018) indicated that the strength superposition of the masonry assemblage components (i.e., masonry shell and grout) was invalid. This was attributed to the fact that the peak stresses of the two components were reached at different strain levels. Moreover, the inefficiency and reduction of compressive strength of grouted masonry compared to that of their ungrouted counterparts were attributed to four main reasons, namely incomplete grout compaction, plastic and drying shrinkage of the grout, stress-strain material incompatibility of masonry assemblage (i.e. masonry block and mortar) and the grout core, and the effect of block geometry and bond pattern (Drysdale and Hamid 2005).

Numerous studies have been conducted to investigate the effect of the grout strength and grouting on the compressive strength of masonry prisms. Boult (1979) concluded that the optimum

42

capacity of masonry prisms can be achieved if the modulus and the limiting strain (i.e., strain at peak stress) of both the block and the grout are matched. Drysdale and Hamid (1979) observed that increasing the grout strength slightly increased the compressive strength of grouted masonry prisms. In addition, it was indicated that the ungrouted masonry demonstrated a higher compressive strength than its grouted counterpart. Furthermore, the superposition of the masonry shell (i.e., ungrouted masonry) strength and the grout strength was found to overestimate the compressive strength of grouted masonry. In addition, it was suggested that the excessive lateral tensile strains exerted by the grout core, due to the vertical compression strains, on the masonry block, resulted in premature failure of the masonry shell characterized by the tensile splitting failure of the masonry shell. The researchers recommended that matching the deformation characteristics would effectively enhance the compressive strength of grouted masonry rather than increasing the grout strength. Baba and Senbu (1986) concluded that the influence of the grout strength on the compressive strength of masonry prisms was dependent on the shape and the characteristics of the masonry blocks. Scrivener and Baker (1988) reported that the grout strength marginally contributes to the determination of the compressive strength of masonry prisms. Yao and Nathan (1989) supported the same findings of Drysdale and Hamid (1979) that increasing the grout strength has a minimal effect on the strength of grouted masonry prisms and the superposition of individual capacities of the masonry shell and the grout core was still invalid. Priestly and Elder (1983) found the masonry shell peak stress matched a strain of 0.0015, whereas the grout attained the peak stress at a strain of 0.002. The premature failure of the masonry shell lowered the peak stress of the masonry prism to 0.0015, corresponding to a much lower capacity. Khalaf et al. (1994) found that for 3-course-high masonry prisms that had different mortar joint strengths and types, the presence of concrete infill (i.e., grout) for both full- and half-block masonry prisms dramatically reduced the compressive strength of the tested prisms. Steadman et al. (1995) addressed the contribution of the strong coarse grout to the highest achieved compressive strength of the tested prisms that exceeded the ungrouted masonry prisms. However, in general, increasing the grout compressive strength was found to increase the capacity of the masonry prisms but not the compressive strength compared to their ungrouted counterparts. Romagna and Roman (2002) showed that for a specific block strength and mortar strength (full bedded prisms), increasing the grout strength resulted in a slight gain in the compressive strength of the masonry prisms. The best results were recorded when the compressive strength of the grouts and the blocks

were almost matched. Fortes et al. (2014) examined the relationship between the ungrouted and grouted masonry compressive strength and the strength of the masonry block using 4 different grout mixtures. It was concluded that ungrouted masonry was more highly efficient than the grouted masonry in terms of the compressive strength. Mohamed (2018) studied the effect of changing the grout compressive strength on the compressive response of c-shaped boundary element prisms. The researcher reported that increasing the grout compressive strength from 15 MPa to 45 MPa resulted in an increase of approximately 50% in the peak stress. It was found that the simple superposition concept of the masonry shell capacity and the grout core capacity was invalid.

There have been limited studies conducted on the effect of grout shrinkage on the compressive strength of grouted masonry prisms. Boult (1979) observed the significant effect of the plastic shrinkage of the grout on the lower compressive strength of grouted masonry. It was reported that plastic shrinkage of the grout due to the absorption of the grout free water by the masonry blocks led to shrinkage cracks at the interface of the masonry shell with the grout cores. It was implied that the widened face shells and webs restricted the shrinkage of the grout cores at each mortar joint resulting in substantial cracks along the grout core, which in turn reduced the contribution of the grout core to the compression capacity of the grouted masonry prisms. This was also in agreement with another research project that was conducted by Drysdale and Hamid (1979). Joyal (2014) examined the effectiveness of two types of anti-shrinkage grout in fully grouted concrete masonry prisms to eliminate the effect of the grout shrinkage. The anti-shrinkage grouts were found to make no significant improvement to the stress drop just after the peak stress. Fonseca et al. (2019) studied the effect of the grout compressive strength, with and without shrinkage compensating admixtures, on the compressive strength of grouted masonry prisms. It was reported that the shrinkage compensating admixture was not as significant as expected in improving the compressive strength of grouted masonry prisms except one series of the tested prisms exhibited better performance than their ungrouted counterparts and that further research is needed to quantify the optimum dosage of the shrinkage admixture for reliable results.

Due to the physical and cost limitations of the laboratories′ testing facilities, testing of full-scale masonry assemblages, components and systems could be unfeasible. Abboud et al. (1990) examined the feasibility of using a one-quarter scale model masonry unit in predicting the response

44

of concrete block masonry walls and connections. The researchers indicated that the model units behaved similarly to the prototype with respect to the material and the assemblage levels and that direct modelling of the prototype concrete block masonry is a feasible and economical technique to investigate the behaviour of masonry systems. Long et al. (2005) found that the stress-strain behaviour of half-scale and full-scale masonry prisms is comparable, especially for the grouted masonry. In addition, the half-scale masonry exhibited similar strength and failure modes to the full-scale prototype. It was concluded that the half-scale masonry can be used as a good model to examine the behaviour of full-scale grouted masonry shear walls.

3.3 Research Significance

Based on the above literature, it can be seen that the compressive strength of grouted masonry is still a point of interest. Moreover, high performance masonry is essential to promote mid- and high-rise reinforced masonry structures for the growing masonry industry. High strength masonry enables reinforced masonry systems to sustain high compressive loads and/or cyclic loads. This can be achieved in reinforced masonry shear wall toes (i.e., boundary elements and webs) as well as reinforced masonry columns subjected to lateral loads. Furthermore, high strength masonry will open the door for prestressed masonry shear walls as high early compressive strength is necessitated. This study focuses on developing high strength grouted masonry with enhanced ultimate strains by omitting the detrimental factors (i.e., plastic and drying shrinkage of the grout) that affect the grouted masonry compressive stress-strain behaviour. To achieve the aims of this study, the influence was investigated of four grout types having different compressive strengths (i.e., regular grout A, regular grout B, non-shrink grout A, and non-shrink grout B) on the masonry prism compressive strength. Regular and non-shrink grouts were used to assess the effect of grout shrinkage on grouted masonry strength. Furthermore, to enhance the bond between the masonry shell and corresponding grout core, wetting of masonry prisms before grouting was investigated. Half-scale and full-scale masonry prisms were tested to examine the effect of scaling on the stress-strain response of grouted masonry. Half-scale masonry prisms were investigated to assess the feasibility of using the results of testing structural elements (i.e., Boundary Elements, Walls, Beams, etc.) constructed with half-scale masonry units in predicting the seismic response of reinforced masonry shear walls.

45

Comparisons of the test results were conducted in terms of the stress-strain response (i.e., peak stress, peak strain, and post-peak behaviour). The test results were compared to their predicted value counterparts computed by literature equations developed by previous researchers to study the effectiveness of these equations in the prediction of masonry prism compressive strength.

3.4 Experimental Program

3.4.1 Test Matrix

Forty-two concrete block masonry prisms were constructed and tested under axial compression concentric loading. These prisms were constructed by a professional mason and tested at the structures Lab of Concordia University. The test matrix was designed to address the literature gap and carefully investigate the effect of test parameters on the axial compressive stress-strain response of concrete masonry prisms. Since this study aims at enhancing the compressive strength of fully grout concrete masonry prisms, it focuses on omitting the detrimental effects that shrinkage of the grout core can have on the masonry prism's strength. Therefore, the Non-shrink grout and prewetting of dry masonry prisms before grouting were selected in order to reduce the effects of grout shrinkage and enhance the bond between the grout core and the masonry shell. Besides, different grout strengths were utilized to examine their effect on dry and pre-wetted masonry prisms' strengths.

The influence of five parameters on the compressive strength of grouted masonry was investigated in this experimental work, namely, wetting of masonry prisms, lining of masonry prisms, grout strength, grout shrinkage and size effect. The details of the masonry prisms are presented in Table 3.1. The masonry prisms were divided into two main groups of full-scale and half-scale prisms. Each group has subgroups to investigate one of the aforementioned parameters, and each subgroup has three identical specimens to satisfy the ASTM 1314-14 requirements for the minimum number of tested prisms. All the prisms were fully grouted except two groups of prisms, which were ungrouted: one group in the full-scale and another group in the half-scale prisms; this was to quantify the compressive strength of ungrouted masonry (i.e., masonry shell).

Table 3.1 Test matrix of half-scale and full-scale masonry prisms

Group number	Group Identifier	Half/Full	Type of Grout	Prism status before grouting	Grout compressive strength (MPa) and (COV%)	
					Grout cylinders (100 x 200 mm)	Grout moulded [a,b] between dry or wet[c] blocks
1	P-0-D-H	Half	---	---	---	---
2	P-REG-B-D-H	Half	Regular B	Dry	57.26 (4.62%)	57.96 (7.51%)
3	P-REG-B-W-H	Half	Regular B	Wet	57.26 (4.62%)	67.56 (6.90%)
4	P-NON-A-W-H	Half	Non-shrink A	Wet	60.38 (6.05%)	55.11 (2.14%)
5	P-NON-B-D-H	Half	Non-shrink B	Dry	69.11 (10.96%)	62.17 (3.39%)
6	P-NON-B-W-H	Half	Non-shrink B	Wet	69.11 (10.96%)	76.25 (6.64%)
7	P-0-D-F	Full	---	---		
8	P-REG-A-D-F	Full	Regular A	Dry	21.04 (7.32%)	32.01 (10.47%)
9	P-REG-B-D-F	Full	Regular B	Dry	57.26 (4.62%)	61.98 (0.86%)
10	P-REG-B-D-F-LIN	Full	Regular B	Dry-lined	57.26 (4.62%)	61.98 (0.86%)
11	P-REG-B-W-F	Full	Regular B	Wet	57.26 (4.62%)	64.48 (3.23%)
12	P-NON-A-W-F	Full	Non-shrink A	Wet	60.38 (6.05%)	57.18 (8.12%)
13	P-NON-B-D-F	Full	Non-shrink B	Dry	69.11 (10.96%)	74.30 (6.25%)
14	P-NON-B-W-F	Full	Non-shrink B	Wet	69.11 (10.96%)	69.75 (8.7%)

[a] Grout moulded between half-scale masonry blocks having dimensions of (90x90x180 mm)

[b] Grout moulded between full-scale masonry blocks having dimensions of (95x95x190 mm)

[c] Blocks are immersed in water for 2 hours before grouting

3.4.2 Construction of Masonry Prisms

According to the ASTM 1314-14 (American Society for Testing and Materials (ASTM) 2014), all the prisms were constructed with two courses high in a stacked bond pattern with a full bedding of 10 mm and 5 mm type S mortar joints for full-scale and half-scale prisms, respectively. The ASTM 1314-14 stipulates that the minimum number of courses of a masonry prism is two with a correction factor of 1.0 for the compressive strength results. This will eliminate the need for correcting the experimental compressive strength results of the tested prisms. The half-scale units (i.e., 90x90x185 mm) are the half-scale module of the commercially available standard stretcher concrete block (i.e., 190x190x390 mm). Figure 3.1 depicts the dimensions of the full-scale and the half-scale units. Figure 3.2 shows the steps of the construction of half-scale and full-scale masonry prisms. The dimensions of the full-scale prisms were 190x390x390 mm, whereas the dimensions of the half-scale prisms were 90x185x185 mm. Four types of grout were used in this experimental work: prepacked regular grout A (Blocfiller 2015); laboratory mixed regular grout B; prepacked non-shrink grout A (Quikrete®non-shrink precision Grout 2015); prepacked non-shrink grout B (SikaGrout®-212 2017). The prepacked regular grout A is a factory-mixed fine grout for filling concrete-masonry cells with a minimum compressive strength of 15 MPa as per ASTM C109. The prepacked non-shrink grout A is a cement-based high strength grout with expansive additives whereas the prepacked non-shrink grout B is a high-strength cementitious grout with shrinking compensating mechanism with a minimum compressive strength of 56 MPa as per ASTM C109. All the prepacked ready-to-use grouts are commercially available in the Canadian market. Each specimen was given a notation for identification; for example, P-REG-D-F-A. The letter P denotes a prism; the abbreviation REG or NON denotes regular grout or non-shrink grout (A or B), respectively; the letter D stands for the status of the prism before grouting either dry (D) or wet (W); the letter F or H is for a full-scale masonry prism or a half-scale masonry prism, respectively; and the letter A denotes the replicate of the three prisms. Before grouting the masonry prisms, the prism was either air dried or immersed in water for two hours. Only one group of the dry prisms was lined with paper towel before grouting. Afterwards, the grout was poured to fill the cells of the concrete block masonry prism with manual compaction for three layers of the grout using a standard tamping rod. For curing purposes, all the specimens were sealed in tight plastic bags to preserve the moisture content of the prisms and achieve the optimum grout strength. To determine the grout compressive strength, three identical grout cylinders were cast, according to CSA-A179-

14, for each grout type. According to ASTM C1019-14, for each moisture content, for each type of grout and for each masonry unit, three identical block moulded grout prisms were constructed at the same time as the prisms′ grouting. Therefore, for consistent construction and testing purposes, the concrete blocks that were intended to mould the grout were also immersed in water simultaneously with the masonry prisms (Figure 3.2). Upon removal from water, the wet masonry prisms were grouted.
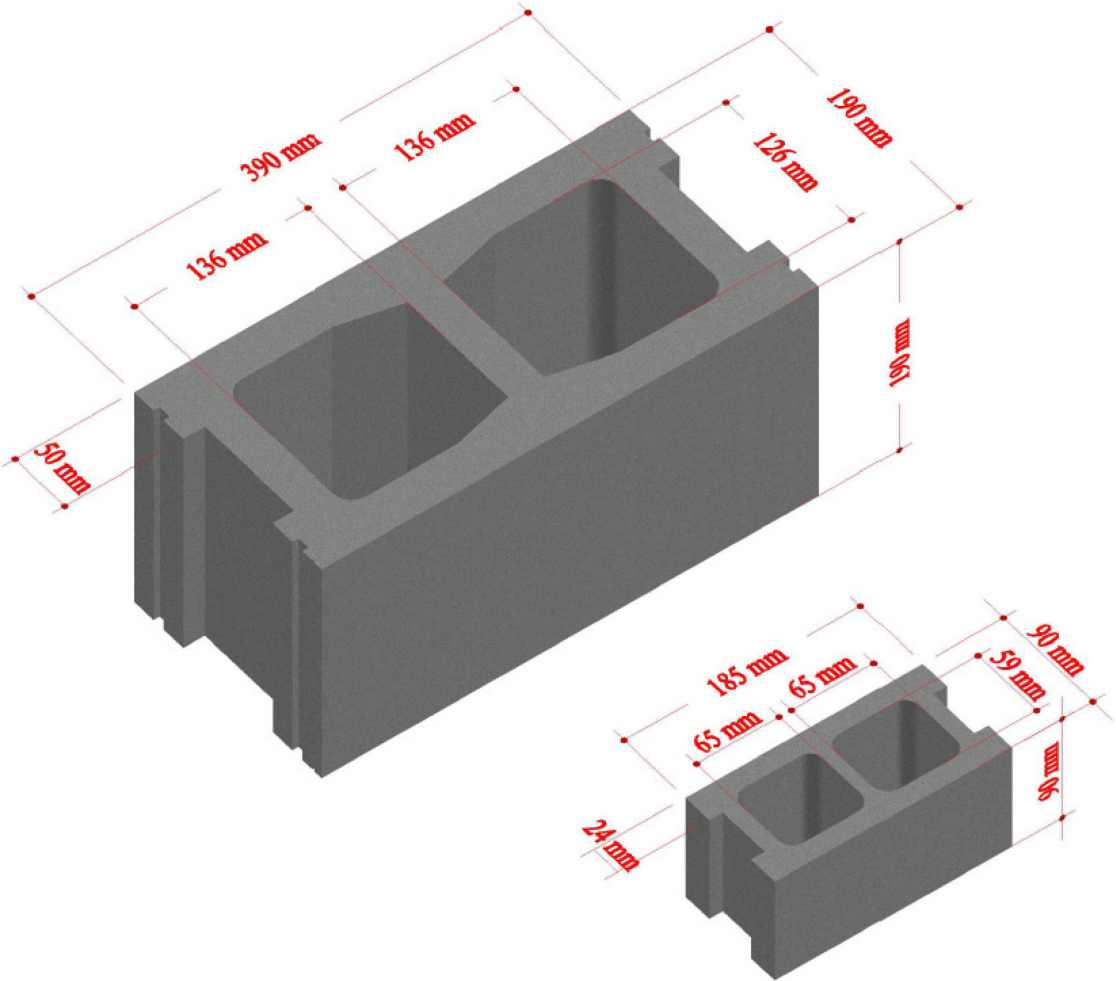
Figure 3.1 Full-scale and half-scale masonry blocks (shape and dimensions)

(a)

(b)
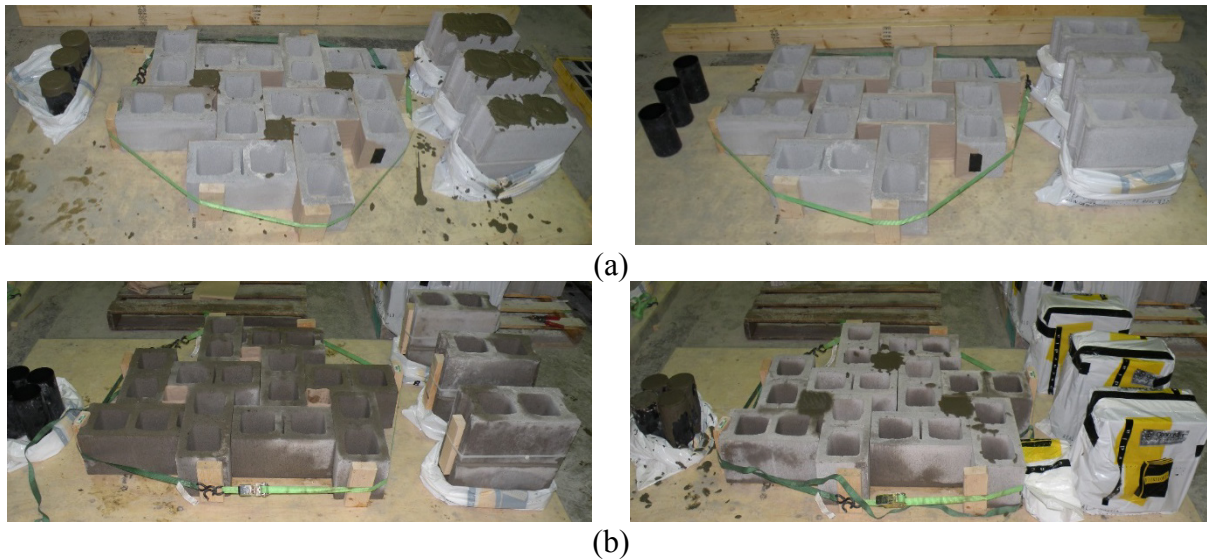
Figure 3.2 Grouting of masonry prisms (a) Full-scale dry masonry prisms; (b) Full-scale wet masonry prisms

3.4.3 Non-shrink grout and wetting of the masonry prisms

Due to the high-water content in masonry grout mixes, excessive plastic and drying shrinkage of the grout cores is inevitable. Vertical shrinkage of the grout cores with respect to the masonry shells can be adjusted by capping the masonry prisms before testing. Nevertheless, lateral shrinkage of grout cores permanently resulted in non-homogeneous behaviour of the masonry assemblage that in turn reduces the contribution of the grout to the capacity of the grouted masonry prisms. Non-shrink grout was utilized for the construction of masonry prisms in order to eliminate the effect of grout shrinkage on the compressive strength of masonry prisms. Moreover, wetting of the masonry prisms just before grouting can be one of the procedures that offset the initial and short-term vertical and lateral shrinkage of the grout cores. Wetting of masonry prisms is conceived as a means of eliminating the shrinkage effect on the compressive strength of the masonry prisms. Meanwhile, grouts with lower water content can be readily used for grouting the masonry prisms, thus avoiding the excessive shrinkage that accompanies the high flowable grouts. Grouting of dry and wet masonry prisms is shown in Figure 3.2.

3.4.4 Material Properties

To determine the compressive strength of the masonry blocks, three units were tested according to ASTM C140. Figure 3.3 shows the compression test of half-scale and full-scale

masonry blocks. High strength gypsum hard capping was used to cap both ends of the tested block to distribute the axial load uniformly on the surface of the specimen. Based on an average net area of 8963 mm^2 (COV = 1.89%), 40,632 mm^2 (COV = 0.47%) for the half-scale and full-scale blocks, respectively, the compressive strength of the half-scale units was 39.0 MPa (COV = 15.7%), whereas the compressive strength of the full-scale blocks was 37.4 MPa (COV = 3.47%). According to ASTM C140, three units from the half-scale and the full-scale blocks were tested to determine the absorption, density and moisture content. The half-scale masonry units have an absorption of 5.35% (COV = 5.34%), a density of 2162 kg/m^3 (COV = 2.79%), and a moisture content of 1.15% (COV = 0.87%). The full-scale units have an absorption of 5.31% (COV = 0.76%), a density of 2243 kg/m^3 (COV = 0.12%), and a moisture content of 1.31% (COV = 2.43%).
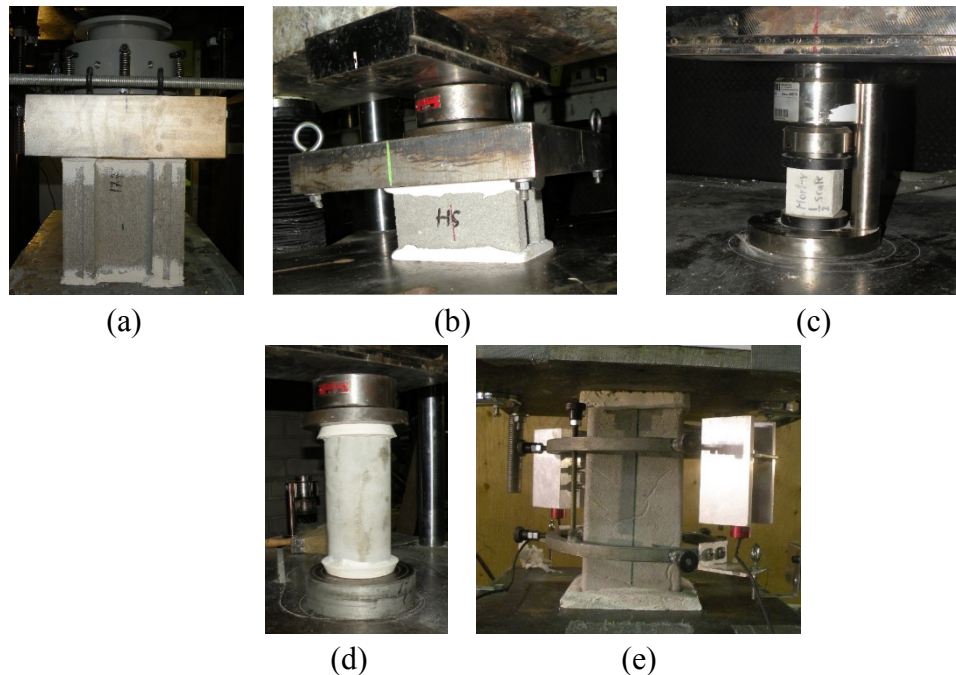
Figure 3.3 Compression test of materials (a) Full-scale masonry block; (b) Half-scale masonry block; (c) Mortar cube; (d) Grout cylinder; and (e) Grout prism

Four types of grout with different mixing ratios were used for the construction of the grouted masonry prisms, namely prepacked regular grout A (Blocfiller 2015) with water to powder ratio of 0.18; laboratory mixed regular grout B with mix proportions of 1:2.6:0.5 for cement, sand, and water by weight, respectively; prepacked non-shrink grout A (Quikrete®non-shrink precision

Grout 2015) with water to powder ratio of 0.20; and prepacked non-shrink grout B (SikaGrout®-212 2017) with water to powder ratio of 0.15.

To determine the compressive strength of the grout, grout cylinders of 100 mm (diameter) x 200 mm (height), block moulded grout 95x95x190 mm for the full-scale prisms and 90x90x180 mm for the half-scale prisms were cast and tested according to CSA-179-14 and ASTM C1019-14, respectively. The grout cylinders and prisms were treated in water and tested at the same time of testing the prisms. Table 3.1 shows that there are no consistent differences between the results of cylinder and block moulded grouts. This could be attributed to the different moulding procedures for the grouts namely non-absorbent cylinder moulds, dry masonry blocks, and pre-wetted masonry blocks. This resulted in various block absorption conditions for the grout leading to inconsistency of the compressive strength between the cylinder and block moulded grouts. It is worth noting that some studies (e.g. Joyal 2014; and Mohamed 2018) showed that the block moulded grout gave higher compressive strength compared to its corresponding cylinder. This was attributed to the absorption of the surrounding dry masonry blocks compared to the non-absorbent cylinder moulds. Other researchers (e.g. Scrivener and Baker 1988; and Sturgeon et al. 1980) showed contradicting results where the block moulded grout exhibited a lower compressive strength than its corresponding cylinder. In this research, the results of block moulded grout are seen to be more representative of the masonry grout core than the non-absorbent cylinders. Therefore, the results of the compressive strength of block moulded grout will be used for superposition of the masonry shell and grout core hereafter.

Ready-to-use type S mortar, commercially available, was used to build the concrete block masonry prisms. The flow of the mortar was determined according to ASTM C1437-13 and was found to be 104%. To determine the compressive strength of the mortar, six mortar cubes of 50x50x50 mm were moulded during the construction of the prisms and tested according to ASTM C109-13. The compression test of mortar cubes yielded a compressive strength of 21.42 MPa (COV = 6.49%).

3.5 Compression Test of Masonry Prisms (Test Setup and Instrumentation)

Figure 3.4 shows the test setup and instrumentations of the half-scale and full-scale masonry prisms. A servo-controlled 5000 kN hydraulic cylinder fixed to a rigid steel frame was used to apply the axial load in a displacement control loading to the masonry prisms. The displacement

control system enables capturing the post-peak behaviour of the tested prisms. All the concrete block masonry prisms (i.e., ungrouted and fully grouted) were tested under uniaxial compression loading. The load of the cylinder was read by a high precision load-cell squeezed between the hydraulic cylinder and the rigid steel girder that transfers the load to the frame columns. Moreover, for more precision and consistent load readings, the load cell is also attached to a highly precise and high-speed scanning data acquisition system to capture the readings of the applied load. For testing the half-scale concrete masonry prisms, two steel plates, each 50 mm thick conforming to ASTM C1314-14, were used as upper and lower bearing plates to distribute the applied axial load to the prism ends uniformly. Meanwhile, a spherical platen was used to ensure axial loading was applied to the masonry prism.

(a)   (b)
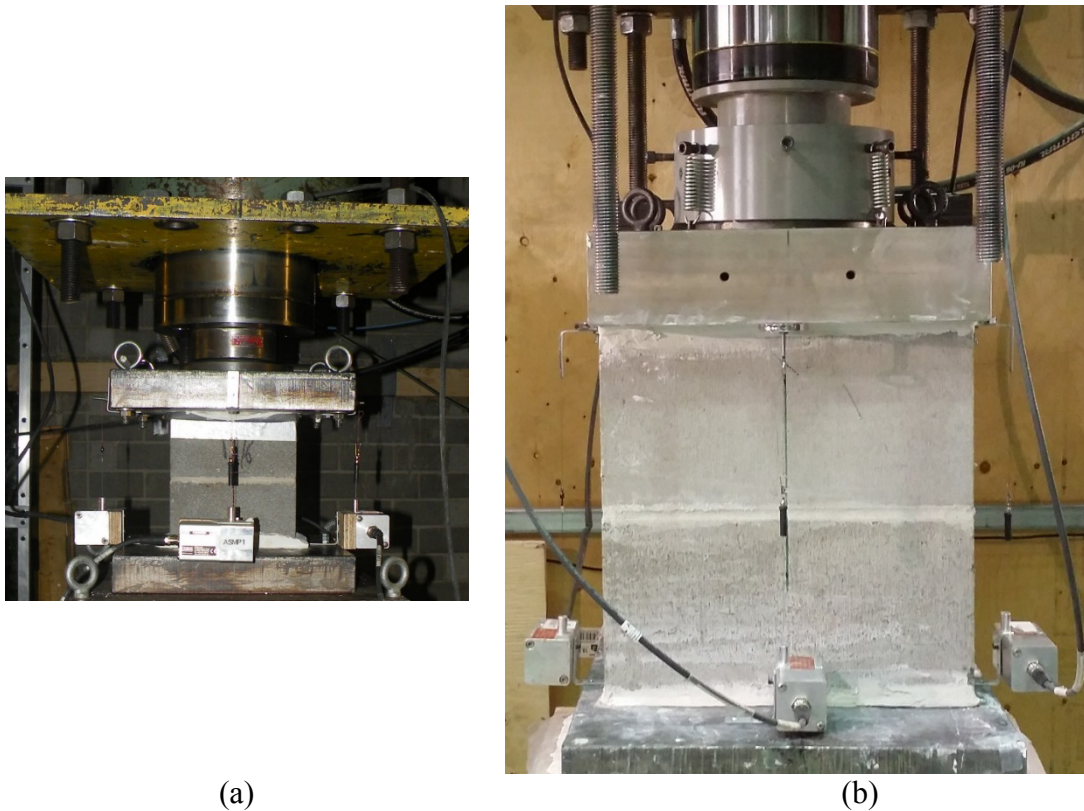
Figure 3.4 Test setup and instrumentation of (a) Half-scale masonry prism; and (b) Full-scale masonry prism

The full-scale masonry prisms were tested using a lower bearing plate of 114.3 mm thick (4.5 inches) and an upper bearing platen of 96 mm (3.75 inches) attached to a spherical platen. Both the upper and lower bearing platens conform to ASTM 1314-14 requirements. Prior to installing

53

the upper and lower steel plates and to avoid the roughness of the finished surfaces of the prism ends, a high strength plaster capping material was applied to the top and the bottom of the prism to better distribute the applied axial load. The spherical head, the upper and lower steel bearing plates and the concrete masonry prisms were all vertically aligned together along with the loading cylinder piston using laser alignment devices to eliminate any eccentricity. The monotonic uniaxial load was applied incrementally using a displacement rate of 0.005 mm/sec up to a strain range of 0.002 – 0.0025 and then dropped to a displacement rate of 0.003 mm/sec until the failure of the prism. This was to allow for capturing the post-peak behaviour of the concrete masonry prisms. To measure the deformations and the longitudinal strains for the masonry prisms, all specimens were equipped with four draw-wire displacement sensors (i.e., potentiometers) with a linearity of 0.05% of the full stroke (i.e., error 0.05%). These potentiometers were attached to the bearing plates and aligned at the centers of the four sides of the prism. The potentiometers measure the displacements along a gauge length equal to the full height of the masonry prism. This gauge length will ensure continuous and consistent readings of the displacements during the ascending branch and the post-peak response of the masonry prism avoiding expected damage to measuring devices due to the premature failure of the masonry face shell. All masonry prisms were tested at 4 – 6 months after the construction of the prisms due to the availability of the testing frame.

3.6 Results and Discussion

For the tested half-scale masonry prism specimens, the uniaxial stress was calculated as the axial force measured by the load cell and divided by the effective net area of 8963 mm^2 for hollow masonry prisms and effective cross-sectional area of 15,965 mm^2 for grouted masonry prisms. It should be noted that the strain readings shown in the stress-strain curves are obtained by averaging the readings of four potentiometers mounted on the four sides of the prism divided by the gauge length (i.e., 185 mm). The results of the half-scale masonry prisms are summarized in Table 3.2. Similarly, for the full-scale masonry prisms, the uniaxial stress was calculated as the axial force measured by the load cell and divided by the effective net area of 40,632 mm^2 for hollow masonry prisms and an effective cross-sectional area of 70,725 mm^2 for grouted masonry prisms. To ensure consistent results, the same four potentiometers were used for testing the full-scale masonry prisms in order to calculate the average strain readings based on a gauge length of 390 mm equal to the height of the prism. For all tested masonry prisms, the initial modulus of elasticity was calculated

based on the chord modulus of elasticity using the endpoints of 0.05 and 0.33 of the maximum compressive stress with corresponding strain data for each prism. The ultimate load, the peak stress, the masonry specified compressive strength, the peak strain and the modulus of elasticity for the tested full-scale masonry prisms are presented in Table 3.3.

3.6.1 Modes of failure

Figure 3.5 shows the failure modes for the tested half-scale and full-scale masonry prisms. For the ungrouted half-scale and full-scale masonry prisms, high compressive strains led to large lateral tensile strains in the mortar joints. This was accompanied with the failure of a substantial part of the mortar joint prior to the onset of vertical and diagonal cracks along the masonry prism. Afterwards, vertical cracks close to the unit's web were observed when approaching the peak stress of the prisms. These cracks continued to propagate to form diagonal cracks along the face shells until the failure of the prisms.

(a)	(b)	(c)	(d)
(e)	(f)	(g)	(h)	(i)
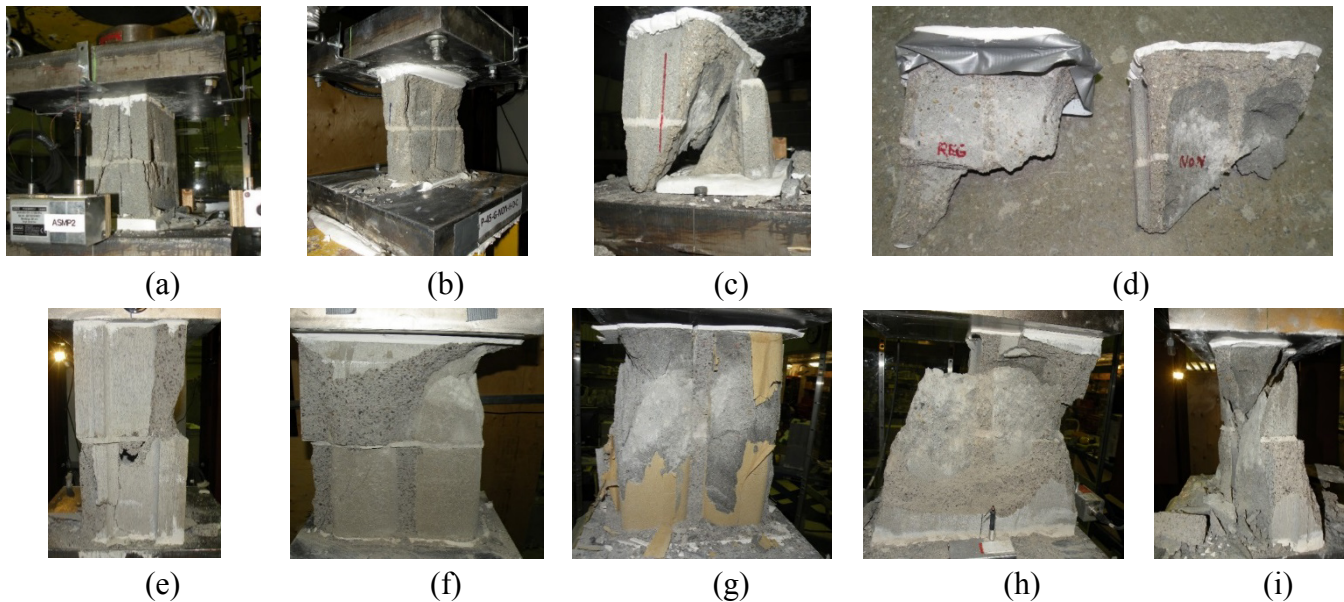
Figure 3.5 Modes of failure of half-scale (a) Masonry shell; (b) Dry masonry prism; (c) Wet masonry prism; (d) Regular (left) and non-shrink (right) grouted wet prisms; and full-scale (e) Masonry shell; (f) Dry masonry prism (g) Lined masonry prism; (h) Regular grouted wet masonry prism; (i) Non-shrink grouted wet masonry prisms

For the grouted masonry prisms, there was a considerable discrepancy between the failure modes of the dry and wet grouted prisms. Dry half-scale masonry prisms exhibited vertical cracks combined with inclined cracks developed firstly in the face shells. Spalling of the face shells was

observed at the peak stress associated with some cracks in the grout cores that remained almost intact. Also, for dry full-scale masonry prisms, the same failure mechanism was observed. Vertical cracks developed in the face shell shortly before reaching the peak stress of the masonry prism. After the peak stress was attained, spalling of the face shell was observed with the excessive crushing of the masonry prisms and the grout cores. In dry masonry prisms, lateral shrinkage of the grout core resulted in a masonry assemblage that has two separate components, the grout core and the face shell. Therefore, spalling of the face shell can be attributed to the excessive lateral strains exerted by the grout core on the masonry face shell resulting in a tensile splitting failure. This observation was reported by many researchers in the literature (e.g. Hamid and Drysdale 1979; Scrivener and Baker 1988). Conversely, the wet masonry prisms exhibited a different mode of failure. Wetting of the masonry prisms before grouting resulted in a well-bonded masonry shell and grout core. This enabled the masonry shell and the grout core to maintain their strengths up to the peak stress with no premature failure of the face shell. Unlike the dry masonry prisms, the wet prisms showed a compression failure characterized by a conical shaped diagonal shear failure pattern. Vertical and diagonal cracks tended to develop on the face shells and the end webs of the masonry units approaching the maximum load. These cracks continued to propagate and widen after the peak stress was attained and up to the failure of the masonry prism. It is worth noting that some wet specimens showed spalling of minor parts of their face shell at the failure of the prism whereas most of the prisms showed no face shell spalling until the failure. Furthermore, following the crushing of the masonry prism, a higher bond between the wet masonry shell and the grout core was observed.

Table 3.2 Test results of half-scale masonry prisms

Group number	Prism Identifier	Ultimate load (kN)		Peak stress (MPa)			Strain at Peak stress		Modulus of Elasticity (MPa)	
		P_{um}	Average (COV%)	f_{max}	Average (COV%)	*Specified strength f'_m*	ε_{max}	Average (COV%)	E_m	Average (COV%)
1	P-0-D-H-A P-0-D-H-B P-0-D-H-C	217.89 218.34 216.99	217.74 0.31	24.31 24.36 24.21	24.29 0.31	24.17	0.00293 0.00298 0.00293	0.00295 0.97967	9,104 10,345 9,012	9,487 7.85
2	P-REG-B-D-H-A P-REG-B-D-H-B P-REG-B-D-H-C	466.44 484.04 486.42	478.97 2.28	29.22 30.32 30.47	30.00 2.28	28.88	0.00338 0.00309 0.00308	0.00318 5.35	13,022 10,356 12,834	12,071 12.33
3	P-REG-B-W-H-A P-REG-B-W-H-B P-REG-B-W-H-C	738.01 689.02 740.29	722.44 4.01	46.23 43.16 46.37	45.25 4.01	42.28	0.00322 0.00308 0.00314	0.00315 2.18	19,607 20,747 22,081	20,812 5.95
4	P-NON-A-W-H-A P-NON-A-W-H-B P-NON-A-W-H-C	792.72 737.17 727.65	752.51 4.67	49.65 46.17 45.58	47.14 4.67	43.53	0.00391 0.00370 0.00379	0.00380 2.69	14,146 13,471 13,297	13,638 3.29
5	P-NON-B-D-H-A P-NON-B-D-H-B P-NON-B-D-H-C	516.57 513.40 501.50	510.49 1.56	32.36 32.16 31.41	31.98 1.56	31.16	0.00317 0.00285 0.00355	0.00319 10.96	11,478 14,555 12,091	12,708 12.81
6	P-NON-B-W-H-A P-NON-B-W-H-B P-NON-B-W-H-C	869.40 713.73 751.45	778.20 10.44	54.46 44.71 47.07	48.74 10.44	40.40	0.00416 0.00341	0.00379 14.01	14,185 15,579	14,882 6.63

Table 3.3 Test results of full-scale masonry prisms

Group number	Prism Identifier	Ultimate load (kN)		Peak stress (MPa)			Strain at Peak stress		Modulus of Elasticity (MPa)	
		P_{um}	Average (COV%)	f_{max}	Average (COV%)	*Specified strength* f'_m	ε_{max}	Average (COV%)	E_m	Average (COV%)
1	P-0-D-F-A	1081.55	1034.61 5.00	26.62	25.46 5.00	23.38	0.00230	0.00228 5.91919	14,178	13,389 6.76
	P-0-D-F-B	979.19		24.10			0.00213		13,588	
	P-0-D-F-C	1043.08		25.67			0.00240		12,401	
2	P-REG-A-D-F-A	1831.42	1943.04 5.78	25.89	27.47 5.78	24.87	0.00295	0.00314 5.82569	11,182	10,804 6.36
	P-REG-A-D-F-B	1941.72		27.45			0.00314		10,010	
	P-REG-A-D-F-C	2055.98		29.07			0.00332		11,219	
3	P-REG-B-D-F-A	2490.03	2491.09 7.33	35.21	35.22 7.33	30.99	0.00308	0.00346 11.17	13,650	13,385 2.64
	P-REG-B-D-F-B	2674.12		37.81			0.00385		13,521	
	P-REG-B-D-F-C	2309.11		32.65			0.00344		12,984	
4	P-REG-B-D-F-LIN-A	2716.18	2671.21 1.65	38.40	37.77 1.65	36.75	0.00328	0.00305 6.36	13,638	14,796 6.85
	P-REG-B-D-F-LIN-B	2669.36		37.74			0.00295		15,521	
	P-REG-B-D-F-LIN-C	2628.10		37.16			0.00293		15,229	
5	P-REG-B-W-F-A	3015.33	2922.23 2.97	42.63	41.32 2.97	39.31	0.00410	0.00356 13.40	13,284	15,288 12.34
	P-REG-B-W-F-B	2907.42		41.11			0.00334		15,552	
	P-REG-B-W-F-C	2843.94		40.21			0.00323		17,030	

Table 3.3 Test results of full-scale masonry prisms (Continued)

Group number	Prism Identifier	Ultimate load (kN) P_{um}	Average (COV%)	Peak stress (MPa) f_{max}	Average (COV%)	Specified strength f'_m	Strain at Peak stress ε_{max}	Average (COV%)	Modulus of Elasticity (MPa) E_m	Average (COV%)
6	P-NON-A-W-F-A	3062.15		43.30			0.00390		11,504	
	P-NON-A-W-F-B	3410.50	3199.16 5.80	48.22	45.23 5.80	40.93	0.00398	0.00389 2.74	14,695	13,899 15.20
	P-NON-A-W-F-C	3124.84		44.18			0.00377		15,499	
7	P-NON-B-D-F-A	2676.51		37.84			0.00271		12,420	
	P-NON-B-D-F-B	2828.06	2883.35 8.30	39.99	40.77 8.30	35.22		0.00285 6.62	14,672	14,687 15.48
	P-NON-B-D-F-C	3145.47		44.47			0.00298		16,968	
8	P-NON-B-W-F-A	3187.52		45.07			0.00347		15,568	
	P-NON-B-W-F-B	3216.09	3199.43 0.46	45.47	45.24 0.46	44.89	0.00370	0.00352 4.71	15,889	15,895 2.08
	P-NON-B-W-F-C	3194.67		45.17			0.00338		16,228	

3.6.2 Effect of grouting and grout strength

Figure 3.6 shows the stress-strain curves for the tested block-moulded grout prisms for regular grout B and non-shrink grout B. For all tested masonry prisms, the presence of the grout resulted in a slight to significant increase in the compressive strength of masonry prisms. Figure 3.7 shows that for half-scale specimens, grouting of dry masonry prisms slightly increased the compressive strength. On the contrary, for wet masonry prisms, introducing the regular grout B and non-shrink grout B to the ungrouted masonry prisms enhanced the compressive strength of the masonry prisms with increases of 86% and 100% compared to their ungrouted counterparts, respectively. Figure 3.8 illustrates the effect of grouting on the compressive strength of dry and wet full-scale prisms. For full-scale dry prisms, grouted masonry prisms constructed with regular grout A and regular grout B showed nearly 8% and 38% higher compressive strength than that of their ungrouted counterparts, respectively. However, grouting of wet masonry prisms was more highly effective than for their dry counterparts. Wet masonry prisms grouted with regular grout B and non-shrink grout B showed 62% and 78% higher compressive strength than ungrouted masonry prisms, respectively. For the dry full-scale masonry prisms, increasing the grout strength from 32 MPa (regular grout A) to 62 MPa (regular grout B) increased the prism compressive strength from 27.47 MPa (COV=5.78%) to 35.22 MPa (COV = 7.33%), respectively.
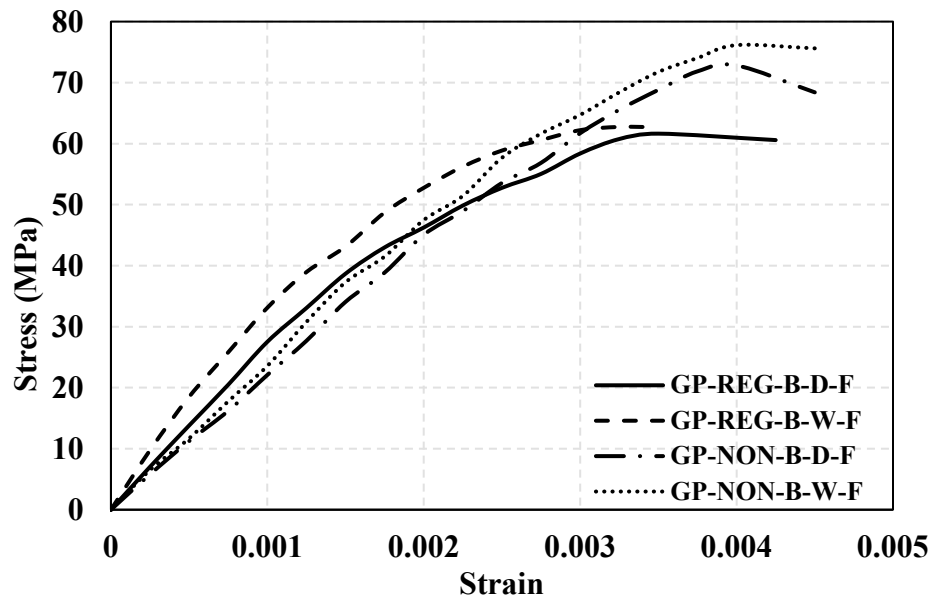
Figure 3.6 Observed compressive stress-strain relationships for full-scale dry and wet regular and non-shrink block-moulded grout prism

Figure 3.9(a) shows that, for wet masonry prisms constructed with non-shrink grout, when the grout strength increased from 55 MPa (non-shrink grout A) to 76 MPa (non-shrink grout B) for half-scale masonry prisms, and from 57 MPa (non-shrink grout A) to 70 MPa (non-shrink grout B) for full-scale masonry prisms, there was no significant increase observed in the prism's compressive strength. An increase of grout compressive strength in dry full-scale prisms rendered a non-proportional increase in the prism compressive strength due to the grout shrinkage. Compared to dry prisms, only the dry masonry prisms constructed with regular grout A (i.e., 32 MPa) exhibited enhanced compressive strength. This can be attributed to the grout strength that was much closer to that of the block strength (i.e., 37.4 MPa). This behaviour was also reported by other researchers (e.g., Khalaf et al. 1994, Roman and Romagna 2002, Sarhat 2016).

It is worth noting that grouting of plain masonry prisms was found to have an increase on the compressive strength of half-scale, full-scale, dry, and wet masonry prisms. Although the results of dry masonry prisms might seem contradicting with the findings of some of the previous researchers (e.g. Drysdale and Hamid 1979; Steadman et al. 1995), however, these results could be attributed to the height of the two-blocks high prisms of this research compared to that of their tested three-blocks and four-blocks high prisms, respectively.

3.6.3 Effect of non-shrinkage grout

Non-shrink grout was used in order to reduce the effects of grout shrinkage on the compressive strength of masonry prisms. The effect of non-shrink grout on the compressive strength of masonry prisms can be observed from Figure 3.7 and Figure 3.8. For full-scale dry masonry prisms, using non-shrink grout B yielded a nearly 16% increase in the prism compressive strength compared to grouted prisms constructed with regular grout B. Similarly, wet masonry prisms grouted with non-shrink grout B showed a 9% higher compressive strength than the masonry prisms grouted with regular grout B. Nevertheless, half-scale masonry prisms showed slightly higher compressive strength for prisms grouted with non-shrink grout B.
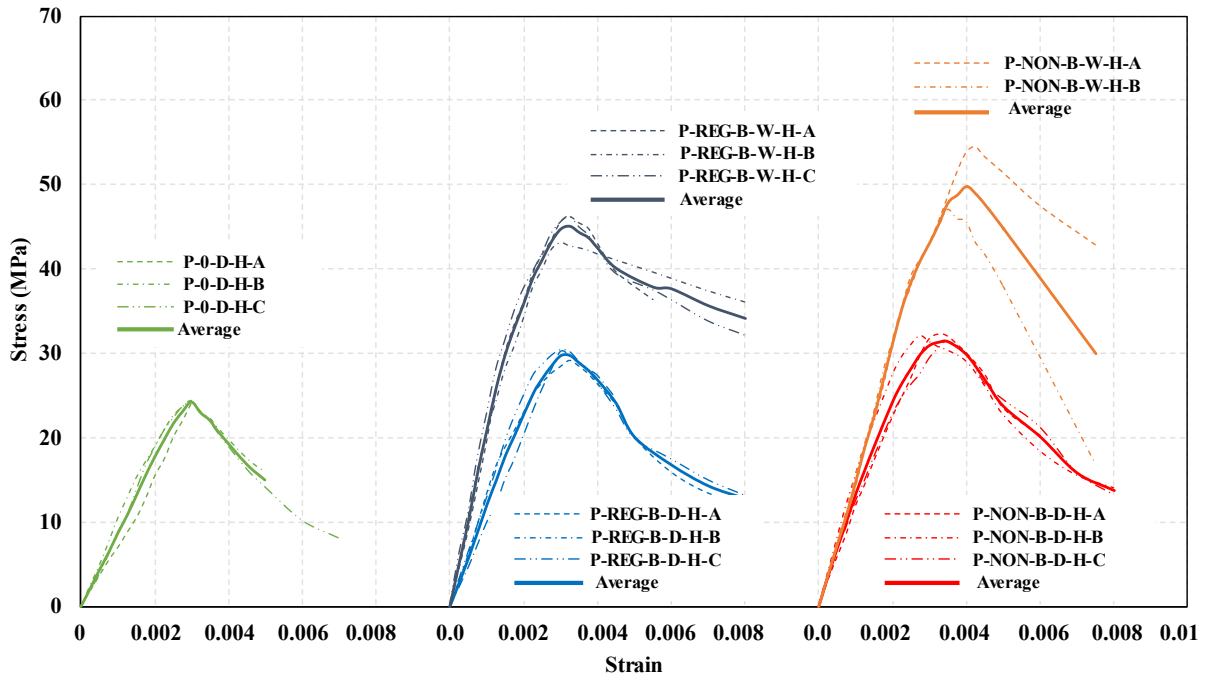
Figure 3.7 Observed compressive stress-strain relationship for half-scale masonry shell and half-scale dry and wet prisms constructed with regular and non-shrink grout
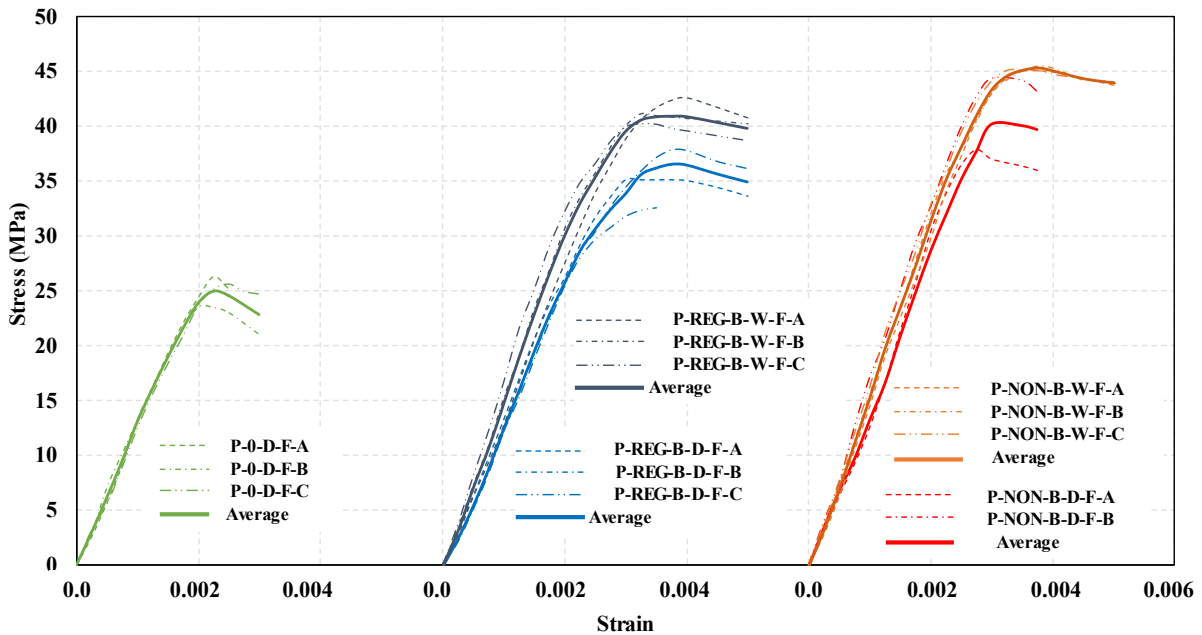
Figure 3.8 Observed compressive stress-strain relationship for full-scale masonry shell and full-scale dry and wet prisms constructed with regular and non-shrink grout

For dry and wet half-scale prisms, masonry prisms grouted with non-shrink grout B were 7% and 8% higher than those grouted with regular grout B, respectively. However, for the strains attained at peak stresses and the initial stiffness, masonry prisms grouted with non-shrink grout exhibited a slightly higher initial modulus of elasticity and lesser strain corresponding to the peak stress compared to prisms grouted with regular grout. Thanks to the lower water content of the non-shrink grout mixtures, masonry prisms constructed with non-shrink grout had less shrinkage separation cracks resulting in more homogeneous masonry assemblage. Moreover, this observation was much clearer in wet masonry prisms, where no shrinkage cracks are observed. However, dry non-shrink grouted masonry prisms experienced spalling of the masonry shell at the failure of masonry prisms where grout cores remained partially intact. Apparently, for all tested masonry prisms, non-shrink grout was shown to reduce the effects of grout shrinkage for dry and wet masonry prisms.

3.6.4 Effect of wetting

Pre-wetting of the masonry shell before grouting enabled the masonry blocks to preserve their moisture content as well as the grout core to maintain its free water content aiming at full hydration of the grout core up to the testing day. This helped the grout core to alleviate both plastic and drying vertical and lateral shrinkage that could have been happen if the masonry blocks were left dry before grouting as described by Boult (1979). Therefore, pre-wetting of the masonry prisms resulted in a homogeneous masonry assemblage including good bond between the masonry shell and the grout core without interface cracks as can be seen in Figure 3.5(c). Wet grouted masonry prisms showed enhanced compressive strength compared to dry grouted prisms. Figure 3.7 shows that, for half-scale masonry prisms grouted with regular grout B and non-shrink grout B, wet prisms were 51% and 52% higher in compressive strength than dry masonry prisms, respectively. On the other hand, for full-scale masonry prisms grouted with regular grout B and non-shrink grout B, wetting of grouted masonry prisms led to an increase of 17% and 11% compared to their dry counterparts, respectively (Figure 3.8). Compared to dry masonry prisms that suffered interface cracks, wet masonry prisms (with or without non-shrink grout) exhibited an enhanced grout core – masonry shell bond with no observed interface cracks. Components of wet masonry prisms showed homogeneous behaviour acting as a single element up to the failure of the prism, as shown in Figure 3.5(d). On the contrary, dry masonry prisms experienced face shell spalling at the failure

of the masonry prisms, as the masonry shell was expected to reach peak stress at a strain corresponding to less than that of the grout core. This resulted in the premature failure of the whole assemblage at a much lower compressive strength compared to that of the wet prism. Similarly to short concrete prisms, wet masonry prisms experienced conical shaped diagonal shear failure of both the masonry shell and the grout core. Masonry prism components (i.e., masonry shell and grout core) were observed to fail simultaneously with no sign of face shell spalling before crushing of the prisms. Failure of the masonry prisms showed that significant interface bonding was achieved between the masonry shell and the grout cores. Although grout cores were known to have higher strains at peak stress compared to the masonry shells (Priestly and Hon 1984; and Mohamed 2018), wet masonry prisms were able to eliminate spalling of the masonry shell up to the failure of the prism. Wet masonry prisms enabled the simple superposition of the grout core and the masonry shell capacities. It is worth noting that dry masonry prisms, however, did not achieve the superposition of masonry prism components as reported by many researchers. This can be observed from the strains attained at peak stresses in both dry and wet masonry prisms. The typical stress-strain response of block moulded grout prisms shows that the grout attained its peak stress at a corresponding axial strain ranging from 0.0035 to 0.004 (Figure 3.6). From Figure 3.8, it can be seen that wet masonry prisms attained their peak stress at a corresponding strain varying between 0.0035 and 0.004. This implies that the grout core was able to fully develop its compressive strain until the failure of the prisms. This resulted in an increase in the compressive strength of the wet grouted masonry prism compared to dry masonry prisms. On the contrary, dry masonry prisms exhibited lower strains corresponding to the peak stress ranging between 0.00285 and 0.00346. Testing of the dry full-scale masonry shell revealed that the peak stress was achieved at a corresponding strain of 0.0023 (COV = 5.9%) (Figure 3.8). This implies that the grout core was not permitted to fully develop its compressive strength due to the incompatible strains at peak stress for both the masonry shell (0.0023) and corresponding grout cores (0.0035 – 0.004) that caused premature failure of the whole assemblage. Also, grout shrinkage and bond failure between the dry masonry shell and corresponding grout core contributed to the lower capacity of the dry masonry prisms. It is worth noting that, although the tests examined full immersion of masonry blocks for 2 hours, wetting may be achieved by water hosing the surface of the masonry blocks to ensure a minimum level of saturation of the blocks to the point that the water can be observed to flow down the face shell of the masonry blocks before grouting (NCMA 1994).

3.6.5 Effect of lining

Lining of masonry prisms with a paper towel as a means of eliminating the initial tensile cracks due to restrained dry shrinkage was not as significant as expected. Figure 3.9(b) shows the comparison of stress-strain responses of dry masonry prisms with and without lining. Dry masonry prisms lined with paper towel preceding grouting with regular grout B showed a slight increase of 7% in the prism compressive strength compared to its regular non-lined counterparts. Lined masonry prisms also showed a higher initial modulus of elasticity and lower strains at peak stresses compared to regular dry grouted prisms. Lining was proposed to investigate the effect of breaking the bond between the masonry shell and the grout core to avoid the tensile cracks induced at this interface due to grout shrinkage. Although lining was expected to yield two separate material components that can be tested simultaneously under compression load to achieve the superposition of both components (i.e., masonry shell and grout core), it could not prevent the water absorption of the grout cores by the surrounding dry masonry blocks. This resulted in lateral tensile strains exerted by the isolated grout cores on the masonry shell causing premature failure of the masonry shell and consequently the whole grouted prism. Most of the grout cores remained intact even after the failure and crushing of the masonry prism. However, it should be noted that lining is not a practical solution for the grout shrinkage problem in terms of the cost and workmanship.

(a)   (b)
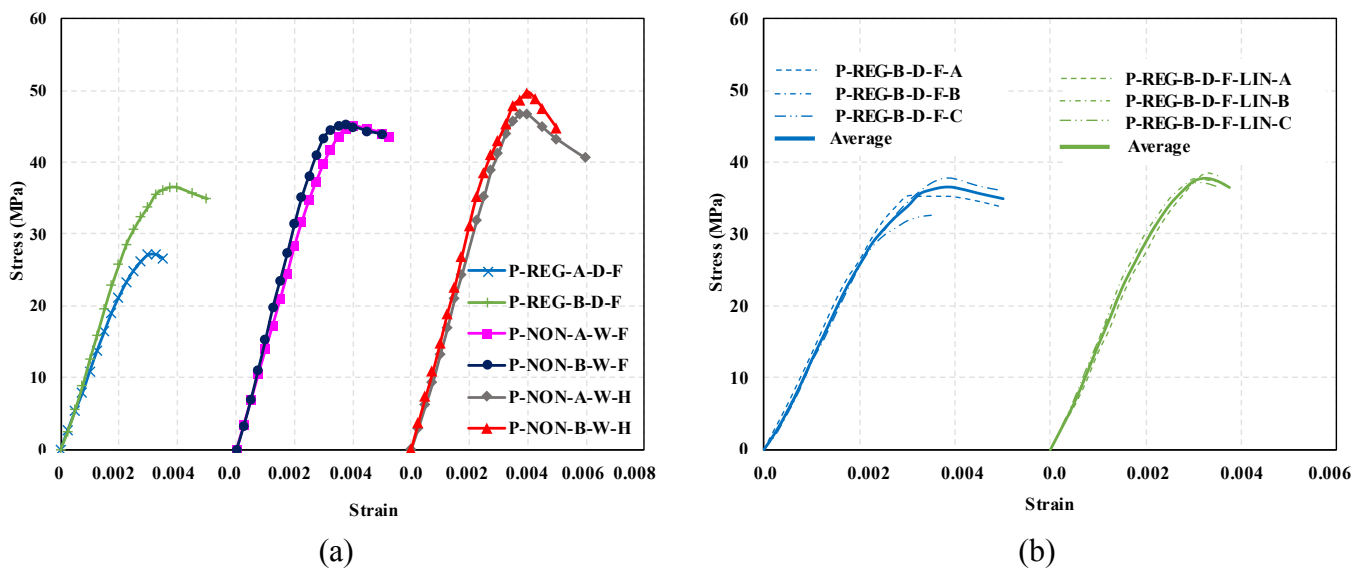
Figure 3.9 Observed stress-strain relationships of (a) Full-scale and half-scale masonry prisms having different grout strengths, and (b) Full-scale masonry prisms with and without lining of their grouted cells

3.6.6 Effect of scaling

Figure 3.10 shows the comparison of stress-strain curves of half-scale masonry prisms and full-scale masonry prisms. For ungrouted masonry, half-scale masonry prisms attained the peak stress at 24.29 MPa (COV= 0.31%) with a corresponding strain of 0.00295 (COV= 0.98%), whereas the full-scale prisms reached the maximum compressive strength of 25.46 MPa (COV= 5.0%) with a corresponding strain of 0.00228 (COV= 5.9%). Dry half-scale and full-scale masonry prisms grouted with regular grout B showed a compressive strength of 30.00 MPa (COV= 2.28%) and 35.22 MPa (COV = 7.33%), respectively. In addition, for dry prisms constructed with non-shrink grout B, half-scale and full-scale masonry prisms demonstrated 31.98 MPa (COV=1.56%) and 40.77 MPa (COV=8.30%), respectively.
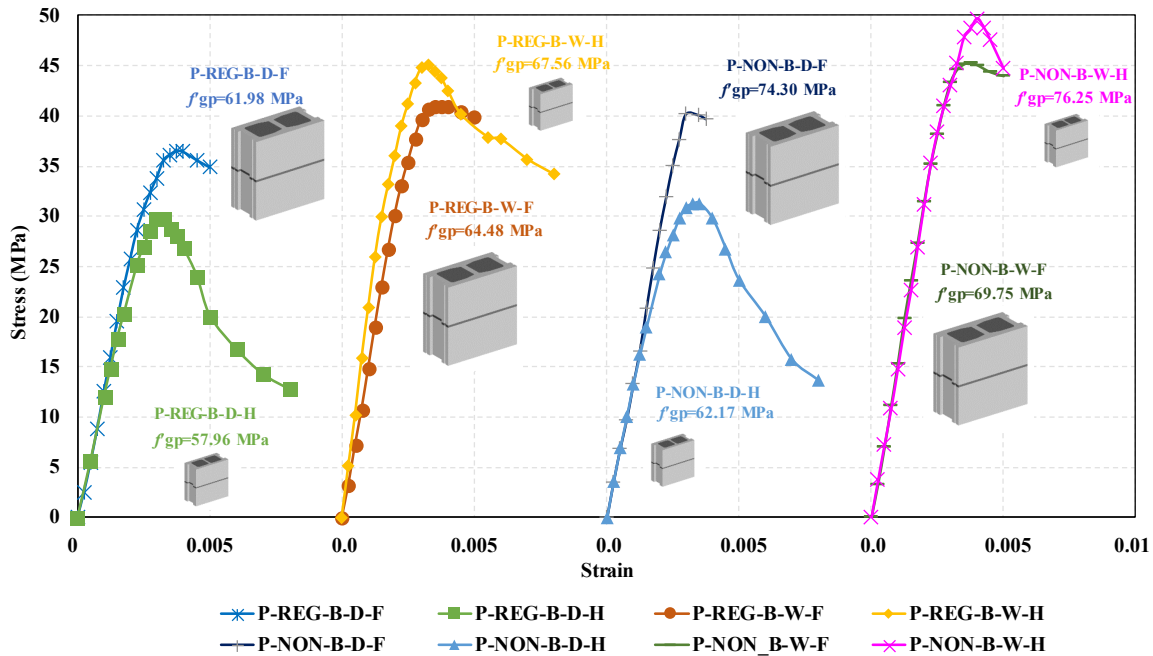
Figure 3.10 Observed stress-strain relationships showing the effect of scaling for dry and wet half-scale and full-scale masonry prisms with regular and non-shrink grouts

For wet masonry prisms constructed with regular grout B, half-scale masonry prisms showed a slightly higher compressive strength of 45.25 MPa (COV = 4.01%) than the full-scale masonry prisms that gained a peak stress of 41.32 MPa (COV = 2.97%). Moreover, wet masonry prisms of non-shrink grout B showed very similar peak stresses of 48.74 MPa (COV = 10.44%) and 45.24 MPa (COV=0.46%) for half-scale and full-scale masonry prisms, respectively. In terms of the

modulus of elasticity, ungrouted full-scale masonry prisms had a slightly higher initial modulus of elasticity compared to their half-scale counterparts. Nonetheless, full-scale and half-scale grouted masonry prisms showed approximately similar strains at peak stresses and an initial modulus of elasticity. For dry masonry prisms, half-scale prisms had higher ultimate strains at failure compared to their full-scale counterparts. In general, half-scale masonry prisms showed enhanced post-peak behaviour in terms of the ultimate strains. Since, for comparison purposes, the rate of loading was similar in half-scale and full-scale masonry prisms, it was suitable to get the full descending branch of the half-scale masonry prisms but not for the full-scale specimens. However, this rate of loading should have been reduced to capture the post-peak behaviour of the full-scale masonry prisms. Moreover, the higher platen effect that confined the half-scale prism ends resulted in non-explosive crushing failure of the half-scale specimens compared to the full-scale prisms. Based on these results, it can be observed that some discrepancies arose, and some deviations were observed for the half-scale masonry prisms compared to their full-scale counterparts. Some deviations were expected due to the differences of the block moulded grout strength, f'_{gp}, of both half-scale and full-scale grouted masonry prisms. For example, it can be noticed from Figure 3.10 that there are differences at peak stress for the tested half-scale and full-scale masonry prisms. This can be attributed to the differences of the block moulded grout strength of both half-scale and full-scale prisms. This difference was maximized to nearly 9 MPa between the peak stress of the half-scale P-NON-B-D-H group of prisms, where the grout strength was 74.3 MPa, and the full-scale P-NON-B-D-F group of prisms where the grout strength was recorded at 62.17 MPa. However, there was good agreement in the initial modulus of elasticity of the dry and wet half-scale and full-scale prisms. The results of the tests highlight the need for more detailed research on the effect of scaling on the overall behaviour of the concrete masonry prisms.

3.6.7 Superposition of masonry shell and grout core

Table 3.4 shows the superposition ultimate load values of the masonry shell and the grout cores along with the experimental results for the tested masonry prisms. It is worth noting that the grout core ultimate load was computed as the multiplication of the block moulded grout prism strength corresponding to each group of prisms by the grout core area of 7002 mm^2 and 30,093 mm^2 for half-scale and full-scale masonry prisms, respectively. It can be seen that the superposition significantly overestimated the dry prisms ultimate loads by 30% and 28% for half-scale masonry

prisms having regular grout B and non-shrink grout B, respectively. This has been discussed by many previous researchers. On the other hand, it is shown that the wet masonry prisms have a high degree of conformity with the superposition predicted values. The superposition peak loads have been exceeded in the experimental results by 4% and 3% for regular grout B and non-shrink grout B, respectively. Wet masonry prisms grouted with non-shrink grout A showed higher experimental results than those predicted by the superposition. This can be attributed to the enhanced behaviour of these prisms due to the usage of non-shrink grout with a grout compressive strength of almost 1.5 times that of the masonry block, along with enhancement behaviour resulting from the wetting scheme. The variation of the masonry blocks′ compressive strengths, as well as that of the block moulded grout cores, also contributed to the underestimation of the superposition in the strength of these prisms.

For full-scale masonry prisms, superposition was shown to significantly overestimate the capacity of dry masonry prisms. This was observed in regular grout B and non-shrink grout B used for grouting the dry masonry prisms where the ultimate capacity was overestimated by 16% and 13%, respectively. It should be noted that for the dry masonry prisms grouted with regular grout A, the superposition was almost achieved. This may be attributed to the compatibility of the grout prism compressive strength of these prisms (i.e., 32 MPa) to that of the masonry block strength (i.e., 37 MPa). It can be inferred that wet masonry prisms – regardless of the type of the grout – attained or even exceeded the computed superposition of the corresponding masonry shell and grout core capacities.

3.6.8 Proposed literature equations for predicting the compressive strength of a grouted masonry prism

Figure 3.11 shows a comparison between the test results of this research and the results of the empirical equations derived by previous researchers to predict the compressive strength of grouted masonry prisms. It is worth noting that the two blocks high stack bonded prisms were selected based on the ASTM 1314-14 provisions. However, literature (e.g. Drysdale and Hamid 1979, Maurenbrecher 1980, Hassanli et al. 2015, Mohamed 2018) showed that there was a significant increase in the peak stress and corresponding peak strain associated with two-courses high prisms. Therefore, to account for these effects, the experimental results of this research work were adjusted according to the correction factors of the aspect ratios (h/t) stipulated in the CSA S304-14 to better

68

correlate the experimental results with the literature masonry prisms having different height-to-thickness (h/t) ratios.

The equations can be summarized as follows:

a) Hamid and Drysdale (1978)

$$f'_m = f'_{sh}(\eta + 0.143\frac{f'_{gp}}{f'_b}) \text{ MPa, grout prism}$$

(3.1)

f'_m : Masonry compressive strength

f'_{sh} : Masonry shell compressive strength; 24.9 MPa

η : net to gross area ratio (i.e. solid ratio) (A_n/A_g); 0.57

f'_{gp} : grout prism compressive strength

f'_b : masonry block compressive strength; 38.2 MPa

It should be mentioned that, for correlation purposes, the values calculated by the Hamid and Drysdale (1978) equation were multiplied by 1.07 hereinafter to account for the difference between the aspect ratio of (h/t) of 3 of the researchers' prisms compared to (h/t) of 2 of these experimental work prisms according to ASTM C1314-14.

b) Sturgeon et al (1980)

$$f'_m = 0.62f'_{sh}\eta + 0.75\mu f'_{gp}(1-\eta) \text{ MPa, grout prism}$$

(3.2)

μ : Grout prism to grout cylinder reduction factor; 0.92

c) Priestly and Hon (1984)

$$f'_m = 5.91\,\eta\,(0.1f'_b + 0.0128f'_{mr}) + 0.86(1-\eta)f'_{gp} \text{ MPa, grout prism}$$

(3.3)

f'_{mr} : mortar compressive strength

d) Khalaf et al. (1994)

$$f'_m = 0.30f'_b + 0.20f'_{mr} + 0.27\,f'_{gp} \text{ MPa, grout prism}$$

(3.4)

To account for the difference between the aspect ratio (h/t) of 3 that was used by Khalaf et al. (1994) and that used in this experimental work of h/t = 2, a factor of 1.07 will be used to convert the values calculated by Eq. (5) according to ASTM 1314-14.

e) **Sarhat (2016)**

$$f'_m = 0.29 f'_b + 0.10 f'_{mr} + 0.21 \mu f'_{gp} + 1.51 \text{ MPa, grout prism} \tag{3.5}$$

It is worth noting that the compressive strength, f'_m values computed from Eq. (5) were multiplied by a factor of 1.22 to account for the aspect ratio (h/t) discrepancy according to ASTM 1314-14 (American Society for Testing and Materials (ASTM) 2014) to convert from (h/t = 5) to (h/t = 2).

f) **Mohamed (2018)**

$$f'_m = f'_{sh} A_n + 0.474 \, (1 - \eta) f'_{gp} \text{ MPa, grout prism} \tag{3.6}$$

It is worth noting that the values computed from Eq. 6 will be multiplied by a factor of 1.22 in order to convert the aspect ratio of 5 to that of 2 according to ASTM 1314-14.

Table 3.4 Superposition of half-scale and full-scale masonry prism results

Group number	Group Identifier	Masonry shell Ultimate load (kN)	Grout Core Ultimate load (kN)	Superposition ultimate load (kN)	Experimental ultimate load (kN)	Ultimate load Difference (%)
1	P-0-D-H	217.7	---	217.7	217.7	---
2	P-REG-B-D-H	217.7	405.8	623.6	479.0	30
3	P-REG-B-W-H	217.7	473.1	690.8	722.4	-4
4	P-NON-A-W-H	217.7	385.8	603.6	752.5	-20
5	P-NON-B-D-H	217.7	435.3	653.1	510.5	28
6	P-NON-B-W-H	217.7	533.9	751.7	778.2	-3
7	P-0-D-F	1034.6	---	1034.6	1034.6	---
8	P-REG-A-D-F	1034.6	963.2	1997.8	1943.0	3
9	P-REG-B-D-F	1034.6	1865.3	2899.9	2491.1	16
10	P-REG-B-D-F-LIN	1034.6	1865.3	2899.9	2671.2	9
11	P-REG-B-W-F	1034.6	1940.3	2974.9	2922.2	2
12	P-NON-A-W-F	1034.6	1720.7	2755.3	3199.2	-14
13	P-NON-B-D-F	1034.6	2235.8	3270.4	2883.3	13
14	P-NON-B-W-F	1034.6	2099.1	3133.7	3199.4	-2

3.6.9 Discussion and comparison of literature equations

Figure 3.11 presents a comparison between the test results of this experimental work and the predicted values of masonry prism specified compressive strength by previously explained literature equations. It is worth noting that the specified masonry compressive strength of the tested prisms was calculated according to Annex C of the CSA S304-14.
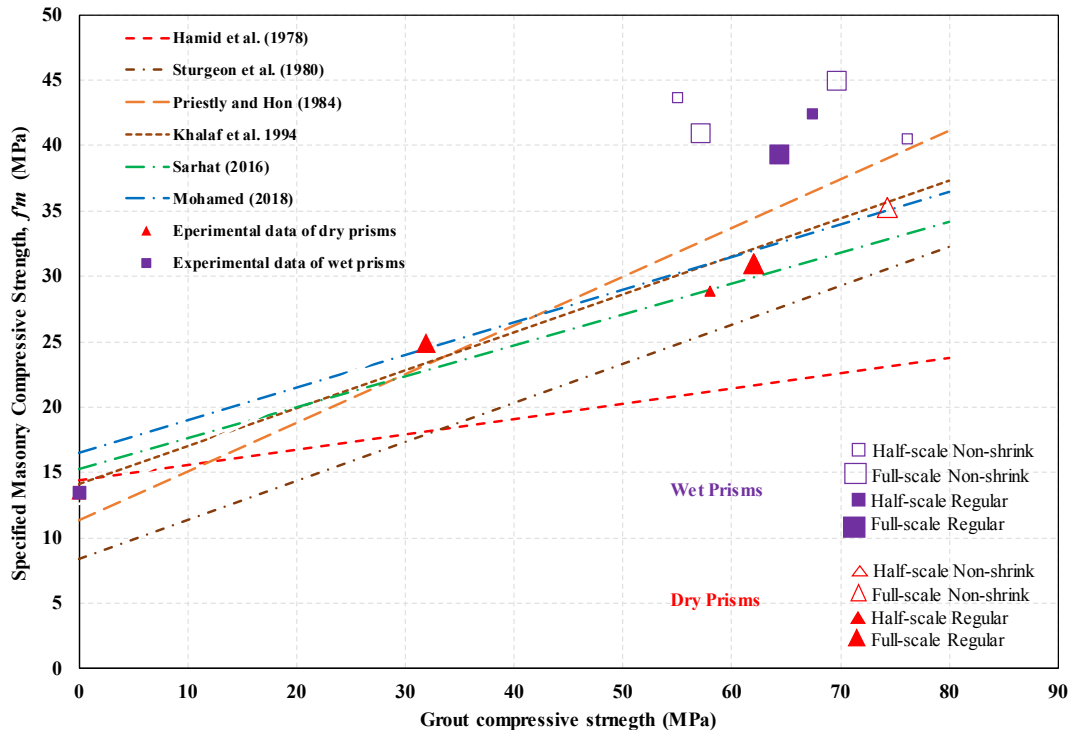
Figure 3.11 Comparison of literature equations with this research results: Hamid et al. (1978), Sturgeon et al. (1980), Priestly and Hon (1984), Khalaf et al. (1994), Sarhat (2016), and Mohamed (2018)

On average, the Hamid et al. (1978) equation was found to underestimate both dry and wet masonry prism compressive strengths by nearly 30% and 47%, respectively. Their equation accounted for the greatest underestimation of the prism compressive strength among its counterparts due to the small proposed portion of the grout share to the prism compressive strength (i.e., 22%).On the other hand, the Sturgeon et al. (1980) equation underestimated the masonry prism compressive strength by 16% and 34% for both dry and wet specimens, respectively. On the contrary, the equation reported by Priestly and Hon (1984) exhibited the most agreement with the experimental results of wet prisms with an underestimation of 15% on average. This can be

attributed to the highest proposed portion of grout contribution to the masonry prism compressive strength which was based on the usage of non-shrink grout in the New Zealand code of practice for the construction and grouting of masonry structures. However, this equation was found to result in unsafe overestimation of the dry prisms′ strength by 8%. Similarly, the proposed equation by Khalaf et al. (1994) showed an average of 2% overestimation of the strength of the dry prism compared to an underestimation of 21% of the compressive strength of wet masonry prisms. It is worth noting that the predicted values computed by the Sarhat (2016) equation showed an average of 5% underestimation for the dry prisms′ compressive strength compared to a 27% underestimation of the wet masonry prisms′ strength. Eventually, the proposed equation by Mohamed (2018) showed an underestimation of 2% and 22% for the dry and wet masonry prisms′ compressive strength, respectively.

Figure 3.11 shows that increasing the grout strength in dry grouted masonry prisms increased the compressive strength of their corresponding prisms and consistent results were observed. Wet full-scale masonry prisms constructed with non-shrink grout exhibited an increase of the compressive strength when the grout strength was increased. However, increasing the compressive strength of non-shrink grout decreased the compressive strength of half-scale wet masonry prisms. The test results show that, for the same grout strength, wetting of dry masonry prisms was found to significantly enhance the compressive strength of grouted masonry prisms compared to their dry counterparts. However, the wet masonry prisms showed no consistent correlation with the grout strength; hence, further research is recommended to determine the proper wetting scheme and to identify the parameters that affect the compressive strength of wet grouted masonry prisms.

3.7 Conclusions

Comprehensive research work was conducted to investigate the influences of various parameters on the reduction of the compressive strength of masonry prisms. The literature showed that shrinkage of the grout core and the bond between the masonry shell and the grout core could contribute to the reduction of grouted masonry compressive strength. To mitigate some of these factors, shrinkage of the grout core was planned to be minimized as well as the grout core–masonry shell bond to be enhanced. In this experimental work, the influence of four different grout types on the grout core shrinkage and the masonry prism compressive strengths and strains was investigated. Moreover, the lining of masonry prisms using paper towel was introduced to break

72

the bond at the interface of the grout core and the masonry shell. This was to complement the understanding of the effect of shrinkage on the prism strength. Furthermore, to enhance the bond between the masonry shell and corresponding grout core, wetting of masonry prisms just before grouting was investigated. Half-scale and full-scale masonry prisms were tested to examine the effect of scaling on the stress-strain response of ungrouted and grouted masonry. Comparisons of the test results were conducted in terms of the stress-strain response and the initial stiffness of the tested masonry prisms. Literature equations developed by previous researchers were examined against the test results presented herein to study the effectiveness of these equations in the prediction of masonry prism compressive strength. Based on the results of the experimental program, the following conclusions can be drawn:

1. Grouting of plain masonry prisms was found to increase the compressive strength of half-scale, full-scale, dry, and wet masonry prisms. The results of dry masonry prisms, however, might seem contradicting to some of the previous researchers which could be attributed to the height of the two courses high masonry prisms.

2. Although increasing the grout compressive strength resulted in a non-proportional increase in the compressive strength of dry masonry prisms, consistent results were recorded with different grout strengths. However, there was no consistent trend for the wet masonry prisms when the grout strength was increased.

3. Masonry prisms constructed with non-shrink grout showed an increase in the compressive strength when compared to masonry prisms grouted with regular grout. However, this increase was not as significant as expected. Stress-strain responses of regular and non-shrink grouted masonry prisms were correlated. It was found that, in general, non-shrink grouted masonry prisms demonstrated a slightly higher initial modulus of elasticity, lesser strain corresponding to the peak stress, and comparable post-peak behaviour compared to regular grouted masonry prisms.

4. Wetting of masonry prisms just before grouting was found to enhance their compressive strength. Wetting enables both the masonry assemblage components (i.e., masonry shell and grout core) to fully develop their compressive strength. Wet masonry prisms were found to achieve the superposition of the grout core and the corresponding masonry shell. Therefore, the authors recommend wetting of masonry blockwork before grouting as a means of enhancing the grouted masonry compressive strength.

5. Superposition of the masonry shell and the grout core strengths was found to highly overestimate dry grouted masonry prism compressive strength. On the contrary, wet masonry prisms demonstrated excellent conformity with the superposition. Hence, it can be concluded that superposition of wet masonry prisms is valid and applicable with different grout strengths.

6. Clearly, wetting of dry masonry prisms is a promising construction procedure that significantly enhanced the compressive strength of grouted masonry. However, further research is required to determine the proper wetting pattern and to ensure consistent results that can be adequately quantified.

7. Lined grouted masonry prisms showed slightly higher compressive strength compared to regular grouted masonry prisms. However, lining was not as significant as expected, despite that its eliminating the effect of tensile cracks due to restrained drying shrinkage. Inserting lining between the shell and the grout resulted in non-homogeneous behaviour of the lined masonry prisms as well as a reduction in the compressive strength compared to the wet masonry prisms.

8. Direct comparisons of the test results of the half-scale masonry prisms and the prototype prisms were established. Half-scale masonry prisms showed a comparable modulus of elasticity and strain at peak strength to their full-scale counterparts. However, some discrepancies in the compressive strength and post-peak behaviour were observed. The test results highlight the need for more detailed research work on the influence of scaling on the overall stress-strain response of the concrete masonry prisms.

In conclusion, based on the test results of the studied parameters, it was evident that the interaction between the tested parameters has a significant influence on the compressive strength of fully grouted concrete masonry prisms. For dry masonry prisms, it is recommended to match the grout compressive strength with that of the concrete masonry units in order to achieve the optimum masonry prisms' compressive strength. Besides, combining high-strength flowable non-shrink grout with high-strength concrete masonry blocks was also found to give considerably high prism's compressive strengths. Prewetting of dry masonry blocks before grouting is also recommended to enhance the compressive strength of fully grouted concrete-masonry columns and gravity walls to enhance their axial load carrying capacity

Chapter 4

Experimental Investigation of Axial Compressive Behaviour of Square and Rectangular Confined Concrete-Masonry Structural Wall Boundary Elements

4.1 Abstract

Reinforced masonry boundary elements (RMBEs) are critical components in determining the lateral response of reinforced masonry structural walls with boundary elements. Fundamental interpretation of the effect of various influential parameters on the RMBEs′ behaviour is essential to enhance their stress-strain response. This study investigates, experimentally, the influence of various design parameters and construction procedures on the axial compressive behaviour of fully grouted RMBEs built with C-shaped concrete-masonry blocks. Thirty-eight unreinforced and RMBEs were constructed and tested under concentric axial loading till failure. The effect of five parameters, namely, the vertical reinforcement ratio, the volumetric ratio of confinement reinforcement, cross-section configuration, stack pattern and running-bond, and pre-wetting of dry masonry shell before grouting, was investigated. The test results showed that increasing the vertical reinforcement ratio of the RMBEs resulted in a significant increase in the peak compressive stress and a considerable reduction in the corresponding strain ductility. Moreover, as the RMBEs volumetric ratio of transverse reinforcement doubled, the strain ductility witnessed a remarkable enhancement, whereas the peak compressive stress experienced an inconsistent trend. RMBEs built with rectangular C-shaped cross-sections exhibited comparable peak stress, smaller drop following the face shell spalling, and better strain ductility than square RMBEs. The running-bond pattern had a negative effect on both the peak stress and the strain ductility of dry RMBEs, although it exhibited comparable or even enhanced response in wet RMBEs compared to those built in the stack pattern. Pre-wetting of dry masonry shell before grouting was found to boost the peak compressive stress of unreinforced and RMBEs significantly. However, it adversely affected their strain ductility. Wet RMBEs showed a steeper post-peak descending branch compared to their dry counterparts. Indeed, the vertical reinforcement ratio and pre-wetting of dry masonry shell were the most critical parameters affecting the RMBEs peak compressive stress, whereas the confinement ratio mostly influenced the strain ductility. This study sheds light on the most critical parameters influencing the stress-strain components (i.e., strength and ductility) of RMBEs.

4.2 Introduction

Unlike reinforced concrete (RC) structural walls (i.e., shear walls), fully grouted reinforced masonry shear walls (RMSWs) with rectangular sections have capacity and ductility limitations because of the restricted arrangement of one layer of vertical reinforcement (i.e., without confinement) due to the limited geometry of the concrete-masonry stretcher blocks. Therefore, confined reinforced masonry boundary elements (RMBEs) can be incorporated at the end zones of a rectangular masonry shear wall to postpone buckling of the vertical reinforcement, enhance the lateral capacity, and boost both curvature and displacement ductility. Research studies that were conducted on the seismic behaviour of reinforced masonry shear walls with boundary elements (RMSW+BEs) (e.g., Albutainy et al. 2017; Aly and Galal 2019, 2020a; b; c; Banting and El-Dakhakhni 2012; Ezzeldin et al. 2016; Shedid et al. 2010) revealed a significant enhancement of strength, stability, and ductility levels compared to their rectangular counterparts. As shown in Figure 4.1, RMBEs resemble masonry columns at the wall toes to thicken its most stressed zones. They are considered the key components to understand the lateral cyclic behaviour of RMSW+BEs; however, minimal research was performed to investigate their compressive behaviour. Therefore, there is a need to investigate, experimentally, the axial compressive stress-strain behaviour of RMBEs to quantify the influence of different design parameters on their performance.
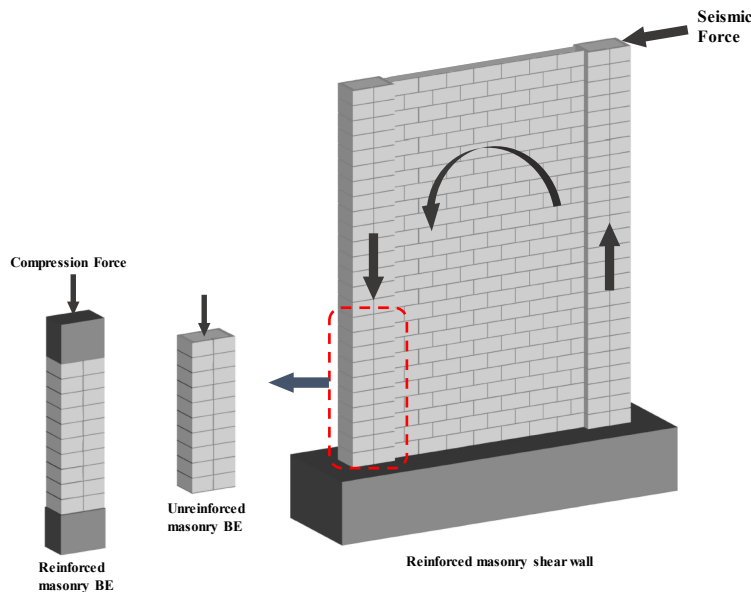
Figure 4.1 Schematic diagram of a reinforced masonry shear wall and its boundary elements

Fundamental understanding of the compressive stress-strain behaviour of RMBEs helps to enhance their response (i.e., strength and strain ductility), which in turn results in high-performance masonry assemblage and components. Besides, this will outweigh the low compressive strength levels assigned to fully grouted masonry in North American Standards (e.g., CSA S304-14 and TMS 402/602-16) and enable the concrete-masonry to be utilized in mid-and high-rise buildings.

Previous researchers conducted experimental and analytical studies to investigate the axial compressive behaviour of unconfined and confined concrete-masonry and develop stress-strain models to capture that behaviour. Priestly and Elder (1983) investigated the influence of the masonry block width of 140 mm and 190 mm, confining steel plates at the mortar joints, and the strain rate on the compressive stress-strain behaviour of masonry prisms. The researchers concluded that the unconfined prisms experienced a premature failure of the masonry shell before crushing the masonry grout core. Also, there was no significant influence for changing the block width on the masonry prisms′ stress-strain behaviour, although the net-to-gross area ratios were different for both blocks. The confining steel plates enhanced the masonry prisms′ post-peak behaviour generating a more gradual falling branch than unconfined prisms. Moreover, increasing the strain rate increased the peak stress (i.e., maximum compressive strength) and resulted in a more steepening descending branch for the confined grouted concrete-masonry prisms. Sajjad (1990) studied different confinement arrangements, namely, mesh confinement, confinement comb, spiral confinement, and spiral cage confinement, to investigate their influence on the compressive behaviour of concrete-masonry prisms. The ultimate compressive strain of masonry prisms confined with the comb and spiral reinforcement experienced an increase of 100% compared to their unreinforced counterparts. Shing et al. (1993) proposed three different confinement configurations: the confinement ring, comb, and spiral cage that can be placed to confine the grout in hollow-grouted concrete-masonry prisms and walls. The researchers concluded that the post-peak behaviour and the ultimate strain of the confined prisms were greatly enhanced compared to unreinforced masonry prisms.

The literature showed that very limited research was conducted on the axial compressive behaviour of RMBEs. Abo El Ezz et al. (2015) aimed at investigating the influence of the confinement reinforcement ratio ranged between 0.008% to 0.038% on the compressive behaviour

and the strain capacity of RMBEs built with standard stretcher concrete-masonry blocks. Unlike a standard masonry block prism, the results showed that the confined RMBEs showed enhanced peak stress and strain capacity compared to the unconfined boundary elements. The peak stress of the confined RMBEs was more than 1.6-2.4 times that of the unconfined MBEs, whereas the strain at 50% strength degradation ranged from 2.2 to 7 times that of the unconfined BEs. As the confinement ratio increased, the strain ductility increased, and the stress-strain falling branch's slope flattened. It is noteworthy that standard stretcher blocks′ geometry limited the confinement configuration studied by Abo El Ezz et al. (2015), which only allowed placing the confinement ties at the mortar joints. Therefore, to promote a practical construction solution for confined RMBEs, Obaidat et al. (2017) utilized C-shaped masonry blocks to construct confined RMBEs with different hoop spacings. The researchers tested 16 full-scale C-shaped RMBEs with different confinement reinforcement ratios almost similar to those tested previously by Abo El Ezz et al. (2015). They inferred that increasing the confinement reinforcement ratio significantly enhanced the post-peak behaviour of the RMBEs in terms of the strain capacity and the falling branch of the stress-strain curve. In another study by Obaidat et al. (2018), thirty half-scale fully grouted C-shaped masonry boundary elements were experimentally tested under axial compression load. The influence of the longitudinal reinforcement ratio, the hoop spacing, and the grout strength on the axial compressive stress-strain response was investigated. Two grout strengths: 15 and 45 MPa, two longitudinal reinforcement ratios: 0.8 and 1.4%, and three volumetric ratios of confinement reinforcement: 0.45, 0.6, and 0.9 %, with hoops spacings 60, 45, and 30 mm, respectively, were studied. It was found that increasing the grout strength and decreasing the hoops′ spacing enhanced the peak stress and post-peak behaviour significantly. Moreover, the presence of the longitudinal reinforcement enhanced the strain ductility of RMBEs compared to their unreinforced counterparts. In a recent paper, Obaidat et al. (2019) investigated the effect of the aspect ratio on the compressive stress-strain behaviour of unconfined and confined masonry boundary elements. Two different aspect ratios, namely, 2 and 3, were examined. All the RMBEs were tested monotonically under axial compressive load until failure. The researchers reported that decreasing the aspect ratio (i.e., height to thickness ratio) resulted in an increase in the peak stress and the post-peak strain capacity of the studied RMBEs.

4.3 Research Significance

The literature showed very limited research on the axial compressive behaviour of unreinforced masonry boundary elements (MBEs) and reinforced masonry boundary elements (RMBEs). Moreover, previous researchers (e.g., Banting and El-Dakhakhni 2014) recommended more investigation and quantification of the concrete-masonry material behaviour with various confinement configurations is beneficial for interpreting the overall seismic response of RMSW+BEs. Furthermore, the CSA S304-14 stipulated geometrical and detailing requirements for confined boundary elements; however, it limits the design masonry ultimate compressive strain to 0.008 at the wall toes. Further investigations are also needed for a reliable application to RMSWs with boundary elements (Abo El Ezz et al. 2015). Therefore, the compressive stress-strain behaviour of RMBEs needs to be deeply investigated. In addition, enhancing the masonry axial compressive stress-strain response will result in high-performance masonry assemblage and components. Moreover, it helps offsetting the limits of the masonry ultimate compressive strains beyond those stipulated in the current CSA S304-14 standards This will enable promoting the reinforced masonry shear walls for the growing masonry industry in North American buildings.

This study aims to enhance both the compressive strength and the ductility of the RMBEs. Five critical parameters influencing the axial compressive stress-strain behaviour of the RMBE were investigated to achieve the aims of this study. These parameters are the vertical reinforcement ratio (ρ_v), the volumetric ratio of confinement reinforcement (ρ_h), the bonding pattern (i.e., stack pattern vs. running-bond), pre-wetting of dry masonry shell before grouting, and the boundary element cross-section configuration (i.e., square vs. rectangular boundary elements). All unreinforced and RMBEs are constructed with C-shaped concrete-masonry units (See Figures 4.2 and 4.3) to accommodate various confinement configurations and hoop spacings that would not have been done if standard stretcher blocks were utilized.

Two vertical reinforcement ratios were investigated for both square and rectangular boundary elements, namely, 0.78% and 1.55%. Moreover, the effect of two volumetric ratios of confining reinforcement, namely, 1.87% and 3.74%, and two bonding patterns, namely, stack pattern and running-bond, were tested. It should be noted that pre-wetting of dry masonry shells before grouting is a procedure recommended by the authors in (AbdelRahman and Galal 2020) to achieve a better bond between the masonry shell and the grout core by reducing the extreme absorption of

the grout water content by surrounding dry masonry blocks. This, in turn, will enhance the RMBEs compressive strength. Furthermore, two cross-sections, namely, square (190x190 mm) and rectangular (190x290 mm), were investigated.

The test results are presented in terms of quantifications and comparisons of the RMBEs stress-strain parameters, namely, the peak stress, the strain corresponding to the peak stress, the strains at 25% and 50% strength degradations, and the strain ductility. Also, comparisons of RMBEs stress-strain curves were conducted to identify the differences between pre-peak and post-peak behaviours, hoop fractures, and failure strains.

Square RMBE (190x190 mm)   **Rectangular RMBE (190x290 mm)**
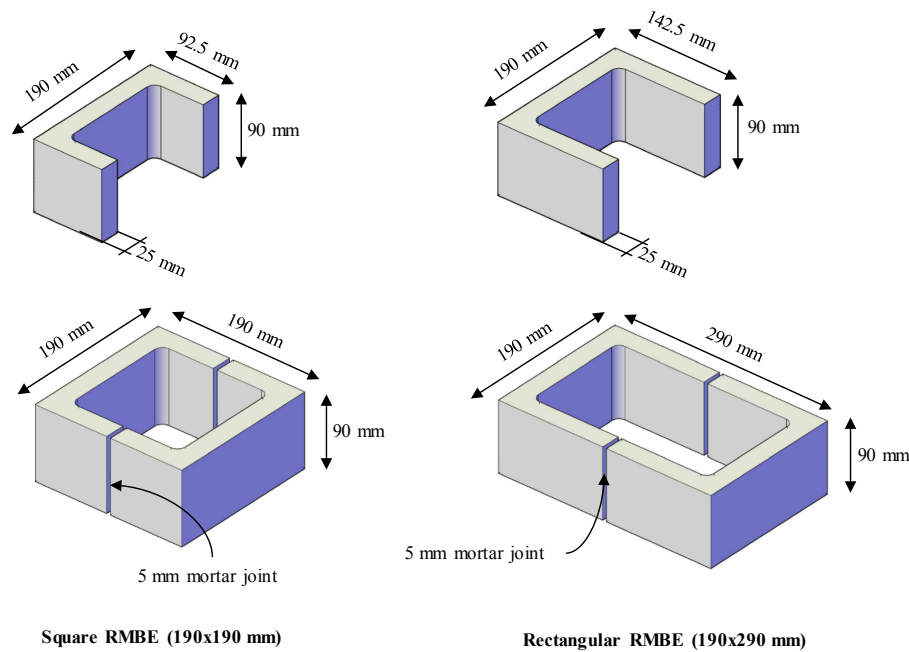
Figure 4.2 Square and rectangular concrete-masonry C-shaped pilaster units for RMBEs

4.4 Experimental Program

4.4.1 Test Matrix

Thirty-eight half-scale fully grouted C-shaped unreinforced and reinforced concrete-masonry boundary elements were constructed and tested monotonically under concentric axial compression load. A professional mason constructed these boundary elements. Table 4.1 presents the details of the tested boundary elements. The test matrix was selected based on the literature gap in order to address design parameters and construction procedures that have a significant influence on the

strength and ductility of RMBEs. The test matrix considered the influence of changing the vertical reinforcement ratio by changing number of the steel bars rather than increasing the bars' diameters in order to study its influence on the ductility of RMBEs. Besides, different geometrical shapes of RMBEs' sections (i.e., square and rectangular) have a significant influence on their stress-strain behaviour. Furthermore, the construction procedures, bonding pattern and prewetting of dry MBEs before grouting, can contribute to enhance or reduce the strength and ductility of RMBEs. The RMBEs were divided into 14 groups; each group has three replicates to account for the statistical purposes of the RMBEs and ensure consistency of the results. In Table 4.1, each specimen was given a designation: the first two letters BE representing the boundary element are followed by the vertical reinforcement amount. Then, D4 or D8 is the confinement hoop size that is followed by D or W, which denote dry or wet masonry shell before grouting, respectively. Afterwards, the abbreviation RUN or REC refers to boundary elements that were built in a running-bond pattern or a rectangular section 190x290 mm. It should be noted that all boundary elements were built with a square section of 190x190 mm in the stack pattern, except those marked with RUN or REC abbreviations. Eventually, the letters A, B, or C were used to distinguish between three RMBEs replicates of the same group. For instance, the specimen BE-8#3-D4-D-B represents the second replicate of three specimens that were constructed with 8-#3 vertical steel bars, confined with D4 hoops, had dry masonry shell before grouting, and built with a square section of 190x190 mm.

Table 4.1 Test matrix of unreinforced and reinforced masonry boundary elements (MBEs, and RMBEs)

Group number	Group Identifier	Number of tested MBEs	Status of MBEs before grouting	Vertical reinforcement		Confining reinforcement		Section rectangularity ratio
				Amount	ρ_v (%)	Amount	ρ_h (%)	R_{BE}
1	BE-0-D	3	Dry	-	-	-	-	1.0
2	BE-0-W	3	Wet	-	-	-	-	1.0
3	BE-0-D-RUN	2	Dry	-	-	-	-	1.0
4	BE-0-W-RUN	2	Wet	-	-	-	-	1.0
5	BE-0-D-REC	2	Dry	-	-	-	-	1.53
6	BE-4#3-D4-D	3	Dry	4-#3	0.787	D4@45	1.87	1.0
7	BE-8#3-D4-D	3	Dry	8-#3	1.573	D4@45	1.87	1.0
8	BE-4#3-D8-D	3	Dry	4-#3	0.787	D8@45	3.74	1.0
9	BE-8#3-D8-D	3	Dry	8-#3	1.573	D8@45	3.74	1.0
10	BE-4#3-D4-W	3	Wet	4-#3	0.787	D4@45	1.87	1.0
11	BE-4#3-D4-D-RUN	3	Dry	4-#3	0.787	D4@45	1.87	1.0
12	BE-4#3-D4-W-RUN	2	Wet	4-#3	0.787	D4@45	1.87	1.0
13	BE-6#3-D4-D-REC	3	Dry	6-#3	0.773	D4@45	1.68	1.53
14	BE-12#3-D4-D-REC	3	Dry	12-#3	1.546	D4@45	1.94	1.53

The first five test matrix groups were unreinforced boundary elements, which were constructed to quantify the unconfined compressive strength of C-shaped boundary elements. The remaining boundary elements were reinforced and confined with either D4 or D8 hoops with a cross-sectional area of 25.81 mm^2 and 51.61 mm^2, respectively, as shown in Figure 4.3. These hoops resulted in two volumetric ratios of confining reinforcement (ρ_h), 1.87% and 3.74 %, respectively. Two vertical reinforcement ratios (ρ_v) were investigated, namely, 0.78% and 1.55%. For RMBE having a cross-section of 190x190 mm, two different bonding patterns were used to construct the masonry BE: stack pattern and running-bond, as indicated in Figure 4.4. The running-bond pattern was employed to alleviate the premature failure of the masonry shell that results in a sudden drop following the peak stress in the stress-strain relationship of RMBEs, as concluded by Obaidat et al. (2018) and Obaidat et al. (2019). Furthermore, pre-wetting of the RMBE masonry shell before grouting was investigated. Pre-wetting is a construction procedure recommended by the authors in (AbdelRahman and Galal 2020) to improve the bond between the masonry shell and its corresponding grout core in concrete-masonry prisms. This, in turn, would enhance the compressive strength of fully grouted RMBEs. As illustrated in Figure 4.4, two groups of rectangular RMBEs with 190x290 mm sections were studied to compare their compressive behaviour with those built with square sections. The 190x290 mm RMBEs had two vertical reinforcement ratios like those used in their square counterparts.
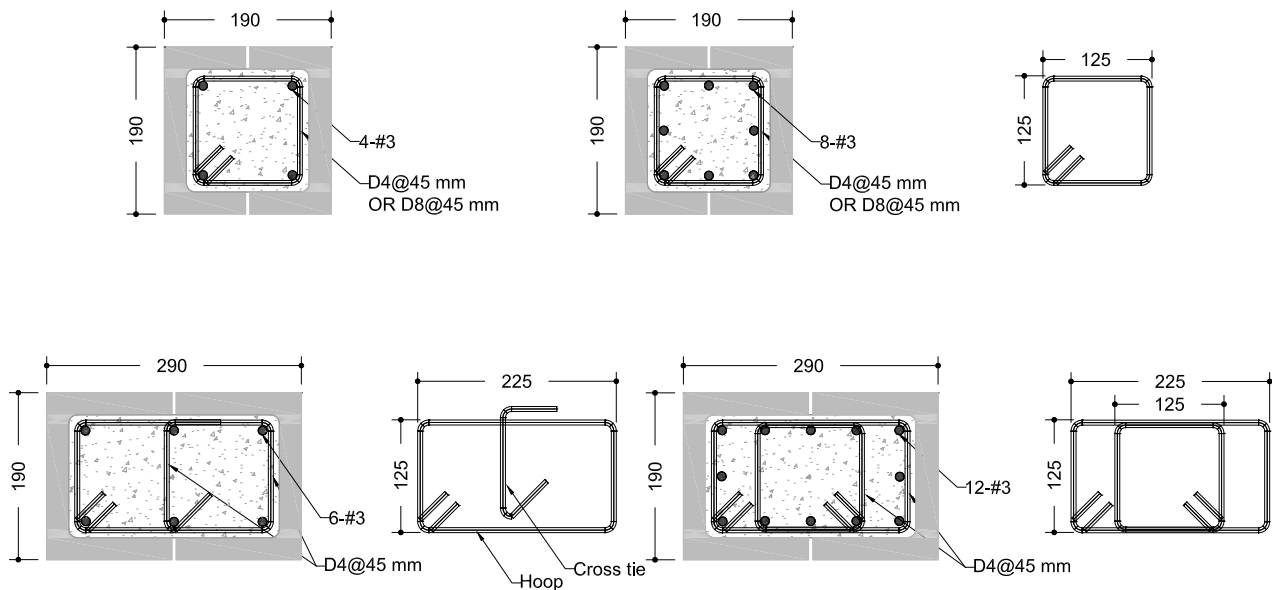
Figure 4.3 RMBEs sections′ details and confinement hoops

#3 vertical reinforcement

D4 or D8 confinement hoops

Grout core

Mortar joints

Concrete footing

| Stack pattern square RMBE (190x190 mm) | Running-bond square RMBE (190x190 mm) | Rectangular RMBE (190x290 mm) |
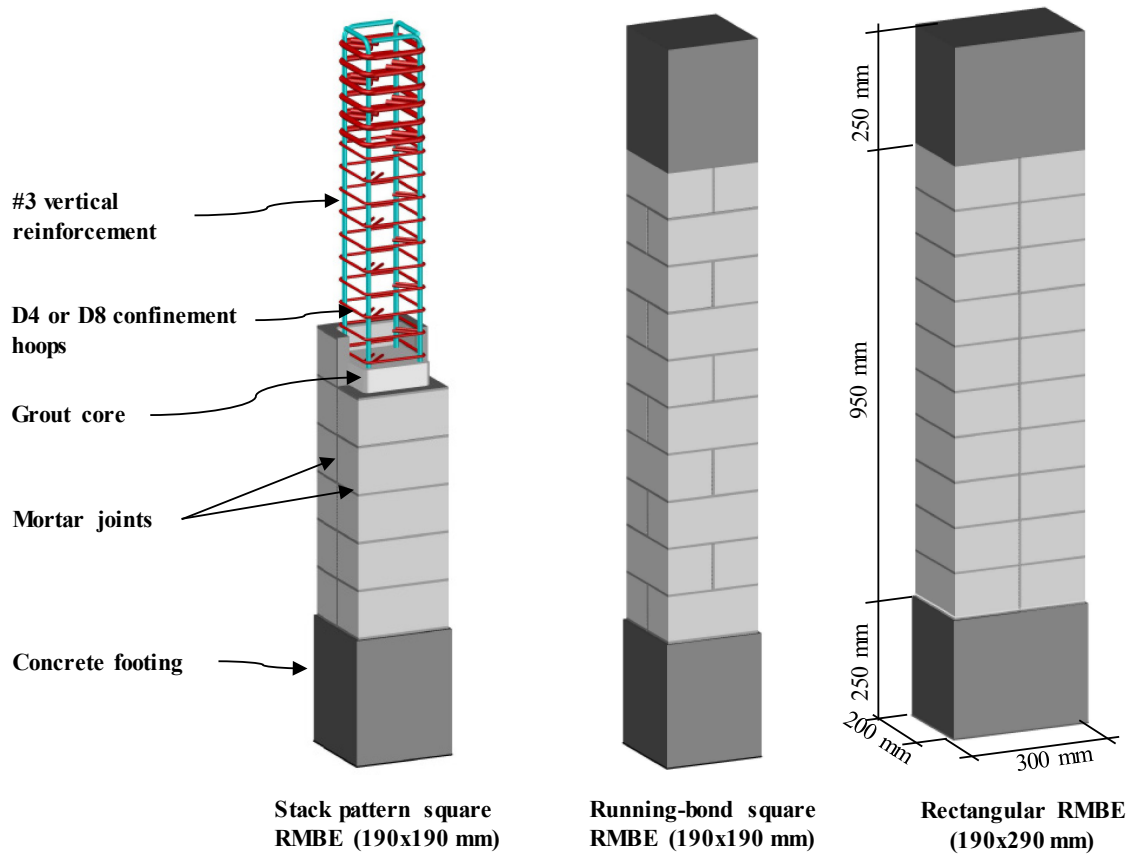
Figure 4.4 Configurations, dimensions, and details of the tested RMBEs

4.4.2 Construction of RMBEs

The construction process began with assembling the reinforcement steel cages consisting of either 4 or 8 vertical steel bars for square RMBEs, and 6 or 12 bars for rectangular RMBEs. Reinforcement bars were laid horizontally on two sawhorses to allow for inserting and fastening the D4 and D8 hoops spaced at 45 mm, as shown in Figure 4.5(a). The vertical steel bars extended continuously along the RMBEs from the bottom footing to the top cap without lap splices. All hoops were anchored at least 55 mm with a 135° hook inside the grout core. However, cross ties were used in the 190x290 mm specimens constructed with six #3 bars were anchored as follows: one side with 135° hook whereas the other side was a standard 90° hook (See Figure 4.3). The confinement hoop dimensions were 125x125 mm for the square RMBEs, whereas 125x225 mm hoop size was utilized for the rectangular RMBEs, as illustrated in Figure 4.3.

83

All hoops were placed alternatively along the RMBE height according to the CSA S304-14 provisions for the seismic hooks. Afterwards, 10M hoops were utilized for the bottom and top concrete footings and installed at a smaller spacing of 35 mm to offset the local failure that might occur in the top concrete cap or the bottom concrete footing and ensure higher confinement at the end regions of the RMBEs. The RMBEs were then concentrically and vertically placed in prefabricated plywood forms to cast the high-strength concrete bottom footing, as illustrated in Figures 4.5(b and c). All the concrete footings were left to cure for seven days in their forms.

Strain gauges were then installed at the vertical steel bars′ mid-height, as indicated in Figure 4.5(d). The RMBEs were released from the plywood form and leveled to construct the masonry blocks by a professional mason. The RMBEs were constructed using C-shaped pilaster blocks cut to the required dimensions either with a length of 190 or 290 mm with a fixed width of 190 mm. All the RMBE were ten courses high and constructed in either the stack pattern or the running-bond, and each course was built using two halves of C-shaped masonry blocks, as shown in Figure 4.5(e). The intended aspect ratio (h/t) of the RMBEs was 5. This was to conform to the CSA S304-14 provisions in which no correction factor is required for the calculated masonry compressive strength when the height-to-thickness (h/t) is greater than or equal to 5. Type S mortar was used to construct the RMBEs with vertical and bed joints of 5 mm each. Figure 4.5(f) shows some of the RMBE after full construction of the masonry blocks. The RMBEs were then strapped to prepare for grouting. Before grouting, the RMBE face shell was either dry or wet. For wet unreinforced MBEs and RMBEs, pre-wetting was applied by water hosing the outer surface of the C-shaped masonry blocks to ensure a minimum level of saturation of the blocks to the point that the water can be observed to flow down the face shell of the masonry blocks before grouting (AbdelRahman and Galal 2020). Afterwards, the grout was proportioned, mixed, and poured in the MBEs and RMBEs, as depicted in Figure 4.5(g). A mechanical vibrator was used to ensure the grout's consistency and flowability and prevent honeycombing along the RMBE height. Grout cylinders were sampled during grouting of the RMBEs according to the CSA A179-14. Finally, separate wooden forms were used for each RMBE to cast the top concrete cap. The total height of the RMBEs was 1450 mm, including 250 mm top concrete cap and 250 mm bottom concrete footing, as shown in Figure 4.5(h).
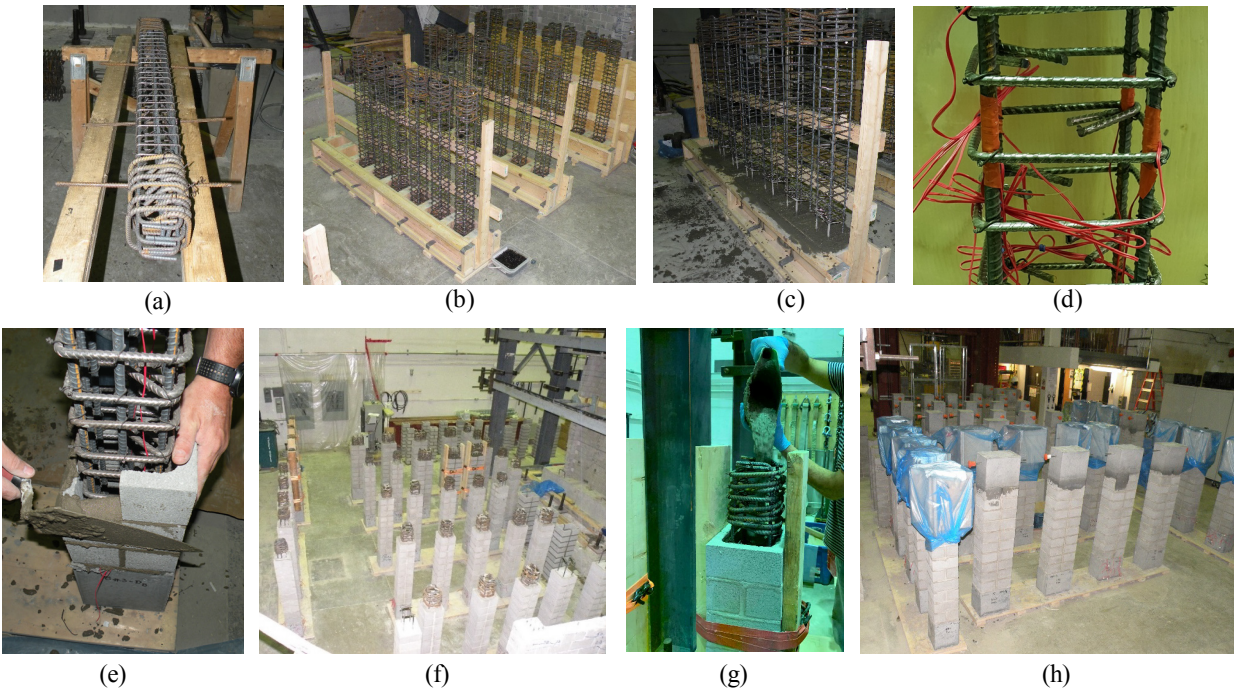
Figure 4.5 Construction procedures of RMBEs: (a) assembling of the reinforcement steel cages; (b) centering the RMBEs in their wooden forms; (c) casting of bottom concrete footing; (d) installing strain gauges; (e) building the RMBEs using masonry blocks; (f) fully-built RMBEs; (g) grouting of RMBEs; and (h) casting and curing of top concrete caps

4.4.3 Material Properties

Deformed reinforcing steel bars #3 (9.5 mm bar diameter) with a cross-sectional area of 71 mm^2 conforming to the ASTM A615 (2015a) specification were used for the construction of the RMBEs. Moreover, structural deformed reinforcing steel wires, namely, D4 and D8 conforming to ASTM A1064 (2018) were used as confining hoops. To determine the tensile stress-strain behaviour (i.e., yield strength and ductility) of the reinforcing steel bars, at least six samples were cut from each prescribed bar sizes and tested according to ASTM A370-15 (2015b) . All bars were instrumented with an extensometer with a 200 mm gauge length and a maximum stroke of 50 mm to measure the bars′ deformations during the tension test. Figure 4.6 shows the stress-strain curves of the tested reinforcing steel bar #3 and deformed wires D4 and D8. As described in Table 4.2, the test results showed that #3 bars have average yield strength of 429 MPa (COV = 3%), whereas the ultimate tensile strength was 679 MPa (COV = 1.6%). Moreover, the average proof yield strength of D4 and D8 hoops were 607 MPa (COV = 3.8%) and 519 MPa (COV = 2.4%), respectively.
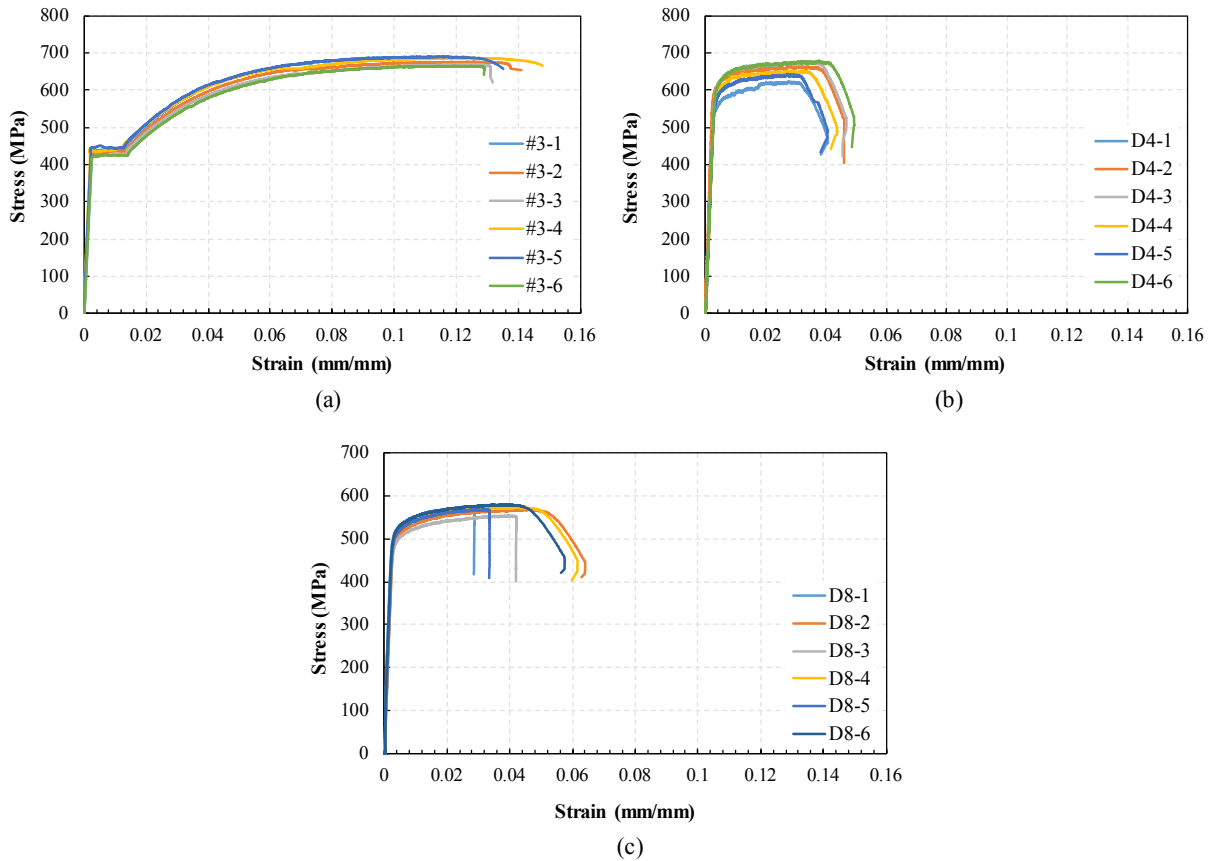
Figure 4.6 Observed stress-strain curves for tested (a) #3 vertical reinforcing bars; (b) D4 confinement hoops; and (c) D8 confinement hoops

The half-scale masonry blocks used to construct the RMBEs were originally cut from a half-scale pilaster concrete-masonry block that resembles the 390x390x190 mm full-scale pilaster block. To compute the compressive strength of the concrete-masonry blocks, 22 concrete-masonry coupons were cut from the half-scale masonry units according to ASTM C140 (2015c) with 25x50x100 mm (thickness x height x length) nominal dimensions. All the coupons were capped with high-strength gypsum capping material and were tested under concentric axial compressive load. Based on an average net area of 2500 mm^2 (i.e., thickness x length = 25x100 mm^2), the tested coupons averaged a high compressive strength of 44.5 MPa (COV = 13.5%), as indicated in Table 4.3.

High-strength laboratory-mixed weigh-batched fine grout was used to construct the RMBEs. The grout's target compressive strength was 45 MPa to match that of the tested masonry blocks.

This was to achieve the optimum compressive strength of fully grouted concrete-masonry prisms, as recommended by previous researchers. Therefore, to achieve the desired strength and the grout's flowability for heavily reinforced RMBEs, trial grout batches were mixed and tested before the onset of grouting the RMBEs. The mix proportions of the high strength grout by weight were 1: 2.6: 0.5 for cement: sand: water. In order to determine the compressive strength of the grout, grout cylinders of 100 mm (diameter) x 200 mm (height) were cast simultaneously with the corresponding RMBEs and tested according to CSA A179-14. The compressive strength of ten grout cylinders averaged 48.7 MPa (COV = 4.6%), as shown in Table 4.3.

Ready-to-use type S mortar bags, commercially available in the Canadian market, were utilized to construct the RMBEs. The compression test of twelve mortar cubes with a 50 mm side length according to ASTM C109-13 revealed that the compressive strength of the mortar was 15.7 MPa (COV = 9.8%).

Table 4.2 Mechanical properties of vertical reinforcement and confinement hoops

Bar size	Nominal diameter (mm)	Nominal area (mm^2)	Yield strength (MPa), (COV%)	Yield strain (mm/mm), (COV%)	Ultimate strength (MPa), (COV%)	Ultimate strain (mm/mm), (COV%)
#3	9.525	71	428.8 (2.96)	0.00224 (9.16)	679.4 (1.59)	0.13082 (12.69)
D4	5.7	25.81	606.6 (3.82)	-	657.0 (3.34)	0.04451 (8.06)
D8	8.1	51.61	518.9 (2.36)	-	570.0 (1.58)	0.04786 (31.68)

A high-strength concrete mix containing ordinary Portland cement blended with 8% silica fume, coarse granite aggregate graded to 2.5–10 mm, and regular sand were used to construct the top concrete cap and the bottom concrete footing of the RMBEs. The bottom footing had nominal dimensions of 200x200x250 mm (width x length x height) for square RMBEs and 200x300x250 mm for rectangular RMBEs with 5 mm all-around construction tolerance for the masonry blocks. The top concrete cap dimensions were 190x190x250 mm (width x length x height) for square RMBEs and 190x290x250 mm for the rectangular ones, as shown in Figure 4.4. According to ASTM C39-15, eight concrete cylinders were sampled and tested under compression load resulting in average compressive strength of 69 MPa (COV = 3.7%) for the concrete top cap and bottom footing, as reported in Table 4.3.

Table 4.3 Mechanical properties of constituent materials of the masonry boundary elements

Material component	Notation	Compressive strength (MPa), (COV%)
Concrete footing cylinder	f'_c	69.2 (3.70)
Masonry block coupon	f_b	44.5 (13.53)
Grout cylinder	f_g	48.7 (4.62)
Mortar cube	f_m	15.7 (9.78)

4.5 Test setup and Instrumentation

A servo-controlled 5000 kN hydraulic actuator attached to a rigid steel testing-frame was utilized to apply the uniaxial load in a displacement-control loading protocol on the unreinforced MBEs and RMBEs. This displacement-control system allows for capturing the post-peak behaviour of the tested RMBEs. Figure 4.7 shows the test setup and sample-tested unreinforced masonry boundary element and a rectangular RMBE. The RMBEs were tested monotonically under incrementally increasing compressive displacement until failure. A highly precise load cell attached to the hydraulic actuator enabled reading the axial force applied by the loading cylinder. The load cell is connected to a data acquisition system to accurately provide real-time data for the applied load and the measured displacements. Before attaching the upper and lower bearing plates to the RMBE ends, high-strength gypsum capping material was used below and above the RMBEs surfaces to eliminate surface roughness, ensure evenness, and uniformly distribute the applied axial load on the tested RMBEs. In addition, two rigid steel bearing plates, each 50 mm thick conforming to ASTM C1314-14, were used at the top and bottom ends of the RMBEs. This was followed by a heavy-duty hardening-steel spherical platen attached at the top steel bearing plate to ensure applying an axial load to the RMBEs. The spherical platen, the upper and lower bearing plates, and the RMBE were all vertically and concentrically aligned along with the hydraulic actuator using laser aligning devices. For the unreinforced and RMBEs, the monotonic uniaxial load was applied incrementally using a slow displacement rate of 0.003 mm/sec up to the failure of the specimens to capture the post-peak falling branch of the compressive stress-strain curve of the tested RMBEs. The test was terminated at ~65-75% strength degradation to capture most of the tested specimens′ post-peak behaviour.

Axial displacements of the RMBEs were monitored by four draw-wire displacement transducers (i.e., potentiometers) with an error of 0.0005 of the full stroke. The four potentiometers

were directly attached to the center of the four sides of the tested RMBEs. These potentiometers had a gauge length equivalent to the central 950 mm masonry boundary element's full height, as shown in Figure 4.7. The premature failure of the concrete-masonry boundary element face shell can significantly damage the measuring devices and interrupt the load-displacement data. Therefore, this gauge length was selected to enable continuous and consistent recording of the measured deformations during the pre-peak (i.e., rising curve) and the post-peak behaviour of the RMBEs such that face shell spalling cannot influence the recorded data.

(a)   (b)
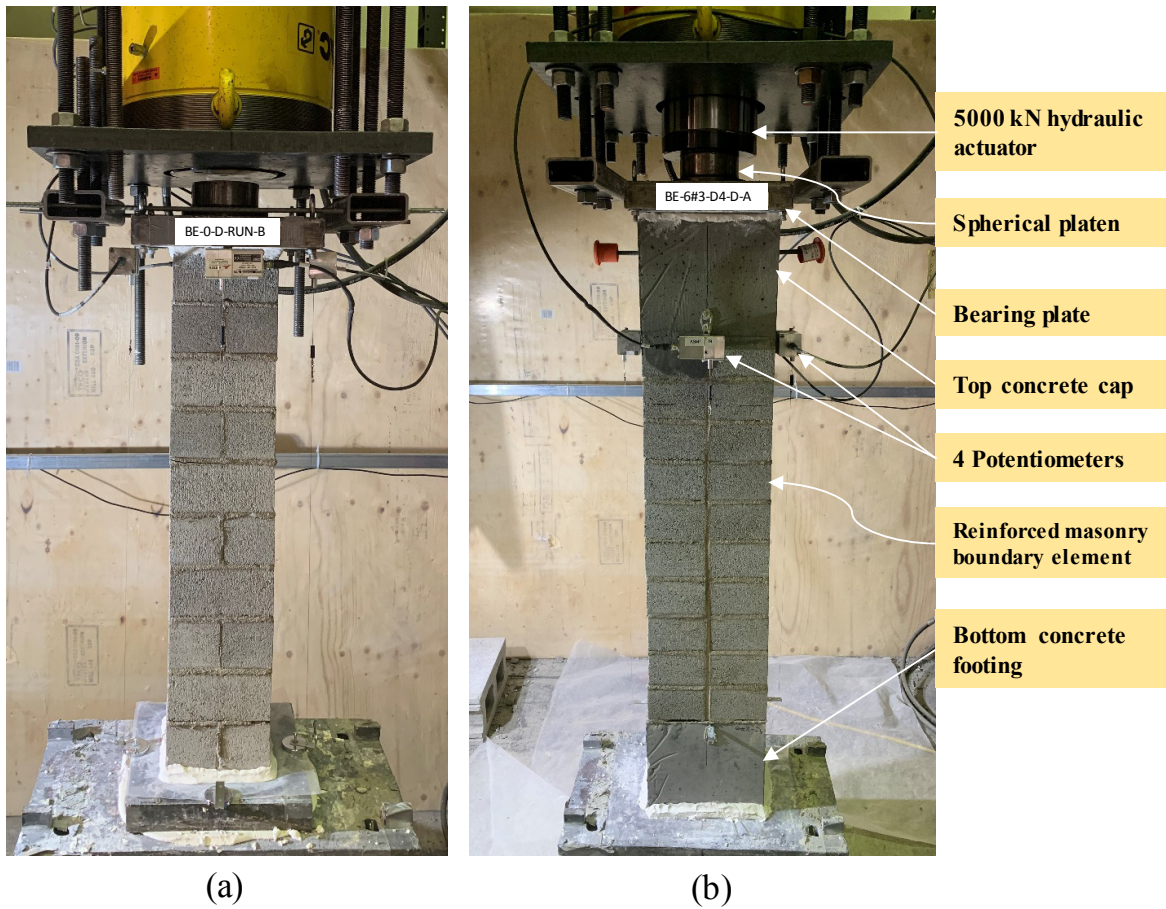
Figure 4.7 Axial compression testing of (a) unreinforced running-bond boundary element; and (b) rectangular reinforced masonry boundary element

It should be noted that the potentiometers were assumed to capture the axial strains of the masonry boundary element (i.e., face shell and grout core) and its corresponding vertical reinforcement assuming strain compatibility (i.e., zero slippage between the grout core and vertical reinforcement). However, to adequately measure the vertical reinforcement's axial strains, electric

resistance strain gauges having a gauge length of 5 mm were installed on the steel rebars, as illustrated in Figure 4.5(d). Additionally, the axial strain gauges were compared with those strains captured by the four potentiometers to validate the compatibility of strains between the vertical reinforcement and its corresponding grout core.

4.6 Test Results and Discussions

Based on the obtained load-displacement data from the compression test of the RMBEs, the axial compressive stress-strain responses were calculated. It shall be noted that the recorded axial load was divided by the nominal cross-sectional area of 190x190 mm for square boundary elements and 190x290 mm for rectangular RMBEs to determine the peak compressive stress (f_{um}). Moreover, the presented axial compressive strain is the average of four strain values determined using the four potentiometers mounted at the centers of the four sides of the RMBEs. It is noteworthy that a potentiometer reading might be excluded or corrected when the potentiometer is significantly affected by face shell spalling. The axial strain values at peak stress (ε_{um}), 25% strength degradation (ε_{75}), and 50% strength degradation (ε_{50}) are calculated by dividing the recorded axial displacements by the central gauge length of the masonry boundary elements (i.e., 950 mm). Besides, the strain ductility ($\mu_{\varepsilon 50}$) was calculated by dividing the strain at 50% strength degradation on the descending branch (ε_{50}) by the strain at peak stress (ε_{um}).

4.6.1 Observed stages of failure

The test results showed different modes and stages of failures for the unreinforced and reinforced masonry boundary elements. Unreinforced MBEs experienced vertical and inclined cracks near the peak stress followed by face shell spalling. Following this, a sudden loss in the axial compressive strength and crushing of the grout core were captured. RMBEs exhibited similar behaviour up to the peak stress, yet completely different post-peak damage propagation. Face shell spalling was captured at the peak stress resulting in a stress drop in the stress-strain behaviour of the RMBEs. This was followed by a noticeable increase in the compressive strength (i.e., second peak stress) due to the grout core confinement. Consequently, buckling of the vertical reinforcement, fracture of confinement hoops, and the grout core crushing were observed. It should be noted that neither the second peak stress after face shell spalling nor fracture of hoops was reported in the RMBEs tested by Obaidat et al. (2018).

Figure 4.8 illustrates different failure modes of the unreinforced and reinforced masonry boundary elements. For dry masonry boundary elements built in the stack pattern, vertical and inclined tensile cracks were observed in the vertical mortar joints and the face shells due to the grout core's lateral expansion when it approaches the peak stress. The peak stress was associated with the face shell's significant spalling, as explained in Figure 4.8(a). On the other hand, Figure 4.8(b) depicts that wet masonry boundary elements showed more cracks at the peak stress with face shell spalling.
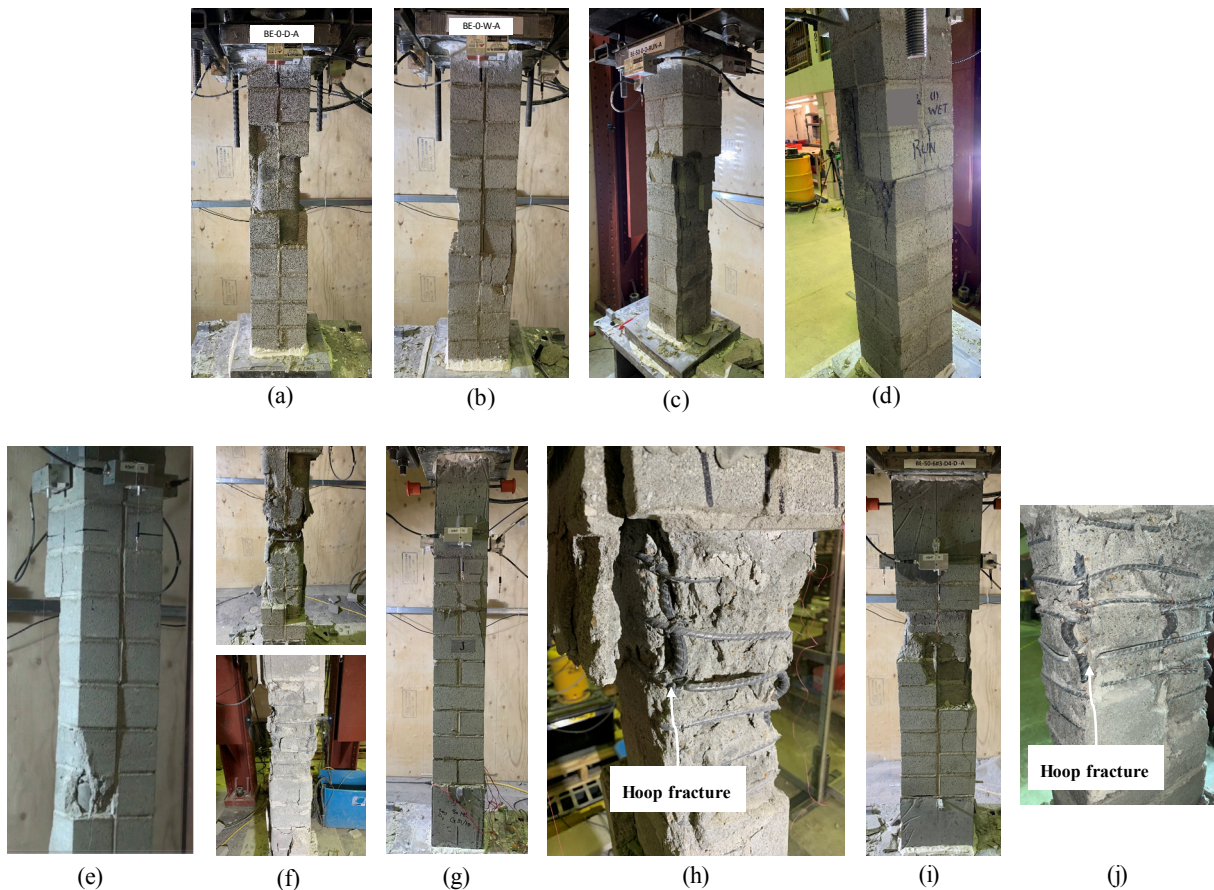
Figure 4.8 Failure stages of: (a) unreinforced stacked dry MBE; (b) unreinforced stacked wet MBE; (c) unreinforced running-bond dry MBE; (d) unreinforced running-bond wet MBE; (e) dry RMBE at 25% strength degradation; (f) dry RMBE at 50% (up) and 75% (down) strength degradation; (g) running-bond dry RMBE at 25% strength degradation; (h) running-bond dry RMBE at 75% strength degradation; (i) rectangular RMBE at 25% strength degradation; and (j) rectangular RMBE at 75% strength degradation

However, it shall be noted that some of the wet masonry boundary elements experienced column-like compression failure characterized by conical shear failure of both the grout core and the face shell, which was not observed in dry masonry boundary elements. Similar observations

were indicated by AbdelRahman and Galal (AbdelRahman and Galal 2020), where wet masonry prisms showed an enhanced bond between the grout core and the masonry shell compared to dry masonry prisms. Running-bond dry masonry boundary elements showed a little different mode of failure than their stack pattern counterparts. They developed inclined and vertical cracks, which were not always in the vertical joints, as observed in MBEs built with the stack pattern, as presented in Figure 4.8 (c). It is worth noting that running-bond masonry boundary elements exhibited enhanced post-peak, gradual descending branches compared to their counterparts built in the stack pattern. The running-bond boundary elements had their face shell spalling at almost ~25-30% strength degradation, whereas stack boundary elements exhibited face shell spalling at the peak stress. Moreover, complete face shell spalling (i.e., masonry shell halves) was observed for stack pattern boundary elements versus incomplete spalling for their running-bond counterparts. This explains the contribution of remaining portions of the face shell to reduce the falling branch's slope in running-bond specimens rather than those of the stack boundary elements.

The wet running-bond boundary elements showed more enhanced performance than their dry counterparts, where the face shell spalling occurred at ~70-75% strength degradation compared to face shell spalling at 25% strength degradation for dry specimens, as indicated in Figure 4.8(d). It is worth mentioning that the pre-wetting of dry masonry boundary elements, either in the stack pattern or the running-bond, resulted in an enhanced compressive strength. This can be attributed to the better bond between the pre-wetted dry masonry shell and the grout core in wet masonry boundary elements.

RMBEs exhibited different modes of failures than their unreinforced counterparts due to the longitudinal and confining reinforcements in the grout core. Figures 4.8(e and f) show the stages of failure for a dry RMBE in which the face shell spalling was associated with the sudden drop at the peak stress. This resulted in a loss of ~35-45% of the tested specimens′ peak compressive stress. This can be attributed to the ratio of the unconfined masonry cover (i.e., masonry face shell and unconfined grout core), which accounts for approximately 57% and 49% of the overall cross-sectional area of the square and rectangular RMBEs, respectively. This indicates that the confined grout core could resist higher axial compression loads compared to its corresponding unconfined masonry counterpart, even though it accounts for a lower cross-sectional area of the RMBEs. Therefore, it should be noted that the unconfined masonry cover shall be minimized in order to

reduce the pronounced drop in the stress-strain response of the RMBEs. However, this should be done according to the provisions of the CSA S304-14 to satisfy construction tolerance and fire resistance requirements (Cusson and Paultre 1994). It is noteworthy that comparable observations were previously reported by Obaidat et al. (2018) for their tested RMBEs built in the stack pattern. Figure 4.8(f) shows the failure of the RMBE at 50% (up) and 75% (down) strength degradations. It can be noticed that at 50% strength degradation, excessive spalling of the grout cover was observed with the grout core being striped, and the onset of reinforcement buckling was captured. At 75% strength degradation, excessive buckling of vertical reinforcement was observed. Figure 4.8(g) shows the onset of face shell spalling at ~25-35% strength degradation for a sample dry running-bond specimen. At ~70-75% strength degradation, the first hoop fracture was recorded, as presented in Figure 4.8(h). It is noteworthy that the test was not terminated at the first hoop fracture; however, the test continued up to ~65-75% strength degradation to capture the full descending branch of the post-peak behaviour of the RMBEs. Like square RMBEs, rectangular specimens showed face shell spalling and a sudden drop in the load-carrying capacity at the peak stress, as shown in Figure 4.8(i). Eventually, Figure 4.8(j) shows the vertical reinforcement bars′ buckling associated with the first hoop fracture at ~65-70% strength degradation of a rectangular RMBE.

4.6.2 Effect of the vertical reinforcement ratio (ρ_v)

Adding more vertical reinforcement to the confined masonry boundary elements reduced the strain ductility ($\mu_{\varepsilon 50}$) and resulted in a significant increase in the peak compressive stress (f_{um}). Figure 4.9 shows the stress-strain curves of the tested square and rectangular confined RMBEs as well as their unreinforced counterparts. The six groups of specimens′ test results, namely, BE-0-D, BE-0-D-REC, BE-4#3-D4-D, BE-8#3-D4-D, BE-6#3-D4-D-REC, and BE-12#3-D4-D-REC, are presented in Tables 4.4 and 4.5. The test results showed that, for square RMBEs, doubling the vertical reinforcement ratio of the RMBEs (ρ_v) from 0.79% to 1.57% resulted in a significant increase in the peak compressive stress (f_{um}) by approximately 20% and 45% for RMBEs confined with D4 and D8 hoops, respectively, as shown in Figure 4.15(a). Similarly, for rectangular RMBEs, increasing ρ_v by 100% resulted in an increase of 23% in the maximum compressive strength for RMBEs having 12-#3 rebars compared to those constructed with 6-#3 bars. This enhancement is attributed to the increased contribution of the vertical reinforcement to the overall

axial load carrying capacity of the RMBEs due to doubling the number of the bars. It should be noted that C-shaped RMBEs tested by Obaidat et al. (2018) did not exhibit significant improvement in the peak compressive stress (f_{um}) with increasing the vertical reinforcement ratio (ρ_v) from 0.8% to 1.4%, although this increase is relatively close to the one utilized in this study. This was because Obaidat et al. increased the vertical reinforcement bars′ diameters from #3 to #4 in lieu of increasing the number of the bars and, hence, this enhancement could not boost the confined grout core contribution to the overall axial load carrying capacity of the RMBEs.
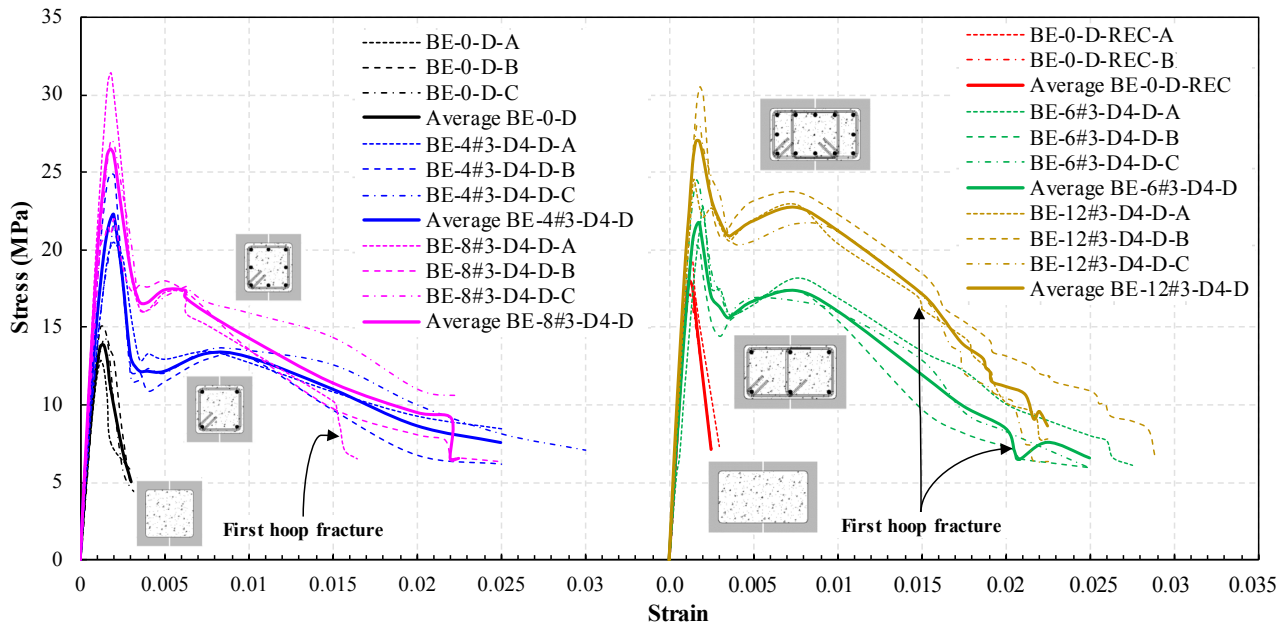
Figure 4.9 Observed compressive stress-strain curves of square and rectangular unreinforced MBEs and RMBEs having different vertical reinforcement ratios

The observed strain at peak stress (ε_{um}), the strains at 25% and 50% strength degradation (ε_{75}) and (ε_{50}), and the strain ductility ($\mu_{\varepsilon 50}$) were influenced by changing ρ_v, as shown in Table 5. However, the strain at peak stress (ε_{um}) experienced the lowest effect associated with increasing the vertical reinforcement ratio (ρ_v) of the RMBEs. The test results showed that increasing ρ_v by 100% significantly influenced the strain at 25% strength degradation (ε_{75}) and the strain ductility ($\mu_{\varepsilon 50}$). For square RMBEs confined with D4 and D8 hoops, ε_{75} increased by 21% and dropped by 20%, respectively. Similarly, for the same group of RMBEs specimens, the strain ductility ($\mu_{\varepsilon 50}$) decreased by 19% and 29%, respectively, as illustrated in Figure 4.16(a). On the contrary, for rectangular RMBEs, ε_{75} was observed to increase by 19%, whereas $\mu_{\varepsilon 50}$ increased by 17%,

respectively. It should be noted that RMBEs with increased vertical reinforcement ratio (i.e., 1.57%) exhibited steeper post-peak descending branch and successive fractures of confinement hoops occurred after attaining 50% strength degradation compared to those with lower ratio $\rho_v = 0.79\%$, as shown in Figure 4.9.

Table 4.4 Test results of unreinforced masonry boundary elements (MBEs)

Group number	BE Identifier	Peak stress (MPa)		Strain at peak stress, ε_{um}		Strain at 75% of the peak stress, ε_{75}		Strain at 50% of the peak stress, ε_{50}		Strain ductility, $\mu_{\varepsilon50}$
		f_{um}	Average (COV%)	ε_{um}	Average (COV%)	ε_{75}	Average (COV%)	ε_{50}	Average (COV%)	$\varepsilon_{50}/\varepsilon_{um}$
1	BE-0-D-A	12.90	14.28 (8.92)	0.00116	0.00131 (11.80)	0.00166	0.00191 (12.85)	0.00246	0.00239 (9.50)	1.82
	BE-0-D-B	15.41		0.00131		0.00215		0.00258		
	BE-0-D-C	14.53		0.00147		0.00191		0.00214		
2	BE-0-W-A	16.99	18.91 (13.92)	0.00156	0.00147 (6.15)	0.00174	0.00198 (17.14)	0.00188	0.00251 (35.28)	1.71
	BE-0-W-B	21.91		0.00146		-		-		
	BE-0-W-C	17.83		0.00138		0.00222		0.00313		
3	BE-0-D-RUN-A	10.86	11.66 (9.70)	-	0.00134 (-)	0.00160	0.00172 (9.87)	0.00275	0.00300 (11.79)	2.24
	BE-0-D-RUN-B	12.46		0.00134		0.00184		0.00325		
4	BE-0-W-RUN-A	18.40	18.43 (0.23)	0.00122	0.00140 (18.18)	0.00167		0.00211		-
	BE-0-W-RUN-B	18.46		0.00158		-		-		
5	BE-0-D-REC-A	19.18	18.22 (7.45)	0.00127	0.00128 (0.55)	0.00193	0.00187 (4.93)	0.00266	0.00249 (9.66)	1.95
	BE-0-D-REC-B	17.26		0.00128		0.0018		0.00232		

Although increasing the vertical reinforcement ratio (ρ_v) enhanced the peak compressive stress (f_{um}) of the tested RMBEs, this improvement was at the expense of the strain capacity at 50% strength degradation (ε_{50}) as well as the strain ductility ($\mu_{\varepsilon50}$). This may be attributed to the premature buckling of the vertical reinforcement in RMBEs constructed with higher vertical reinforcement ratio $\rho_v = 1.57\%$ (i.e., BE-8#3-D4-D, BE-8#3-D8-D, and BE-12#3-D4-D-REC) compared to those with lower ratio $\rho_v = 0.79\%$ (i.e., BE-4#3-D4-D, BE-4#3-D8-D, and BE-6#3-D4-D-REC). Since the above-mentioned groups of specimens have approximately the same volumetric ratio of confining reinforcement (ρ_h), earlier buckling in the former RMBE groups is related to the absence of additional confinement hoops that could have been adequately restrained the additional vertical reinforcement from buckling. Therefore, the first hoop fracture was attained sooner for RMBEs with higher ρ_v compared to those with lower ρ_v. This, in turn, resulted in rapid

deterioration of the grout core post-peak strength leading to a much steeper descending branch followed by crushing of the grout core in RMBEs with extra vertical reinforcement, as shown in Figure 4.9. This confirms previous observations reported for reinforced concrete (RC) members tested by Mander et al. (1988). The first hoop fracture was observed earlier for column sections in which the vertical reinforcement had a larger axial load-carrying capacity than those with lower reinforcement capacity.

4.6.3 Effect of the volumetric ratio of confining reinforcement (ρ_h)

Figure 4.10 depicts the compressive stress-strain behaviour of RMBEs constructed with different volumetric ratios of confining reinforcement (ρ_h), namely, 1.87% and 3.74%. Test results of the RMBEs of the groups of specimens BE-4#3-D4-D, BE-4#3-D8-D, BE-8#3-D4-D, and BE-8#3-D8-D are reported in Table 5. The test results revealed that the presence of the confinement hoops D8 (ρ_h = 3.74%) in RMBEs built with 8-#3 bars resulted in an increase of 11% in the peak compressive stress (f_{um}) and 15% in the strain ductility ($\mu_{\varepsilon 50}$) when compared to those of the RMBEs constructed with D4 hoops (ρ_h = 1.87%), as illustrated in Figures 4.15b and 4.16b. Moreover, it was observed that as the volumetric confinement ratio (ρ_h) increased from 1.87% to 3.74% in RMBEs with 4-#3 vertical bars led to an increase of 31% in the strain ductility ($\mu_{\varepsilon 50}$), as can be seen from Figure 4.16(b). On the contrary, RMBEs with 4-#3 vertical bars confined with D8 hoops demonstrated a slight reduction of 9% in the peak stress (f_{um}) compared to those confined with D4 hoops. It is noteworthy that increasing the confinement ratio (ρ_h) for an RMBE section with constant vertical reinforcement ratio (ρ_v) was expected to increase both the peak stress and the strain ductility; this was observed in most of the tested RMBEs. Nevertheless, the slight reduction of 9% in the peak compressive stress of the RMBEs with 4-#3 bars and increased (ρ_h) can be attributed to the variation of the material properties of the concrete-masonry blocks and their corresponding grout cores estimated at 13.5% and 4.6%, respectively (See Table 4.3).

Although increasing the volumetric ratio of confining reinforcement (ρ_h) of the RMBEs resulted in a significant boost in the corresponding strain ductility ($\mu_{\varepsilon 50}$), the strain at peak stress (ε_{um}) and the strain at 25% strength degradation (ε_{75}) exhibited inconsistent results. These minimal discrepancies can be attributed to the fact that most of the ε_{um} and ε_{75} values were observed at the peak stress and the stress drop portion of the stress-strain falling branch of the RMBEs. This stress drop is not controlled by either the vertical reinforcement ratio (ρ_v) or the confinement ratio (ρ_h),

yet by the sudden face shell spalling attained at the masonry peak compressive stress (f_{um}). Consequently, the enhancement provided by increasing ρ_h was quite reflected on improving the strain ductility ($\mu_{\varepsilon50}$) rather than the strains at peak stress (ε_{um}) and 25% strength degradation (ε_{75}).

Table 4.5 Test results of reinforced masonry boundary elements (RMBEs)

| Group number	BE Identifier	Peak stress (MPa) f_{um}	Average (COV%)	Strain at peak stress, ε_{um}	Average (COV%)	Strain at 75% of the peak stress, ε_{75}	Average (COV%)	Strain at 50% of the peak stress, ε_{50}	Average (COV%)	Strain ductility, $\mu_{\varepsilon50}$ $\varepsilon_{50}/\varepsilon_{um}$
6	BE-4#3-D4-D-A	20.84	22.46 (9.52)	0.00197	0.00189 (9.39)	0.00300	0.00263 (12.31)	0.01531	0.01541 (17.40)	8.14
	BE-4#3-D4-D-B	24.88		0.00169		0.00245		0.01278		
	BE-4#3-D4-D-C	21.65		0.00202		0.00243		0.01814		
7	BE-8#3-D4-D-A	31.56	26.92 (17.60)	0.00169	0.00183 (8.21)	0.00258	0.00318 (29.85)	0.00707	0.01206 (38.11)	6.58
	BE-8#3-D4-D-B	22.09		0.00199		0.00427		0.01300		
	BE-8#3-D4-D-C	27.1		0.00182		0.00268		0.01612		
8	BE-4#3-D8-D-A	18.42	20.52 (11.48)	0.00166	0.00175 (8.25)	0.00387	0.00343 (13.95)	0.02553	0.01872 (32.57)	10.68
	BE-4#3-D8-D-B	23.07		0.00192		0.00349		0.01686		
	BE-4#3-D8-D-C	20.08		0.00168		0.00292		0.01377		
9	BE-8#3-D8-D-A	29.54	29.78 (3.30)	0.00201	0.00190 (4.97)	0.00283	0.00273 (3.32)	0.01455	0.01444 (1.34)	7.59
	BE-8#3-D8-D-B	30.86		0.00187		0.00272		0.01422		
	BE-8#3-D8-D-C	28.94		0.00183		0.00265		0.01456		
10	BE-4#3-D4-W-A	31.52	31.42 (0.85)	0.00188	0.00205 (12.05)	0.00327	0.00319 (4.08)	0.0048	0.00677 (29.57)	3.31
	BE-4#3-D4-W-B	31.12		0.00233		0.00326		0.0067		
	BE-4#3-D4-W-C	31.63		0.00193		0.00304		0.0088		
11	BE-4#3-D4-D-RUN-A	23.63	22.25 (5.44)	0.00162	0.00175 (6.59)	0.00232	0.00239 (3.72)	0.01121	0.01198 (34.50)	6.83
	BE-4#3-D4-D-RUN-B	21.72		0.00182		0.00249		0.00829		
	BE-4#3-D4-D-RUN-C	21.39		0.00182		0.00236		0.01645		
12	BE-4#3-D4-W-RUN-A	32.58	33.15 (2.43)	0.00193	0.00197 (2.87)	0.00327	0.00416 (30.26)	0.00462	0.00637 (38.85)	3.23
	BE-4#3-D4-W-RUN-B	33.72		0.00201		0.00505		0.00812		
13	BE-6#3-D4-D-REC-A	23.03	22.90 (7.51)	0.00210	0.00172 (19.27)	0.00248	0.00243 (1.95)	0.01829	0.01581 (14.43)	9.19
	BE-6#3-D4-D-REC-B	21.12		0.00149		0.00239		0.0138		
	BE-6#3-D4-D-REC-C	24.55		0.00157		0.00241		0.01534		
14	BE-12#3-D4-D-REC-A	24.95	28.09 (10.25)	0.00149	0.00164 (7.93)	0.00249	0.00290 (19.78)	0.01904	0.01768 (7.18)	10.78
	BE-12#3-D4-D-REC-B	30.61		0.00172				0.01746		
	BE-12#3-D4-D-REC-C	28.7		0.00171		0.0033		0.01653		
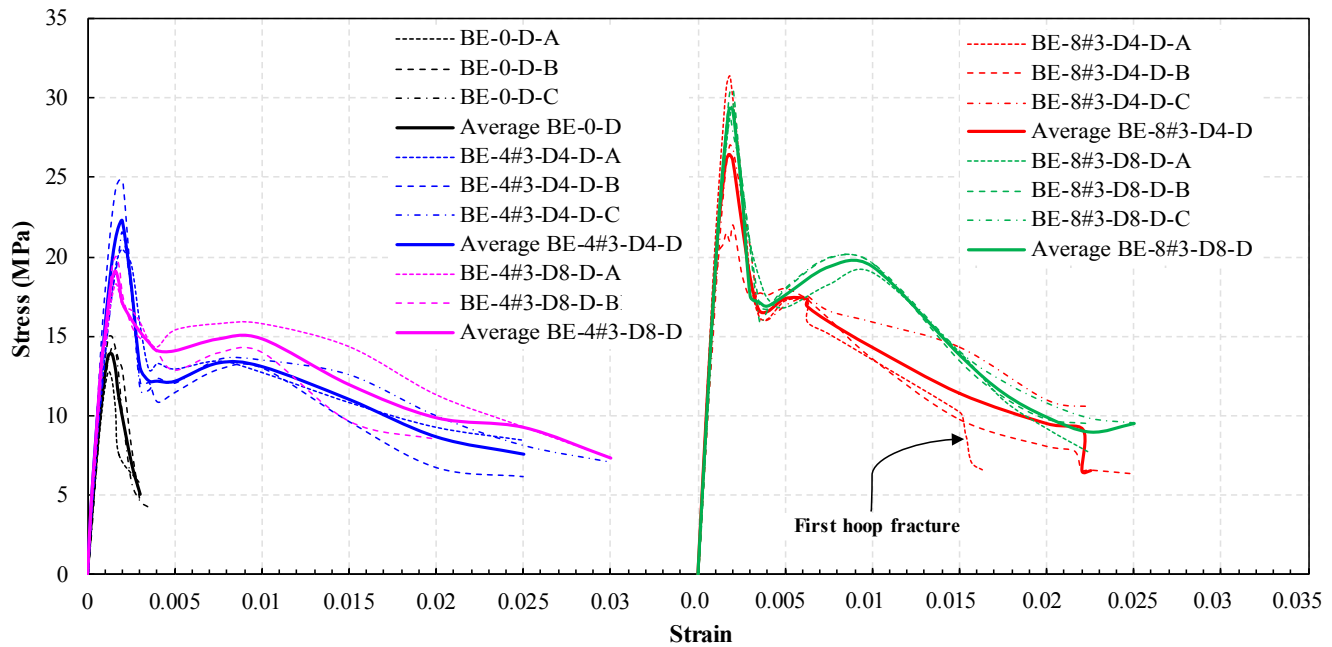
Figure 4.10 Observed compressive stress-strain curves of square unreinforced MBEs and RMBEs having different horizontal and vertical reinforcement ratios

Figure 4.10 shows that following the face shell spalling, RMBEs built with D8 confinement hoops exhibited higher stresses corresponding to approximate strains range between 0.005 and 0.02, compared to those constructed with D4 confinement hoops. This is due to the D8 confinement hoops′ enhancement to the confined grout core rather than those with D4 hoops. Besides, the results showed that RMBEs with doubled ρ_h showed enhanced axial strains at failure (i.e., at ~65-75% strength degradation) compared to their counterparts.

4.6.4 Effect of the boundary element cross-section configuration (square vs. rectangular)

The influence of changing the masonry boundary element's cross-section configuration (i.e., geometry) on the compressive stress-strain response of RMBEs can be observed from Figures 4.11(a and b). This influence was investigated in RMBEs with two different vertical reinforcement ratios (ρ_v), namely, 0.79% and 1.57% and for both the square and rectangular specimens. It is worth noting that the vertical reinforcement ratio (ρ_v) was similar in both square and rectangular RMBEs to facilitate the test results′ correlation. The results showed that the average masonry peak stress (f_{um}) for RMBEs was not significantly affected by changing the RMBEs cross-section rectangularity ratio (R_{BE}) from 1.0 (i.e., square) to 1.53 (i.e., rectangular), as shown in Figure

4.15(c). However, rectangular unreinforced MBEs exhibited around 20% higher peak stress (f_{um}) compared to their square counterparts. Moreover, the masonry strain at peak stress (ε_{um}) was marginally influenced when the RMBE cross-section changed from a square to a rectangular counterpart. It is noteworthy that rectangular RMBEs having ρ_v of either 0.79% or 1.57% experienced lower values of ε_{um} compared to their square counterparts. Similar findings were observed for the values of the strains at 25% strength degradations (ε_{75}). On the contrary, it was found that the strain ductility ($\mu_{\varepsilon50}$) greatly enhanced for rectangular RMBEs compared to those of the square RMBEs. Figure 4.16(c) shows that RMBEs groups 13 and 14 (i.e., BE-6#3-D4-D-REC and BE-12#3-D4-D-REC) with a rectangularity ratio $R_{BE} = 1.53$ exhibited an increase of 13% and 64% compared to groups 6 and 7 (i.e., BE-4#3-D4-D and BE-8#3-D4-D) with a square section of $R_{BE} = 1.0$, respectively. The significant improvement that was observed in the BE-12#3-D4-D-REC group compared to that of the BE-8#3-D4-D group of specimens can be attributed to the contribution of the confinement ratio (ρ_h) that was higher in the former compared to the latter.

Figures 4.11(a and b) show that rectangular RMBEs exhibited enhanced post-peak performance compared to their square counterparts. The pronounced stress drop due to the masonry face shell spalling at the peak stress was significantly reduced in RMBEs with rectangular cross-sections compared to those with square sections. This can be attributed to the reduction in the face shell ratio to the total cross-sectional area of the rectangular RMBEs (i.e., 39%) compared to that of the square RMBE section (i.e., 45.7%). This resulted in an enhanced post-peak strength for the rectangular RMBEs for a given strain level compared to their square counterparts.
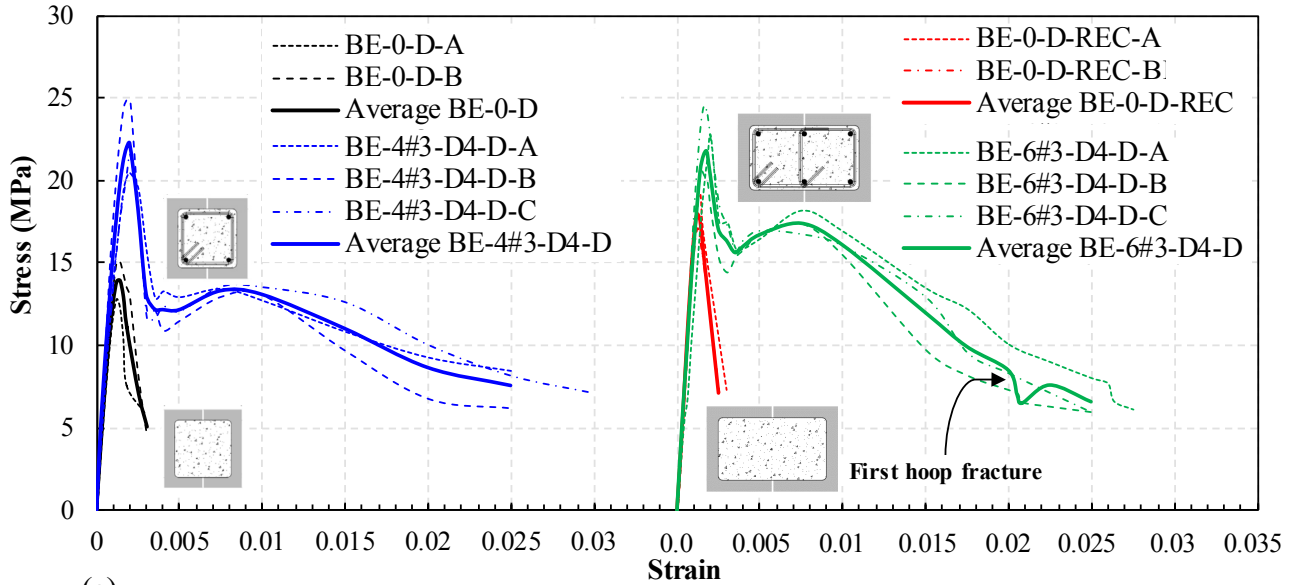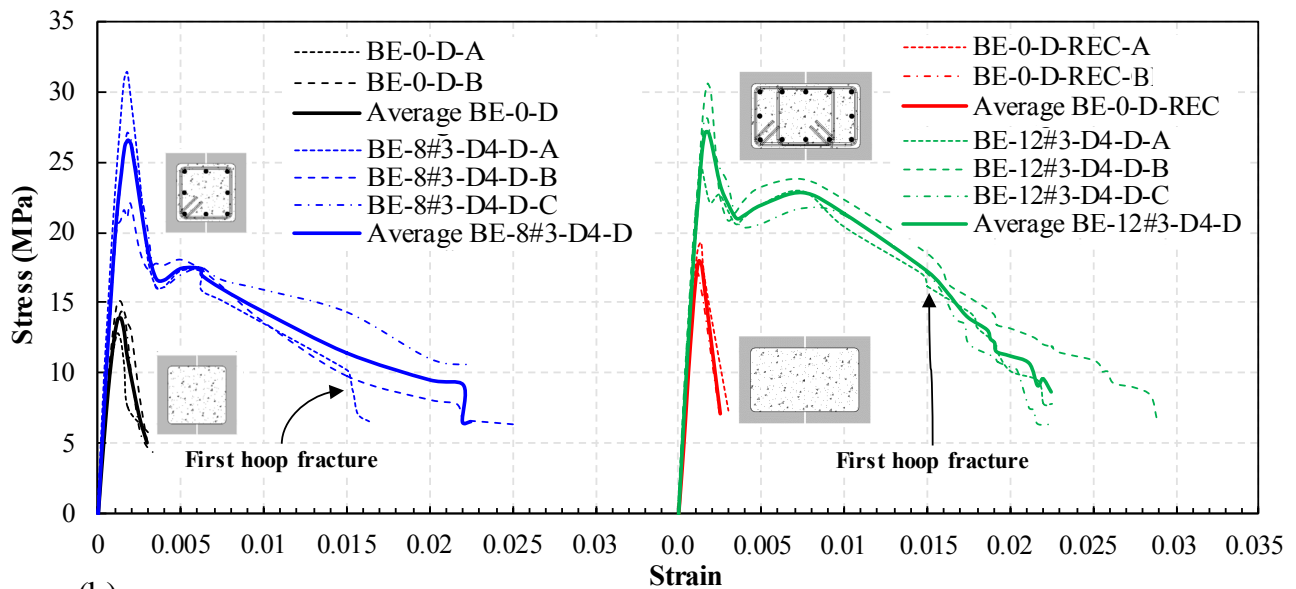
Figure 4.11 Observed compressive stress-strain curves of unreinforced MBEs and RMBEs having different cross-section configurations for (a) Specimens constructed with $\rho_v = 0.79\%$; and (b) Specimens constructed with $\rho_v = 1.57\%$

4.6.5 Effect of the masonry bond pattern (stack pattern vs. running-bond)

Stack pattern and running-bond RMBEs showed comparable stress-strain responses in both dry and wet conditions. The compressive stress-strain relationships of the tested RMBEs built using the stack pattern and running-bond in dry and pre-wetted specimens are shown in Figures

4.12(a and b). The test results of the investigated groups of specimens, namely, BE-0-D, BE-0-W, BE-0-D-RUN, BE-0-W-RUN, BE-4#3-D4-D, BE-4#3-D4-W, BE-4#3-D4-D-RUN, and BE-4#3-D4-W-RUN are described in Tables 4.4 and 4.5. Unreinforced dry running-bond masonry boundary elements showed, on average, a compressive strength (f_{um}) 18% less than those constructed in the stack pattern. This may be attributed to the discontinuous mortar head joints in the running-bond boundary elements in which these joints fall short of transmitting the axial load along the height of the boundary elements. Many researchers reported similar findings (e.g., Drysdale and Hamid 2005; Maurenbrecher 1980; Mohamed 2018; Scrivener and Baker 1988); where running-bond stretcher masonry prisms exhibited a compressive strength ranged between 75% and 99% lower than that of their stacked counterparts. Contrarily, wet running-bond MBEs showed comparable peak stress (f_{um}) to MBEs laid in the stack pattern. It is noteworthy that the considerable difference in the behaviour between dry and wet, stack- and running-bond MBEs is that wet boundary elements achieved a significant bond between the masonry shell and the grout core (i.e., homogeneous masonry assemblage). Consequently, this could alleviate the running-bond pattern's adverse effect on the compressive strength (f_{um}) of the wet running-bond specimens. As mentioned earlier, dry MBEs exhibited lower compressive strength (f_{um}) in running-bond specimens compared to those constructed in the stack pattern. This is due to the shrinkage that occurred between the grout core and its corresponding face shell (i.e., separate masonry components), which could not offset the negative influence of the running-bond pattern on their peak compressive stress (f_{um}). It should be noted that the CSA S304-14 requires the construction pattern (stack or running-bond) of the masonry prisms to match that of the corresponding masonry structure in the field. Therefore, both stack pattern and running-bond were tested to investigate their influence on the compressive stress-strain response of RMBEs and ensure the feasibility of using running-bond patterns in RMSW with MBEs. For dry RMBEs, the masonry peak stress (f_{um}) was approximately the same for stack- and running-bond specimens. Conversely, Figure 4.15(d) shows that for wet running-bond RMBEs, f_{um} was 5% higher than that of the RMBEs constructed with a stack pattern. In addition, the results showed that, for dry and wet, unreinforced MBEs and RMBEs, both stack pattern and running-bond specimens demonstrated comparable masonry strains at peak stress (ε_{um}). The strain ductility ($\mu_{\varepsilon 50}$) were nearly similar in wet RMBEs having stack- or running-bond patterns. Nonetheless, this was not the case for dry RMBEs, where running-bond specimens showed lower strain ductility values than their stacked counterparts.
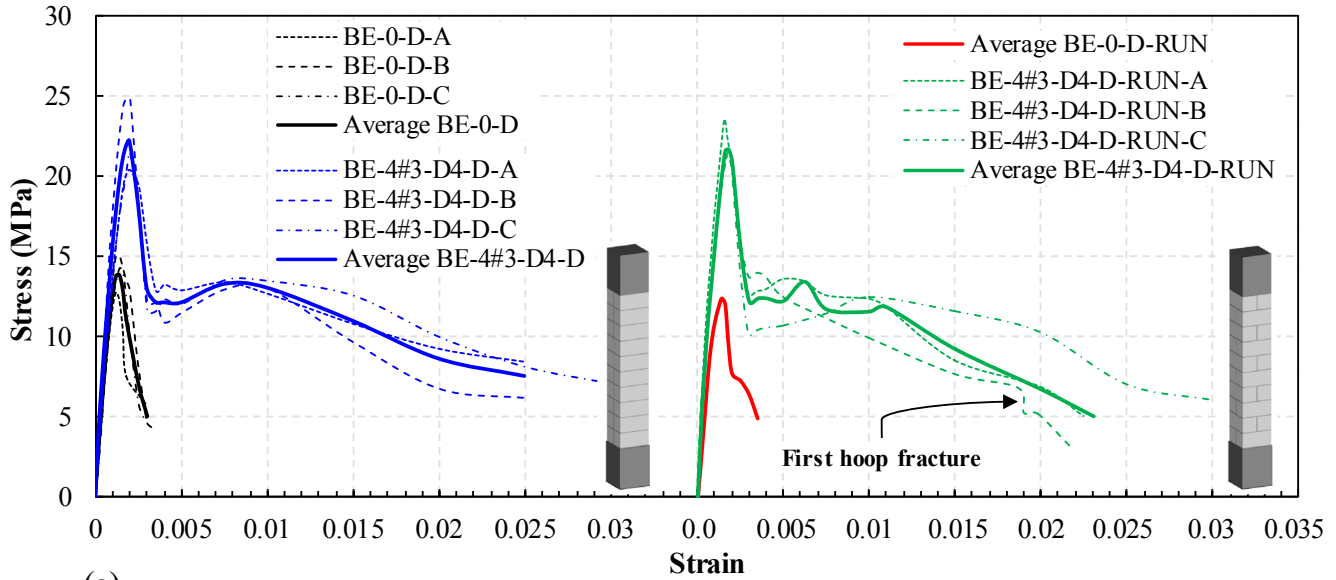
(a)
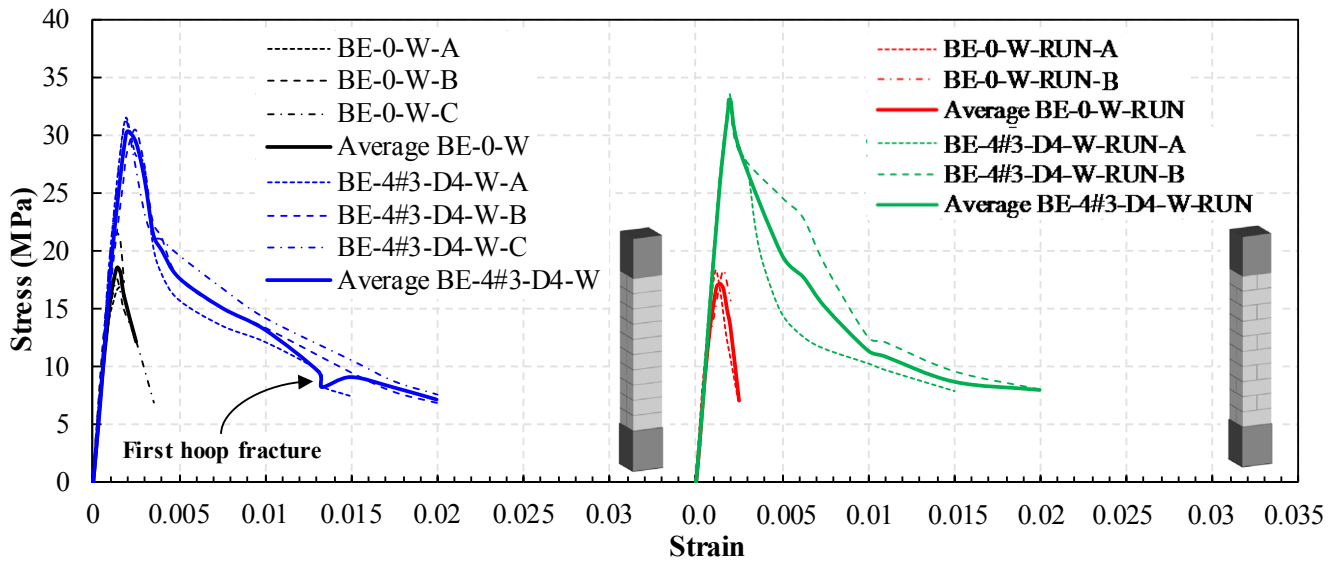
(b)

Figure 4.12 Observed compressive stress-strain curves of unreinforced and RMBEs constructed with stack and running-bond patterns for (a) Dry RMBEs; and (b) Wet RMBEs

Figures 4.12(a and b) depict that dry and wet RMBEs constructed in either stack pattern or running-bond exhibited slightly different post-peak behaviours but similar strains at failure. Also, for strain values that ranged between 0.01 and 0.025, corresponding to 50% and 25% strength degradations, dry running-bond RMBEs showed steeper post-peak descending branches than their stacked counterparts. Obviously, the running-bond pattern negatively affected both the peak stress

(f_{um}) and the strain ductility ($\mu_{\varepsilon 50}$) in dry RMBEs, although it exhibited comparable or enhanced response in wet RMBEs compared to specimens built in the stack pattern.

4.6.6 Effect of pre-wetting of dry masonry face shell before grouting

Figures 4.13(a and b) show the influence of pre-wetting of dry masonry shells before grouting on the axial compressive stress-strain response of stack pattern and running-bond RMBEs, respectively. The test results of the eight groups of the RMBEs, namely, 1, 2, 3, 4, 6, 10, 11, and 12, are listed in Tables 4.4 and 4.5. It was observed that prewetting of the dry masonry shell before grouting greatly enhances the peak compressive stress (f_{um}) of the unreinforced and reinforced stack- and running-bond MBEs. Unreinforced MBEs constructed with pre-wetted masonry shells exhibited an increase in f_{um} by 24.5% and 37% for stack- and running-bond specimens compared to their dry counterparts, respectively, as illustrated in Figure 4.13. The peak compressive stress (f_{um}) was found to increase by 40% and 49% for wet RMBEs built in the stack- and running-bond patterns, respectively, compared to their dry counterparts, as shown in Figure 4.15(e). This significant enhancement in the masonry peak stress (f_{um}) can be attributed to the improved bond between the pre-wetted masonry shell and its corresponding grout core, which was achieved by alleviating the influence of the grout core shrinkage. This observation was previously reported by AbdelRahman and Galal (AbdelRahman and Galal 2020) in their tested concrete-masonry prisms. The strain at peak stress (ε_{um}) was enhanced by 9% and 4% for wet stack- and running-bond unreinforced MBEs, respectively, compared to those of the dry specimens. In addition, the results showed that pre-wetting of dry RMBEs resulted in an increase in the strain corresponding to the peak stress (ε_{um}) by 8% and 13% for stack- and running-bond specimens, respectively.

The axial compressive stress-strain responses of the dry and pre-wetted RMBEs experienced some discrepancies in their corresponding post-peak behaviours, as shown in Figure 4.13. Dry RMBEs displayed a compressive stress-strain response characterized by three stages: rising branch up to the peak stress, then a sudden drop due to face shell spalling, and a gradual falling branch following the face shell spalling. However, wet RMBEs showed a compressive stress-strain relationship consisting of two branches: rising curve up to the peak stress followed by a gradual descending branch up to the specimens′ failure.
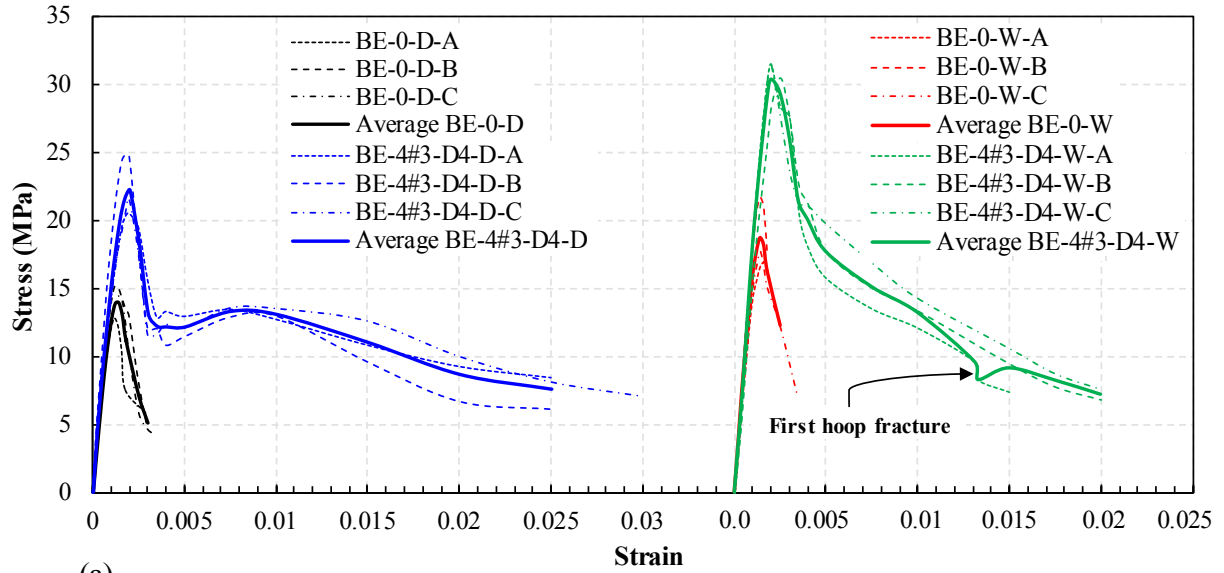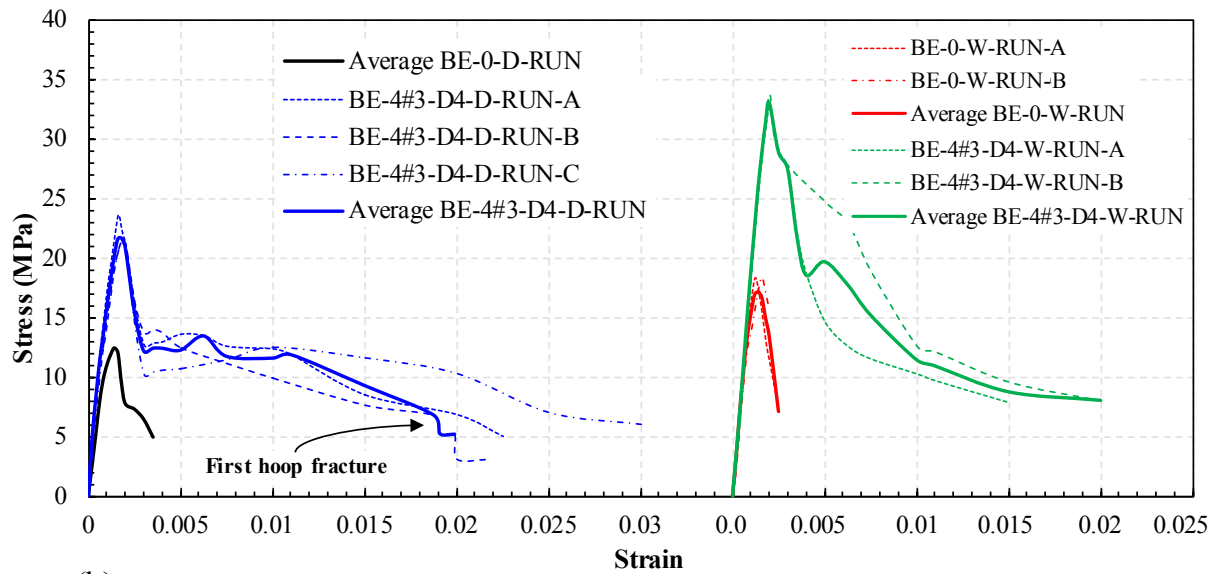
Figure 4.13 Observed compressive stress-strain curves of dry and wet unreinforced and RMBEs constructed with (a) Stack pattern and (b) Running-bond pattern

It is noteworthy that dry RMBEs showed enhanced strain ductilities ($\mu_{\varepsilon 50}$) compared to their wet counterparts. This might be attributed to the steeper falling branch of the wet RMBEs, as shown in Figure 4.13. The relatively steeper post-peak behaviour of wet RMBEs compared to those constructed with dry masonry shell can be attributed to the higher peak compressive stress (f_{um}) attained by the former. This can be explained by the behaviour of RC columns with relatively close cross-section configurations tested by Mander et al. (1988) and Cusson and Paultre (1995).

Comparisons of test results of RC columns built with normal strength concrete tested by Mander et al. (1988) and high strength RC columns investigated by Cusson and Paultre (1995) revealed that RC columns with higher concrete compressive strength showed steeper post-peak response relative to those with normal strength concrete. Moreover, Cusson and Paultre (1994) illustrated the adverse effect that increasing the concrete compressive strength (f'_c) had on the confined concrete core enhancement in strength, strain ductility, and the toughness (i.e., area under the stress-strain curve). This would explain why wet RMBEs experienced a higher peak compressive stress (f_{um}), yet lower strain ductility ($\mu_{\varepsilon50}$) and much steeper post-peak behaviour compared to their dry counterparts.

4.6.7 Compatibility of strains

Selected RMBEs specimens were equipped with strain gauges mounted on the vertical reinforcement rebars to compare their strain values with those measured for the RMBEs by the potentiometers. Figure 4.14 illustrates the relationship between the axial compressive strains recorded from the vertical reinforcement strain gauges and those observed from the corresponding potentiometers in two different RMBE specimens. From this figure, it can be observed that both the vertical reinforcement strains and the RMBEs strains matched up to a strain averaged ~0.0018-0.0022. This means that the compatibility of strains between the vertical reinforcement rebars and the corresponding grout core was captured up to the above-mentioned strains, typically the masonry strains at peak stresses (ε_{um}) for all tested RMBEs. However, it can be seen from Figures 4.14(a and b) that upon attaining the masonry strain at peak stress (ε_{um}), the vertical steel strains deviated from those recorded by the potentiometers. This can be attributed to the face shell spalling upon which a significant portion of the RMBEs cross-section is lost. Therefore, the axial strains recorded from the potentiometers considering the remaining cross-sectional area after face shell spalling did not match those from the vertical steel rebars where the bond between the grout core and the reinforcement started to weaken.

(a)

(b)
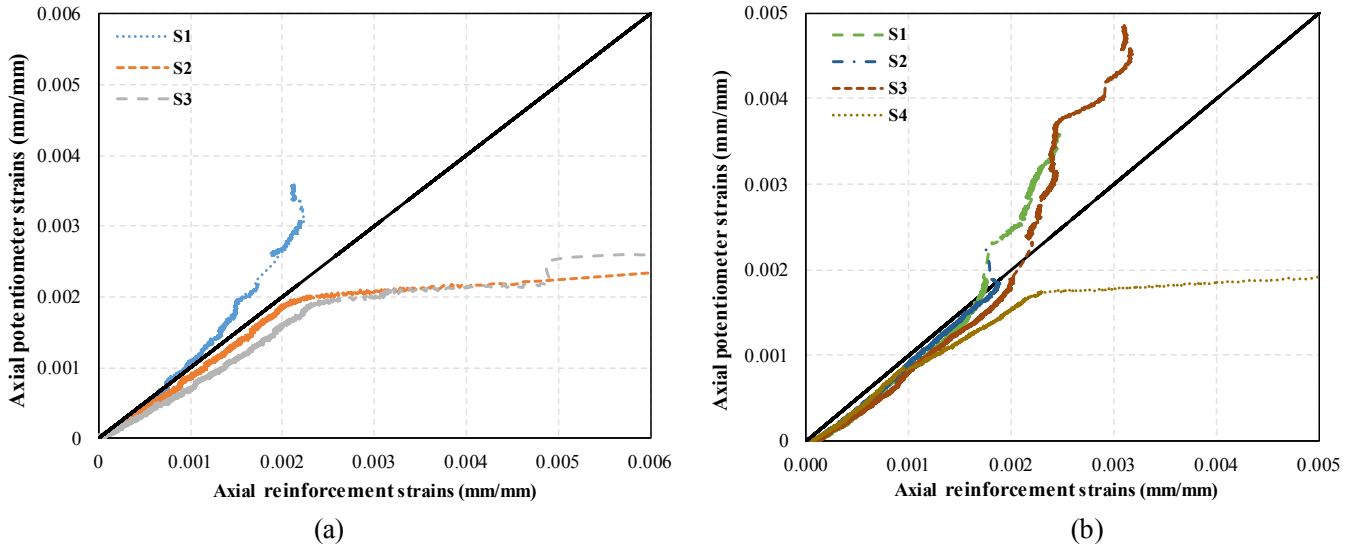
Figure 4.14 Correlation of the observed axial strains from the vertical reinforcement strain gauges and the potentiometers for selected RMBEs specimens (a) BE-4#3-D4-D-A; and (b) BE-4#3-D4-D-RUN-B

(a)

(b)

(c)

(d)

(e)
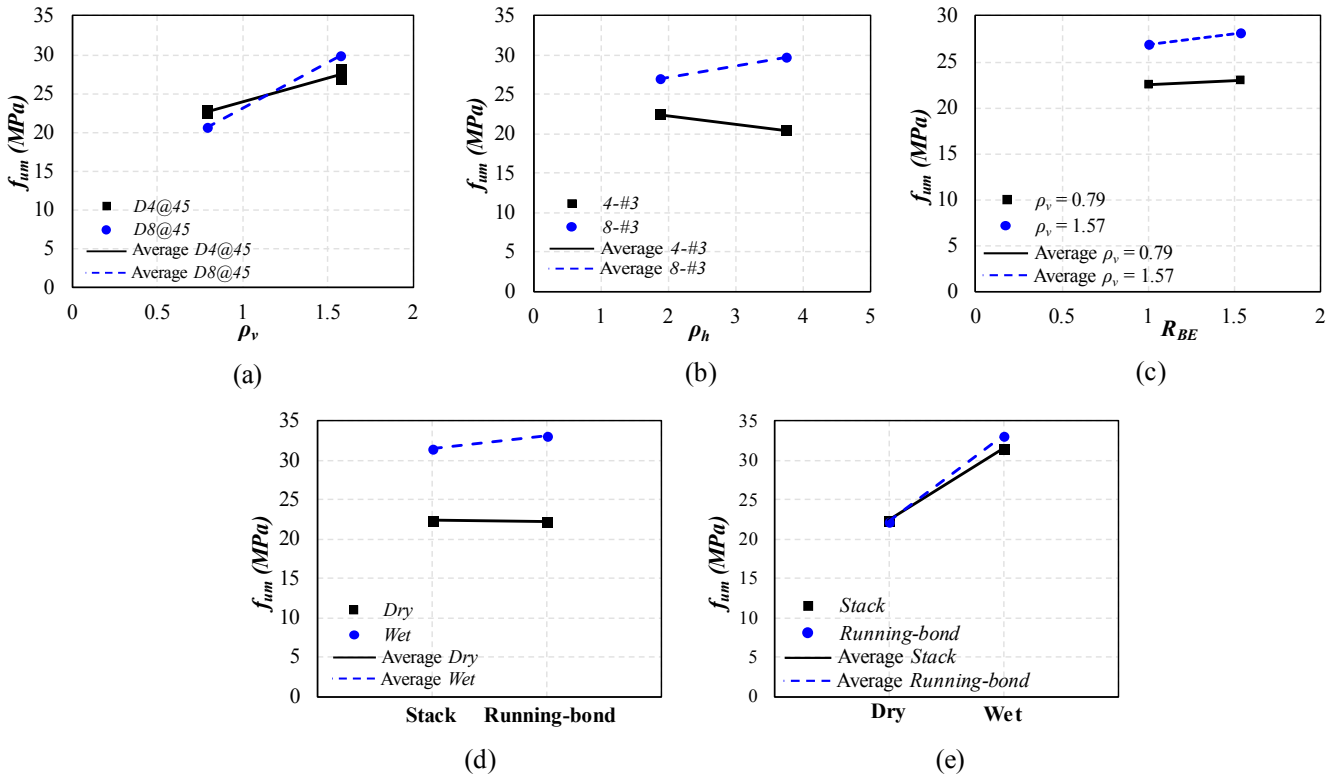
Figure 4.15 Relationship between the RMBEs peak stress (f_{um}) and (a) vertical reinforcement ratio (ρ_v); (b) confinement ratio (ρ_h); (c) cross-section rectangularity (R_{BE}); (d) bonding pattern; and (e) pre-wetting of dry masonry shells
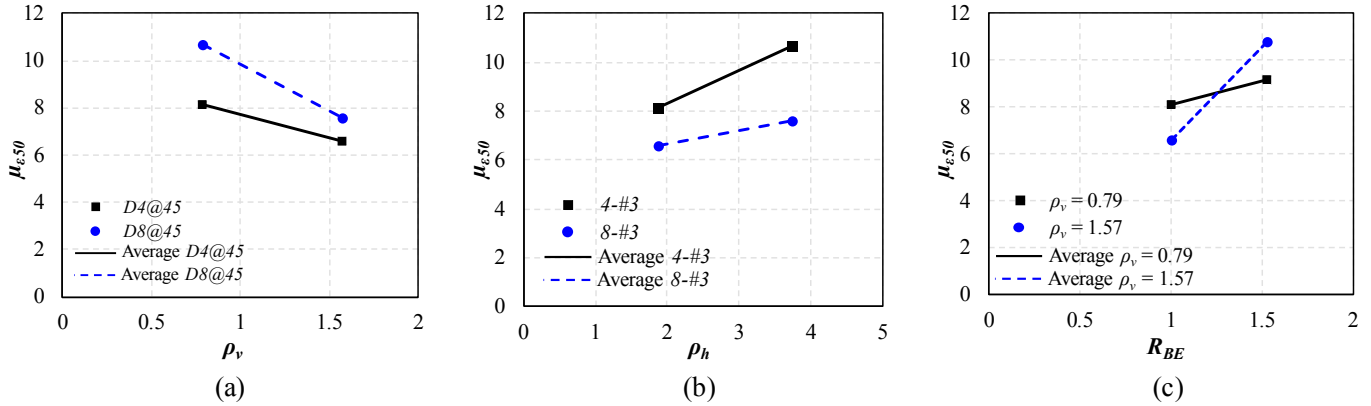
Figure 4.16 Relationship between the RMBEs strain ductility ($\mu\varepsilon50$) and (a) vertical reinforcement ratio (ρ_v); (b) confinement ratio (ρ_h); and (c) cross-section rectangularity (R_{BE})

4.7 Summary and Conclusions

Very limited research was conducted on the compressive stress-strain behaviour of unreinforced and reinforced masonry boundary elements (MBEs and RMBEs), although they are key pillars to understanding the seismic response of reinforced masonry shear walls with masonry boundary elements (RMSW+BEs). Previous research efforts focused on limited test parameters such as the grout compressive strength and the confinement ratio; however, many parameters affecting the RMBEs behaviour are yet to be quantified. Consequently, this study aimed at investigating the axial compressive stress-strain response of unreinforced MBEs and RMBEs to substantially contribute to the limited state-of-the-art, enhance the interpretation of the behaviour of these structural elements, and identify the most critical parameters and quantify their influence on the stress-strain behaviour of RMBEs. The experimental program was designed to investigate five key parameters, namely, the vertical reinforcement ratio (ρ_v), the volumetric ratio of confinement reinforcement (ρ_h), the cross-section configuration (square versus rectangular), the bonding pattern (stack pattern versus running-bond), and pre-wetting of dry masonry shell before grouting on the axial compressive behaviour of MBEs and RMBEs. Experimental testing of thirty-eight MBEs and RMBEs was conducted to evaluate the peak compressive stress (f_{um}), the strain corresponding to the peak stress (ε_{um}), the strain at 25% strength degradation (ε_{75}), the strain at 50% strength degradation (ε_{50}), and the strain ductility ($\mu_{\varepsilon50}$). Moreover, comparisons of the test results were performed in terms of the stress-strain curves; correlations of the test variables with

the peak compressive stress (f_{um}) and the strain ductility ($\mu_{\varepsilon 50}$) were reported. Based on the experimental results of this study, the following conclusions can be drawn:

1. A rising curve characterizes unreinforced MBEs stress-strain response to peak stress and a sudden falling branch following peak stress. On the contrary, MBEs built with running-bond patterns showed a more gradual descending branch than those constructed in the stack pattern. RMBEs exhibited four stages of stress-strain response: ascending branch to the peak stress, followed by a pronounced drop due to face shell spalling, then second peak stress, and a gradual descending branch up to the failure of the specimen. Wet RMBEs, however, did not experience the second peak compressive stress after face shell spalling compared to their equivalent dry counterparts.

2. Indeed, the most critical parameters affecting the peak compressive stress (f_{um}) of RMBEs are the pre-wetting of the dry masonry shell before grouting and increasing the vertical reinforcement ratio (ρ_v), respectively. On the other hand, RMBEs strain ductility ($\mu_{\varepsilon 50}$) was greatly enhanced by increasing the volumetric ratio of the confinement reinforcement (ρ_h) more than the other test parameters. In addition, the noticeable drop in the compressive stress following the face shell spalling in RMBEs was significantly reduced in specimens with rectangular sections compared to their square counterparts.

3. Based on the experimental results of the dry RMBEs with different confinement steel ratios, vertical reinforcement ratios, and cross-sections, it was found that the recorded strain values at 50% strength degradations are multiples (i.e., 1.5~2.25) of the design masonry ultimate compressive strain of 0.008 that is prescribed by the CSA S304-14. The test results showed that this is an arbitrary and conservative value. Therefore, it is recommended that upcoming versions of the CSA S304 shall correlate the design masonry ultimate compressive strain to the confinement configurations and cross-sectional shape of the RMBEs that are incorporated within the RMSW+BEs.

4. Increasing the vertical reinforcement ratio (ρ_v) enhanced the peak compressive stress (f_{um}) of RMBEs built with either square or rectangular cross-sections. However, RMBEs with higher reinforcement ratios (ρ_v) experienced the first hoop fracture sooner than those constructed with a lower ratio (ρ_v). Consequently, the former exhibited rapid deteriorating post-peak behaviour, lesser strain ductility ($\mu_{\varepsilon 50}$), and earlier crushing of the grout core than the latter. This was

attributed to the absence of additional adequate confinement that could have been prevented the premature buckling of unrestrained vertical bars.

5. Although the RMBEs were equipped with confinement hoops that were designed according to the CSA S304-14 provisions for the buckling prevention ties in boundary elements, RMBEs with higher vertical reinforcement ratios experienced low strain ductility levels. Therefore, it is recommended that increasing the vertical reinforcement ratio in RMBEs, especially when increasing the number of steel bars, to be associated with increasing the confinement ratio. This is to ensure that the additional bars are laterally restrained and alleviate their deterioration effect on the RMBEs' strain ductility.

6. The strain ductility ($\mu_{\varepsilon50}$) of the tested RMBEs experienced a remarkable improvement as the volumetric ratio of the confinement reinforcement (ρ_h) increased. RMBEs confined with D8 hoops showed higher second peak stresses following the face shell spalling than those built with D4 hoops. Moreover, RMBEs with D4 confinement reinforcement experienced hoop ruptures compared to none in those confined with D8 hoops. Increasing the confinement ratio (ρ_h) resulted in an increase in the peak stress (f_{um}) in RMBEs with 8-#3 vertical reinforcement, whereas inconsistent results were observed for those constructed with 4-#3 rebars.

7. Clearly, rectangular RMBEs showed enhanced performance than their square counterpart, especially the stress drop following the face shell spalling was significantly minimized. This was attributed to the lower ratio of the face shell to the overall cross-sectional area in RMBEs with rectangular sections (i.e., 39%) compared to those constructed with square counterparts (i.e., 46%). Strain ductility ($\mu_{\varepsilon50}$) was amplified by 13% and 64% in rectangular RMBEs built with 6-#3 and 12-#3 rebars compared to square boundary elements with 4-#3 and 8-#3, respectively. However, changing the RMBEs cross-section from a square to a rectangular counterpart had no substantial influence on their peak compressive stresses (f_{um}).

8. Unreinforced dry MBEs built with running-bond pattern showed less compressive strength (f_{um}) than those laid in the stack pattern. This was because the discontinuous mortar head joints did not transmit the axial compressive load along the specimen height, as many researchers indicated. Conversely, wet running-bond specimens had approximately similar strength as those with the stack pattern. Wet RMBEs laid in the running-bond pattern had higher peak stress (f_{um}) than those constructed in the stack pattern. Apparently, pre-wetting of running-bond MBEs alleviated the staggered mortar joints' adverse effect on their peak stresses (f_{um}).

9. Pre-wetting of dry unreinforced and reinforced MBEs substantially enhanced their compressive strength (f_{um}). This can be attributed to the enhanced bond achieved at the masonry shell–grout core interface. However, the enhancement of the compressive strength of wet MBEs adversely affected the strain ductility ($\mu_{\varepsilon 50}$) of the corresponding RMBEs. This was due to the reduction in the strain at 50% strength degradation (ε_{50}) of wet RMBEs specimens compared to the RMBEs built with dry masonry shell.

In summary, this study presents valuable results to assess the axial compressive behaviour of unreinforced and reinforced masonry boundary elements. The axial compressive strength of MBEs and RMBEs can be enhanced by pre-wetting of dry masonry shell before grouting and/or increasing the vertical reinforcement ratio in a given RMBE cross-section. This should be associated with adequate confinement to the corresponding grout core to further enhance the strain ductility, prevent premature buckling of unrestrained vertical rebars, and rapid deterioration of the grout core strength. Further research is still needed to quantify the influence of other parameters on the axial behaviour of RMBEs and enrich the available research outcome in this field. Additionally, there is a need to investigate the axial cyclic behaviour of reinforced masonry boundary elements to better simulate the response of RMBEs of reinforced masonry shear walls subjected to reversed cyclic loading.

Chapter 5

Monotonic and Cyclic Stress-Strain Models for Confined Concrete-Masonry Shear Wall Boundary Elements

5.1 Abstract

Simulation of the seismic response of fully grouted reinforced masonry shear walls (RMSWs) built with reinforced masonry boundary elements (RMBEs) necessitates reliable nonlinear models of their RMBEs. The axial monotonic and cyclic full stress-strain curves of RMBEs are essential to predict the lateral cyclic response of RMSWs with boundary elements. Therefore, a reliable stress-strain constitutive model for the axial monotonic and cyclic behaviour or RMBEs is needed. The authors recently investigated the axial monotonic compressive behaviour of unconfined and confined MBEs built with different sections′ configurations, vertical reinforcement arrangements, transverse confinement ratio, and different construction procedures. In the current study, the authors investigate the cyclic behaviour of some RMBEs whose counterparts were previously tested under axial monotonic compression. In addition, more specimens with different confinement configurations and different grout strengths were tested. Comparisons of test results showed that increasing the vertical reinforcement ratio increased the axial load carrying capacity of RMBEs but decreased their strain ductility. On the other hand, increasing the confinement ratio of transverse reinforcement introduced a significant enhancement to the confined masonry core resulting in a higher strain ductility than their counterparts built with lower confinement. Besides, using low grout compressive strength significantly reduced the strain ductility of RMBEs. Rectangular RMBEs showed higher peak stress, less stress drop at peak stress, and enhanced post-peak behaviour compared to their square counterparts. Comparisons of RMBEs that were tested under monotonic and cyclic behaviour revealed that the monotonic stress-strain curves form skeleton (i.e., envelope) curves of their cyclically tested counterparts. Moreover, monotonic and cyclic stress-strain models for confined and unconfined concrete-masonry boundary elements subjected to axial compression loading were developed. The proposed models showed good-to-excellent agreement with the experimental results, predicting the stress-strain rising curve, stress drop, and post-peak behaviour. Furthermore, unloading and reloading curves, strength degradations, and softening of reversal and reloading branches due to cyclic degradations were well-captured by the proposed model.

5.2 Introduction

Seismic design of reinforced masonry shear walls (RMSWs) constructed with end confined reinforced masonry boundary elements (RMBEs) requires reliable experimental and analytical information of their masonry boundary elements (MBEs). Since these masonry boundary elements form the confined zones at the masonry structural walls extremities (See Figure 5.1), their cyclic behaviour is a critical pillar in predicting the lateral cyclic response of reinforced masonry shear walls with boundary elements (RMSW+BEs). Experimental and numerical investigations (e.g., Aly and Galal 2019, 2020) of RMSW+BEs revealed considerable enhancement in their strength, stability, and ductility limits due to the confined end zones added at the wall toes (i.e., RMBEs) compared to rectangular walls (i.e., without masonry boundary elements). However, these numerical studies lacked an axial cyclic constitutive model for confined masonry to predict the cyclic behaviour of RMSW+BEs. Instead, they used confined concrete models available in the literature to represent the concrete-masonry material model because fully grouted concrete-masonry resembles its concrete counterpart (Aly and Galal 2019). Minimal research efforts were conducted on the axial monotonic and cyclic behaviour of concrete-masonry boundary elements. Therefore, this study investigates the axial compressive cyclic behaviour of RMBEs built with different vertical reinforcement arrangements, confinement configurations, grout strengths, construction procedures, and cross-sections. In addition, this study proposes monotonic and cyclic models to predict the full compressive stress-strain curves of RMBEs. These models can be utilized with numerical and analytical tools to better predict the cyclic behaviour of RMSW+BEs. This can be achieved by capturing the confinement enhancement introduced by the RMBEs and their influence on the estimated ductility available in structural walls. This enables design engineers of concrete-masonry structures to better employ RMSW+BEs in mid- and high-rise buildings with more reliability of their estimated ductility.

The literature showed that limited research was conducted on the axial cyclic behaviour of confined concrete-masonry, particularly for RMBEs. Moreover, previous researchers investigated the monotonic behaviour of confined concrete-masonry to develop analytical or empirical stress-strain curves of confined masonry under concentric axial compression. Priestley and Elder (1983) tested five-courses high masonry prisms confined with steel confinement plates at the mortar joints. The researchers also proposed a model for the unconfined and confined masonry based on

the literature and their experimental results by modifying the Kent and Park model (1971) for confined concrete prisms.

Reinforced masonry boundary element (RMBE)

Reinforced masonry shear wall with boundary elements (RMSW+BEs)
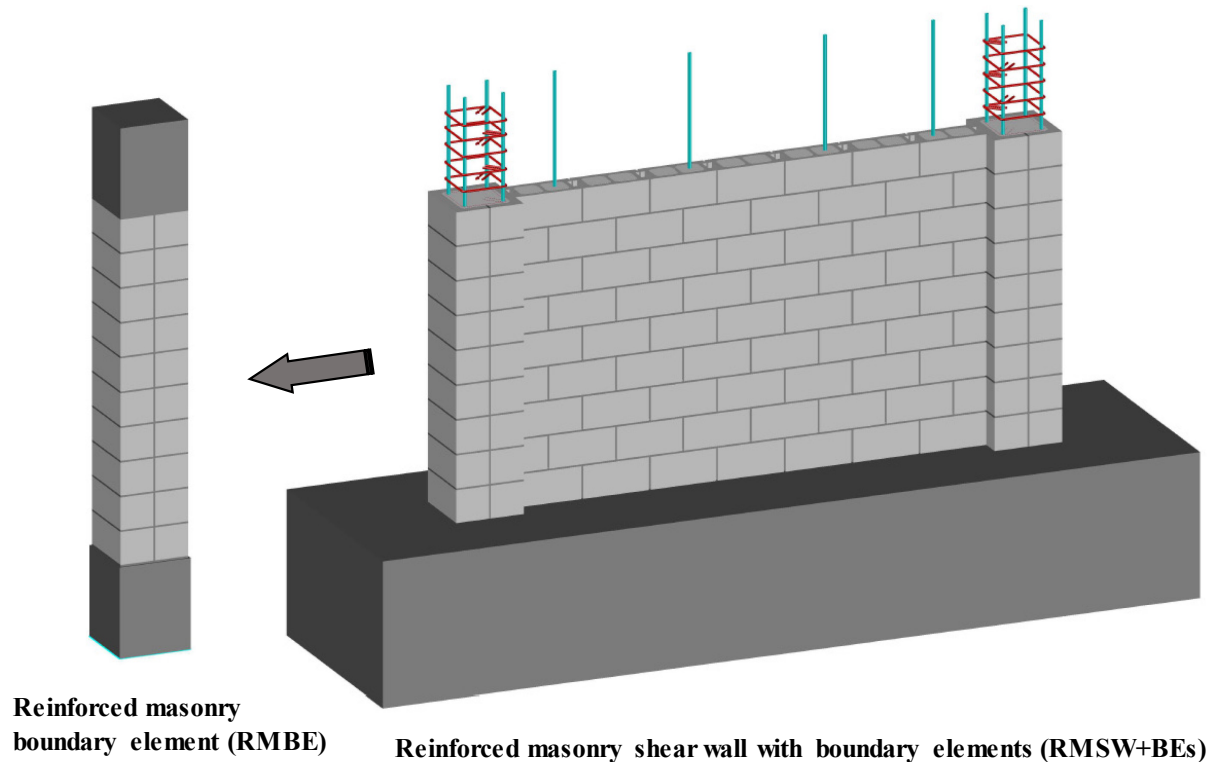
Figure 5.1 Schematic diagram of a reinforced masonry shear wall with square boundary elements

Dhanaseker and Shrive (2002) tested three-courses high concrete-masonry prisms built in the stack-pattern with standard 390x190x190 mm masonry blocks. They investigated two types of confined fully grouted prisms to confine the grout cells such that the compressive strength of grouted masonry exceeds that of their ungrouted counterparts. Dhanaseker and Shrive (2002) developed stress-strain equations for masonry prisms′ cyclic behaviour. The equations were modified based on previously developed equations for concrete and masonry available in the literature (e.g., Kent and Park model). Abo El Ezz et al. (2015) studied, experimentally, the compressive behaviour of full-scale unconfined and confined RMBEs. The researchers reported that confined boundary elements demonstrated enhanced post-peak behaviour than their unconfined counterparts. The researchers developed a simplified analytical stress-strain model for the monotonic compressive stress-strain behaviour of unconfined and confined MBEs based on the Kent and Park model (1971) and calibrated it using their experimental results. It is worth

mentioning that this model has some limitations, such as it did not account for the confined core dimensions and the contribution of vertical reinforcement to the stress-strain behaviour of RMBEs. Obaidat et al. (2018, 2019) utilized the experimental results of thirty-three half-scale confined RMBEs to develop and calibrate an empirical model to predict the monotonic compressive stress-strain response RMBEs. It is noteworthy that testing of the Obaidat et al. (2019) model with higher confinement ratios showed its shortcoming in capturing the stress-strain curves of RMBEs.

The predicted stress-strain curves of confined RMBEs with different vertical reinforcement ratios and confinement configurations using the above-mentioned literature models were not applicable to tested RMBEs under axial monotonic compression loading (Obaidat et al. 2018). Therefore, refined stress-strain models are required to predict the envelope and cyclic stress-strain responses of RMBEs with different sections and confinement configurations. These models can be incorporated in numerical software tools to predict the overall lateral cyclic response of RMSW+BEs considering the stored ductility at the end-confined zones of the shear walls. Thus, based on this study's experimental results and those reported in (AbdelRahman and Galal 2020), stress-strain models for monotonic and cyclic behaviour of RMBEs were developed. The proposed models followed similar approaches to an existing confined concrete model developed by Mander et al. (1988a) but with modifications and refinements such that they are suitable for unconfined and confined concrete-masonry.

5.3 Experimental Program

5.3.1 Test matrix

Thirty-nine half-scale C-shaped unreinforced MBEs and RMBEs were constructed and tested under concentric axial compression. Twenty-six RMBEs specimens were tested under axial cyclic compression, whereas thirteen MBEs were tested under monotonic compression to estimate the compressive strength (f'_{mu}) of unreinforced unconfined MBEs prisms. Each group of specimens included three replicates of the same specimen. Table 5.1 describes the details of unreinforced MBEs and RMBEs tested in this study. Each specimen was labeled to identify the specimens during construction, testing, and comparison. So, each specimen identification begins with the two letters BE that stand for boundary element, followed by the nominal grout strength, either 20 MPa or 50 MPa, then the amount of the vertical steel. Afterwards, D4 or D8 is the confinement hoops size followed by the letter D or W that denote dry and wet masonry shell before grouting,

respectively. This is followed by the abbreviation MON or CYC, which stand for monotonic or cyclic, respectively. Monotonic tests were conducted and described in (AbdelRahman and Galal 2020). The letters A, B, and C refer to the replicates of the same group of specimens. So, BE-20-8#3-D4-D-CYC-A is the first replicate of RMBEs group of specimens constructed with 20 MPa grout strength, eight #3 vertical steel bars, confined with D4 confinement hoops, had its masonry shell dry before grouting, and tested under axial cyclic compression. It should be noted that the utilized hoops′ spacing was 45 mm for all confined RMBEs except for one group of specimens where the spacing was reduced to 30 mm. This group of specimens is marked by the D4/30 abbreviation that denotes D4 confinement hoops at 30 mm spacing. Moreover, it is worth noting that the last two groups of specimens having six #3 (6-#3) and twelve #3 (12-#3) vertical bars were rectangular RMBEs, as illustrated in Figure 5.2. These rectangular RMBEs were employed to investigate different cross-sections of confined RMBEs (i.e., square versus rectangular).
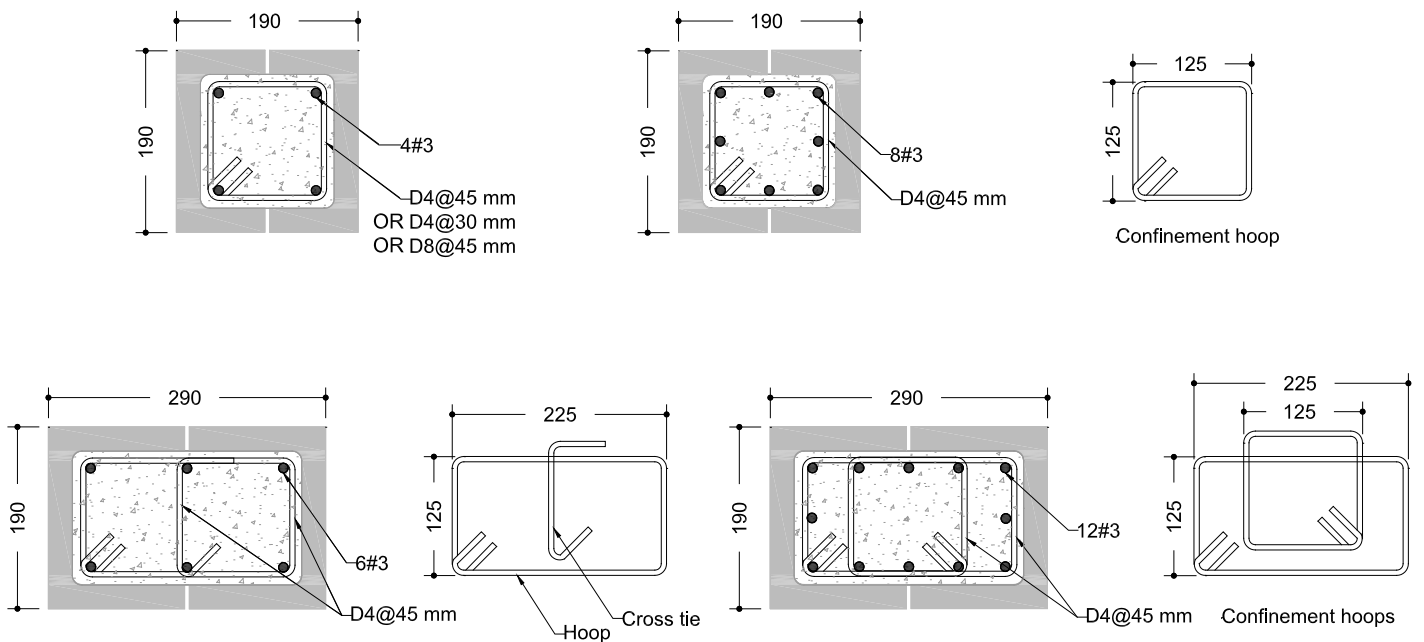
Figure 5.2 RMBEs sections′ details and confinement hoops

115

Table 5.1 Test matrix of unreinforced and reinforced masonry boundary elements (MBEs, and RMBEs)

Group number	Group Identifier	Monotonic / Cyclic	Grout compressive strength (MPa)	Number of tested MBEs	Status of BEs before grouting	Vertical reinforcement		Confining reinforcement		Section rectangularity ratio
						Amount	ρ_v (%)	Amount	ρ_h (%)	R_{BE}
1	BE-20-0-D	Monotonic	20	3	Dry	-	-	-	-	1.0
2	BE-20-0-W		20	2	Wet	-	-	-	-	1.0
3	BE-50-0-D*		50	3	Dry	-	-	-	-	1.0
4	BE-50-0-W*		50	3	Wet	-	-	-	-	1.0
5	BE-50-0-D-REC*		50	2	Dry	-	-	-	-	1.53
6	BE-20-4#3-D4-D-CYC	Cyclic	20	3	Dry	4-#3	0.787	D4@45	1.87	1.0
7	BE-20-8#3-D4-D-CYC		20	3	Dry	8-#3	1.573	D4@45	1.87	1.0
8	BE-50-4#3-D4-D-CYC		50	2	Dry	4-#3	0.787	D4@45	1.87	1.0
9	BE-50-8#3-D4-D-CYC		50	3	Dry	8-#3	1.573	D4@45	1.87	1.0
10	BE-50-4#3-D4/30-D-CYC		50	2	Dry	4-#3	0.787	D4@30	2.76	1.0
11	BE-50-4#3-D8-D-CYC		50	3	Dry	4-#3	0.787	D8@45	3.74	1.0
12	BE-20-4#3-D4-W-CYC		20	2	Wet	4-#3	0.787	D4@45	1.87	1.0
13	BE-50-4#3-D4-W-CYC		50	2	Wet	4-#3	0.787	D4@45	1.87	1.0
14	BE-6#3-D4-D-CYC		50	3	Dry	6-#3	0.773	D4@45	1.68	1.53
15	BE-12#3-D4-D-CYC		50	3	Dry	12-#3	1.546	D4@45	1.94	1.53
16	BE-4#3-D4-D-MON*	Monotonic	50	3	Dry	4-#3	0.787	D4@45	1.87	1.0
17	BE-8#3-D4-D-MON*		50	3	Dry	8-#3	1.573	D4@45	1.87	1.0
18	BE-4#3-D8-D-MON*		50	3	Dry	4-#3	0.787	D8@45	3.74	1.0
19	BE-8#3-D8-D-MON*		50	3	Dry	8-#3	1.573	D8@45	3.74	1.0
20	BE-6#3-D4-D-MON*		50	3	Dry	6-#3	0.773	D4@45	1.68	1.53
21	BE-12#3-D4-D-MON*		50	3	Dry	12-#3	1.546	D4@45	1.94	1.53

* AbdelRahman and Galal

In this study, five test parameters were investigated, namely, the vertical reinforcement ratio (ρ_v), the volumetric ratio of confinement reinforcement (ρ_h), the grout compressive strength (f_g), the cross-section configuration (i.e., rectangularity ratio, R_{BE}), and pre-wetting of dry masonry shells before grouting. As such, two vertical reinforcement ratios (ρ_v), namely, 0.78% and 1.55%, and three confinement ratios (ρ_h), namely, 1.87%, 2.76%, and 3.74%, were investigated. Moreover, the grout compressive strength (f_g) changed from 20 MPa to 50 MPa to study the influence of the grout compressive strength on the compressive behaviour of RMBEs. Furthermore, two types of cross-section configurations were examined, namely, square 190x190 mm and rectangular 190x290 mm with rectangularity ratios (R_{BE}) of 1.0 and 1.53, respectively. Besides, the influence of pre-wetting of the dry masonry shell before grouting was assessed, as previously recommended in (AbdelRahman and Galal 2020), to enhance the masonry compressive strength.

It is worth noting that this test matrix was designed to enable direct correlations of the axial cyclic compressive behaviour of RMBEs to those tested in (AbdelRahman and Galal 2020) under monotonic compression. The monotonic and cyclic curves of these specimens were utilized to calibrate the stress-strain models for axial and cyclic compressive behaviour of square and rectangular RMBEs.

5.3.2 Construction of RMBEs

RMBEs construction started with assembling the reinforcement cages. All RMBEs were built with #3 vertical reinforcement rebars with a nominal diameter of 9.5 mm and a cross-sectional area of 71 mm^2. The steel cages were fabricated with either four #3 (4-#3) or eight #3 (8-#3) bars for square RMBEs while rectangular RMBEs had either six #3 (6-#3) or twelve #3 (12-#3) steel cages, as shown in Figure 5.2. Reinforcement cages were confined with either D4 (d_b = 5.73 mm, A_b = 25.8 mm^2) or D8 (d_b = 5.73 mm, A_b = 25.8 mm^2) structural deformed wires. The vertical steel extended along the full height of RMBEs without lab splices. As shown in Figure 5.2, D4 and D8 confinement hoops were anchored at least 55 mm with the 135° seismic hook inside the grout core and were alternatively placed along the RMBEs, as stipulated in the CSA S304-14 (Canadian Standards Association (CSA) 2014a). Rectangular RMBEs reinforced with six #3 rebars included seismic cross-ties with a 135° seismic hook from one end and a standard 90° hook from the other end. Figure 5.3 shows a 3D schematic diagram of square and rectangular RMBEs and a steel

cage's sample details. Confinement hoops of 10M bars and a smaller spacing of 35 mm were utilized at the top and bottom ends of the RMBEs steel cages, as shown in Figure 5.3. These confinement enhancements were employed to ensure proper detailing and alleviate the local concrete failure that could have happened during the testing of the RMBEs.
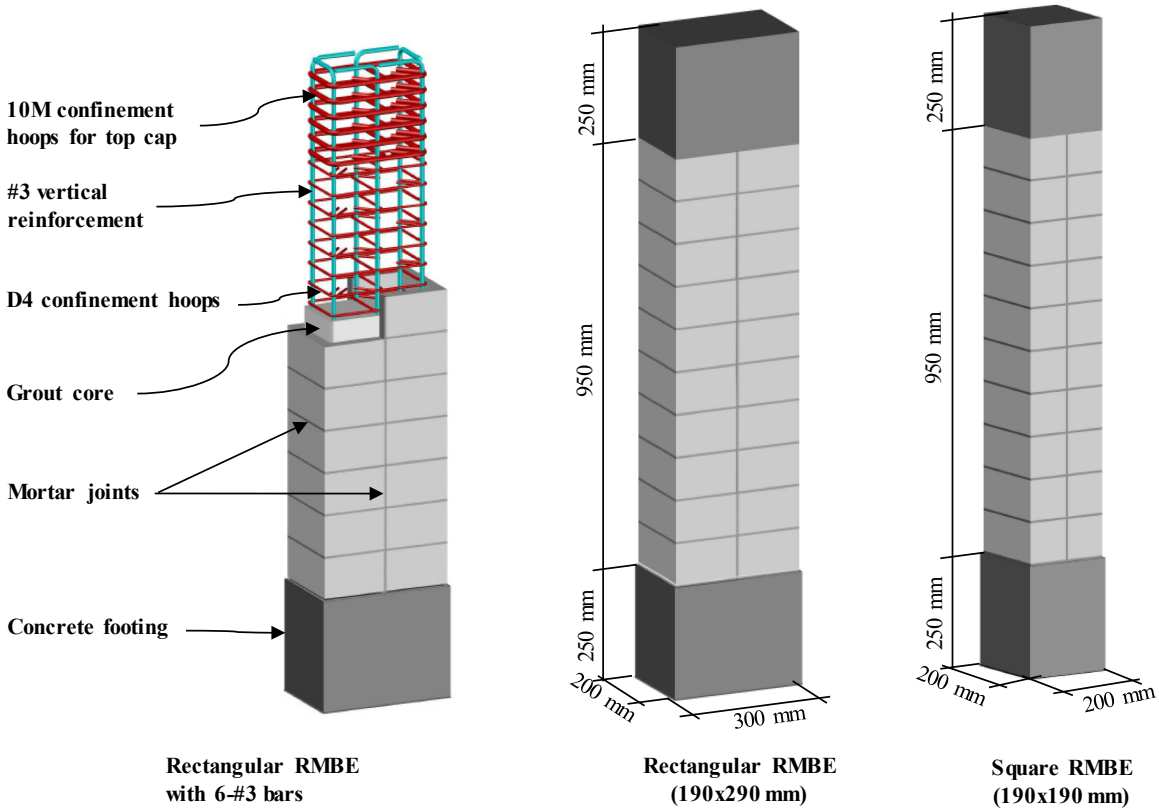
Figure 5.3 Dimensions and details of tested reinforced masonry boundary elements (RMBEs)

As shown in Figure 5.4(a), prefabricated wooden forms were utilized to cast the concrete bottom footings after assembling the steel cages, as illustrated in Figures 5.4(b and c). After curing the bottom concrete footing, the steel cages were disassembled and prepared to install the electrical strain gauges on the vertical steel rebars, as depicted in Fig 4(d). These strain gauges were mounted at the RMBEs steel rebars' mid-height to measure reinforcement strains while testing the RMBEs. Following this, a professional mason used C-shaped concrete-masonry units to construct the RMBEs masonry shells using a structural mortar type S with 5 mm mortar joints, as shown in Figure 5.4(e). Two halves of C-shaped masonry units were utilized, each having the dimensions

of 92.5 x 190 x 90 x 25 mm for square MBEs, whereas 142.5x190x90x25 mm for rectangular MBEs representing width x length x height x thickness, respectively.
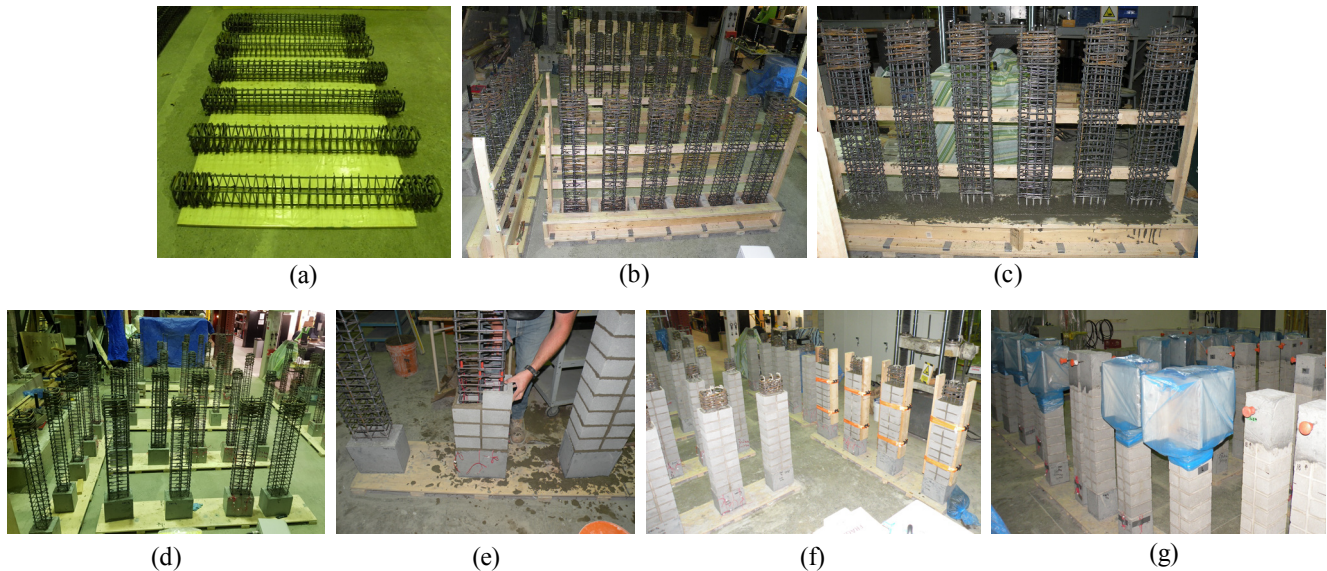
Figure 5.4 Construction procedures of RMBEs: (a) assembled reinforcement steel cages; (b) centering the RMBEs in their wooden forms; (c) casting of bottom concrete footing; (d) removed bottom concrete footing forms (e) building the RMBEs using masonry blocks; (f) fully-built and grouted RMBEs; and (g) top concrete caps cast and cured

Before grouting, the masonry shells were either dry or wet. Wet masonry shells were pre-wetted by water hosing the C-shaped masonry blocks′ outer surface to the point that the water can be observed to flow down the blocks′ outer surface (AbdelRahman and Galal 2020). This procedure was to ensure the saturation of the concrete-masonry blocks before grouting of wet RMBEs. All MBEs and RMBEs were strapped, as shown in Figure 5.4(f), to prevent any unexpected failure of the masonry shells before grouting. Grout patches were proportioned, mixed, and cast in the MBEs and RMBEs to fill the specimens. The RMBEs were left to cure in the dry lab environment. Afterwards, the concrete top caps were cast on the top of the hardened grout using individual concrete wooden forms, as illustrated in Figure 5.4(g). The aspect ratio AR = h/t of the RMBEs was 5 to conform to the CSA S304-14 (2014a) provisions where the masonry compressive strength is not subjected to a correction factor.

119

5.3.3 Material properties

Vertical steel bars #3 conforming to ASTM A615 (American Society for Testing and Materials (ASTM) 2015a) and structurally deformed wires D4 and D8 conforming to ASTM A1064 (2018) were utilized to fabricate the steel cages of the RMBEs. Six samples of each of the bars and wires were tested under axial tension according to ASTM A370 (2015b) to determine their tensile characteristics (i.e., yield strength, yield strain, ultimate strength, and ultimate strain). Table 5.2 describes the results of the tensile tests of the tested bars. Moreover, the test setup and the stress-strain curves of the tested bars are illustrated in Figure 5.5. The test results showed that the #3 bars yield strength was 429 MPa (COV = 3%) and the ultimate strength was 679 MPa (COV = 1.6%). Besides, D4 and D8 confinement hoops showed an average proof strength of 607 MPa (COV = 3.8%) and 519 MPa (COV = 2.4%), respectively.

(a)

(b)

(c)
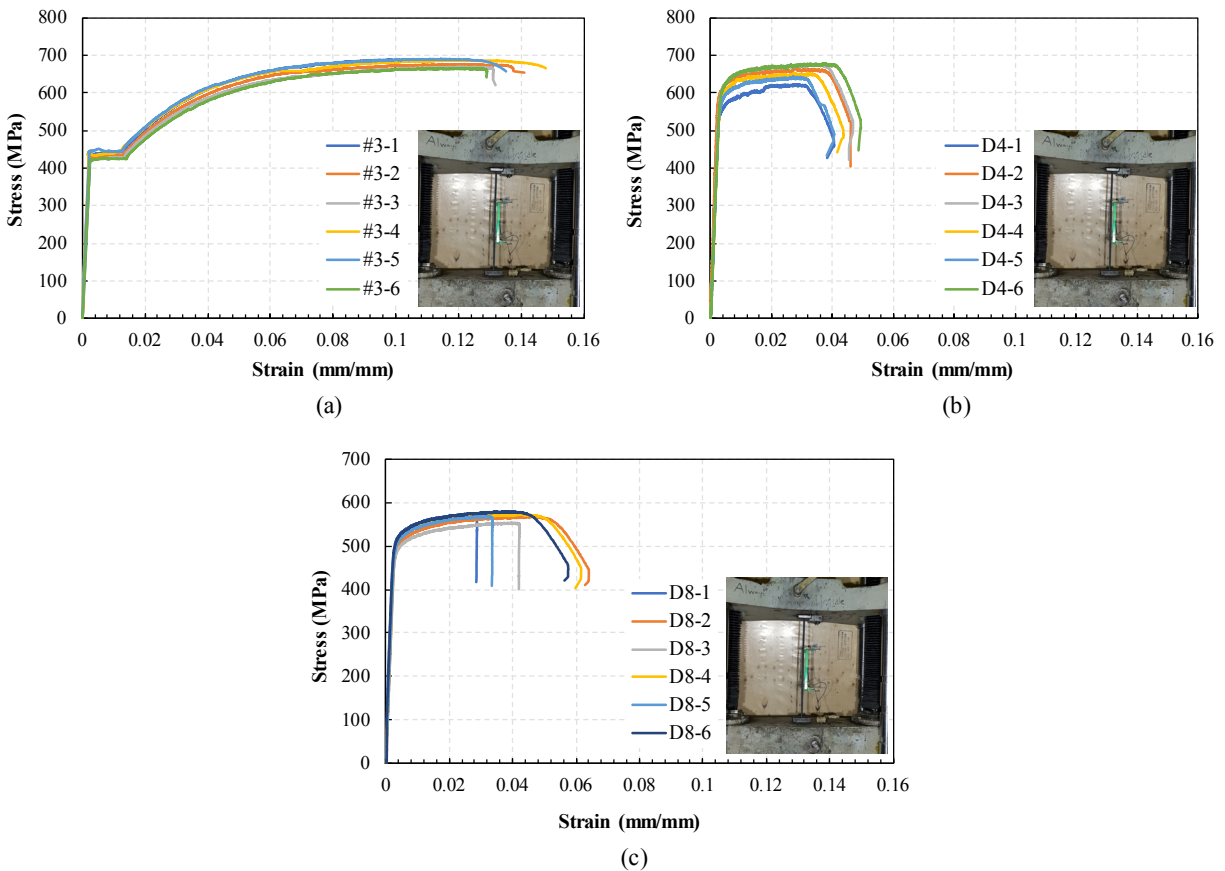
Figure 5.5 Experimental stress-strain curves for tested (a) #3 vertical reinforcing bars; (b) D4 confinement hoops; and (c) D8 confinement hoops

Table 5.2 Mechanical properties of vertical reinforcement and confinement hoops

Bar size	Nominal diameter (mm)	Nominal area (mm^2)	Yield strength (MPa), (COV%)	Yield strain (mm/mm), (COV%)	Ultimate strength (MPa), (COV%)	Ultimate strain (mm/mm), (COV%)
#3	9.525	71	428.8 (2.96)	0.00224 (9.16)	679.4 (1.59)	0.13082 (12.69)
D4	5.7	25.81	606.6 (3.82)	-	657.0 (3.34)	0.04451 (8.06)
D8	8.1	51.61	518.9 (2.36)	-	570.0 (1.58)	0.04786 (31.68)

Table 5.3 shows the properties of the constituents′ materials utilized to construct the MBEs. Twenty-two masonry coupons with the dimensions of 25x50x100 mm (thickness x height x length) were cut from the C-shaped masonry units and tested according to ASTM C140 (2015c) to compute the compressive strength of masonry blocks (f_b). The tested masonry coupons showed an average strength of 44.5 MPa (COV = 13.5%) based on a nominal loading area of 2500 mm^2. Besides, type S structural mortar was utilized to build the RMBEs. Fifty millimeter mortar cubes were tested under compression according to ASTM C109 (2013). Twelve mortar cubes were tested and showed an average mortar compressive strength (f_m) of 15.7 MPa (COV = 9.8%). During grouting of the RMBEs, grout cylinders were sampled in order to determine the compressive strength of the grout (f_g). Two types of grout were utilized to investigate the grout strength's influence on RMBEs compressive behaviour. The mix proportions by weight of the low strength grout (i.e., 20 MPa) were 1: 4: 0.8, and for high strength grout were 1: 2.5: 0.5 for cement: sand: water, respectively.

Table 5.3 Mechanical properties of constituent materials of the masonry boundary elements

Material component	Notation	Compressive strength (MPa), (COV%)
Concrete footing cylinder	f'_c	69.2 (3.70)
Masonry block coupon	f_b	44.5 (13.53)
Low strength grout cylinder	f_g	25.4 (6.81)
High strength grout cylinder	f_g	48.7 (4.62)
Mortar cube	f_m	15.7 (9.78)

Grout cylinders (100x200 mm) were sampled and tested according to CSA A179-14 (2014b). The average grout strength of eight 20 MPa grout cylinders was 25.4 MPa (COV = 6.81%),

whereas testing ten 50 MPa grout cylinders yielded an average strength of 48.7 MPa (COV = 4.6%). Also, testing of eight concrete cylinders according to ASTM C39 (2015d) showed an average compressive strength (f_c') of 69 MPa (COV = 3.7%) of top and bottom concrete footings.

5.4 Test setup and Instrumentation

A rigid steel testing frame provided with a 5000 kN hydraulic actuator was utilized to test the MBEs and RMBEs using a displacement-control protocol. Displacement-control loading enables capturing the post-peak behaviour of the RMBEs to monitor the differences in the descending branches, second peaks, hoop fractures, and failure strains. Figure 5.6 illustrates the test setup and sample tested specimens under the 5000 kN actuator. A high-strength plaster capping material was applied below and above the RMBEs to distribute the axial compressive loading on the specimens and eliminate finishing surface roughness. Afterwards, top bearing steel plate of 50 mm thick conforming to ASTM C1314 (2014) was placed on the top of the capping material and leveled to ensure pure axial loading through the testing time. A heavy-duty spherical platen was then placed on the top of the upper bearing plate, as shown in Figure 5.6. Alignment laser devices were then utilized to center the RMBEs under the actuator. Although some of the tested specimens showed rupture of confinement hoops, the test was continued to cover the post-peak behaviour of the tested RMBEs. The test was terminated at a strain corresponding to ~60-75% strength degradation on the monitored stress-strain curve's falling branch. As shown in Figures 5.6(a and b), four potentiometers were mounted on the four sides of the RMBEs to measure their axial deformations with a gauge length equal to the 950 mm clear height of the RMBEs. The chosen potentiometer's gauge length is attributed to the fact that face shell spalling can entirely damage the measuring devices if mounted in the mid-height of the RMBEs. Also, only concentrated deformations at mid-height would have been captured, which would not represent the axial displacements along the RMBEs′ total height. Therefore, it was necessary to keep the potentiometers safe to provide continuous readings of the axial displacements along the tested specimens′ height.
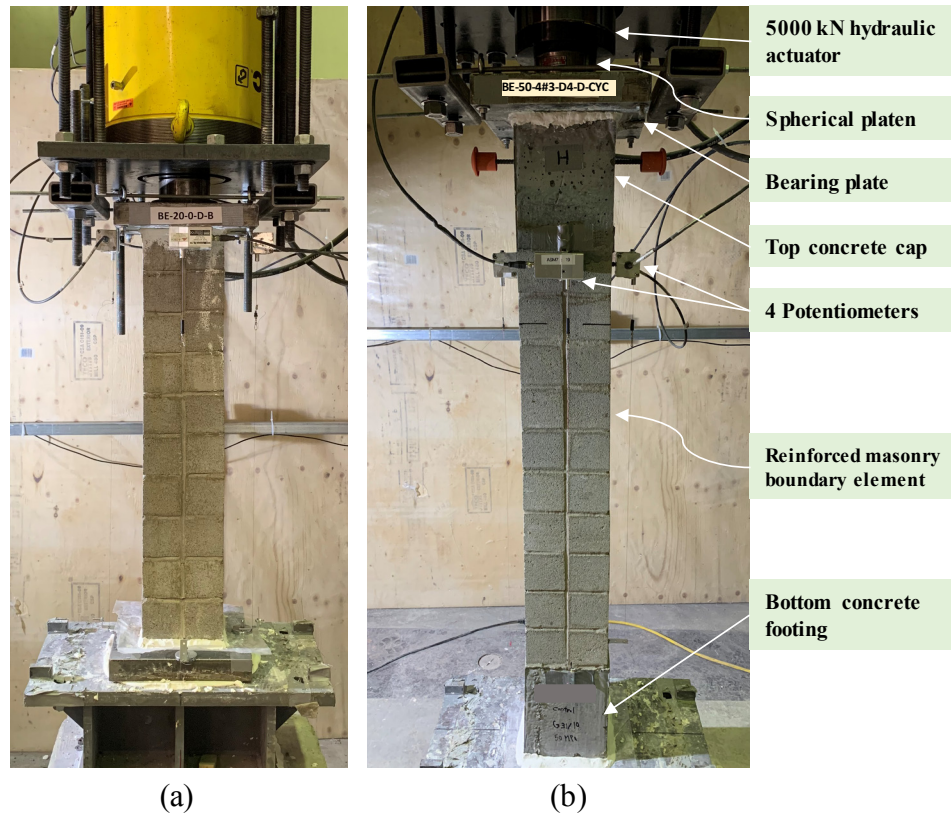
Figure 5.6 Axial compression testing of (a) unreinforced masonry boundary element; and (b) reinforced masonry boundary element

5.5 Test Protocol

Unreinforced MBEs were tested monotonically under incrementally increasing axial compression up to the failure of specimens. A displacement-control rate of 0.003 mm/sec was utilized for the MBEs test (i.e., rising and falling branches). On the other hand, the RMBEs were tested under axial cyclic compression. The cycles ranged between a specific value at the desired strain level and nearly zero stress. Before the peak stress of RMBEs, a displacement-rate of 0.003 mm/sec was employed for the stress-strain rising branch, whereas a displacement rate of 0.01 mm/sec was used for the unloading branches. After the peak stress of RMBEs, a displacement-control rate of 0.005 mm/sec was utilized for the reloading branches, whereas a rate of 0.01 mm/sec was kept for the unloading branches. Based on the experimental results of RMBEs (AbdelRahman and Galal 2020; Obaidat et al. 2018, 2019), their peak stresses were found to be attained at corresponding strains vary from 0.0016 to 0.0024 mm/mm (i.e., an average of 0.002). As such, strain increments of approximately 0.002 mm/mm were used between the cycles of the RMBEs.

For each strain level, RMBEs were subjected to a single unloading and reloading cycle. It should be noted that each RMBE was tested in a calendar day where no creep effects were considered.

5.6 Test Results

Stress-strain curves of MBEs and RMBEs were calculated based on the recorded axial loads and corresponding axial deformations. The peak stress (f_{m-max}) was calculated by dividing the maximum compressive load by a nominal cross-section area of 190x190 mm for square RMBEs and 190x290 mm for rectangular RMBEs. It is noteworthy that the shown stress-strain curves of the tested specimens are for the full cross-sectional area of the RMBEs and not for the confined masonry core only. Besides, the axial strain at peak stress (ε_{m-max}) and at 50% strength degradation (ε_{50}) were determined by dividing the recorded axial displacements by their 950 mm gauge lengths. The presented strain values are the averages of four strain readings recorded by the four potentiometers of the tested RMBEs. Cyclic stress-strain responses of specimens are presented to compare the studied test parameters′ influence on the axial cyclic behaviour of RMBEs. Tables 5.4 and 5.5 present the values of strain ductility ($\mu_{\varepsilon_{50}}$) calculated by dividing the strain at 50% strength degradation (ε_{50}) by the strain at peak stress (ε_{m-max}).

Stress-strain curves of the tested unreinforced MBEs characterized by two-branches: a rising curve up to the peak stress (f_{m-max}) and a sudden falling branch following the peak stress. Figures 5.7(a-c) show the modes of failure of unconfined unreinforced MBEs. On the contrary, RMBEs envelope curves were characterized by four branches: a rising curve to the peak stress, a sudden drop to ~55-65% of the peak stress following the face shell spalling, then a gradual increase to the second peak stress, and a gradual descending branch to the failure strain or test termination. Unlike its reinforced concrete (RC) counterpart, RMBEs showed a significant face shell spalling that contributed to a pronounced reduction of the axial load carrying capacity compared to the concrete cover spalling in RC members, as shown in Figures 5.7 (d-g). This stress drop was because of the significant face shell to the overall cross-sectional area ratio of the RMBEs (45.7%).

Table 5.4 Test results of unreinforced masonry boundary elements (MBEs)

Group number	BE Identifier	Test	Peak stress (MPa)		Strain at peak stress, $\varepsilon_{m\text{-}max}$		Strain at 50% of the peak stress, ε_{50}		Strain ductility, $\mu_{\varepsilon50}$
			$f_{m\text{-}max}$	Average (COV%)	$\varepsilon_{m\text{-}max}$	Average (COV%)	ε_{50}	Average (COV%)	$\varepsilon_{50}/\varepsilon_{m\text{-}max}$
1	BE-20-0-D-A	Monotonic	17.56	19.33 (9.77)	–	0.00156 (5.91)	0.00192	0.00192 (0.00)	1.23
	BE-20-0-D-B		21.32		0.00149		0.00192		
	BE-20-0-D-C		19.12		0.00162		–		
2	BE-20-0-W-A	Monotonic	24.68	23.86 (4.86)	0.00209	0.00194 (11.33)	–	–	–
	BE-20-0-W-B		23.04		0.00178		–		
3	BE-50-0-D-A*	Monotonic	12.90	14.28 (8.92)	0.00116	0.00131 (11.80)	0.00246	0.00239 (9.50)	1.82
	BE-50-0-D-B*		15.41		0.00131		0.00258		
	BE-50-0-D-C*		14.53		0.00147		0.00214		
4	BE-50-0-W-A*	Monotonic	16.99	18.91 (13.92)	0.00156	0.00147 (6.15)	0.00188	0.00251 (35.28)	1.71
	BE-50-0-W-B*		21.91		0.00146		–		
	BE-50-0-W-C*		17.83		0.00138		0.00313		
5	BE-50-0-D-REC-A*	Monotonic	19.18	18.22 (7.45)	0.00127	0.00128 (0.55)	0.00266	0.00249 (9.66)	1.95
	BE-50-0-D-REC-B*		17.26		0.00128		0.00232		

*Tested by AbdelRahman and Galal
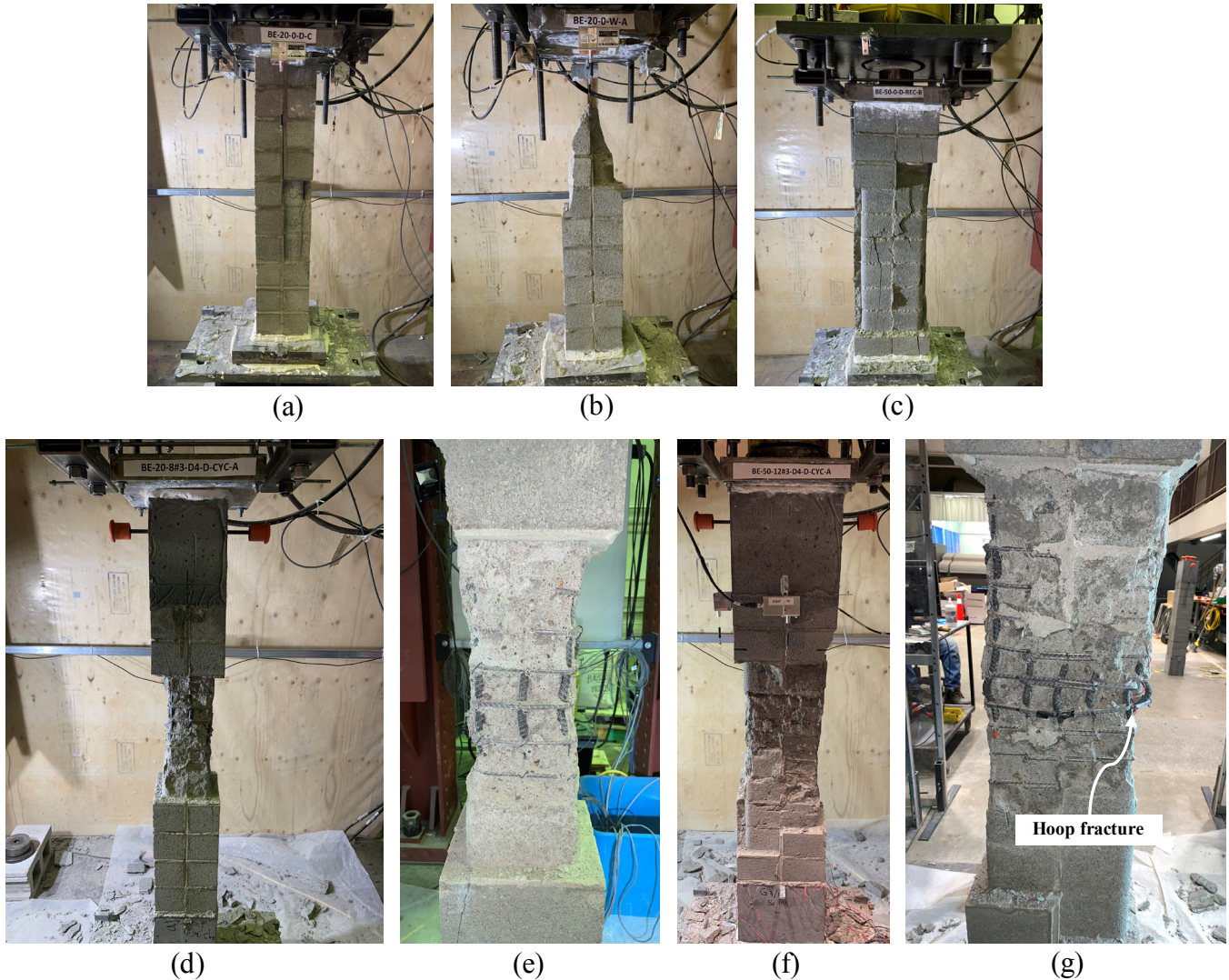
Figure 5.7 Typical failure modes of: (a) unreinforced dry MBE; (b) unreinforced wet MBE; (c) unreinforced dry rectangular MBE; (d) dry RMBE at 75% strength degradation; (e) buckling of vertical steel; (f) rectangular RMBE at 30% strength degradation; and (g) rectangular RMBE at 75% strength degradation

The cyclic response of specimens showed that characteristics of RMBEs under axial cyclic compression are comparable to their RC counterparts. In Figures 5.8–5.11, typical stress-strain cyclic curves show that unloading from strains less than the strain at peak stress ($\varepsilon_{m\text{-}max}$) still induces residual (i.e., plastic) strains. This phenomenon was explained by Martinez and Elnashai (1997) for confined concrete in which plastic strains were observed when unloading strain (ε_{un}) exceed that corresponding to 35% of the peak stress on the rising curve. Moreover, as the unloading strain (ε_{un}) increased, cyclic loops became bulgier, indicating more energy dissipation. Also, high

126

unloading stiffness values were observed at the onset of unloading branches. However, the greater the unloading strains (ε_{un}), the much steeper unloading curves (i.e., softening) were observed, especially when approaching zero stress. Besides, reloading stiffness significantly decreased with additional strain increments.

5.6.1 Effect of test parameters on the cyclic stress-strain response of RMBEs

The influence of changing the vertical reinforcement ratio (ρ_v) on the stress-strain cyclic behaviour of the tested RMBEs is presented in Figure 5.8. Increasing ρ_v resulted in a significant increase in the peak stress of tested RMBEs. Test results of square RMBEs constructed with 20 MPa and 50 MPa grouts, and rectangular RMBEs with 50 MPa grout, showed that doubling ρ_v increased the peak compressive stress ($f_{m\text{-}max}$) by 20%, 30%, and 40.8%, respectively. Contrarily, the strain ductility at 50% strength degradation ($\mu_{\varepsilon_{50}}$) experienced slight-to-significant reduction due to the improvement of ρ_v.
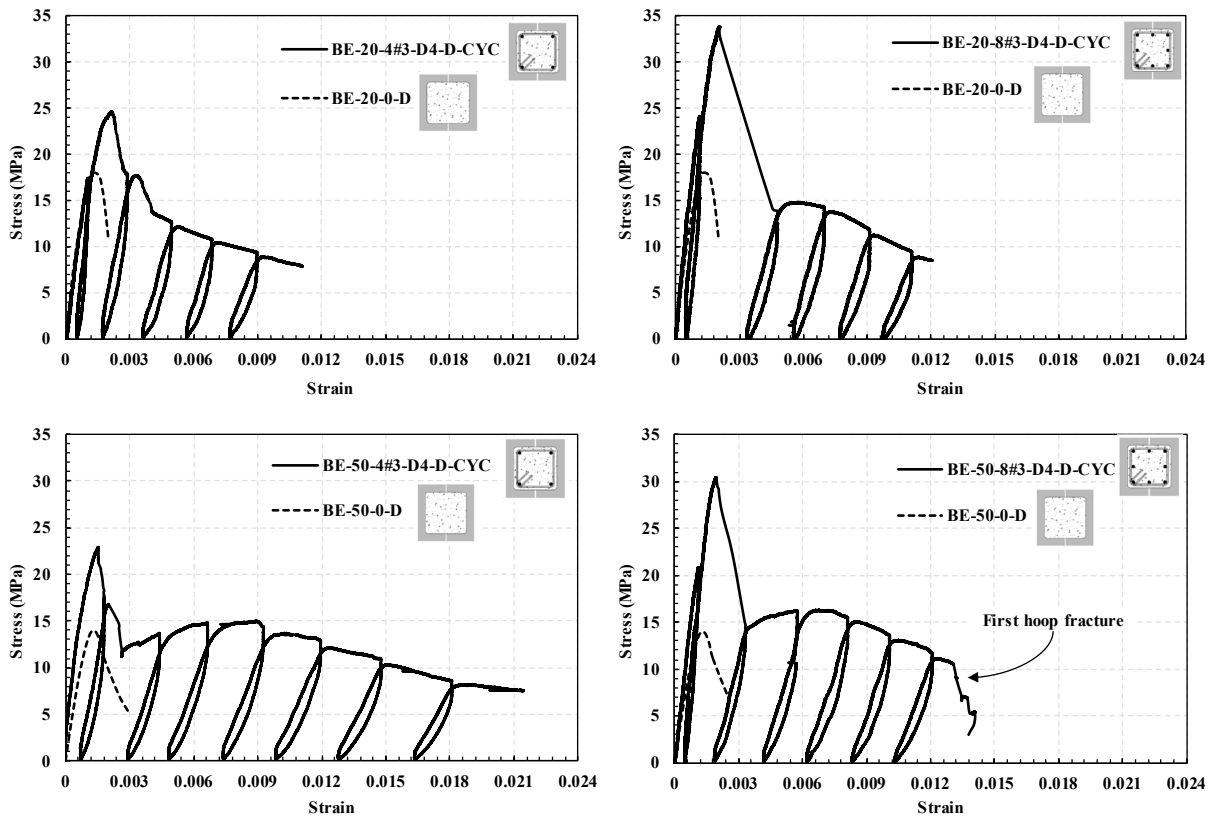
Figure 5.8 Effect of vertical reinforcement ratio on the cyclic stress-strain curves of RMBEs built with different grout strengths

Table 5.5 Test results of RMBEs tested under axial cyclic compression

Group number	BE Identifier	Test	Peak stress (MPa)		Strain at peak stress, $\varepsilon_{m\text{-}max}$		Strain at 50% of the peak stress, ε_{50}		Strain ductility, $\mu_{\varepsilon 50}$
			$f_{m\text{-}max}$	Average (COV%)	$\varepsilon_{m\text{-}max}$	Average (COV%)	ε_{50}	Average (COV%)	$\varepsilon_{50}/\varepsilon_{m\text{-}max}$
6	BE-20-4#3-D4-D-CYC-A	Cyclic	26.15	26.89 (10.14)	0.00182	0.00205 (9.90)	0.00395	0.00440 (11.65)	2.15
	BE-20-4#3-D4-D-CYC-B		29.91		0.00221		0.0043		
	BE-20-4#3-D4-D-CYC-C		24.61		0.00211		0.00496		
7	BE-20-8#3-D4-D-CYC-A	Cyclic	33.8	32.37 (14.53)	0.00203	0.00218 (9.28)	0.0044	0.00462 (27.04)	2.12
	BE-20-8#3-D4-D-CYC-B		36.2		0.0021		0.0035		
	BE-20-8#3-D4-D-CYC-C		27.12		0.00241		0.00597		
8	BE-50-4#3-D4-D-CYC-A	Cyclic	22.94	21.01 (12.99)	0.00225	0.00235 (5.73)	0.01448	0.01448	6.17
	BE-50-4#3-D4-D-CYC-B		19.08		0.00244		–		
9	BE-50-8#3-D4-D-CYC-A	Cyclic	33.43	29.82 (13.25)	0.00224	0.00201 (10.18)	0.00945	0.00959 (16.47)	4.78
	BE-50-8#3-D4-D-CYC-B		25.6		0.00186		0.01124		
	BE-50-8#3-D4-D-CYC-C		30.44		0.00192		0.00809		
10	BE-50-4#3-D4/30-D-CYC-A	Cyclic	23.58	23.03 (3.38)	0.00171	0.00171 (0.41)	0.02332	0.02347 (0.87)	13.76
	BE-50-4#3-D4/30-D-CYC-B		22.48		0.0017		0.02361		
11	BE-50-4#3-D8-D-CYC-A	Cyclic	28.33	24.65 (14.67)	0.00173	0.00180 (3.69)	0.01584	0.01801 (17.01)	9.98
	BE-50-4#3-D8-D-CYC-B		21.1		0.00186		–		
	BE-50-4#3-D8-D-CYC-C		24.53		0.00182		0.02017		
12	BE-20-4#3-D4-W- A-CYC	Cyclic	29.96	30.155 (0.91)	0.00215	0.00229 (8.36)	0.0037	0.00361 (3.53)	1.58
	BE-20-4#3-D4-W- B-CYC		30.35		0.00242		0.00352		
13	BE-50-4#3-D4-W- A-CYC	Cyclic	25.43	26.65 (6.47)	0.00197	0.00191 (4.83)	0.00815	0.00669 (30.86)	3.51
	BE-50-4#3-D4-W- B-CYC		27.87		0.00184		0.00523		
14	BE-50-6#3-D4-D-CYC-A	Cyclic	22.12	21.70 (3.50)	0.00224	0.00191 (16.02)	0.0171	0.01765 (26.37)	9.26
	BE-50-6#3-D4-D-CYC-B		22.15		0.00184		0.01329		
	BE-50-6#3-D4-D-CYC-C		20.82		0.00164		0.02255		
15	BE-50-12#3-D4-D-CYC-A	Cyclic	31.72	30.57 (3.45)	0.00192	0.00198 (6.79)	0.01642	0.01732 (9.38)	8.76
	BE-50-12#3-D4-D-CYC-B		30.33		0.00188		0.01635		
	BE-50-12#3-D4-D-CYC-C		29.65		0.00213		0.0192		

For the same above-mentioned groups of specimens, $\mu_{\varepsilon_{50}}$ decreased by 1.3%, 25.7%, and 5.4%, respectively, when ρ_v increased from 0.79% to 1.57%. Stress-strain curves of tested RMBEs showed that RMBEs with higher ρ_v exhibited slightly steeper post-peak falling branch than those with lower ρ_v. This behaviour can be attributed to the premature buckling of extra vertical reinforcement in the former compared to the latter. This buckling was attained sooner for RMBEs with higher ρ_v due to the absence of additional confinement hoops that could have been restrained the additional reinforcement against buckling. However, stress-strain cyclic curves showed that rectangular RMBEs with higher ρ_v dissipated more energy through cyclic loops. This can be attributed to the additional axial deformations of vertical steel and the higher post-peak stresses. This behaviour was noticed at most strain levels up to a strain of 0.02 mm/mm. Aly and Galal (2020) reported similar observations for RMSW+BEs with higher concentrated reinforcement at walls boundary elements.

Figure 5.9 shows the stress-strain cyclic curves of RMBEs with different confinement configurations. Two changes of confinement configurations were investigated: the spacing of hoops (i.e., D4 at 45 mm versus D4 at 30 mm) and the diameter of confinement hoops (i.e., D4 at 45 mm versus D8 at 45 mm). Increasing the confinement ratio (ρ_h) led to a minimal increase in the peak stress and a substantial boost in the strain ductility of tested RMBEs. As the confinement ratio (ρ_h) increased from 1.84% (D4 hoops at 45 mm) to 2.76% (D4 hoops at 30 mm) and 3.74% (D8 hoops at 45 mm), the strain ductility ($\mu_{\varepsilon_{50}}$) witnessed an increase of 114% and 55%, respectively. Stress-strain cyclic behaviour of the above-mentioned groups of specimens illustrate the improvement of the post-peak behaviour of RMBEs with higher ρ_h. Moreover, RMBEs constructed with D8 confinement hoops and D4 hoops spaced at 30 mm showed flatter falling branches compared to RMBEs with D4 hoops spaced 45 mm, as shown in Figure 5.9. Although RMBEs confined with D4 hoops at 30mm had a confinement ratio (2.76%) lower than RMBEs with D8 hoops at 45 mm (3.74%), the former showed enhanced post-peak behaviour than the latter. This enhancement is attributed to enhancing the effective confined core area in case of reducing the confinement hoops spacing rather than increasing their diameters. Similar observations were reported for RC columns with different confinement arrangements tested by Mander et al. (Mander

et al. 1988b). Cyclic loops of RMBEs with higher ρ_h were greater than those of RMBEs built with lower ρ_h indicating more energy dissipations and higher ductility for the former.
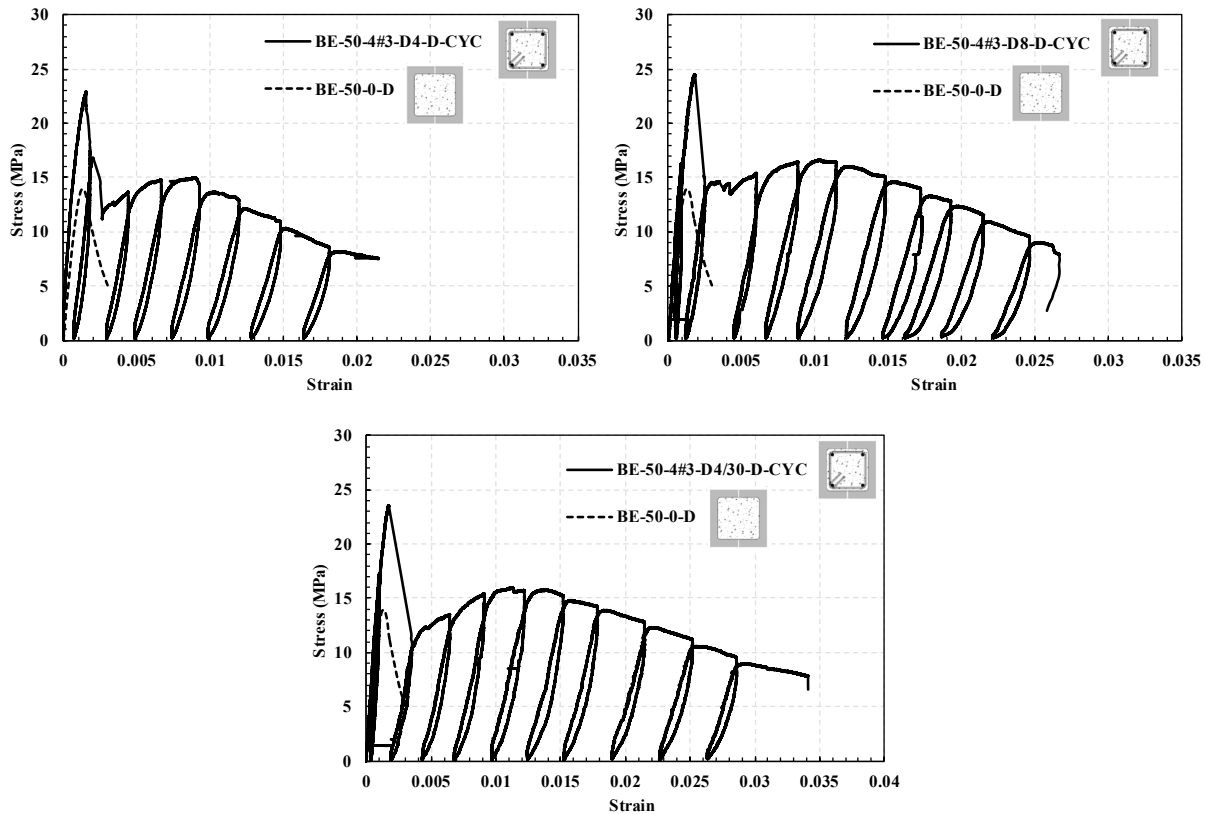
Figure 5.9 Effect of transverse confinement steel ratio on the cyclic stress-strain curves of tested RMBEs

Rectangular RMBEs showed enhanced cyclic behaviour than their square counterparts. Figure 5.10 shows stress-strain cyclic responses of RMBEs constructed with square (R_{BE} = 1.0) and rectangular (R_{BE} = 1.53) RMBEs. Changing the rectangular ratio (R_{BE}) had an insignificant effect on the peak stress of RMBEs. However, RMBEs constructed with rectangular sections showed much less stress drop at peak stress than those built with square sections, as can be seen from Figure 5.10. This lower stress drop can be attributed to reducing the face shell to the overall sectional area ratio of rectangular sections (39.7%) compared to their square counterparts (45.7%). Besides, as the rectangularity ratio (R_{BE}) increased from 1.0 to 1.53, the displacement ductility ($\mu_{\varepsilon_{50}}$) increased by 43.7% and 83%, for RMBEs with ρ_v of 0.79% and 1.57%, respectively. RMBEs with rectangular sections showed bulgier cyclic loops compared to those with square sections due to the enhancement of the post-peak behaviour of the former than the latter.
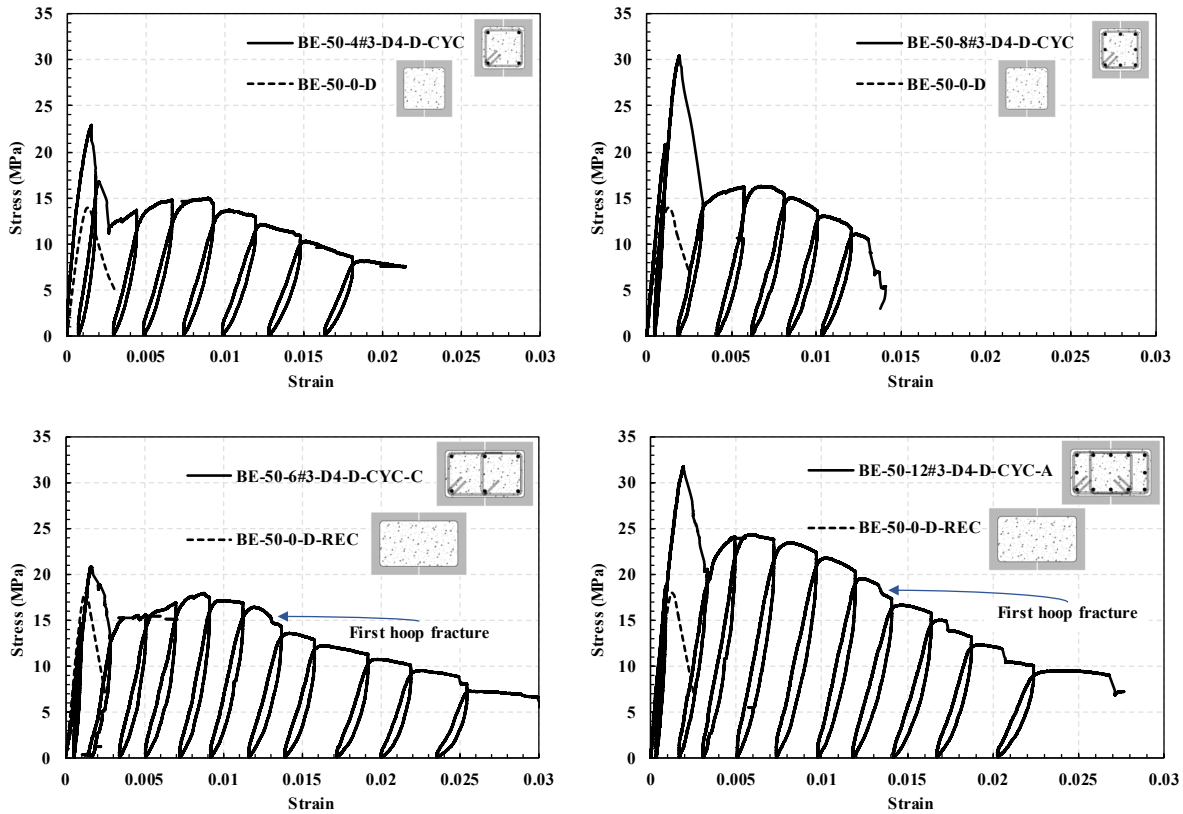
Figure 5.10 Experimental cyclic stress-strain curves of square and rectangular RMBEs having different vertical reinforcement ratios

Figure 5.8 presented the stress-strain cyclic curves of RMBEs constructed with different grout compressive strengths (i.e., 20 MPa versus 50 MPa). Increasing the grout compressive strength from 20 MPa to 50 MPa decreased the peak stress by 14.6% and 7.6% for RMBEs built with 4-#3 and 8-#3 vertical steel, respectively. This reduction can be attributed to the excessive absorption of the high strength 50 MPa grout's water content by the surrounding dry masonry blocks associated with its low water-to-cement (W/C) ratio of 0.5. This absorption resulted in plastic and drying shrinkage of the grout core resulting in a lesser contribution from the grout core to the axial load capacity of tested RMBEs. Nevertheless, the highly flowable 20 MPa grout with a high W/C ratio of 0.8 allowed the dry masonry blocks to absorb the additional water content (i.e., W/C of 0.8 versus 0.5), resulting in increased grout strength contribution to the axial compression capacity of tested RMBEs with 20 MPa grout.

On the other hand, RMBEs with higher grout strength of 50 MPa showed much more enhanced strain ductilities and post-peak behaviours than those constructed with 20 MPa grout, as

shown in Fig 8 and Table 5.5. The strain ductility increased by 200% and 125% as the grout compressive strength increased from 20 MPa to 50 MPa, for RMBEs constructed with 4-#3 and 8-#3 vertical steel, respectively. Although RMBEs grouted with 20 MPa grout strength showed slightly higher peak stresses, they showed much worse post-peak behaviour and less ductility than those constructed with 50 MPa grout. Since RMBEs are intended to be used with RMSW+BEs where ductility is a critical demand, it is not recommended to use low grout compressive strength in walls′ masonry boundary elements due to its dramatically low strain ductility levels. Instead, combining high-strength non-shrink flowable grout with high strength masonry blocks can be the optimum solution for achieving high strength and ductility levels for walls′ boundary elements, as previously recommended by AbdelRahman and Galal (2020).

Pre-wetting of dry masonry shell before grouting enhanced the peak stress and reduced the strain ductility of the tested RMBEs. Also, it enhanced the unreinforced MBEs prisms′ strength significantly. Figure 5.11 shows the stress-strain curves of the tested dry and pre-wetted RMBEs. Pre-wetting of dry masonry shell resulted in an increase of 12% and 16% in the peak compressive stress (f_{m-max}) for RMBEs constructed with 20 MPa and 50 MPa grout, respectively. However, the strain ductility ($\mu_{\varepsilon 50}$) dropped by 26.5% and 45% for wet RMBEs with 20 MPa and 50 MPa grout strength, respectively, compared to their dry counterparts. Dry RMBEs grouted with 20 MPa grout showed similar post-peak behaviour to their wet counterparts. However, this was not the case for RMBEs built with 50 MPa grout, where dry RMBEs with low masonry prism strength showed enhanced post-peak behaviour compared to wet RMBEs with high masonry prism strength. These results confirm RC columns′ results tested by Cusson and Paultre (1994), where columns with high strength concrete showed less ductility and toughness than those constructed with normal strength concrete.

Although pre-wetting is a proposed construction procedure to enhance the masonry compressive strength of fully grouted RMBEs, it negatively affected the studied RMBEs′ strain ductility. Since this study investigated one pre-wetting scheme versus a limited confinement configuration and grout strengths, further experimental research is required to quantify its influence and confirm its applicability on half-scale and full-scale RMBEs and RMSW+BEs constructed with different longitudinal steel arrangements, various confinement configurations, different section geometries, and multiple grout strengths.

132
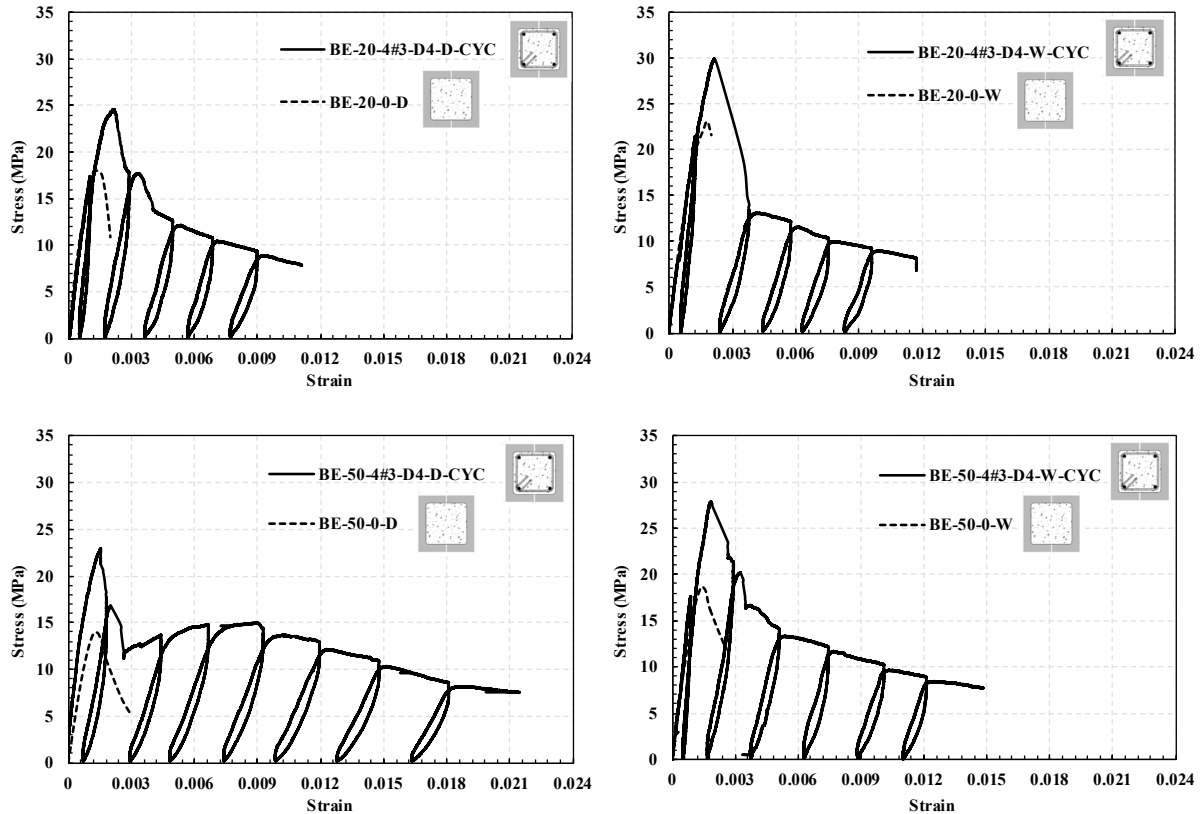
Figure 5.11 Effect of pre-wetting on the cyclic stress-strain curves of tested RMBEs built with different grout strengths

5.7 Comparison of The Envelope and Cyclic Stress-Strain Curves

The RMBEs that were tested under monotonic axial compression and reported in (AbdelRahman and Galal 2020) are used to compare their results with those tested under axial cyclic compression in this study. Table 5.6 shows the results of the RMBEs tested monotonically by (AbdelRahman and Galal 2020). Monotonic and cyclic stress-strain curves of selected specimens are compared. As previously defined by Karsan and Jirsa (1969) and Yankelevsky and Reinhardt (1987), it should be remembered that envelope curves refer to stress-strain curves that are obtained from the monotonic tests conducted on specimens′ companions to those tested under cyclic loading. Figure 5.12 shows the comparisons of monotonic (envelope) and cyclic stress-strain curves of tested RMBEs. Test results show that the envelope and cyclic curves are comparable. In general, most of the cyclically tested RMBEs stress-strain curves were approximately tangent to their counterparts′ envelope curves, as shown in stress-strain curves of BE-50-8#3-D4-D-CYC and BE-50-12#3-D4-D-CYC. Besides, wet RMBEs constructed with 50

MPa grout showed a stress-strain cyclic response that did not exceed its envelope curve. On the other hand, the BE-50-6#3-D4-D-CYC cyclic stress-strain curves slightly passed their corresponding envelope curves. The constituent materials′ properties (i.e., C-shaped masonry blocks, grout patches, and mortar patches) might have contributed to the observed differences between the cyclic and envelope curves. These differences were previously explained by Karsan and Jirsa (1969), where changes in concrete properties between monotonically and cyclically tested specimens can significantly alter their stress-strain relationships. In general, RMBEs with different geometry and reinforcement configurations had their envelope curves in good agreement with their counterparts′ cyclic curves. Therefore, the monotonic curves of RMBEs can be utilized as the envelopes of their cyclic curves′ counterparts at different strain levels.
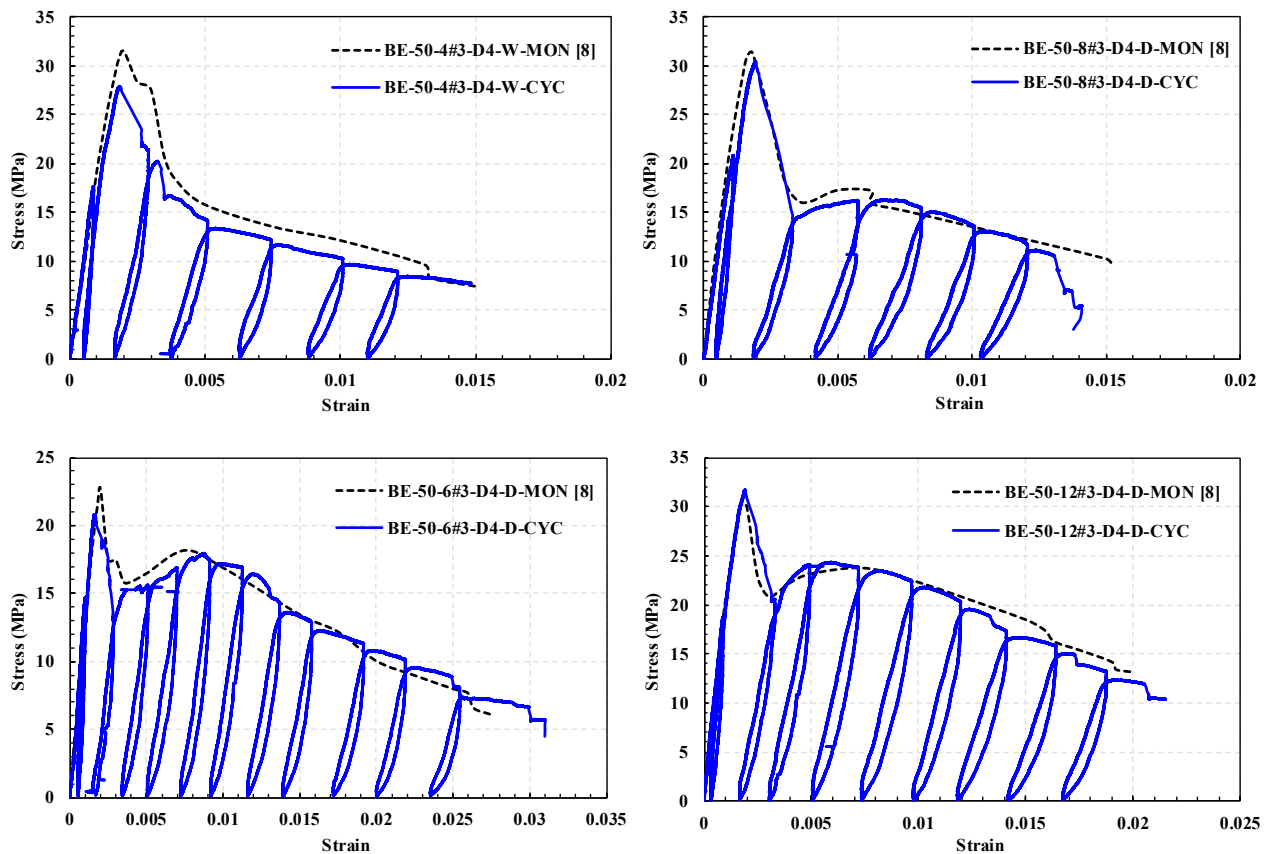
Figure 5.12 Comparison of experimental monotonic (envelope) and cyclic stress-strain curves of tested RMBEs

Table 5.6 Test results of RMBEs tested by AbdelRahman and Galal under axial monotonic compression

Group number	BE Identifier	Test	Peak stress (MPa) $f_{m\text{-}max}$	Average (COV%)	Strain at peak stress, $\varepsilon_{m\text{-}max}$	Average (COV%)	Strain at 50% of the peak stress, ε_{50}	Average (COV%)	Strain ductility, $\mu_{\varepsilon 50}$ $\varepsilon_{50}/\varepsilon_{m\text{-}max}$
16	BE-4#3-D4-D-MON-A*	Monotonic	20.84	22.46 (9.52)	0.00197	0.00189 (9.39)	0.01531	0.01541 (17.40)	8.14
	BE-4#3-D4-D-MON-B*		24.88		0.00169		0.01278		
	BE-4#3-D4-D-MON-C*		21.65		0.00202		0.01814		
17	BE-8#3-D4-D-MON-A*	Monotonic	31.56	26.92 (17.60)	0.00169	0.00183 (8.21)	0.00707	0.01206 (38.11)	6.58
	BE-8#3-D4-D-MON-B*		22.09		0.00199		0.01300		
	BE-8#3-D4-D-MON-C*		27.1		0.00182		0.01612		
18	BE-4#3-D8-D-MON-A*	Monotonic	18.42	20.52 (11.48)	0.00166	0.00175 (8.25)	0.02553	0.01872 (32.57)	10.68
	BE-4#3-D8-D-MON-B*		23.07		0.00192		0.01686		
	BE-4#3-D8-D-MON-C*		20.08		0.00168		0.01377		
19	BE-8#3-D8-D-MON-A*	Monotonic	29.54	29.78 (3.30)	0.00201	0.00190 (4.97)	0.01455	0.01444 (1.34)	7.59
	BE-8#3-D8-D-MON-B*		30.86		0.00187		0.01422		
	BE-8#3-D8-D-MON-C*		28.94		0.00183		0.01456		
20	BE-6#3-D4-D-MON-A*	Monotonic	23.03	22.90 (7.51)	0.00210	0.00172 (19.27)	0.01829	0.01581 (14.43)	9.19
	BE-6#3-D4-D-MON-B*		21.12		0.00149		0.0138		
	BE-6#3-D4-D-MON-C*		24.55		0.00157		0.01534		
21	BE-12#3-D4-D-MON-A*	Monotonic	24.95	28.09 (10.25)	0.00149	0.00164 (7.93)	0.01904	0.01768 (7.18)	10.78
	BE-12#3-D4-D-MON-B*		30.61		0.00172		0.01746		
	BE-12#3-D4-D-MON-C*		28.7		0.00171		0.01653		

*Tested by AbdelRahman and Galal

5.8 Proposed Stress-Strain Model for Monotonic (Envelope) Behaviour of RMBEs

5.8.1 Model concept

Unlike RC concrete members, fully grouted RMBEs have a significant portion of their cross-sections left with no confinement. This is due to the limited geometry of the concrete-masonry units, construction tolerance, and the grout cover to the confined core. Unconfined masonry accounts for almost ~45-60% of the overall cross-sectional area of RMBEs. Therefore, this unconfined part challenges the development of a stress-strain model to predict the envelope curve of RMBEs reliably. Therefore, the present model's concept is based on the summation of the axial loads of the RMBEs components, namely, unconfined masonry (i.e., masonry face shell and grout cover), confined masonry core, and vertical steel. These components contribute to the overall stress-strain state based on its respective area to the overall sectional area, as shown in Figure 5.13.
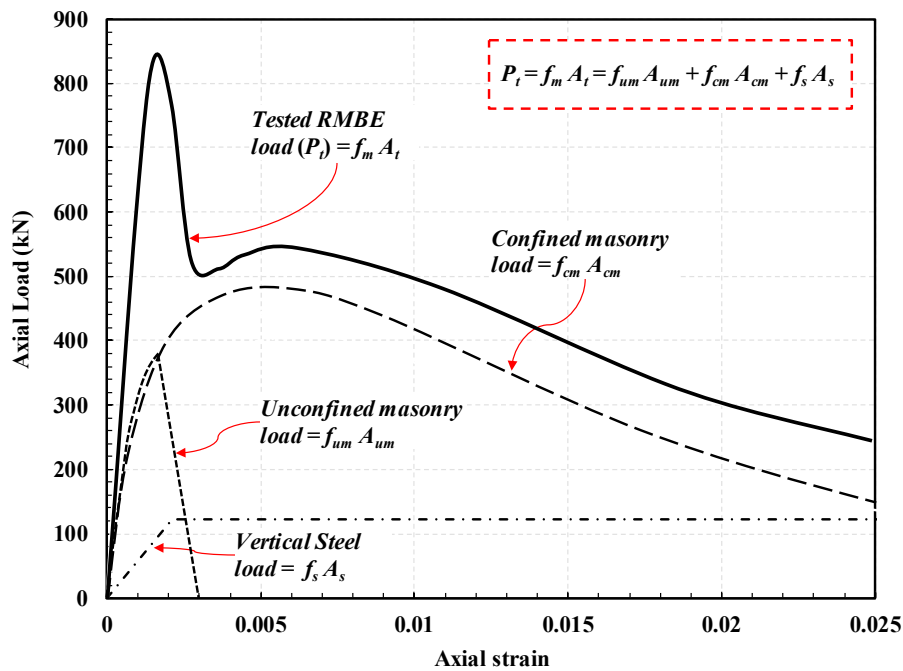
Figure 5.13 Axial monotonic load-strain curves of unconfined masonry, confined masonry core, vertical steel, and tested RMBEs

So, the stress at any point on the stress-strain envelope of RMBEs can be obtained from the following equations (Eq.):

$$f_m = \frac{P_t}{A_t} \tag{5.1}$$

$$P_t = f_{um}A_{um} + f_{cm}A_{cm} + f_sA_s \tag{5.2}$$

where f_m is the masonry compressive stress at given masonry strain; P_t is the total axial compression resisted by the RMBEs section; A_t is the total cross-section area of RMBEs; f_{um} is the unconfined masonry stress; A_{um} is the unconfined masonry area; f_{cm} is the confined masonry stress; A_{cm} is the confined core area; f_s is the vertical steel stress; and A_s is the vertical steel area. To get the stress f_m at a given strain ε_m, the unconfined masonry stress, the confined core stress, and the reinforcement stress should be known. Figure 5.13 shows the individual load-strain relationships of RMBE's components that are utilized to get the envelope curve of the RMBEs.

5.8.2 Model formulation and calibration

In the present model, the stress-strain curves for unconfined masonry and confined masonry were developed. As explained earlier, the failure of unconfined masonry causes a pronounced drop in the stress-strain response of RMBEs estimated by ~45-50% of their peak compressive stress. Before attaining the masonry peak stress ($f_{m\text{-}max}$), it is clear that unconfined masonry and confined masonry core have similar stresses. The vertical steel stress (f_s) is calculated based on the corresponding masonry strain multiplied by the steel modulus of elasticity (E_s), as shown in Figure 5.13. It is assumed that the compatibility of strains between the unconfined masonry, the confined masonry core, and the vertical reinforcement is valid and applicable along the predicted stress-strain curves. The present model is based on a procedure similar to that used by Mander et al. (1988a) for their confined concrete model but modified such that it is suitable for unconfined and confined fully grouted masonry. Figure 5.14 shows the proposed monotonic stress-strain curves for unconfined masonry and confined masonry core.

a) Before the confined masonry's peak stress

As shown in Figure 5.14, up to the peak stress of unconfined masonry (f'_{um}), the unconfined masonry and confined masonry core stresses are given by the following equation that was previously proposed by Popovics (Popovics 1973) and adopted by Mander et al. (Mander et al. 1988a) for confined concrete:

$$f_{um} = f_{cm} = \frac{f_{cm-max} \; x \; r}{r - 1 + x^r} \qquad (5.3)$$

where $f_{cm\text{-}max}$ is the peak stress of confined masonry core; x is the ratio between a given masonry strain (ε_m) and the strain at the confined masonry peak stress ($\varepsilon_{cm\text{-}max}$) and is calculated by the following Eq.:

$$x = \frac{\varepsilon_m}{\varepsilon_{cm-max}} \tag{5.4}$$

where ε_{cm-max} is given by the following equation:

$$\varepsilon_{cm-max} = \varepsilon_{mo} \left[1 + 5 \left(\frac{f_{cm-max}}{f'_{um}} - 1\right)\right] \tag{5.5}$$

where f'_{um} and ε_{mo} are the unconfined masonry peak stress and its corresponding strain, respectively. It should be noted that based on the compression tests conducted on unconfined MBEs prisms of a height-to-thickness ratio of 5 tested by Obaidat et al. (2018), by the authors paper (AbdelRahman and Galal 2020), and in this study, ε_{mo} typically ranged between 0.0015 to 0.002.

$$r = \frac{E_m}{E_m - E_{sec}} \tag{5.6}$$

where r is the factor guiding the stress-strain rising curve of the confined masonry core; and E_m is the masonry modulus of elasticity, which can be calculated by the following equation:

$$E_m = 5000 \sqrt{f'_{um}} \tag{5.7}$$
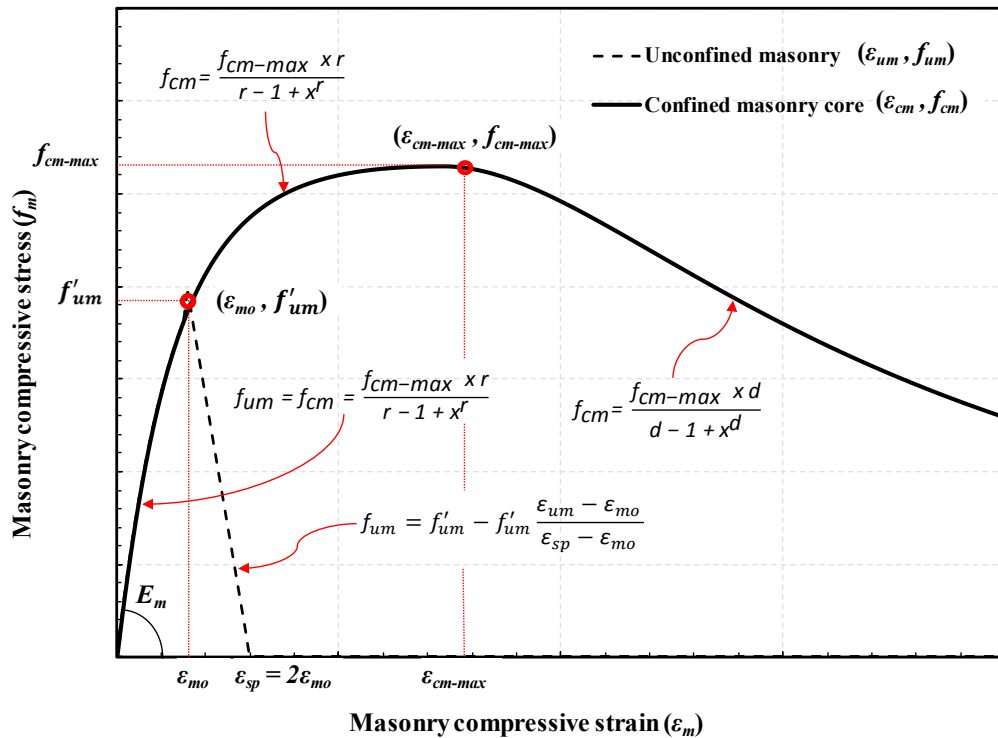
Figure 5.14 Proposed monotonic (envelope) stress-strain model for unconfined masonry and confined masonry core

where E_{sec} is the secant modulus of the confined core at peak stress and given by

$$E_{sec} = \frac{f_{cm-max}}{\varepsilon_{cm-max}} \tag{5.8}$$

where f_{cm-max} is calculated by

$$f_{cm-max} = -1.254 + 2.254 \sqrt{1 + \frac{7.94\, f_l'}{f_{um}'}} - 2\frac{f_l'}{f_{um}'} \tag{5.9}$$

For square RMBEs, the effective lateral confining stress (f_l') is calculated by the following equation:

$$f_l' = \frac{1}{2}\, k_e\, \rho_h\, f_{yh} \tag{5.10}$$

where ρ_h is the volumetric ratio of confinement steel to the confined masonry core; f_{yh} is the yield strength of the transverse confinement steel; and k_e is the confinement factor, which is defined by the following equation:

$$k_e = \frac{(1 - \sum_{i=1}^{n} \frac{(w_i')^2}{6 b_c d_c})(1 - \frac{s'}{2 b_c})(1 - \frac{s'}{2 d_c})}{(1 - \rho_{cc})} \tag{5.11}$$

where w_i' is the ith clear distance between adjacent vertical steel bars; ρ_{cc} is the ratio of vertical steel to the confined core area; s' is the clear vertical spacing between adjacent confinement hoops; b_c and d_c are the confined masonry core dimensions measured between centerlines of confinement hoops in x and y directions, respectively, where $b_c \geq d_c$.

It should be noted that for rectangular RMBEs, the confinement factor k_e is calculated based on the effective lateral confining stresses in x and y directions calculated by

$$f_{lx} = \rho_x\, f_{yh} \tag{5.12}$$
$$f_{ly} = \rho_y\, f_{yh} \tag{5.13}$$

where ρ_x and ρ_y = the volumetric ratio of confinement hoops to the confined core in x and y directions, respectively. Based on the values of f_{lx} and f_{ly}, the k_e can be obtained from figure 4 illustrated elsewhere by Mander et al. (1988a).

As shown in Figure 5.14, after attaining the peak stress of unconfined masonry (f_{um}'), the unconfined masonry is assumed to have a linear falling branch reaching zero stress at the spalling strain (ε_{sp}). It is noteworthy that the spalling strain (ε_{sp}) is assumed to be as twice as the unconfined masonry strain (ε_{mo}) at peak stress (f_{um}'), and is defined by

$$\varepsilon_{sp} = 2\, \varepsilon_{mo} \tag{5.14}$$

The linear falling branch of the unconfined masonry is defined by

$$f_{um} = f'_{um} - f'_{um} \frac{\varepsilon_{um} - \varepsilon_{mo}}{\varepsilon_{sp} - \varepsilon_{mo}} \tag{5.15}$$

where ε_{um} is the unconfined masonry strain at given unconfined masonry stress (f_{um}).

b) After the confined masonry's peak stress

Upon attaining the unconfined masonry peak stress, the confined masonry core will not be affected by the unconfined masonry failure and will continue gaining more strength due to the enhancement introduced by the confinement hoops, as illustrated in Figure 5.14. It is noteworthy that Eq. 5.3 is still valid up to the confined core peak stress ($f_{cm\text{-}max}$) and its corresponding strain (ε_{cm-max}).

Mander et al. (1988a) utilized the parameter r to guide both the rising and falling branches of the stress-strain curves of confined concrete, which was found to be not suitable for confined masonry in this study. Comparisons of the predicted stress-strain response of confined masonry core by the Mander et al. model with the experimental results revealed that using the same parameter r for the falling branches resulted in highly overestimated confined core stresses than those obtained from the experimental tests of 52 confined masonry boundary elements. Therefore, the falling branch of the confined masonry core will be controlled by the new proposed parameter d, which replaces the parameter r in Mander et al. model, and guides the strength degradation of the confined masonry core. The following equation defines the parameter d as follows:

$$d = exp\ (0.00977f_p - 0.47375R_{BE} + 0.01936\rho_h + 0.38801\rho_v + 0.9217) \tag{5.16}$$

where f_p is the compressive strength of a MBE prism with a height-to-thickness ratio of 5; R_{BE} is the rectangularity ratio of the tested RMBEs (R_{BE}= 1.0 for square RMBEs and 1.53 for the 190x290 mm rectangular RMBEs); ρ_h is the volumetric ratio of confinement steel; and ρ_v is the vertical steel ratio to the RMBE area. It should be noted that Eq. 5.16 is calibrated based on a regression analysis of the experimental results described by the authors in (AbdelRahman and Galal 2020) to best fit the tested RMBEs. The stress-strain curves of the confined masonry cores were established to get the values of the stress-strain descending branch guiding parameter d. The confined masonry core stress was obtained by subtracting the axial compression loads carried by the vertical steel and the unconfined masonry and then divided by the confined core area, as illustrated in Fig 13. So, if d is the parameter guiding the stress-strain falling branch, Eq. 5.3 can be reformulated as follows:

$$f_{cm} = \frac{f_{cm-max} \; x \; d}{d - 1 + x^d}$$

(5.17)

Equation 17 is used only for the confined masonry core after attaining its peak stress (f_{cm-max}) at its corresponding strain ε_{cm-max}.

5.8.3 Comparison of the model and experimental results

Figure 5.15 shows the stress-strain curves predicted by the present model and those obtained from the experimental investigations of axial monotonic compression tests on RMBEs reported in (AbdelRahman and Galal 2020). The proposed model was able to predict the stress-strain curves of the confined and unconfined masonry. It was observed that there is good agreement between the predicted stress-strain responses and those of the experimental results. The proposed model was compared with the results of RMBEs constructed with different transverse confinement ratios, vertical reinforcement ratios, prism strengths, and section geometry (i.e., square versus rectangular).
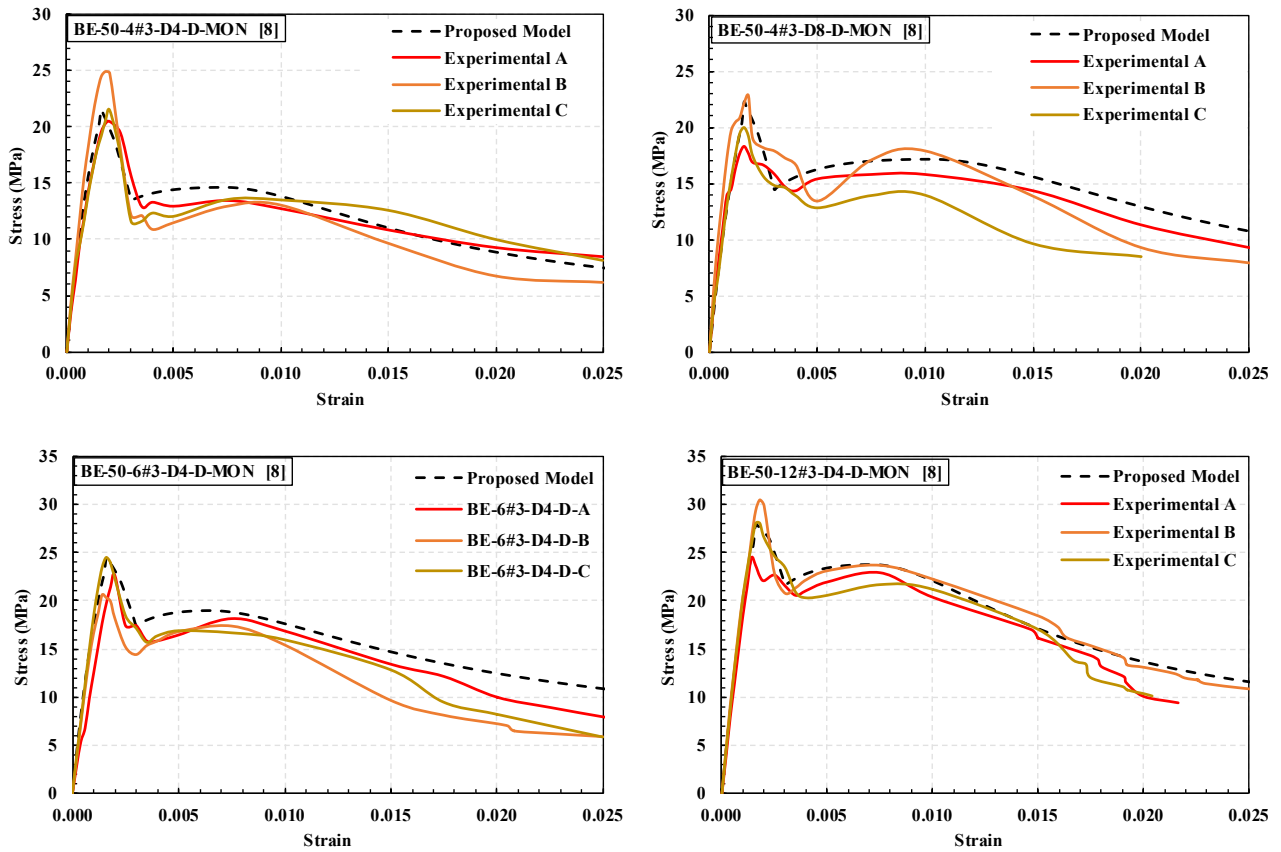
Figure 5.15 Comparison of experimental monotonic stress-strain curves of tested RMBEs and proposed model

Table 5.7 shows the percentage of difference between the proposed model and experimental results of RMBEs that were tested under either monotonic or cyclic axial compression loading. The model showed excellent agreement with the experimental rising branch of the stress-strain curves up to the peak stress and good agreement with the stress drop corresponding to the unconfined masonry's failure (i.e., at face shell spalling). Moreover, the model could predict the second peak stress observed in the experimental stress-strain curves due to the confinement hoops' enhancement to the confined masonry core; this observation was not captured by previous stress-strain models proposed for confined masonry. Furthermore, introducing the stress-strain descending branch parameter d resulted in well-captured strength degradation following the second peak stress.

Table 5.7 Percentage of difference between the proposed model and experimental results

	difference %		
BE Identifier	$f_{m\text{-}max}$	$\varepsilon_{m\text{-}max}$	ε_{50}
BE-4#3-D4-D-MON-A	3.07	-23.13	1.23
BE-4#3-D4-D-MON-B	-15.72	-5.63	17.55
BE-4#3-D4-D-MON-C	-0.70	-26.25	-17.03
BE-4#3-D8-D-MON-A	17.03	-3.75	-6.38
BE-4#3-D8-D-MON-B	-3.92	-20.00	29.75
BE-4#3-D8-D-MON-C	9.55	-5.00	-
BE-6#3-D4-D-MON-A	5.61	-31.25	11.64
BE-6#3-D4-D-MON-B	13.44	6.88	-
BE-6#3-D4-D-MON-C	-0.61	1.88	25.89
BE-12#3-D4-D-MON-A	10.57	6.88	1.86
BE-12#3-D4-D-MON-B	-9.71	-7.50	10.00
BE-12#3-D4-D-MON-C	-2.87	-6.87	14.79
BE-50-4#3-D4-D-CYC-A	-6.60	3.13	3.47
BE-50-8#3-D4-D-CYC-B	-3.23	-16.25	13.54
BE-50-8#3-D4-D-CYC-C	-22.74	-20.00	-
BE-50-4#3-D8-D-CYC-B	4.95	-16.25	-
BE-50-4#3-D8-D-CYC-C	-10.50	-13.75	8.32
BE-50-12#3-D4-D-CYC-A	-13.69	-20.00	15.36
BE-50-12#3-D4-D-CYC-B	-8.71	-17.50	15.72
BE-50-12#3-D4-D-CYC-C	-6.27	-33.13	1.03

5.9 Proposed Stress-Strain Model for Cyclic Behaviour of RMBEs

As mentioned earlier and illustrated in Figure 5.12, comparisons of the monotonic and cyclic experimental curves of confined RMBEs revealed that the monotonic curves form envelope (skeleton) curves to their cyclic counterparts. Therefore, the proposed model of the monotonic stress-strain curve is utilized to predict the cyclic behaviour of confined RMBEs. Many researchers (e.g., Karsan and Jirsa 1969, Sinha et al. 1964) confirmed similar findings in their concrete models. Based on these assumptions, the following sections present the proposed model equations for the cyclic response of RMBEs under axial compression. The methodology used in the present model is based on the existing Mander et al. (1988a) model for confined concrete, but with modifications and refinements such that they adapt to unconfined and confined concrete-masonry. It should be noted that, as mentioned earlier, RMBEs built with low strength grout of 20 MPa or those built with wet masonry shells showed dramatically low strain ductility levels and steeper post-peak behaviour compared to RMBEs constructed with 50 MPa grout or dry masonry shells, respectively. This reduction in the ductility is not recommended for RMBEs or RMSW+BEs designed for high ductility demand. Therefore, the results of these RMBEs were omitted from the calibration of the proposed axial cyclic model.

5.9.1 Unloading branches

Figure 5.16 shows the proposed axial cyclic compression model of confined masonry. For unloading from the monotonic compression curve, a plastic (residual) strain (ε_p) based on the coordinates of the reversal (unloading) point (ε_{un}, f_{un}) shall be computed. This strain (ε_p) is located at the intersection of the unloading secant modulus with the horizontal strain axis, as shown in Fig 16. It depends on the initial masonry modulus of elasticity (E_m) and the unloading secant modulus.

A common strain point, ε_a, corresponding to the intersection of the initial tangent and unloading secant slopes is defined by

$$\varepsilon_a = a \sqrt{\varepsilon_{un} \, \varepsilon_{cm-max}} \tag{5.18}$$
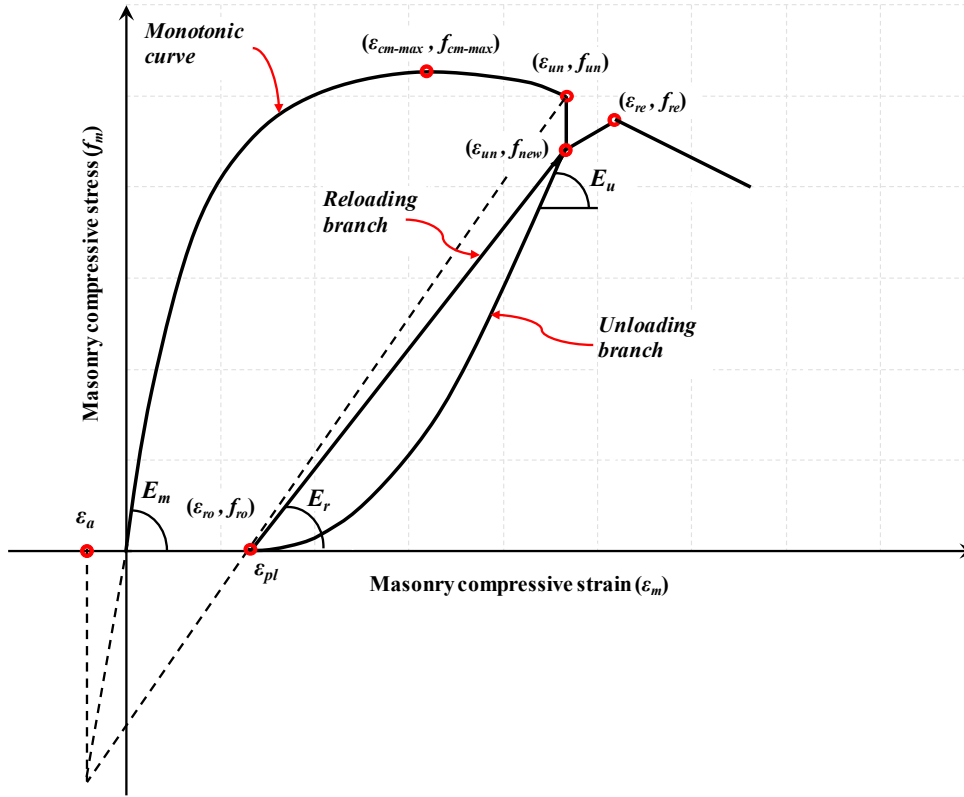
Figure 5.16 Proposed cyclic stress-strain model for confined masonry

The proposed equations by Mander et al. (1988a) for the parameter *a* were found not suitable for confined masonry because they underestimated the plastic strains, ε_p. Therefore, the value of *a* is replaced by the following equations:

$$a = \frac{\varepsilon_{un}}{0.8\, \varepsilon_{cm-max}} \qquad for \qquad \varepsilon_{un} \leq \varepsilon_{cm\text{-}max} \tag{5.19}$$

$$a = \frac{\varepsilon_{cm-max}}{0.8\, \varepsilon_{un}} \qquad for \qquad \varepsilon_{un} > \varepsilon_{cm\text{-}max} \tag{5.20}$$

Then, the plastic strain ε_p is defined by

$$\varepsilon_{pl} = \varepsilon_{un} - \frac{(\varepsilon_{un} + \varepsilon_a)\, f_{un}}{(f_{un} + E_m\, \varepsilon_a)} \tag{5.21}$$

From the experimental observations of the tested RMBEs, it is assumed that the unloading curve passes through a vertical straight line connecting the point of unloading (ε_{un}, f_{un}) and the point of degrading strength ($\varepsilon_{un}, f_{new}$), as previously explained by Yankelevsky and Reinhardt (1987) in their cyclic model for concrete. This assumption was found reasonable and applicable in all tested RMBEs under axial cyclic compression in this study.

Following the point of strength degradation $(\varepsilon_{un}, f_{new})$, the unloading curve is then defined by a modified form of Eq. 5.3 based on the unloading stress (f_{un}) as follows:

$$f_m = f_{un} - \frac{f_{un} \, y \, s}{s - 1 + y^s} \tag{5.22}$$

$$y = \frac{\varepsilon_m - \varepsilon_{un}}{\varepsilon_{pl} - \varepsilon_{un}} \tag{5.23}$$

where s is a parameter guiding the unloading curve and given by

$$s = \frac{E_u}{E_u - E_{sec-un}} \tag{5.24}$$

In which E_{sec-un} is the unloading secant modulus that is given by

$$E_{sec-un} = \frac{f_{un}}{\varepsilon_{un} - \varepsilon_{pl}} \tag{5.25}$$

where E_u is the tangent modulus of elasticity to the unloading curve at the point of strength degradation $(\varepsilon_{un}, f_{new})$ and given by

$$E_u = bcE_m \tag{5.26}$$

$$b = \frac{f_{un}}{f'_{um}} \geq 1 \tag{5.27}$$

Mander et al. (1988a) proposed an equation for the coefficient c based on trial and error to best fit their RC experimental results. However, their equation was found not applicable to confined masonry after attaining its peak stress (f_{cm-max}). Thus, the coefficient c is replaced by

$$c = \left(\frac{\varepsilon_{cm-max}}{\varepsilon_{un}}\right)^{0.5} \geq 1 \tag{5.28}$$

5.9.2 Reloading branches

Figure 5.16 describes the stress-strain curves for unloading and reloading branches in which the coordinates of the point of reloading are $(\varepsilon_{ro}, f_{ro})$. Reloading can occur from zero stress, which indicates that $\varepsilon_{ro} = \varepsilon_{pl}$ or from a general stress point where reloading starts at $(\varepsilon_{ro}, f_{ro})$. Due to the cyclic degradation of RMBEs, the new stress point (f_{new}) is assumed to be located on the curve of common points. According to Karsan and Jirsa (1969) and Sinha et al. (Sinha et al. 1964b), the curve of common points is the locus of the intersection of the unloading and reloading branches of the same cycle where the new stress points (f_{new}) are located. It is also assumed that a straight line is fitted between the reloading point $(\varepsilon_{ro}, f_{ro})$ and the point of strength degradation $(\varepsilon_{un}, f_{new})$. The new stress point (f_{new}) is assumed to be given by the following equation:

$$f_{new} = 0.88 f_{un} + 0.08 f_{ro} \tag{5.29}$$

On the straight line between the reloading point $(\varepsilon_{ro}, f_{ro})$ and the point of strength degradation $(\varepsilon_{un}, f_{new})$, the masonry stress is calculated by:

$$f_m = f_{ro} + E_r \left(\varepsilon_m - \varepsilon_{ro} \right) \tag{5.30}$$

where E_r is the reloading branch slope and given by

$$E_r = \frac{f_{ro} - f_{new}}{\varepsilon_{ro} - \varepsilon_{un}} \tag{5.31}$$

Afterwards, a straight line is fitted between the point of strength degradation $(\varepsilon_{un}, f_{new})$ and the common return point on the envelope stress-strain curve $(\varepsilon_{re}, f_{re})$, as shown in Figure 5.16. It should be noted that the Mander et al. model used a different equation for (ε_{re}) which was found highly underestimating the return strains for tested RMBEs. Therefore, ε_{re} is replaced by

$$\varepsilon_{re} = \varepsilon_{un} + \frac{f_{un} - f_{new}}{E_r \left(\frac{f'_{um}}{f_{cm-max}} \right)} \tag{5.32}$$

The return stress (f_{re}) on the envelope stress-strain curve can be computed from Eq. 5.3 or Eq. 5.17 for the confined masonry core's ascending curve and descending branch, respectively.

5.9.3 Comparison of the proposed cyclic model and experimental results

Figure 5.17 shows sample comparisons of the predicted stress-strain cyclic behaviour by the proposed model and the experimental curves of tested RMBEs (see Table 5.7). In this comparison, the proposed cyclic model exhibited a good-to-excellent agreement with the experimental curves. Selected RMBEs specimens of BE-50-4#3-D4-D-CYC, BE-50-4#3-D8-D-CYC, BE-50-8#3-D4-D-CYC, and BE-50-12#3-D4-D-CYC groups were utilized to validate the proposed model. From Figure 5.17, it is apparent that the unloading curves were well-captured by the proposed model. Moreover, the model was able to capture softening of the unloading branches that increased with increasing the unloading strain (ε_{un}). Besides, the plastic strains (ε_{pl}) were captured within a very reasonable range, mostly when unloading occurs from the envelope curve after the confined masonry peak stress. Furthermore, reloading branches and the new stress points due to cyclic degradation were well-captured. It should be noted that the reduction of the steel's modulus of elasticity (E_s) due to cyclic loading was calculated based on the equation proposed by Dodd and Restrepo-Posada (1995), where they proposed a constitutive model to predict the cyclic response of reinforcing steel. The summation of the unconfined masonry, confined masonry core, and corresponding vertical steel axial loads at any given strain level resulted in well-captured stress-strain cyclic curves of the tested RMBEs.
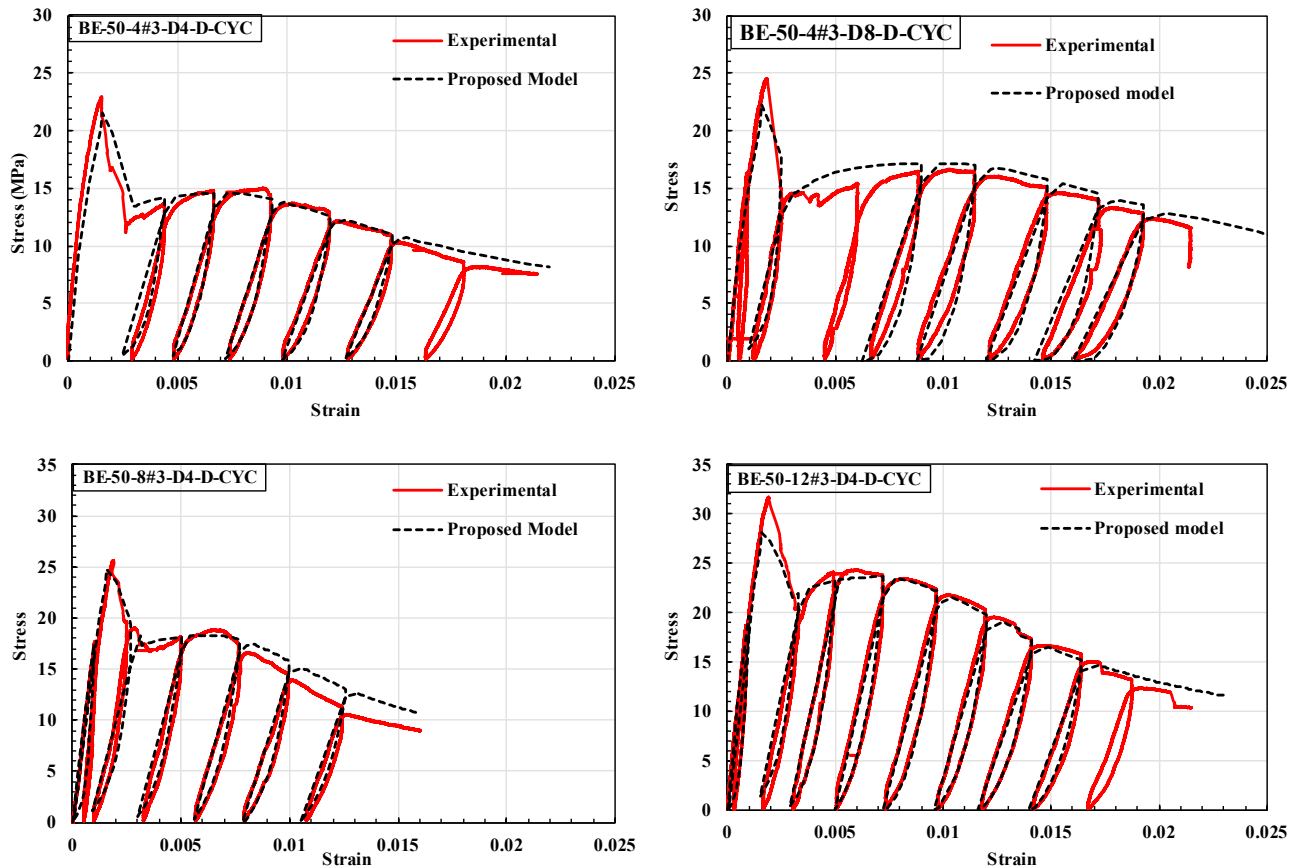
Figure 5.17 Comparison of experimental cyclic stress-strain curves of tested RMBEs and proposed model

5.10   Conclusions

Comprehensive research on the monotonic and cyclic axial compressive behaviour of unconfined and confined concrete-masonry boundary elements was conducted. These boundary elements form the end-confined zones of RMSW+BEs. Therefore, it was crucial to have experimental data of unconfined and confined RMBEs to predict the seismic behaviour of RMSW+BEs. Besides, the seismic design of RMSW+BEs necessitates reliable stress-strain models (i.e., monotonic and cyclic) of confined masonry to adequately estimate the available ductility from the confined masonry cores at the wall toes.

In this study, the axial cyclic compressive behaviour of RMBEs built with square and rectangular sections, different vertical steel arrangements, various confinement configurations, and different grout strengths were studied. Moreover, starting from an existing model for confined concrete, using the experimental results of this study and the results reported in (AbdelRahman

and Galal 2020), stress-strain models for the axial monotonic and cyclic compressive behaviour of confined RMBEs were proposed. Based on this study, the following conclusions were drawn:

1. Fully grouted RMBEs experienced a significant drop in the stress-strain curve due to face shell spalling at peak stress (i.e., unconfined masonry failure). Unlike RC members, RMBEs′ unconfined part accounts for ~45-60% of the overall cross-section area of the RMBEs. However, the confined masonry core was found to have peak stress higher than that of the unconfined part due to the confinement hoops′ strength enhancement.

2. The cyclic response of fully grouted RMBEs showed that increasing the unloading strain increased the expected residual strains, resulted in steeper unloading branches, reduced the reloading branches′ stiffness, and yielded bulgier cyclic loops due to accumulated damage.

3. Increasing the vertical reinforcement ratio of RMBEs resulted in a significant increase in their axial load carrying capacity; however, it reduced the strain ductility at 50% strength degradation and led to a steeper post-peak behaviour.

4. Improvement of the transverse steel confinement ratio resulted in an insignificant increase in the RMBEs peak stress but yielded surprising enhancements in their strain ductilities.

5. Reduction of confinement hoops′ spacing introduced more effective confinement than increasing the confinement hoops size, although the former's confinement ratio was less than the latter.

6. Rectangular RMBEs showed comparable peak stresses, enhanced cyclic responses, less stress drop at peak stresses, and enhanced post-peak behaviours compared to their square counterparts.

7. Although RMBEs built with 20 MPa grout strength showed higher peak stresses than those constructed with 50 MPa grout, they exhibited much lower strain ductility and steeper post-peak behaviour. Therefore, such low grout strengths are not recommended for masonry boundary elements incorporated in RMSW+BEs designed for high ductility demand.

8. Pre-wetting of dry masonry shells before grouting led to enhanced peak stresses in tested wet RMBEs; however, their strain ductility was considerably less than those constructed with dry masonry shells. Due to its negative effect on the tested RMBEs′ strain ductility, pre-wetting of ductile RMSW+BEs can not be suggested unless further detailed experimental results of different pre-wetting schemes of RMBEs and RMSW+BEs with different sections and confinement configurations are available to confirm its applicability.

148

9. From an existing confined concrete model, monotonic and cyclic axial compressive models were proposed for unconfined and confined concrete-masonry boundary elements. These models were found to give good-to-excellent agreement with the experimental results of monotonic and cyclic tested RMBEs. The models were able to capture most characteristics of the envelope and cyclic behaviour of RMBEs, namely, rising curve up to the peak stress, stress drop at peak stress, second peak stress due to confinement enhancement, post-peak behaviour, unloading and reloading branches, residual strains, and cyclic degradation.

10. More research efforts towards the behaviour of RMBEs with different geometry, construction procedures, and reinforcement configurations are still encouraged. The proposed models are open for any enhancement that contributes to the state-of-the-art and further enhances the available tools incorporated with numerical analysis software to properly simulate and predict the cyclic behaviour of RMSWs built with masonry boundary elements.

Chapter 6

Sensitivity of the Seismic Response of Fully Grouted Reinforced Masonry Shear Walls with Boundary Elements to its Design Parameters

6.1 Abstract

Seismic design of concrete-masonry structures built with reinforced masonry shear walls with boundary elements (RMSW+BEs) depends on the walls′ configurations (i.e., geometry) as well as the corresponding design parameters (e.g., masonry compressive strength, and vertical reinforcement ratio of boundary elements, etc.). This paper aims at investigating, numerically, the sensitivity of the nonlinear seismic response of RMSW+BEs having different wall configurations against critical design parameters in order to better facilitate the optimization of the seismic design of RMSW+BEs buildings. In this study, four wall configurations, namely, the wall's aspect ratio, the level of the axial stress, the masonry boundary element (MBE) size, and the wall's length were investigated. Moreover, four design parameters, namely, the masonry maximum compressive strength, the masonry strain at peak stress, the masonry modulus of elasticity, and the MBE vertical reinforcement ratio were studied. These combinations yielded valuable data accumulated from the nonlinear behaviour of one-hundred and thirty-five (135) RMSW+BEs. The results showed that as the wall's aspect ratio and the level of the axial compressive stress increase, the displacement ductility decreases. In addition, increasing the walls MBE size as well as the wall length resulted in an increase in the wall's ultimate lateral capacity and the displacement ductility. It was found that the walls′ lateral yield capacity and lateral ultimate capacity are highly sensitive to the change of the vertical reinforcement ratio of the MBEs compared to the other design parameters. RMSW+BEs displacement ductility was highly sensitive to the change of the masonry strain at peak stress when compared to their design parameter counterparts. The lateral effective stiffness of the walls is greatly influenced by the change of the vertical reinforcement ratio of the MBE as well as the masonry modulus of elasticity. This study shed light on identifying the most critical design parameters and configurations and quantifying their influence on the seismic design of RMSW+BEs.

6.2 Introduction and Background

Reinforced concrete-masonry shear walls (RMSWs) have been widely used in construction of many North American buildings. However, planar (i.e., rectangular) reinforced masonry shear walls were found to have stability, capacity, and ductility limitations due to the restricted arrangement of one row of vertical reinforcement rebars with no confinement due to the available configuration of the concrete masonry blocks. As such, introducing a confined concrete masonry core (i.e., masonry boundary element, MBE) to the outermost ends of a rectangular shear wall enhances the stability and ductility of the RMSWs. This boundary element (BE) allows placing a steel cage of at least 4 reinforcing steel bars confined with hoops to be incorporated at the wall extremities. This contributes to alleviating the buckling of the vertical reinforcement bars in the compression zone at high displacement levels and enhancing the stability of the RMSWs. Moreover, increasing the confinement within the boundary elements decreases the depth of the compression zone of the shear walls at the ultimate state which in turn enhances the inelastic strain capacity of the shear wall and enhance the curvature ductility leading to an overall enhanced response of the RMSWs. Therefore, reinforced masonry shear walls with boundary elements (RMSW+BEs) can be deemed as a robust, yet ductile, seismic force resisting system which was found to achieve higher ductility levels with no sudden loss of strength compared to their planar counterparts. Furthermore, this allows RMSW+BEs to meet the requirements of the high inelastic curvature demands while design of structural walls shall satisfy design codes provisions of the compression zone depth (c)–to–wall length (l_w) ratio. Therefore, there is a need to investigate, numerically, the most critical design parameters affecting the seismic performance of such walls in order to facilitate for the design engineer to optimize the design of concrete-masonry buildings having RMSW+BEs in moderate and high seismicity zones. The literature showed that structural masonry walls with boundary elements exhibited ductile seismic response. However, compared to the available literature and the number of studies that were conducted on rectangular RMSWs, there is a limited number of studies were performed on the seismic behaviour of RMSW+BEs to date. Moreover, limited numerical studies were conducted to investigate the seismic performance and collapse capacity of RMSW+BEs. These studies focused on some parameters that influence the seismic behaviour of RMSW+BE such as the level of the axial compressive stress, the vertical reinforcement in the boundary element, the wall's aspect ratio, and the confinement level in the wall's boundary elements. Shedid et al. (2010) tested seven RMSWs under displacement-control

151

quasi-static cyclic loading. Rectangular walls, walls with flanges, and end confined walls were investigated. The researchers reported that significant energy dissipation levels were associated with the inelastic response of the flanged walls and walls with boundary elements. Moreover, high ductility levels were achieved with minimal strength degradations compared to their rectangular counterparts. Banting and El-Dakhakhni (2014) investigated, experimentally, the seismic performance of five RMSW+BEs subjected to quasi-static reversed cyclic loading. The researchers studied two parameters, namely, the wall aspect ratio and the vertical reinforcement ratio on the seismic response of these walls. Three different aspect ratios were investigated, namely, 1.5, 2.15, and 3.23 and two vertical reinforcement ratios were studied, namely, 0.69% and 1.17%. It was inferred that increasing the wall's aspect ratio resulted in an increase in the plastic hinge length and a reduction in the lateral capacity of the masonry shear walls. Moreover, increasing the vertical reinforcement ratio of the walls resulted in an increase in the lateral capacity and the top drift, a significant drop in the displacement ductility, and a slight decrease in the curvature ductility of the tested walls. Hamzeh et al. (2018) developed fragility curves for RMSW+BEs based on a numerical study of the seismic response of thirty-six RMSW+BEs. The researchers investigated the influence of the level of the axial compressive stress, the vertical reinforcement ratio, and the aspect ratio ranging from 1.5 to 3.75 on the seismic response of RMSW+BEs. It was observed that decreasing the level of the axial compressive stress, the vertical reinforcement ratio, and the aspect ratio resulted in a significant enhancement in the displacement ductility. Nevertheless, increasing the axial compressive stress and the vertical reinforcement ratio, and decreasing the aspect ratio of the walls led to an increase in the lateral capacity of the studied walls. The seismic performance of ductile reinforced masonry shear wall buildings was investigated by Aly and Galal (2019). In their numerical study, they investigated the seismic response and the collapse capacity of six archetype buildings having height limits exceeding those stipulated in the NBCC (2015) in two different seismicity regions (i.e., moderate and high). The studied buildings were found to have a collapse probability within the acceptance limits of the FEMA P695 (2009). In their findings, the researchers reported that the addition of the boundary elements to the wall toes using high strength C-shaped pilaster blocks combined with high strength grout greatly enhanced the overall system ductility and the seismic behaviour. Moreover, the researchers recommended 70 m and 50 m height limits to the buildings in the moderate and high seismicity regions, respectively. Aly and Galal (2020a, b) studied, experimentally, the influence of different design parameters on the lateral non-

linear cyclic response of RMSW+BEs. They investigated the effect of the boundary element configurations (i.e., C-shaped vs stretcher blocks), the vertical reinforcement lap splice at the plastic hinge region, the shear span-to-depth ratio of the walls, the vertical reinforcement ratio in the MBEs, and the MBE size (i.e., 190x190mm and 190x290mm) on the seismic performance of RMSW+BEs. The test results showed that using C-shaped MBE blocks enhanced the constructability and the seismic performance of the RMSW+BEs. Moreover, the lap splice of the vertical reinforcement at the plastic hinge region was found to enhance the initial lateral stiffness of the walls and increase their strength and stiffness degradation rate. The shear span-to-depth ratio was found to have a significant influence on the lateral strength and stiffness as well as the non-linear behaviour of the walls. Increasing the vertical reinforcement ratio in the MBEs was found to greatly enhance the energy dissipation of the walls whereas increasing the MBE size enhanced the displacement ductility of the tested RMSW+BEs.

6.3 Research Significance

Based on the numerous studies performed on the reinforced masonry components (i.e., shear walls) or on the system level (i.e., multistory buildings), it can be inferred that RMSW+BE is still considered a point of interest where more studies, in-depth investigations, and quantifications are yet to come. The literature highlighted the possibility of the RMSW+BEs to be adopted as practical and efficient seismic force resisting systems that can be employed in moderate and high seismicity zones. The objective of this study is to facilitate the optimization of the seismic design of concrete-masonry buildings built using RMSW+BEs and enhance the overall seismic response of such buildings in a hazardous earthquake event. This will be achieved through determining the most significant design parameters affecting the seismic response components of the RMSW+BEs, namely, the wall's lateral ultimate capacity (Q_u), the wall's lateral yield capacity (Q_y), the effective elastic stiffness of the wall (K_{eff}), the wall's secant stiffness at 2.5% drift ($K_{2.5\%}$), and the wall's displacement ductility ($\mu_{\Delta 0.8Qu}$) in order to satisfy the code requirements and the ductility demands as well. This study focuses on investigating, numerically, the sensitivity of the seismic response of RMSW+BEs to the design parameters, namely, the masonry compressive strength (f'_m), the masonry compressive strain at peak stress (ε_{mu}), the masonry modulus of elasticity (E_m), and the vertical reinforcement ratio of the confined MBEs (ρ_{vBE}). Furthermore, the wall configurations, namely, the MBE cross-section configuration, the shear wall aspect ratio (AR) (i.e., changing both

153

length and height), and the level of the axial stress (*AS*) were also studied. The outcome of this numerical investigation provides significant data that helps better understanding and quantifying the most significant factors affecting the seismic design of RMSW+BEs buildings.

In this study, RMSWs with different boundary elements cross-sections (390x400, 390x600, 390x800 mm), different storey heights representing low, mid, and high-rise buildings (2, 5, and 8 storeys), different axial stresses (0.2 and 0.3 MPa/storey) were examined. These walls were studied to investigate the sensitivity of the seismic response of RMSW+BEs to the change of ±30% as upper and lower bounds of the design parameters f'_m, ε_{mu}, E_m, and ρ_{vBE}. A 2D macro-modelling approach is utilized to predict the non-linear seismic response of the RMSW+BEs using SeismoStruct software (2018). The numerical model is well-calibrated using the material and geometrical models and is validated using available experimental data of RMSWs in the literature. The RMSW+BEs were modeled and analyzed using static time history non-linear analysis to predict the seismic performance of the walls. Quantification of the seismic response is conducted in terms of the RMSW+BEs lateral yield capacity (Q_y), lateral ultimate capacity (Q_u), effective elastic stiffness (K_{eff}), secant stiffness at 2.5% drift ($K_{2.5\%}$), and displacement ductility at 20% strength degradation ($\mu_{\Delta0.8Qu}$). Comparisons of the walls′ backbone curves as well as tornado charts showing the influence of the previously mentioned design parameters on the seismic response of RMSW+BEs having different heights, configurations, and axial stresses are reported.

6.4 Test Matrix and Details of the RMSW+BEs

One-hundred and thirty-five fully grouted full-scale RMSW+BEs were modeled using SeismoStruct (2018). Table 6.1 describes the details of the fifteen reference RMSW+BEs. The RMSW+BEs were designed according to the CSA S304-14 (2014) provisions. The test matrix was divided into five groups where each group consists of three main RMSW+BEs. The test matrix was carefully designed to investigate various design parameters and wall configurations affecting the seismic behaviour of RMSW+BEs. The four wall configurations, namely, the wall aspect ratio (*AR* = height-to-length ratio; h_w/l_w), the boundary element size, the level of the axial compressive stress, and the length of the wall were investigated. As can be seen in Table 6.1, there are three wall aspect ratios (*AR*) range between 1.66 and 6.65 were considered. Two axial stresses (*AS*) namely 0.2 and 0.3 MPa per storey were studied. The RMSW+BEs cross-sectional configurations and the reinforcement details are illustrated in Figure 6.1.

154
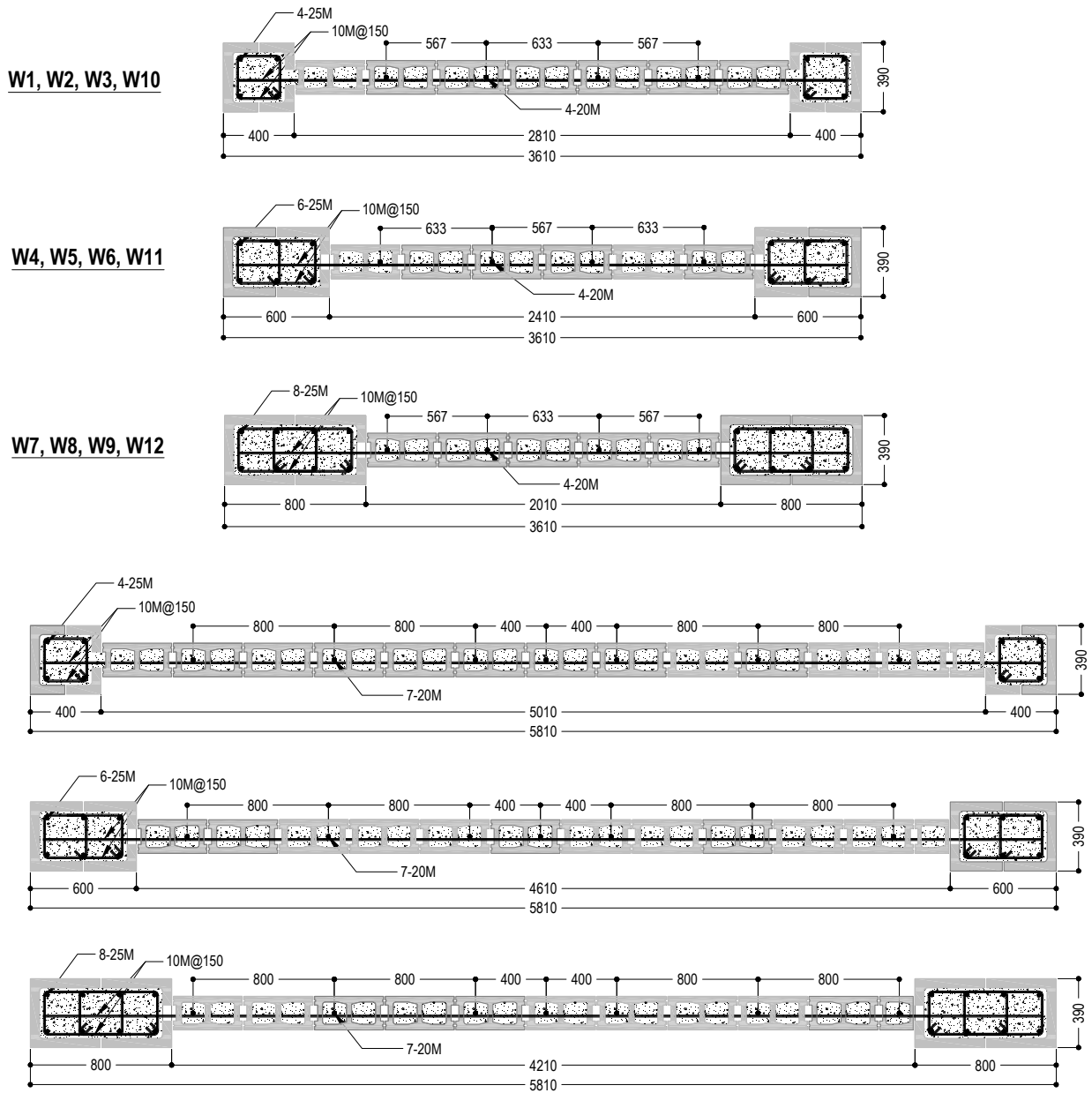
Figure 6.1 Details of studied reinforced masonry shear walls with boundary elements

155

Table 6.1 Test matrix of the studied reinforced masonry shear walls with boundary elements (RMSW+BEs)

| | | | | | | Masonry Boundary element (MBE) | | | | Web | | | |
| | | | | | | Vertical reinforcement | | Horizontal reinforcement | | Vertical reinforcement | | | |
Wall No.	Wall identifier	Length (mm)	Heigh t (m)	Aspect ratio	No. of storeys	Amount	$\rho_{v\,BE}$ (%)	Amount	MBE cross-section	Amount	ρ_v (%)	Axial stress per storey (MPa)	Total axial stress (MPa)
1	Sq-BE-Low	3610	6	1.66	2	4-25M	1.28	10M@150	390x400	4-20M	0.22	0.2	0.4
2	Sq-BE-Mid	3610	15	4.16	5	4-25M	1.28	10M@150	390x400	4-20M	0.22	0.2	1
3	Sq-BE-High	3610	24	6.65	8	4-25M	1.28	10M@150	390x400	4-20M	0.22	0.2	1.6
4	R1-BE-Low	3610	6	1.66	2	6-25M	1.28	10M@150	390x600	4-20M	0.26	0.2	0.4
5	R1-BE-Mid	3610	15	4.16	5	6-25M	1.28	10M@150	390x600	4-20M	0.26	0.2	1
6	R1-BE-High	3610	24	6.65	8	6-25M	1.28	10M@150	390x600	4-20M	0.26	0.2	1.6
7	R2-BE-Low	3610	6	1.66	2	8-25M	1.28	10M@150	390x800	4-20M	0.31	0.2	0.4
8	R2-BE-Mid	3610	15	4.16	5	8-25M	1.28	10M@150	390x800	4-20M	0.31	0.2	1
9	R2-BE-High	3610	24	6.65	8	8-25M	1.28	10M@150	390x800	4-20M	0.31	0.2	1.6
10	Sq-BE-High-AS2	3610	24	6.65	8	4-25M	1.28	10M@150	390x400	4-20M	0.22	0.3	2.4
11	R1-BE-High-AS2	3610	24	6.65	8	6-25M	1.28	10M@150	390x600	4-20M	0.26	0.3	2.4
12	R2-BE-High-AS2	3610	24	6.65	8	8-25M	1.28	10M@150	390x800	4-20M	0.31	0.3	2.4
13	Sq-BE-High-L2	5810	24	4.14	8	4-25M	1.28	10M@150	390x400	7-20M	0.22	0.2	1.6
14	R1-BE-High-L2	5810	24	4.14	8	6-25M	1.28	10M@150	390x600	7-20M	0.24	0.2	1.6
15	R2-BE-High-L2	5810	24	4.14	8	8-25M	1.28	10M@150	390x800	7-20M	0.26	0.2	1.6

Sq = Square boundary element with dimensions 390x400 mm

R1 = Rectangular boundary element with dimensions 390x600 mm

R2 = Rectangular boundary element with dimensions 390x800 mm

Three different MBE sizes were investigated, namely, 390x400 mm, 390x600 mm, and 390x800 mm in order to represent a wide range of cross-section configurations of the RMSW+BEs. Furthermore, two different wall lengths: 3610 mm and 5810 mm were investigated using the same wall height of 24000 mm to better correlate the results of the RMSW+BEs having the same aspect ratio, yet different wall lengths. Among the studied walls, three different numbers of storeys were considered: 2, 5, and 8 storeys. These numbers of storeys represent low-rise (2 storeys), medium-rise (5 storeys), and high-rise (8 storeys) masonry shear wall buildings. All the RMSW+BEs were designed using 25M vertical reinforcing steel bars (Area = 500 mm^2) in the MBEs with a constant ρ_{vBE} of 1.28% whereas 20M (Area = 300mm^2) rebars were used in the walls′ webs according to each group of walls. All the RMSW+BEs were detailed by 10M bars at a spacing of 150 mm as confinement hoops within the MBE cross-sectional area. Each wall was given an identification to facilitate the comparison between the RMSW+BEs based on the boundary element shape and size (i.e., square versus rectangular), the wall height (i.e., Low, Mid, High), the axial stress (AS), and the length of the wall (l_w). For example, the wall R1-BE-High-AS2 represents a reinforced masonry shear wall with 390x600 mm rectangular boundary elements with a total height of 24000 mm (8 storeys) where the axial stress AS2 is 0.3 MPa/storey.

6.5 Sensitivity Analysis

As shown in Figure 6.2, the four design parameters, namely, the masonry compressive strain at peak stress (ε_{mu}), the masonry modulus of elasticity (E_m), the masonry compressive strength (f'_m), and the MBE vertical reinforcement ratio (ρ_{vBE}) are utilized to develop the sensitivity analysis with upper and lower bounds of ±30% for each of the four abovementioned parameters in order to investigate their effect on the seismic behaviour of the studied RMSW+BEs. Each wall shown in Table 6.1 was modeled using ±30% of the reference design values f'_m, ε_{mu}, E_m, and ρ_{vBE}. Hence, each wall has 9 models: the reference wall (listed in Table 6.1), and 8 other walls that have 2 variations (± 30%) for the 4 studied design parameters f'_m, ε_{mu}, E_m, and ρ_{vBE}.

6.6 Nonlinear Numerical Modelling Approach

Recently, many researchers used different modelling approaches to better simulate the nonlinear behaviour of RMSWs. Various studies were performed on the numerical modelling of RMSWs using micro-modelling (e.g., Giambanco et al. 2001) where the main elements of the

RMSWs are modeled in detail (i.e., the masonry block, the mortar-masonry interface, the mortar joints, and the reinforcing bars). Therefore, the micro-modelling methodology (i.e., nonlinear Finite Element Modelling) is beneficial in capturing the local behaviour and failure of the masonry components (Ezzeldin et al. 2016). On the contrary, macro-modelling approach is the one that, recently, many researchers have adopted to facilitate the simulation of the non-linear seismic response of RMSWs using various software packages and their embedded tools such as that of the OpenSees (McKenna et al. 2000) or the SeismoStruct (2018) ones. Therefore, in the current study, a macro-modelling approach is adopted to simulate the seismic response of the RMSW+BEs using the available tools of the SeismoStruct (2018).
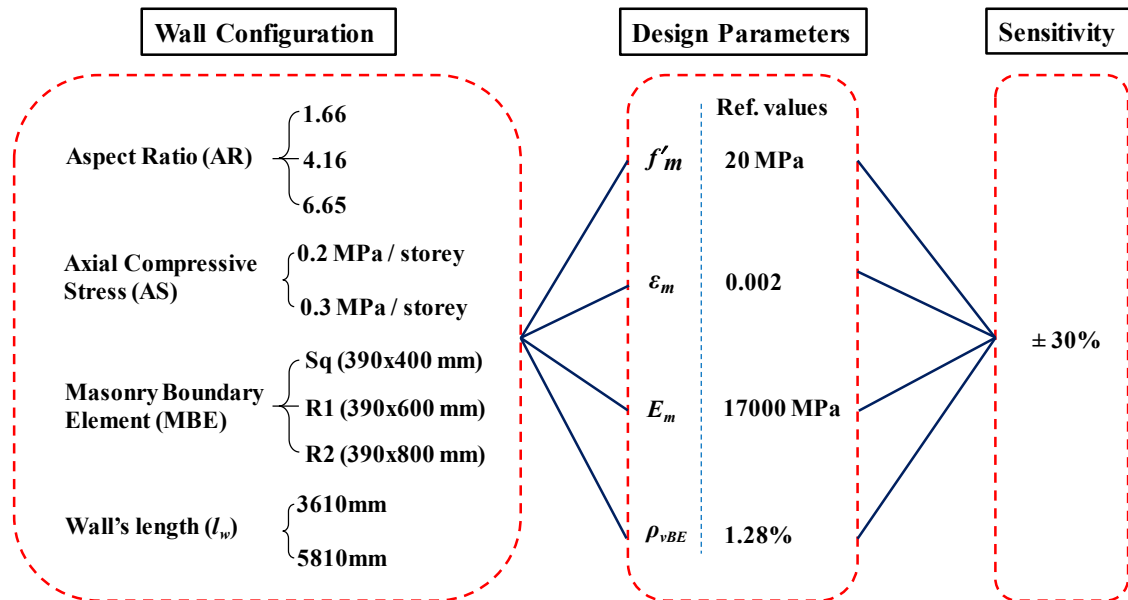
Figure 6.2 Details of the studied wall configurations and design parameters in RMSW+BEs

6.6.1 Geometrical, Element, and Section Models

Distributed inelasticity has been widely utilized in earthquake engineering and numerous studies (e.g., Ezzeldin et al. 2016, Hamzeh et al. 2018, Hosseinzadeh and Galal 2020, and Aly and Galal 2020c), in which the inelastic deformations are distributed over the element length and the reinforcement bars yielding is permitted at any integration section along the element length. In this paper, displacement-based beam-column fiber-elements with distributed plasticity were utilized to model the seismic performance of the RMSW+BEs. These elements are characterized by a constant axial strain and a linear curvature along the element length. Also, they are assigned fiber

sections where each section is discretized to a finite number of fibers. Each fiber is then given a uniaxial stress-strain relationship based on the assigned material model (i.e., unconfined masonry, confined masonry, or reinforcing steel bars). As such, the sectional stress-strain state and the moment-curvature relationship can be obtained by the integration of the individual fibers' nonlinear stress-strain responses. The displacement-based elements follow a standard finite-element approach, in which the element deformations are interpolated from an approximate displacement field that enforce constant axial strain and linear curvature along the element length. Due to the formulation nature of displacement-based beam-column elements and the assumption of linear curvature along their length, a proper selection of the number of elements per a structural member is required in order to capture the high order distributions of the non-linear deformations associated with the plastic hinge of the RMSW+BEs.

Since the response of the displacement-based beam-column elements is susceptible to the choice of the number of elements and the element length, especially the first element length where the plastic deformations are localized above the RMSWs fixed-base, previous researchers recommended that the first element length above the RMSWs base shall be chosen as multiples of the plastic hinge length in order to ensure precise results. Moreover, the interpolation from an approximate displacement field results in concentration of strains at the extreme integration point (i.e., the first integration point near the wall base) rather than the first element level (Calabrese et al. 2010). In SeismoStruct (2018), each element is assigned two integration sections. Therefore, the first element length is chosen to be as twice as the plastic hinge length, (i.e., $2l_p$), where each integration section accounts for one plastic hinge length (l_p). This regularization ensures that the strain localizations are concentrated at the integration section of the plastic hinge length and be accommodated within the numerical integration along the element. It should be noted that the plastic hinge length is calculated based on the equation that was suggested by Bohl and Adebar (2011). This equation accounts for the axial load effects and the moment-shear ratio of the walls.

Figure 6.3 illustrates the formulation of the geometrical model of the RMSW+BEs while Figure 6.4 presents the discretization of the fiber-section of the RMSW+BEs with the material models being used to calibrate the numerical model. SeismoStruct (2018) suggests using 4-5 elements per structural member to better predict and approximate the non-linear response of this member. In order to address the number of the elements, a sensitivity analysis is performed to

quantify the optimum number of elements required to simulate the seismic response of RMSW+BEs using four, six, and eight elements whilst the first element length is fixed at $2l_p$.
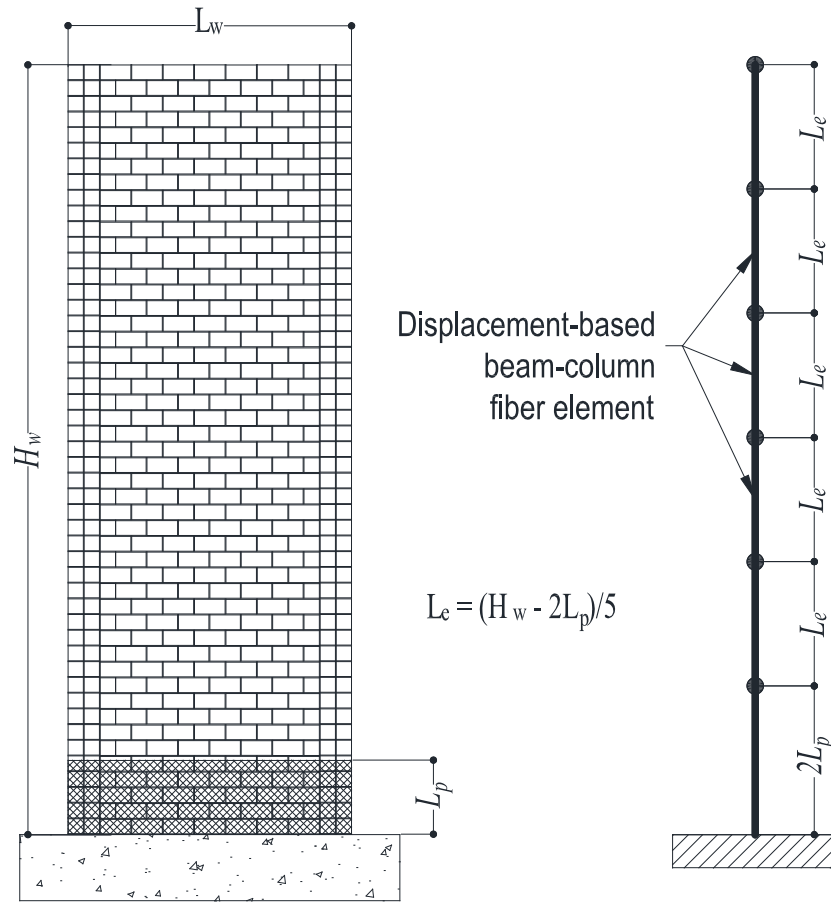

Figure 6.3 Schematic diagram of the numerical model
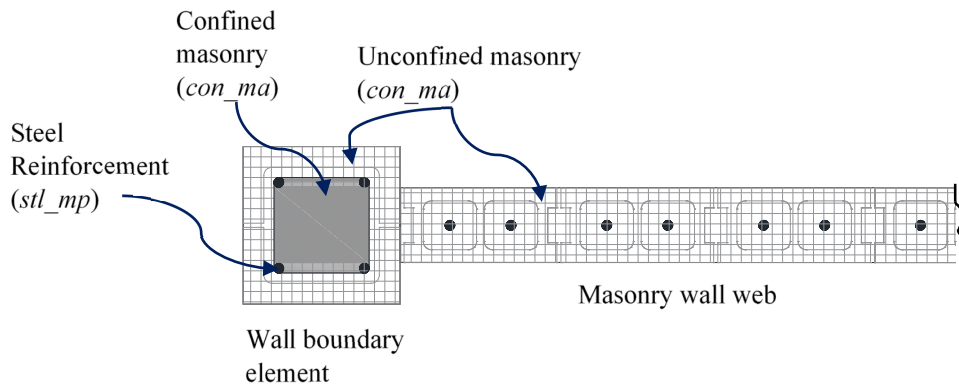
$$L_e = (H_W - 2L_p)/5$$

Figure 6.4 Cross-sectional material distribution and non-linear material model employed in the numerical model

The numerical model results were compared to the experimental results of wall W6 reported by Shedid et al. (2010) and showed no significant differences arose when using four, six, or eight elements per wall, as presented in Figure 6.5(a). However, it was observed that increasing the number of elements resulted in more strength degradation and less energy dissipation compared to the actual response of the validated walls. On the contrary, reducing the number of elements was found to overestimate the walls' lateral capacity, and the model could not approximate their nonlinear behaviour. Furthermore, it can be noticed from Figure 6.5(b) that reducing the first element length to l_p instead of $2l_p$ resulted in underestimating the capacity and the energy dissipation. It also led to very rapid strength and stiffness degradation, and the model couldn't capture the hysteretic behaviour at high drift levels (i.e., high deformations at the plastic hinge region) compared to the validated experimental walls. This can be attributed to the concentrated plastic deformation at only half of the first element length in the case of using the first element length equals to l_p. This results in a significant difference between the calculated and actual curvatures at the wall plastic hinge region. Therefore, the geometrical model formulation with the first element length of $2l_p$ and six elements per modelled wall is deemed accurate and effective in capturing the capacity, stiffness, and nonlinear behaviour of the RMSW+BEs.

A sensitivity analysis was performed to determine the optimum number of sectional fibers to better capture the overall section stress-strain state and the overall flexural response of the RMSW+BEs as these fibers are utilized at the integration sections of the element. As such, a sensitivity analysis for the number of fibers ranges between 200 and 700 is conducted and compared with wall W6 from Shedid et al. (2010) to evaluate the influence of the number of sectional fibers on the lateral load–displacement hysteretic behaviour of wall W6. Figure 6.5(c) shows that there was no significant difference observed when the number of the fibers increased from 200 to 700. However, the hysteretic behaviour of the wall having 700 fibers was found to average the hysteretic responses of the investigated walls and well approximate the non-linear response of wall W6, particularly in the post-peak behaviour. Based on this comparison, the number of the sectional fibers was opted to be 700 since this large number of fibers didn't substantially affect the analysis time of the RMSW+BEs. It is worth mentioning that although the fiber model cannot accurately capture the shear deformations, however, these shear deformations were found to be dramatically minimized with increasing the aspect ratio of the RMSW+BEs. In addition, experimentally tested RMSWs that were used for the validation of the numerical model

161

of this study were well-designed to fail in flexure (i.e., flexural dominated). This means that the shear strength of the walls is significantly greater than the ultimate flexural strength in order to offset the possibility of having undesired sudden shear failure which can be catastrophic in earthquake events. Furthermore, to minimize the influence of such a limitation in the fiber model on the seismic response of the studied RMSW+BEs, the test matrix of the RMSW+BE is carefully chosen such that all the walls have an aspect ratio greater than 1.5 and it varies from 1.66 to 6.65 to reduce the shear deformations with the increased aspect ratios.

6.6.2 Material Model

Since the adopted fiber modelling approach depend on the integration of the individual fiber's uniaxial stress-strain relationship to obtain the sectional overall stress-strain state, the material uniaxial stress-strain relationship that is assigned to the fibers play a vital role to enhance the simulation of the flexural response of RMSW+BEs. However, due to the scarcity of research work that was conducted to investigate the axial cyclic response of fully grouted concrete-masonry, there are no available constitutive models associated with most of the software utilized to predict the seismic response of RMSWs. As a result, the concrete-masonry material was simulated using the available concrete material model, *con_ma*, by Mander et al. (1988) adopted in SeismoStruct (2018). Recently, many researchers (e.g., Aly and Galal 2019; Ezzeldin et al. 2016; Hamzeh et al. 2018) have been utilizing the concrete material model by Mander et al. (1988) to simulate the nonlinear response of RMSW+BEs and archetype buildings. This can be attributed to the fact that the Mander et al. (1988) concrete model exhibited a reasonable accuracy while simulating the flexural seismic response of RMSW+BEs. Also, the fully grouted concrete-masonry material resembles its regular concrete counterpart in many aspects (i.e., cementitious materials constituents, aggregates, etc.). Furthermore, the RMSW+BEs are typically designed to be flexural dominated where they are provided with a well-confined grout core at the end zones of the walls to satisfy high ductility demands. Therefore, the unconfined masonry part (i.e., face shell) spalling has a minimal influence on the fully grouted RMSW+BEs lateral cyclic behaviour.
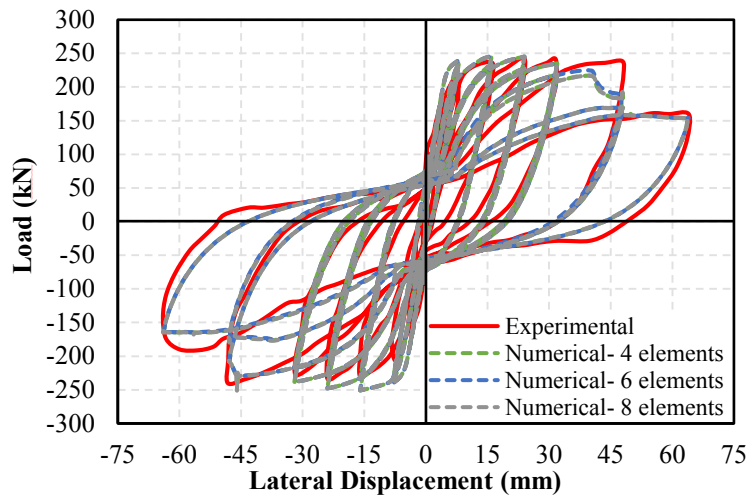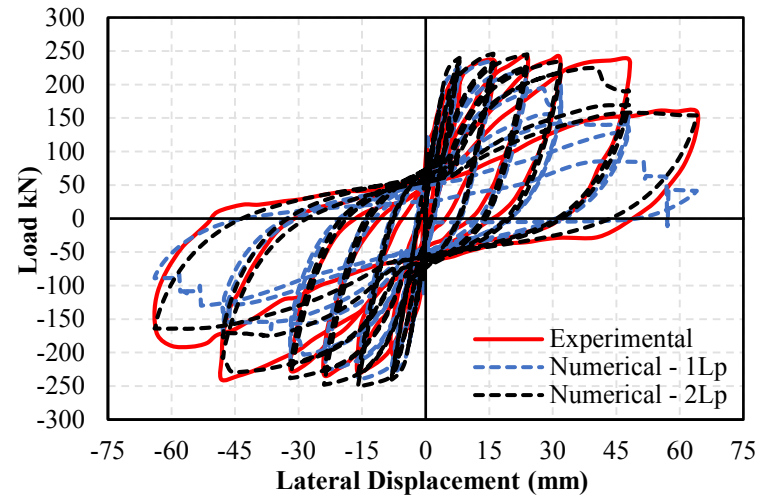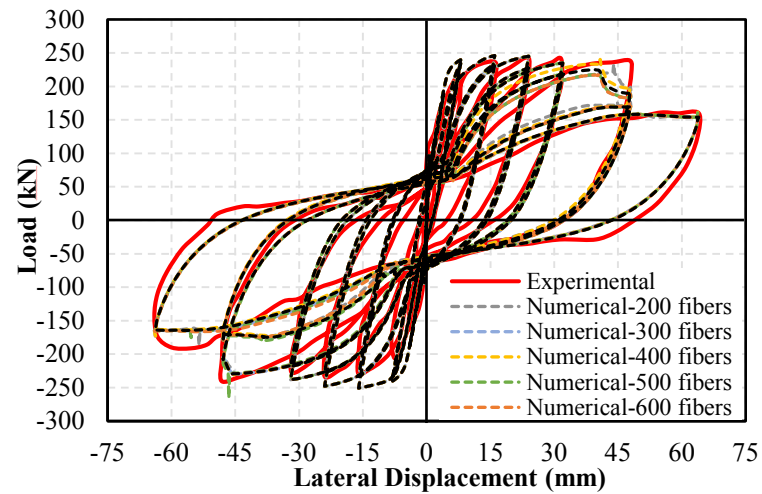
Figure 6.5 Load-displacement hysteresis for the sensitivity analysis of (a) the number of elements per wall; (b) the first element length; and (c) the number of fibers per wall's section compared with wall W6 from Shedid et al. (2010)

Therefore, the Mander et al. concrete material model (i.e., *con_ma*) embedded in SeismoStruct (2018) is selected in the current study based on the aforementioned recommendations. The Mander et al. (1988) non-linear concrete material model is calibrated using the maximum masonry compressive strength (f'_m), the strain corresponding to the maximum compressive strength (ε_{mu}), the maximum tensile strength (f_{tm}), and the masonry modulus of elasticity (E_m). This model is also adaptable to the confinement factor of the confined reinforced MBE, based on which, the cyclic rules, the masonry compressive strength, and its corresponding strain are modified. In order to investigate the robustness of the modelling approach, the model is validated against various experimental results available in the literature (such as Banting and El-Dakhakhni 2014; Shedid et al. 2010) to ensure the validity of using the Mander et al. (1988) concrete material model in lieu of the unavailable concrete-masonry material models to capture the flexural behaviour of the RMSWs. It is worth mentioning that, for validation purposes, the values of the masonry compressive strength (f'_m) and its corresponding strain (ε_{mu}) were obtained from the experimental results of the walls reported in Banting and El-Dakhakhni (2014) and Shedid et al. (2010). However, in the current study, the value of the masonry compressive strength (f'_m) was selected as 20 MPa and its corresponding strain (ε_{mu}) was chosen as 0.002, and the masonry modulus of elasticity (E_m) was computed based on the CSA S304-14 (2014) provisions (i.e., $E_m = 850\,f'_m$). These values were selected based on experimental results reported by various researchers for the compressive stress-strain relationship of their tested masonry prisms (e.g., AbdelRahman and Galal 2020; Banting 2013; Obaidat et al. 2018; Priestley and Elder 1983).

The nonlinear cyclic response of the reinforcing steel bars is attained using the Menegotto and Pinto (1973) material model (*stl_mp*) that is available in SeismoStruct (2018). This model is simple, readily calibrated, and capable of capturing the yield strength, the strain hardening effects, Bauschinger effect, and the strength degradation due to cyclic loading. Moreover, this model is mainly defined using the reinforcement steel modulus of elasticity (E_s), the yield strength (f_y), the strain hardening parameter, the fracture/buckling strain, and other calibrating coefficients that are employed to capture the shape of pre- and post-yield transition zones, Bauschinger effect, and pinching of the hysteretic behaviour. It is noteworthy that the yield strength (f_y) and the modulus of elasticity (E_s) were adopted from the experimental results reported by Banting and El-Dakhakhni (2014) and Shedid et al. (2010) to validate the numerical model. Nonetheless, for the current study, the yield strength (f_y) of 400 MPa and the modulus of elasticity (E_s) of 200 GPa were

employed. Table 6.2 shows the material properties that are assigned to the concrete-masonry and the reinforcing steel bars that are used to develop the non-linear numerical model herein after.

Table 6.2 Material properties assigned to the concrete-masonry and reinforcing steel in the numerical model

Material property	Value
Masonry compressive strength, f'_m (MPa)	20
Masonry modulus of elasticity, E_m (MPa)	$850\,f'_m$
Masonry strain at peak stress, ε_{mu}	0.002
Elasticity modulus of steel, E_s (GPa)	200
Vertical and horizontal steel yield strength, f_y (MPa)	400
Strain hardening parameter	0.005
Transition curve initial shape parameter	18.8
Transition curve shape calibrating coefficient A1	18.5
Transition curve shape calibrating coefficient A2	0.4
Isotropic hardening calibrating coefficient A3	0
Isotropic hardening calibrating coefficient A4	1
Fracture/buckling strain	0.1

6.6.3 Model Validation

In order to ensure the robustness of the numerical modelling approach, the numerical model along with its calibrated material models were validated against experimental results of RMSWs (i.e., rectangular and with boundary elements) available in the literature. The experimental results of the RMSWs were selected based on the studies reported by Banting and El-Dakhakhni (2014) and Shedid et al. (2010) on the seismic response of RMSWs with and without boundary elements using quasi-static cyclic loading. It should be noted that rectangular RMSW was selected among the validation walls to ensure the capability of the numerical model to capture the seismic performance of RMSWs with different cross-sections. Figure 6.6 shows the details of RMSWs utilized for the validation of the numerical model. As such, rectangular wall W1 and RMSW+BEs W3 and W6 from Shedid et al. (2010) and W2 from Banting and El-Dakhakhni (2014) were chosen to be validated against the developed numerical model. It is worth mentioning that both studies were conducted on half-scale RMSWs with and without MBEs with various axial stress levels and wall aspect ratios. The most valuable aspect of choosing these walls for the numerical modelling

validation is that they incorporate various axial stresses ranging from 0.89 MPa to 1.09 MPa and aspect ratios varying between 1.48 and 3.23. These aspects ensure the variety of the validated RMSWs against the numerical model to show the capability of the model to capture the seismic response of the RMSWs. Table 6.3 describes the details and the reported material properties of the RMSWs adopted from the literature to be used for the validation of the numerical model. It is worth pointing out that the material properties reported by Banting and El-Dakhakhni (2014) and Shedid et al. (2010) were employed in the numerical model to calibrate the concrete-masonry material model (Mander et al. 1988, *con_ma*) and the reinforcing steel bars (Menegotto and Pinto 1973, *stl_mp*) to reproduce the hysteretic response of their experimental results. Moreover, to numerically simulate the seismic performance of the experimental walls, the axial force was applied on the walls and the horizontal displacements were imposed at the top of the walls using the same displacement-controlled loading protocol based on a static time history analysis scheme available in SeismoStruct (2018).
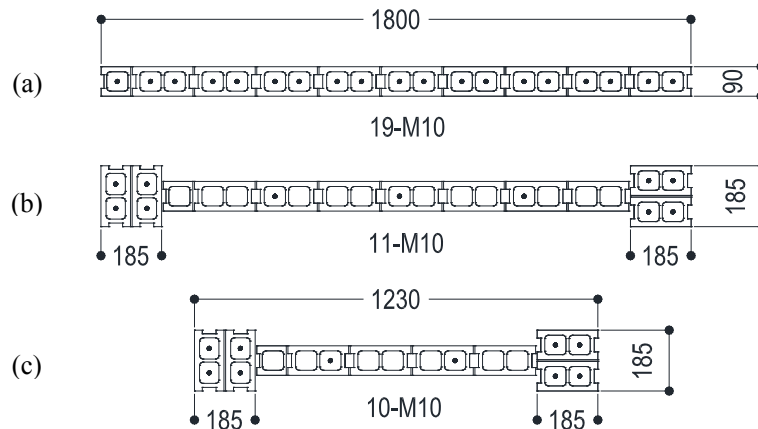
Figure 6.6 Details of the walls utilized for the validation of the numerical model: (a) W1 Shedid et al. (2010); (b) W3 and W6 Shedid et al. (2010); and (c) W2 Banting and El-Dakhakhni (2014)

Figure 6.7 depicts the load-displacement hysteresis of the experimentally tested RMSWs by Banting and El-Dakhakhni (2014) and Shedid et al. (2010) and that of the numerical model. One can see that there is good agreement between the experimental results and that of the numerical model where the model is seen to have the capability to capture the most significant parameters of the seismic response such as the yield strength, the lateral capacity, the stiffness and strength degradation with different displacement increments, and the pinching behaviour of the walls.

Hence, the model was found to be reliable and able to capture the flexural response of the RMSWs with and without boundary elements with a reasonable error ranged from 10 to 20% when compared to its experimentally tested counterparts. It is worth noting that these experimentally tested shear walls were designed such that they are flexurally-dominated which in turn helped the numerical model to capture, accurately, their seismic performance in terms of the hysteretic behaviour. This can be attributed to the fact that mentioned earlier, that is, the model formulation is based on the fiber modelling approach where these elements cannot adequately capture the shear deformations. Therefore, the walls that were chosen for the validation purpose had an aspect ratio of greater than 1.0 (i.e., ~1.5-3.23) to overcome such a limitation.
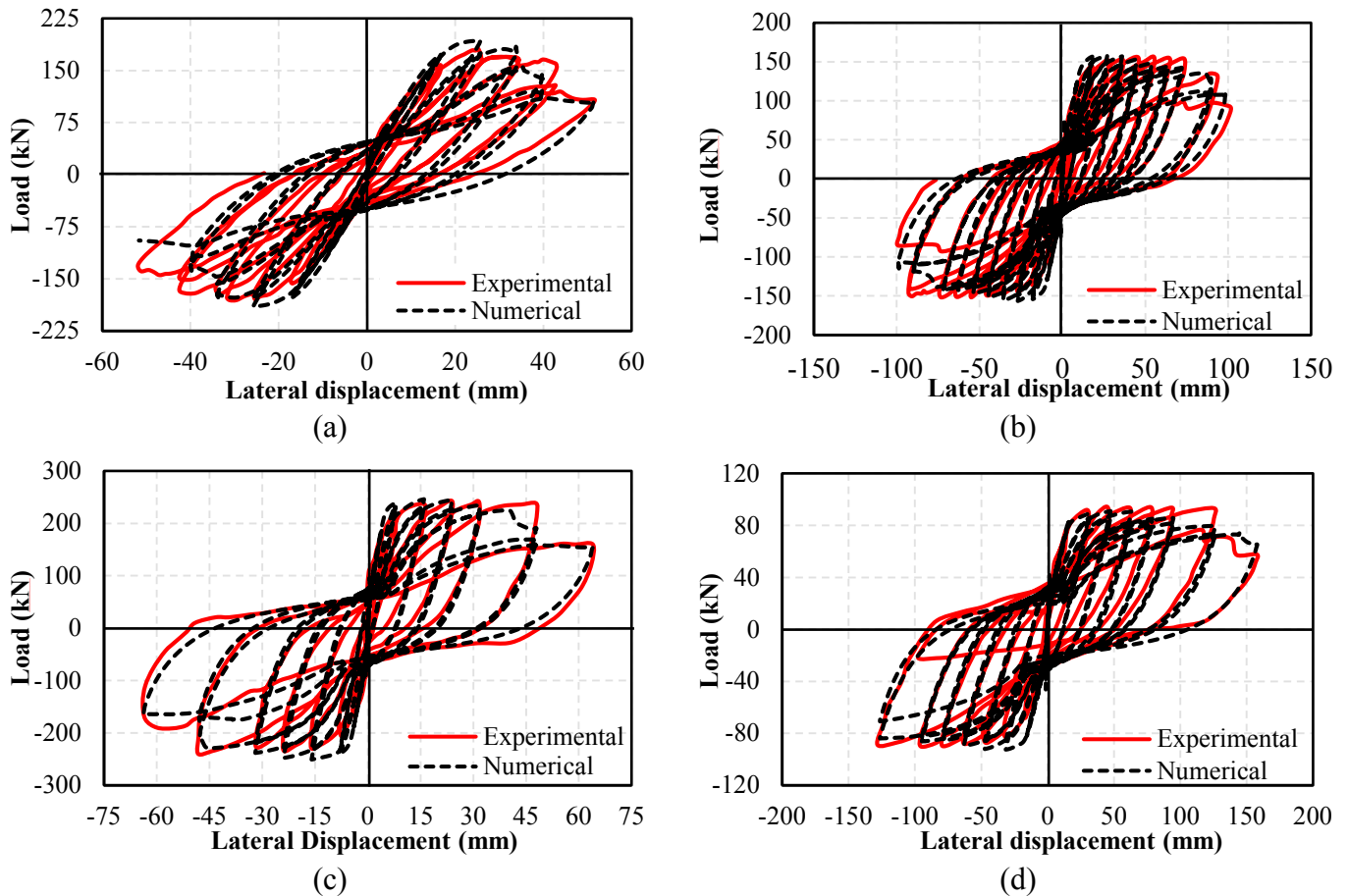
Figure 6.7 Validation of the proposed numerical model against experimental results from (a) wall W1 from Shedid et al. (2010); (b) wall W3 from Shedid et al. (2010); (c) wall W6 from Shedid et al. (2010); and (d) wall W2 from Banting and El-Dakhakhni (2014)

167

Table 6.3 Details and material properties of the RMSWs utilized for the model validation

| Wall identifier | Reference | Length (mm) | Height (m) | Vertical reinforcement | | | Horizontal reinforcement | | | Masonry | Axial stress (MPa) | Aspect ratio |
				Amount	ρ_v (%)	f_y (MPa)	Amount	ρ_h (%)	f_y (MPa)	f'_m (MPa)		
W1	Shedid et al. (2010)	1802	3.99	19-M10	1.17	495	D4@95	0.3	534	16.4	1.09	2.21
W3	Shedid et al. (2010)	1802	3.99	11-M10	0.55	495	D4@95	0.3	534	16.4	0.89	2.21
W6	Shedid et al. (2010)	1802	2.66	11-M10	0.55	495	2-D4@95	0.6	534	16.4	0.88	1.48
W2	Banting and El-Dakhakhni (2014)	1235	3.99	10-M10	0.69	496	D4@95	0.3	582.5	17.3	0.89	3.23

6.7 Analysis of the Numerical Modelling Results

A sensitivity analysis was performed to evaluate the influence of the different aforementioned design parameters as well as the wall's configurations on the seismic response of the RMSW+BEs. As shown in Figure 6.2, the walls′ configurations, namely, the aspect ratio, the boundary element size, the length of the wall, and the level of the axial compressive stress were examined. The sensitivity analysis was performed to asses and quantify the effect of ±30% changing of the masonry compressive strain at peak stress (ε_{mu}), the masonry compressive strength (f'_m), the masonry modulus of elasticity (E_m), and the MBE vertical reinforcement ratio (ρ_{vBE}) on the cyclic response of RMSW+BEs considering the abovementioned walls′ configurations. It is noteworthy that the tornado charts of the sensitivity analysis will show the influence of changing the design parameters on the seismic response components of each studied wall (i.e., Q_u, Q_y, K_{eff}, $K_{2.5\%}$, and $\mu_{\Delta0.8Qu}$) normalized to their corresponding components (i.e., $Q_{u,ref}$, $Q_{y,ref}$, $K_{eff,ref}$, $K_{2.5\%,ref}$, and $\mu_{\Delta0.8Qu,ref}$) of the reference walls listed in Table 6.1. The RMSW+BEs were subjected to fully-reversed displacement-controlled cycling loading using the static time history non-linear analysis tool that is available in SeismoStruct (2018). The fully-reversed cycling loading was applied using multiples of the yield displacement (Δ_y) and the cycles were performed until the RMSW+BEs reach an 80% of its lateral ultimate load, $0.8Q_u$ (i.e., 20% strength degradation). Table 6.4 shows the numerical model results of the reference RMSW+BEs, namely, the values of the lateral yield capacity, Q_y, the lateral ultimate capacity, Q_u, the lateral load at 2.5% drift ($Q_{2.5\%drift}$), and the displacement ductility computed at 20% strength degradation ($\mu_{\Delta0.8Qu}$). As shown in Figure 6.8, the displacement ductility ($\mu_{\Delta0.8Qu}$) of the RMSW+BEs was calculated based on the ratio between the lateral displacement at 20% strength degradation ($\Delta_{0.8Qu}$) and the lateral yield displacement (Δ_y). Moreover, the lateral load at 2.5% drift ($Q_{2.5\%drift}$) was tabulated in order to quantify the influence of the design parameters on the lateral secant stiffness of the RMSW+BEs at the maximum allowable drift value (i.e., 2.5%) stipulated in the CSA S304-14 (2014). The lateral load-displacement envelopes were developed from the numerical results of the RMSW+BEs and sample curves are presented in Figure 6.9.
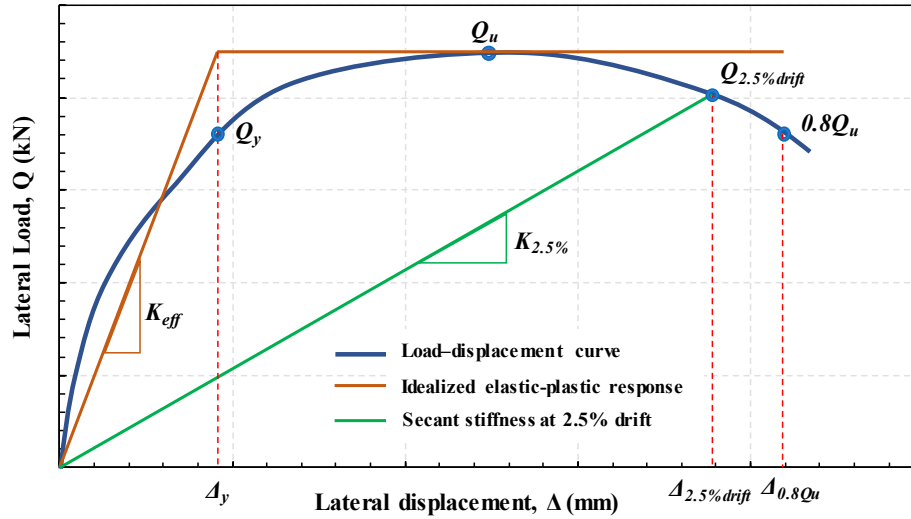
Figure 6.8 Lateral load-displacement envelope and idealized elastic-plastic response of a sample RMSW+BEs

Table 6.4 Results of the reference RMSW+BEs

Wall No.	Wall identifier	Q_y (kN)	Q_u (kN)	$Q_{2.5\%drift}$ (kN)	$\mu_{\Delta 0.8Qu}$
W1	Sq-BE-Low	622.22	807.53	671.56	21.00
W2	Sq-BE-Mid	322.69	370.14	328.40	10.00
W3	Sq-BE-High	235.81	259.31	238.76	6.00
W4	R1-BE-Low	773.42	1041.36	869.30	26.00
W5	R1-BE-Mid	388.23	460.92	414.74	10.12
W6	R1-BE-High	279.8	316.34	282.71	6.00
W7	R2-BE-Low	908.01	1254.91	1073.84	24.00
W8	R2-BE-Mid	432.46	543.12	491.90	10.00
W9	R2-BE-High	312.48	367.77	344.60	6.00
W10	Sq-BE-High-AS2	273.01	293.95	239.80	4.00
W11	R1-BE-High-AS2	319.12	352.4	312.80	5.00
W12	R2-BE-High-AS2	353.75	404.74	360.90	5.00
W13	Sq-BE-High-L2	511.53	590.3	484.10	7.09
W14	R1-BE-High-L2	581.87	697.03	601.50	8.65
W15	R2-BE-High-L2	658.29	795.45	684.00	9.00

6.7.1 Effect of the wall's aspect ratio

Figure 6.9(a) shows the lateral load-displacement envelopes for RMSW+BEs W1, W2, and W3. It can be seen that the aspect ratio of the walls greatly affected the ultimate capacity (Q_u) of the RMSW+BEs which decreased significantly when the aspect ratio increased. For walls with an axial stress of 0.2 MPa/storey and a square MBE, the ultimate capacity (Q_u) of walls W2 and W3 decreased by 55% and 68% when the aspect ratio increased from 1.66 to 4.16, and 6.65, respectively, compared to that of wall W1. For walls with an axial stress of 0.2 MPa/storey and MBE size of 390x600 mm, Q_u of walls W5 and W6 decreased by 55% and 70% as the aspect ratio surged from 1.66 to 4.16, and 6.65, respectively, with comparison to wall W4. Also, increasing the aspect ratio from 1.66 to 4.16, and 6.65 yielded a decrease of 57% and 70% in Q_u of walls W8 and W9 compared to their wall W7 counterpart. It should be noted that the significant drop of the ultimate capacity of the RMSW+BEs is attributed to the increase of the walls′ heights while the sectional moment capacity remained constant. Increasing the aspect ratio of the RMSW+BEs resulted in a significant drop in their displacement ductility which can be noticed from the reported values presented in Table 6.4. For walls with MBE size of 390x400 mm, increasing the aspect ratio from 1.66 to 4.16 and 6.65 resulted in a decrease of 52% and 71% in the displacement ductility ($\mu_{\Delta0.8Qu}$) for walls W2 and W3, respectively, when compared to wall W. Similar results were observed for walls W5 and W6 when compared to W4 as well as W8 and W9 when compared to their W7 counterpart. It is worth noting that the displacement ductility of the walls with higher aspect ratios significantly dropped due to attaining the 20% strength degradation more rapidly than the walls with lesser aspect ratios. Similar findings for RMSWs with square MBEs were also reported by previous researchers (e.g., Banting and El-Dakhakhni 2014; Hamzeh et al. 2018; Shedid et al. 2010). It can be inferred that with different MBE configurations (square and rectangular), increasing the aspect ratio of the RMSW+BEs has a deteriorating effect on both the lateral capacity (Q_u) and the displacement ductility ($\mu_{\Delta0.8Qu}$).
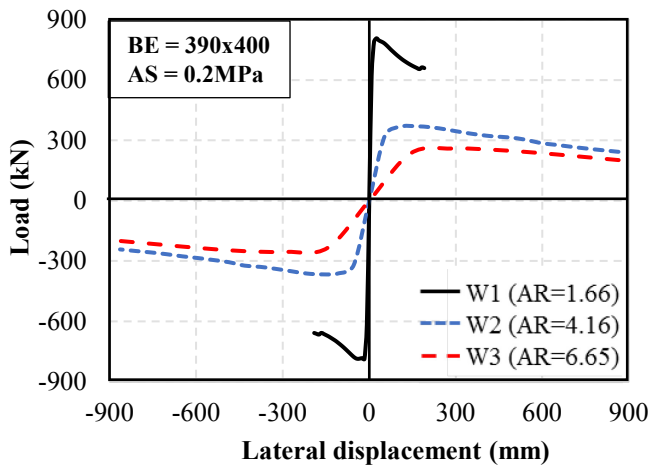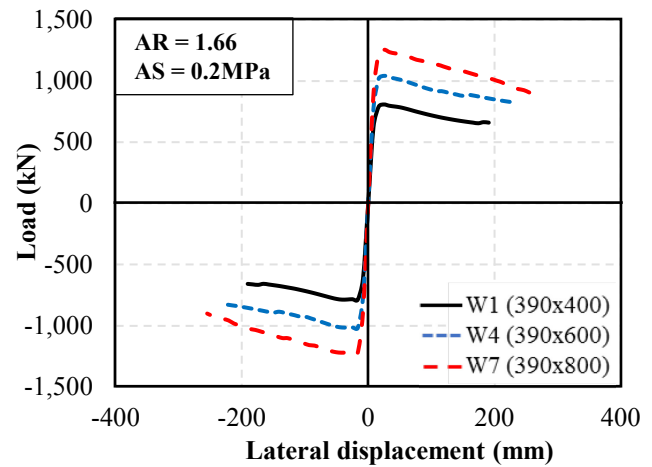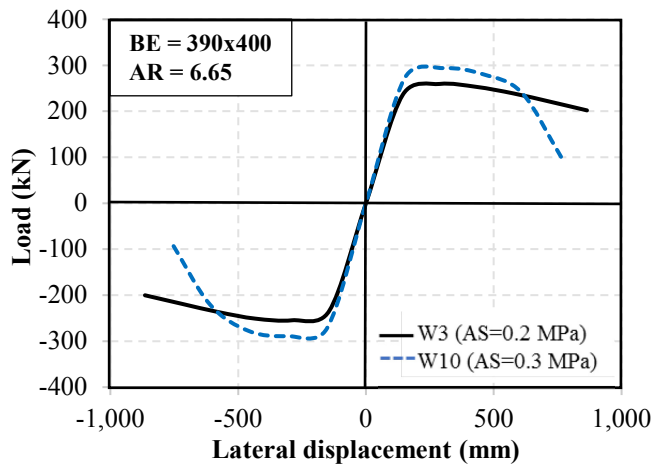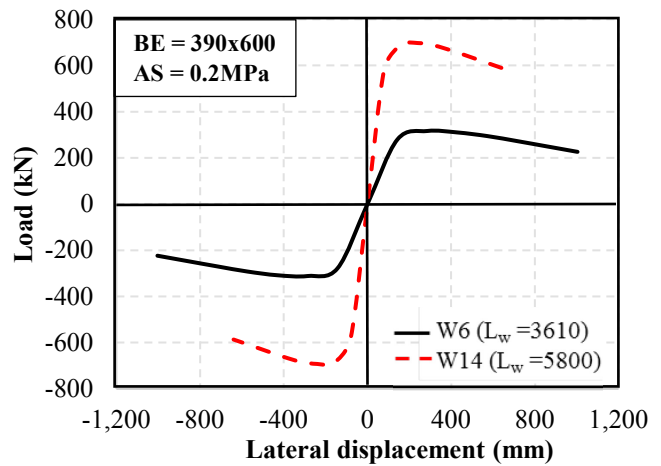
Figure 6.9 Lateral load-displacement hysteresis envelopes for RMSWs with (a) BEs = 390x400 mm and AS = 0.2 MPa/storey, (b) AR = 1.66 and AS = 0.2 MPa/storey, (c) BEs = 390x400 mm and AR = 6.65, and (d) BEs = 390x600 and AS = 0.2 MPa/storey

6.7.2 Effect of the wall's masonry boundary element configuration

Three different boundary elements configurations namely square Sq (390x400 mm), rectangular R1 (390x600 mm), and rectangular R2 (390x800 mm) were assessed with constant length of the walls and constant boundary element vertical reinforcement ratios to quantify the influence of changing the boundary element size on the seismic behaviour of RMSW+BEs. Figure 6.9(b) shows a sample comparison of the lateral load-displacement envelopes of walls W1, W4, and W7. As shown in Figure 6.9(b), increasing the MBE size resulted in a significant increase in

the ultimate capacity (Q_u) of the RMSW+BEs. For walls with an aspect ratio (AR) of 1.66 and an axial stress of 0.2 MPa/storey, Q_u increased by 29% and 55% for walls W4 and W7, respectively, when the MBE size increased to 390x600 mm and 390x800 mm compared to their square MBE wall W1. Also, for walls with $AR = 4.16$, Q_u of walls W5 and W8 improved by 24% and 47% as the MBE section increased to 390x600 mm and 390x800 mm, respectively, when compared to that of the wall W2. Moreover, compared to wall W3 with square MBE, increasing the MBE cross-section to 390x600 mm and 390x800 mm for walls W6 and W9 resulted in an increase of 22% and 42% in their ultimate capacity, Q_u, respectively. As such, it can be noticed that there is an inversely proportional relationship between the rate of increase of Q_u of the walls (when increasing the MBE size) and the increase of the aspect ratio. The significant increase in Q_u varied from 22% to 57% can be attributed to the increase of the confined MBE cross-sectional area at the most compressed zone of the wall extremities which allowed for more vertical reinforcement bars to be confined. Increasing the MBE size in RMSW+BEs resulted in an enhancement in their respective displacement ductility ($\mu_{\Delta 0.8Qu}$). For walls with $AR = 1.66$, increasing the MBE size to 390x600 mm and 390x800 mm for walls W4 and W7 enhanced $\mu_{\Delta 0.8Qu}$ by 24% and 14%, respectively, when compared to wall W1. On the other hand, increasing the MBE size for walls with $AR = 4.16$ and those with $AR = 6.65$ had no substantial influence on their displacement ductility. As mentioned earlier, the increase of the MBE size led to an enhanced displacement ductility due to the increase of the confined compression zone at the wall toes which in turn delayed buckling of the vertical reinforcement bars.

6.7.3 Effect of the wall's axial stress

Figure 6.9(c) shows the comparison of sample load-displacement hysteretic envelops for walls with different axial stresses (AS). The RMSW+BEs lateral capacity (Q_u) experienced a slight-to significant increase as the axial compressive stress increased. For walls with $AR = 6.65$ and a square MBE, Q_u increased by 13% when the axial stress raised from 0.2 MPa to 0.3 MPa per storey. Also, for walls with $AR = 6.65$ and rectangular MBE R1 (390x600 mm), Q_u amplified by 11% as the axial stress increased by 50%. Similarly, increasing the axial stress from 0.2 MPa to 0.3 MPa per storey resulted in an increase of 10% in the ultimate capacity (Q_u) for walls with $AR = 6.65$ and rectangular MBE R2 (390x800 mm). This slight increase in the lateral ultimate capacity of the RMSW+BEs can be attributed to the increase of the sectional moment capacity due to the

173

higher axial compressive stress applied on the wall section. On the contrary, an increase in the RMSW+BEs axial compressive stress resulted in a considerable decrease in their displacement ductility. For walls with $AR = 6.65$ and square Sq MBE (390x400 mm), rectangular R1 MBE (390x600 mm), and rectangular R2 MBE (390x800 mm), when the axial stress per storey increased from 0.2 MPa to 0.3 MPa, $\mu_{\Delta0.8Qu}$ dropped by 33%, 17%, and 17%, respectively. Increasing the axial compressive stress on the RMSW+BEs increases the depth of the compression zone at both the yield and the ultimate states which in turn boosts the yield displacement (Δ_y) and reduces the ultimate displacement (Δ_u). Therefore, this results in a significant reduction in the displacement ductility of the RMSW+BEs (Paulay and Priestly 1992).

6.7.4 Effect of the wall's length

High-rise RMSW+BEs buildings′ lateral ultimate capacity (Q_u) and displacement ductility ($\mu_{\Delta0.8Qu}$) can be hindered due to the effect of the high aspect ratios of the walls. Increasing the RMSW+BEs length significantly enhances their seismic performance as it outweighs the high aspect ratio effects. Figure 6.9(d) shows the influence of increasing the wall length on the load-displacement envelopes of different RMSW+BEs. For walls with axial stress $AS = 0.2$ MPa/storey and square Sq MBE (390x400 mm), rectangular R1 MBE (390x600 mm), and rectangular R2 MBE (390x800 mm), as the wall length (l_w) increased by 60%, Q_u witnessed an increase of more than 100%. In addition, $\mu_{\Delta0.8Qu}$ experienced an increase of 18%, 44%, and 50% when the wall length increased by 60% for walls W13, W14, and W15 compared to walls W3, W6, and W9 with shorter wall length, respectively.

6.7.5 Sensitivity of the wall's lateral yield capacity (Q_y) to the design parameters

Figure 6.10 shows the tornado charts that illustrate the sensitivity of the RMSW+BEs yield strength (Q_y) to the design parameters with different walls′ aspect ratios, MBE sizes, axial stresses, and walls lengths. As indicated in Figure 6.10, the vertical reinforcement ratio of the boundary element (ρ_{vBE}) is the most influential parameter affecting Q_y, whereas the masonry compressive strain at peak stress (ε_{mu}) has no substantial influence on Q_y. Moreover, both the masonry compressive strength (f'_m) and the masonry modulus of elasticity (E_m) have almost equivalent effect on Q_y. For walls with axial stress $AS = 0.2$ MPa/storey and MBEs of 390x400 mm, 390x600 mm, and 390x800 mm, Q_y was found to be more sensitive to the change of ρ_{vBE} for walls with lower aspect ratio $AR = 1.66$, as shown in Figures 6.10(a and b).

174
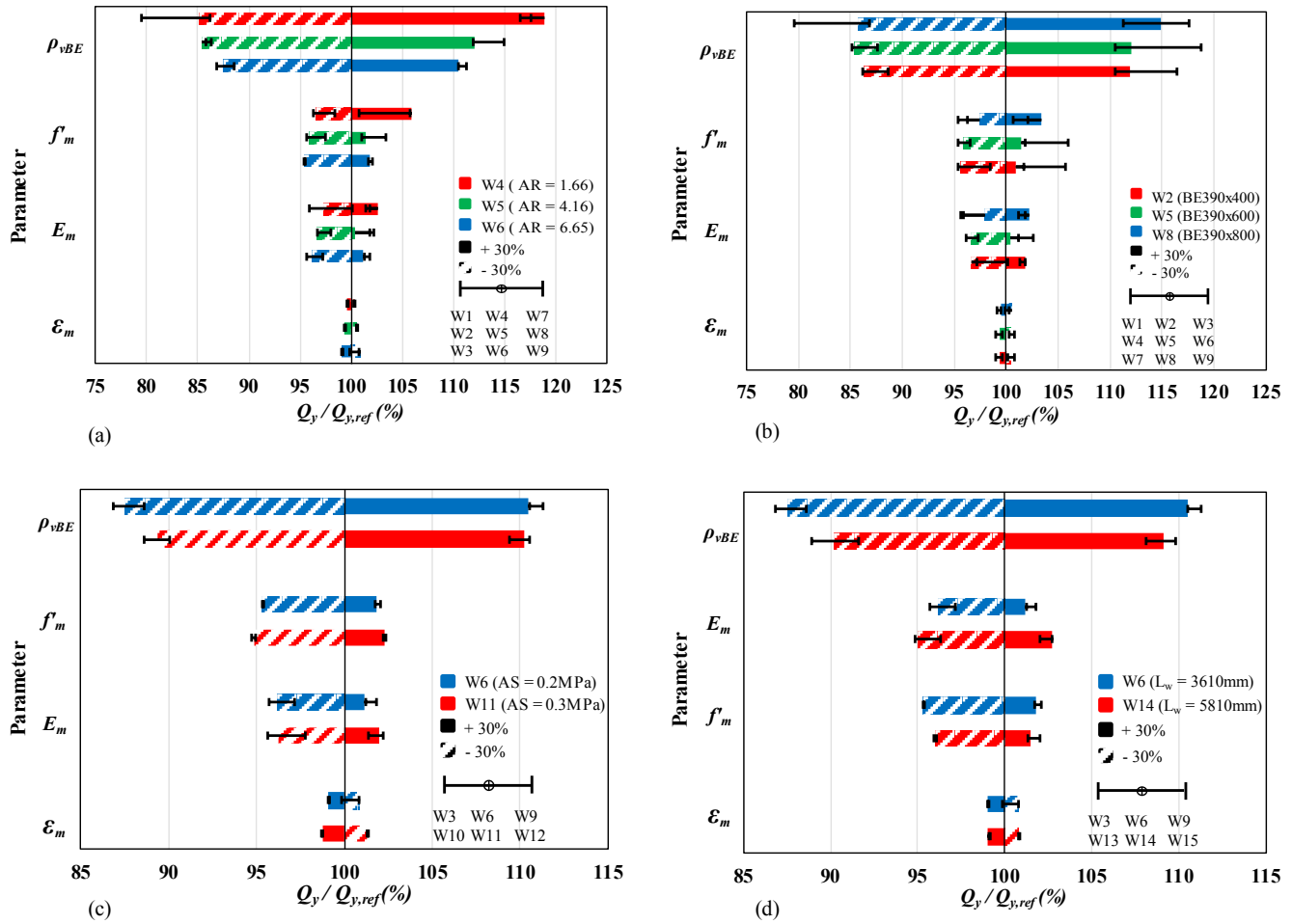
Figure 6.10 Sensitivity of the lateral yield capacity (Q_y) to ±30% changing of ε_{mu}, f'_m, E_m, and $\rho_{v\,BE}$ for RMSW+BEs having different (a) BE sizes and aspect ratios; (b) aspect ratios and BE sizes; (c) BE sizes and axial stresses; and (d) BE sizes and wall lengths

The ±30% change in ρ_{vBE} resulted in nearly ±20% change in Q_y for walls with $AR = 1.66$, respectively. This change declined to almost ±15% for walls with $AR = 4.16$ and to ±10% for walls with $AR = 6.65$. In addition, an increase of +30% in f'_m and E_m resulted in a minimal increase within 5% in Q_y, whereas a reduction of 30% in f'_m and E_m led to less than 5% reduction Q_y. It is worth noting that a change of ±30% in ε_{mu} had negligible effect on Q_y. Figure 6.10(c) shows that Q_y was higher sensitive to the change of ρ_{vBE} for walls with axial stress AS = 0.2 MPa/storey than those with axial stress $AS = 0.3$ MPa/storey. Furthermore, it was found that Q_y was more sensitive to the change of the design parameters for walls with shorter length $l_w = 3610$ mm than walls with $l_w = 5810$ mm, as depicted in Figure 6.10(d). It can be inferred that there is a direct proportional

relationship between ρ_{vBE} and Q_y which can be attributed to the increase/decrease of the yield moment capacity of the walls as the reinforcement ratio increases/decreases, respectively.

6.7.6 Sensitivity of the wall's lateral ultimate capacity (Q_u) to the design parameters

Figure 6.11 shows the tornado charts depicting the influence of each of the design parameters on the lateral ultimate capacity (Q_u) of the RMSW+BEs. It is observed that the change of the boundary element vertical reinforcement ratio (ρ_{vBE}) is the most influencing parameter on Q_u. Apparently, a change of ±30% in ρ_{vBE} yielded a direct change of nearly ±20% in Q_u for walls with axial stress $AS = 0.2$ MPa/storey and different MBEs configurations, respectively, as shown in Figure 6.11(a). In addition, it was found that the masonry compressive strength (f'_m), the masonry modulus of elasticity (E_m), and the masonry compressive strain (ε_{mu}) had negligible effect (around 3%) on Q_u. Similar to the yield strength (Q_y) of the RMSW+BEs, Q_u was found to be more sensitive for walls with aspect ratio $AR = 1.66$ compared to those with higher aspect ratios $AR = 4.16$ and 6.65. Furthermore, Q_u was more sensitive for walls with greater MBE size (i.e., 390x800 mm) than those with smaller MBE sizes (i.e., 390x400 mm and 390x600 mm), as illustrated in Figure 6.11(b). Nevertheless, Q_u was less sensitive for walls with higher axial stress (i.e., 0.3 MPa/storey) than those with $AS = 0.2$ MPa/storey, as indicated in Figure 6.11(c). This was also observed for walls with longer wall lengths $l_w = 5810$ mm compared to those with $l_w = 3610$ mm, as shown in Figure 6.11(d). It is worth mentioning that the considerable increase/decrease of Q_u due to the increase/decrease of the ρ_{vBE} can be attributed to the change in the ultimate moment capacity of the RMSW+BEs while the wall height remained constant.
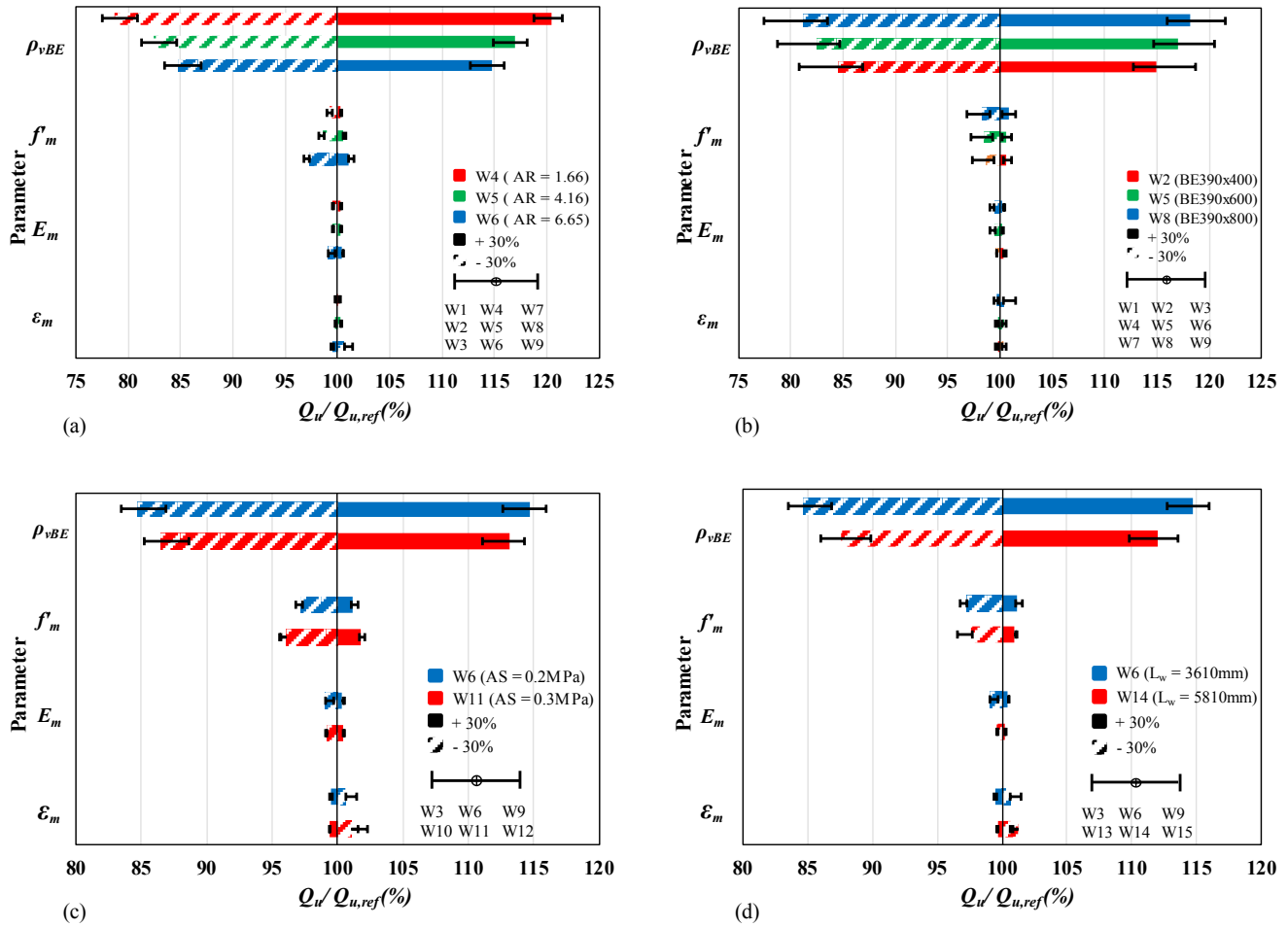
Figure 6.11 Sensitivity of the lateral ultimate capacity (Q_u) to ±30% changing of ε_{mu}, f'_m, E_m, and $\rho_{v\,BE}$ for RMSW+BEs having different (a) BE sizes and aspect ratios; (b) aspect ratios and BE sizes; (c) BE sizes and axial stresses; and (d) BE sizes and wall lengths

6.7.7 Sensitivity of the wall's displacement ductility ($\mu_{\Delta 0.8Qu}$) to the design parameters

The tornado charts that illustrate how much the displacement ductility ($\mu_{\Delta 0.8Qu}$) was sensitive to the design parameters are shown in Figure 6.12. In general, $\mu_{\Delta 0.8Qu}$ was extremely sensitive to the change of ε_{mu} and E_m, respectively. Besides, $\mu_{\Delta 0.8Qu}$ was found to be intensively sensitive to the 30% reduction in those design parameters rather than their 30% increase. Figure 6.12(a) shows that a reduction of 30% in the masonry compressive strain (ε_{mu}) resulted in a tremendous drop of nearly 60% in $\mu_{\Delta 0.8Qu}$ for walls with axial stress AS = 0.2 MPa/storey and aspect ratios ranged between 1.66 and 6.65. Moreover, as the masonry modulus of elasticity (E_m) reduced by 30%, $\mu_{\Delta 0.8Qu}$ dramatically declined by nearly 40%. On the contrary, $\mu_{\Delta 0.8Qu}$ experienced an improvement

of just ~10-15% as ε_{mu} and E_m increased by 30%. It is worth noting that $\mu_{\Delta 0.8Qu}$ was higher sensitive for walls with aspect ratio $AR = 1.66$ compared to those with higher aspect ratios: $AR = 4.16$ and 6.65. It is also noticeable that the 30% reduction of f'_m had significant effect of around 15-20% on $\mu_{\Delta 0.8Qu}$, whereas the change of ρ_{vBE} had an effect of 10% on $\mu_{\Delta 0.8Qu}$.
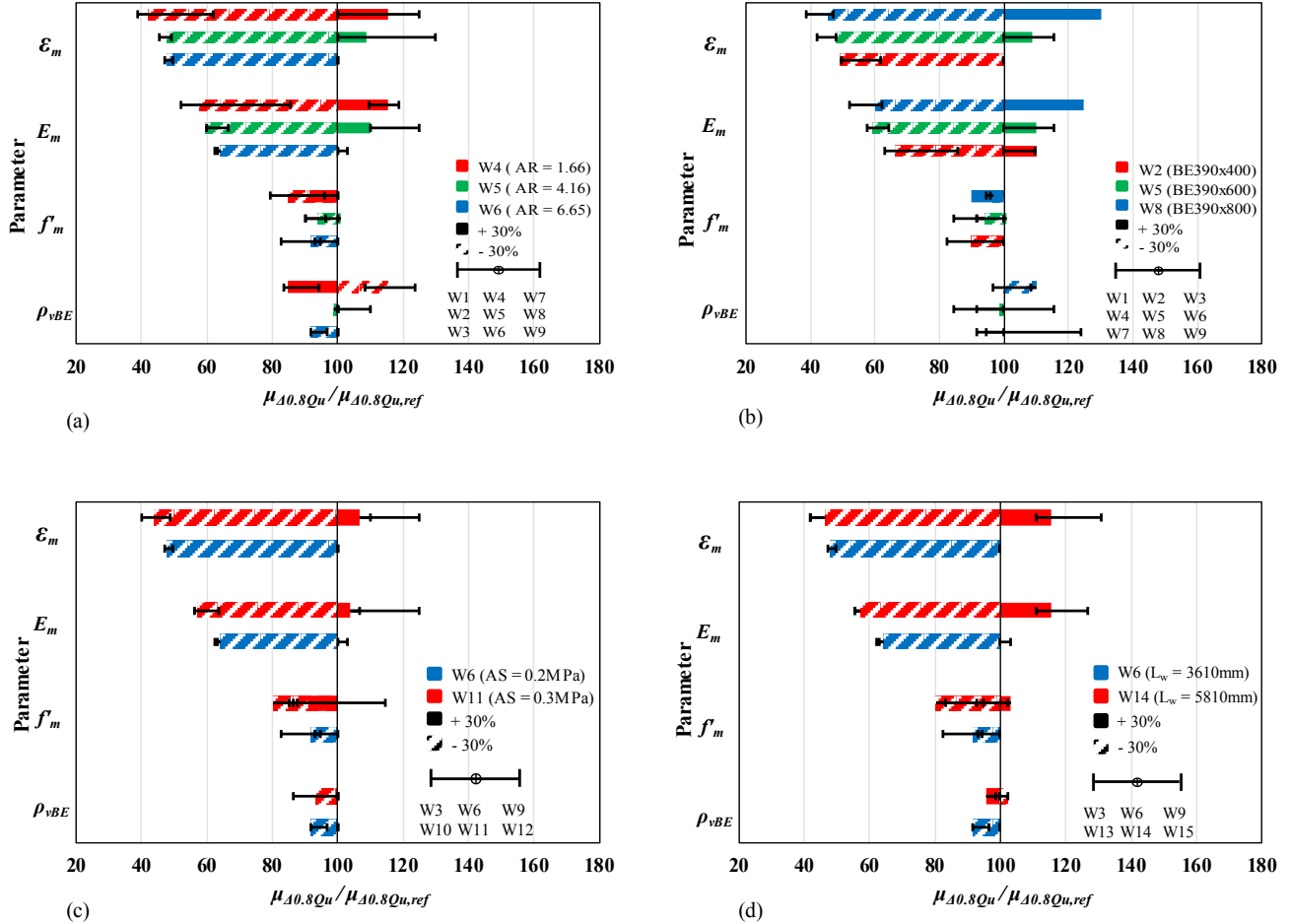
Figure 6.12 Sensitivity of the displacement ductility ($\mu_{\Delta 0.8Qu}$) to ±30% changing of ε_{mu}, f'_m, E_m, and ρ_{vBE} for RMSW+BEs having different (a) BE sizes and aspect ratios; (b) aspect ratios and BE sizes; (c) BE sizes and axial stresses; and (d) BE sizes and wall lengths

For walls with similar MBE configurations, $\mu_{\Delta 0.8Qu}$ was found to be more sensitive for walls with $AS = 0.3$ MPa/storey than walls with 50% lower axial stress, as illustrated in Figure 6.12(c). Similar observations were reported for walls with greater length (i.e., 5810 mm) when compared to walls with shorter length (i.e., 3610 mm), as shown in Figure 6.12(d). The directly proportional relationship of the masonry compressive strain at peak stress (ε_{mu}) with the displacement ductility

($\mu_{\Delta 0.8Qu}$) can be attributed to the critical effect the former has on the displacement ductility. The reduction in the masonry strain at peak stress (ε_{mu}) greatly reduces the ultimate curvature of the RMSW+BE which in turn lower its curvature ductility. Since the curvature ductility is directly proportional to the displacement ductility of the RMSW+BEs, decreasing ε_{mu} extremely lessens both the curvature and displacement ductilities.

6.7.8 Sensitivity of the effective elastic stiffness (K_{eff}) to the design parameters

The lateral effective elastic stiffness of the RMSW+BEs (K_{eff}) is calculated based on the equal displacement approach suggested by Seif ElDin (2016). In this method, the idealized elastic-plastic response of the RMSW+BEs is obtained by extending a line commencing at the origin intersects with a horizontal line tangent to the lateral ultimate capacity (Q_u) at the yield displacement (Δ_y), as shown in Figure 6.8. This idealization ensures that the idealized displacement ductility ($\mu_{\Delta,id}$) is equal to the actual calculated displacement ductility ($\mu_{\Delta 0.8Qu}$). Hence, the effective elastic stiffness (K_{eff}) of each wall is computed by dividing the wall's lateral ultimate capacity (Q_u) by the lateral yield displacement (Δ_y), as illustrated in Figure 6.8.

Figure 6.13 shows the tornado charts of the influence of the design parameters f'_m, ε_{mu}, E_m, and ρ_{vBE} on the effective elastic stiffness (K_{eff}) of the studied RMSW+BEs. The results presented in Figures 6.13(a and b) showed that K_{eff} of all the examined walls with different configurations was mostly influenced by the vertical reinforcement ratio (ρ_{vBE}) and the masonry modulus of elasticity (E_m), respectively. Introducing a change of $\pm$ 30% in ρ_{vBE} and E_m resulted in a change in the walls′ lateral effective stiffness (K_{eff}) by nearly $\pm$ 18% and $\pm$ 5%, respectively. Moreover, it was found that changing the masonry maximum compressive strength (f'_m) as well as the masonry strain at peak stress (ε_{mu}) did not have a significant influence on K_{eff}. The tornado charts demonstrate that the K_{eff} of the RMSW+BEs having low aspect ratio AR = 1.66 and MBE of 390x800 mm were more influenced by the change of ρ_{vBE} rather than their counterparts. Furthermore, for walls with lower axial stress AS = 0.2 MPa/storey and shorter wall length l_w = 3610 mm, K_{eff} was found to be highly sensitive to the change of all the design parameters compared to their counterparts, as illustrated in Figures 6.13(c and d). It is noteworthy that K_{eff} exhibited more sensitivity to the change of the masonry maximum compressive strength (f'_m) for RMSW+BEs having low axial stress AS = 0.2 MPa/storey and shorter wall length l_w = 3610 mm, as shown in Figures 6.13(c and d).
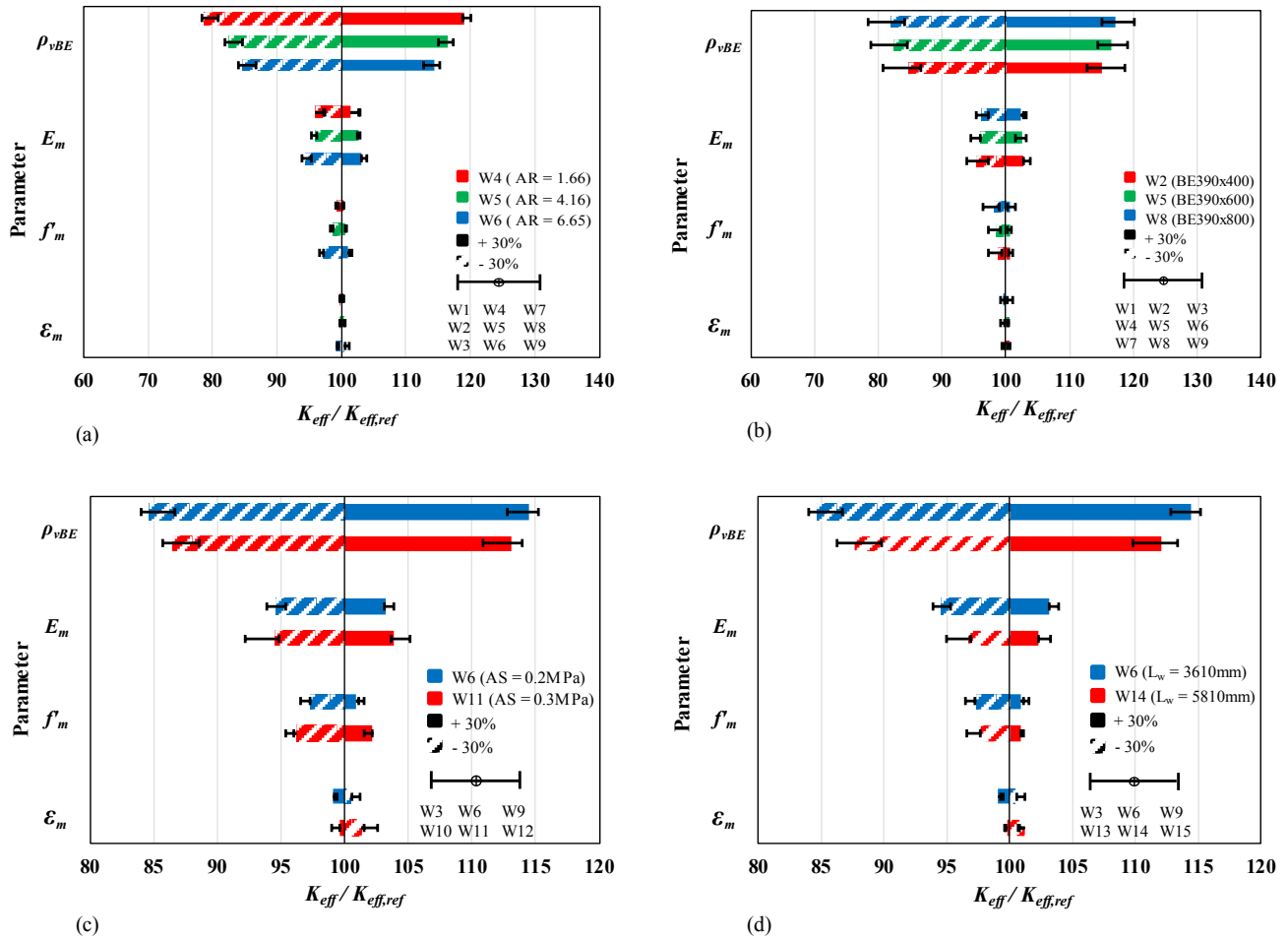
Figure 6.13 Sensitivity of the lateral effective stiffness (K_{eff}) to ±30% changing of ε_{mu}, f'_m, E_m, and $\rho_{v\,BE}$ for RMSW+BEs having different (a) BE sizes and aspect ratios; (b) aspect ratios and BE sizes; (c) BE sizes and axial stresses; and (d) BE sizes and wall lengths

6.7.9 Sensitivity of the secant stiffness ($K_{2.5\%}$) to the design parameters

The tornado charts illustrating the influence of changing the design parameters on the lateral secant stiffness at 2.5% drift ($K_{2.5\%}$) of the RMSW+BEs are presented in Figure 6.14. The $K_{2.5\%}$ is calculated by dividing the lateral capacity of the RMSW+BEs at 2.5% drift ($Q_{2.5\%drift}$) by its corresponding lateral displacement $\varDelta_{2.5\%drift}$. Figure 6.14 shows that the masonry compressive strain at peak stress (ε_{mu}) and the masonry modulus of elasticity (E_m) had the greater effect on $K_{2.5\%}$ for all the RMSW+BEs under investigation. In addition, it is obvious that the influence of decreasing ε_{mu} and E_m by 30% on $K_{2.5\%}$ was higher than increasing the same parameters by 30%. This means that $K_{2.5\%}$ was much more sensitive to the reduction of ε_{mu} and E_m, compared to their increase. Figure 6.14(a) shows that as ε_{mu} decreased by 30%, $K_{2.5\%}$ dropped by an average of 40%,

whereas when E_m reduced by 30%, $K_{2.5\%}$ dropped by nearly 35%, for walls with axial stress of 0.2 MPa/storey and different aspect ratios (i.e., 1.66, 4.16, 6.65). Nonetheless, the change of ±30% in the vertical reinforcement ratio of the MBEs (ρ_{vBE}) was found to have ±~15-20% effect on $K_{2.5\%}$, respectively.
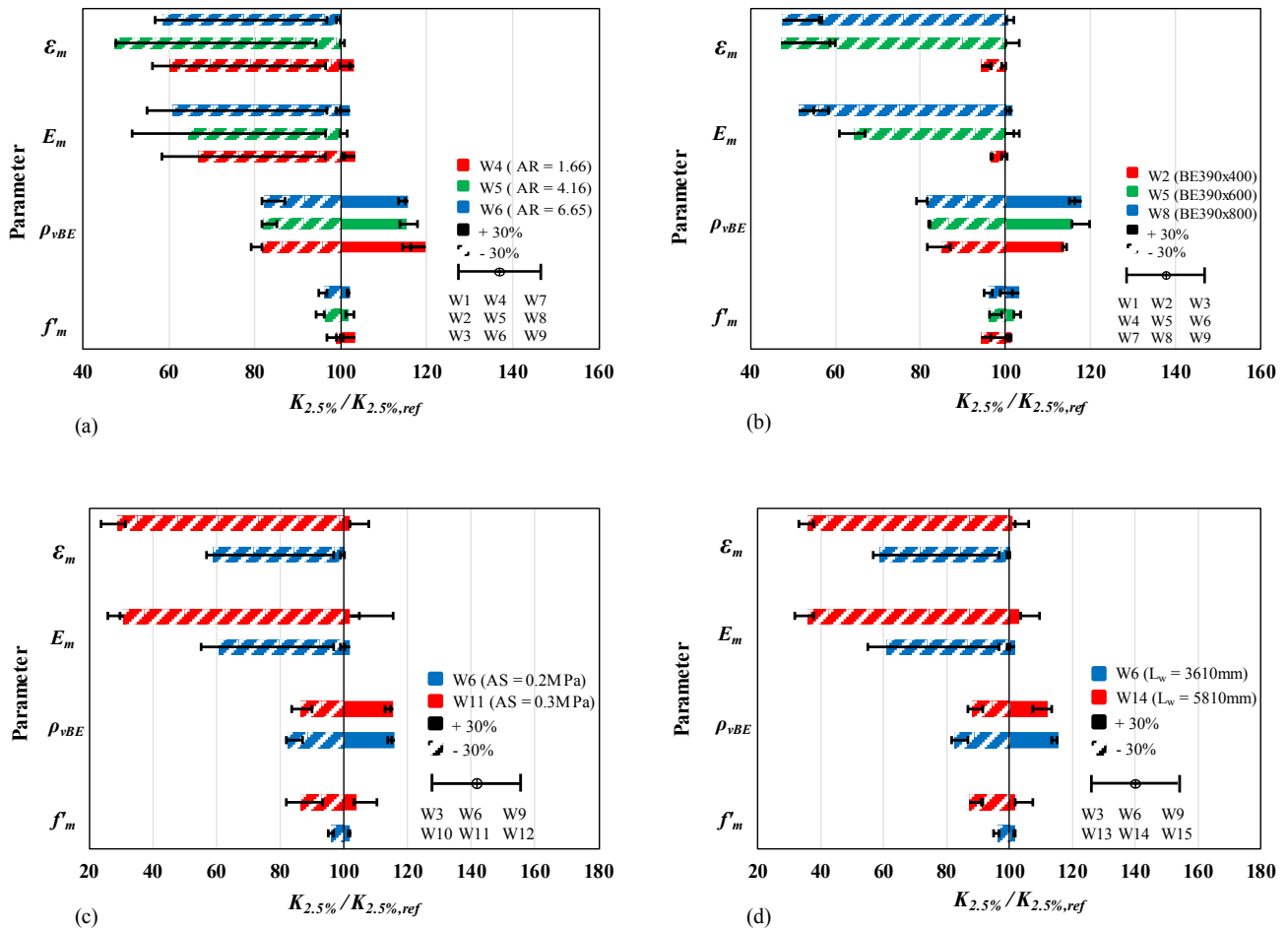
Figure 6.14 Sensitivity of the lateral effective stiffness ($K_{2.5\%}$) to ±30% changing of $\varepsilon_{mu}, f'_m, E_m,$ and ρ_{vBE} for RMSW+BEs having different (a) BE sizes and aspect ratios; (b) aspect ratios and BE sizes; (c) BE sizes and axial stresses; and (d) BE sizes and wall lengths

The ±30% change in the masonry compressive strength (f'_m) had different effects on $K_{2.5\%}$, in which $K_{2.5\%}$ changed by around 5% for walls with $AS = 0.2$ MPa/storey and $l_w = 3610$ mm and almost 15% for walls with higher axial stress $AS = 0.3$ MPa/storey and longer wall length $l_w = 3610$ mm, as depicted in Figures 6.14(a to d). Figure 6.14(c) shows that $K_{2.5\%}$ experienced a deteriorating behaviour estimated at nearly 70% drop when ε_{mu} and E_m decreased by 30% for walls

with higher axial stress (0.3 MPa/storey) compared to 40% drop for walls with lower axial stress (0.2 MPa/storey). However, increasing ε_{mu} and E_m by 30% had no significant influence on $K_{2.5\%}$ of the same group of walls. On the other side, $K_{2.5\%}$ was found to have more sensitivity to walls with higher wall length l_w = 5810 mm compared to their shorter length l_w = 3610 mm counterparts, as shown in Figure 6.14(d). The critical effect that the reduction of 30% in the masonry compressive strain at peak stress (ε_{mu}) had on the lateral stiffness of the RMSW+BEs ($K_{2.5\%}$) can be attributed to the rapid strength degradation (i.e. reduction in $Q_{2.5\%drift}$) which was not offset by its corresponding lateral displacement $\Delta_{2.5\%drift}$. Moreover, the deterioration of the lateral stiffness ($K_{2.5\%}$) may be attributed to the premature crushing of the most stressed compression zones at the wall extremities due to the assigned low ε_{mu} which in turn accelerate the reinforcement bars buckling resulting in rapid degradation of the RMSW+BEs hysteretic response.

6.8 Conclusions

Comprehensive numerical research work with a wide-range sensitivity analysis for the nonlinear cyclic response of RMSW+BEs was performed in this paper. This study investigated the influence of four wall's configurations, namely, the aspect ratio, the level of the axial compressive stress, the boundary element size, and the wall length on the seismic performance of RMSW+BEs. Furthermore, a detailed sensitivity analysis was performed to quantify the influence of four key design parameters, namely, the masonry compressive strain at peak stress (ε_{mu}), the masonry modulus of elasticity (E_m), the masonry compressive strength (f'_m), and the vertical reinforcement ratio of the boundary elements (ρ_{vBE}) on the seismic response components of the RMSW+BEs. Comparisons of the numerical results were conducted and presented in terms of the load-displacement hysteretic envelope curves as well as tornado charts showing the influence of the design parameters on the seismic behaviour of RMSW+BEs. This was achieved through the comparisons of each wall's seismic response components, namely, the lateral yield capacity (Q_y), the lateral ultimate capacity (Q_u), the effective elastic stiffness (K_{eff}), the secant stiffness at 2.5% drift ($K_{2.5\%}$), and the displacement ductility ($\mu_{\Delta0.8Qu}$) to its reference wall counterpart. Based on the numerical results of this study, the following conclusions were drawn:

1. The aspect ratio (*AR*) of the RMSW+BEs was found to have a significant effect on the seismic response of RMSW+BEs. The results showed that increasing the walls′ aspect ratio from 1.66

to 6.65 had a detrimental effect on the lateral ultimate capacity (Q_u) and the displacement ductility ($\mu_{\Delta 0.8Qu}$) of the RMSW+BEs having different wall's configurations.

2. Unlike increasing the wall's aspect ratios (AR), as the masonry boundary element (MBE) size increased, both the lateral ultimate capacity (Q_u) and the displacement ductility ($\mu_{\Delta 0.8Qu}$) increased.

3. Increasing the level of the axial compressive stress (AS) resulted in a slight increase in Q_u and a significant decrease in $\mu_{\Delta 0.8Qu}$. Results indicated that as the axial compressive stress increased by 50%, Q_u experienced an average increase of 11% for walls with aspect ratio of 6.65 and different MBE configurations. However, $\mu_{\Delta 0.8Qu}$ was found to decrease averagely by 22% when the axial compressive stress increased by 50%.

4. Increasing the wall length by 60% had a noticeable enhancement on the seismic response of RMSW+BEs. For walls having different MBE cross-sections and axial stress of 0.2 MPa/storey, Q_u was increased by almost 120%, whereas $\mu_{\Delta 0.8Qu}$ increased by nearly 38% when the walls length increased by 60%.

5. The lateral yield capacity (Q_y) of the RMSW+BEs was found to be highly sensitive to changing the vertical reinforcement ratio of the boundary elements (ρ_{vBE}). However, the influence of the masonry compressive strength (f'_m), the masonry modulus of elasticity (E_m), and the masonry compressive strain at peak stress (ε_{mu}) had insignificant effect on Q_y. It is noteworthy that Q_y for walls with lower aspect ratios, lower axial compressive stress, smaller wall length, and bigger boundary element size was more sensitive to the change of ρ_{vBE} compared to the other design parameters.

6. Changing the vertical reinforcement ratio (ρ_{vBE}) by ±30% was found to have the greater effect on the lateral ultimate capacity (Q_u) of the RMSW+BEs. Nevertheless, the masonry modulus of elasticity (E_m) and the masonry compressive strain at peak stress (ε_{mu}) were found to have no effect on Q_u. The masonry compressive strength (f'_m) was found to have a greater influence on Q_u compared to the effect of ε_{mu} and E_m. RMSW+BEs having lower aspect ratio, lower axial stress, shorter wall length, and bigger MBE sizes were found to be more sensitive to the change of ρ_{vBE} compared to their counterparts.

7. Decreasing the masonry compressive strain at peak stress (ε_{mu}) by 30% had a detrimental effect on the displacement ductility ($\mu_{\Delta 0.8Qu}$) of the RMSW+BEs compared to an increase of 30% of the same parameter. Moreover, $\mu_{\Delta 0.8Qu}$ was found to be extensively affected by the reduction

of ε_{mu}, E_m, and f'_m, respectively. On the contrary the change of ρ_{vBE} had marginal effect on $\mu_{\Delta 0.8Qu}$.

8. The lateral effective elastic stiffness (K_{eff}) of the RMSW+BEs was found to be highly sensitive to changing ρ_{vBE} and E_m when compared to the other design parameters. Moreover, K_{eff} of RMSW+BEs having larger MBE size (i.e., 390x800 mm) and lower aspect ratio $AR = 1.66$ was more sensitive to changing the ρ_{vBE} rather than their counterparts. Changing the masonry strain at peak stress (ε_{mu}) and the masonry compressive strength (f'_m) exhibited negligible influence on K_{eff}.

9. The secant stiffness of the RMSW+BEs at 2.5% drift ($K_{2.5\%}$) was greatly influenced by the reduction of the masonry compressive strain at peak stress (ε_{mu}) and the modulus of elasticity (E_m) rather than their increasing. On the contrary, changing the MBE vertical reinforcement ratio (ρ_{vBE}) by ±30 had an equal effect (i.e., ± ~20%) on $K_{2.5\%}$. RMSW+BEs having higher axial compressive stress and larger wall length were more sensitive to the change in ε_{mu} and E_m compared to their counterparts.

In conclusion, based on the results of this study, the seismic design of RMSW+BEs buildings can be optimized through careful choice of its design parameters. Enhancing the RMSW+BEs lateral yield capacity (Q_y), the lateral ultimate capacity (Q_u), and the lateral effective elastic stiffness (K_{eff}) can be achieved by increasing the vertical reinforcement ratio (ρ_{vBE}) and the masonry compressive strength (f'_m). On the other hand, reduction of the masonry strain at peak stress (ε_{mu}) and/or the masonry modulus of elasticity (E_m) greatly hinder the walls′ displacement ductility ($\mu_{\Delta 0.8Qu}$) and the secant stiffness at 2.5% drift ($K_{2.5\%}$). It is noteworthy that this study is limited to RMSW+BEs having the previously proposed values of the corresponding design parameters f'_m, ε_{mu}, E_m, and ρ_{vBE} with their ±30% changes. Further numerical and experimental investigations of the seismic response of RMSW+BEs with more wall's configurations (i.e., heights, and cross-sections, etc.) and various values of the design parameters are recommended for more comprehensive and reliable generalization of this study.

Chapter 7

Summary, Conclusions, and Recommendations

7.1 Summary

This thesis introduces in-depth experimental, analytical, and numerical investigations of fully grouted concrete-masonry prisms, RMBEs, and RMSW+BEs. The objectives of this thesis were achieved by examining the axial compressive behaviour of ungrouted and fully grouted concrete-masonry prisms, unreinforced MBEs, and confined RMBEs that were tested under axial monotonic and cyclic compression loading. Moreover, this thesis proposes axial and cyclic stress-strain models for confined RMBEs subjected to concentric axial compression. Furthermore, a numerical study focused on the sensitivity of the seismic response of RMSW+BEs to critical design parameters and various wall configurations was performed. This research work proposes alternatives to enhance the fully grouted RCM's compressive strength and ductility as well as recommendations to optimize the seismic design of RMSW+BEs by careful choice of the design parameters.

The first phase of this thesis′ experimental work investigated the axial compressive stress-strain behaviour of forty-two ungrouted and fully grouted concrete-masonry prisms. It aimed at developing high strength fully grouted masonry by omitting the detrimental factors (e.g., plastic and drying shrinkage of the grout) that affect its compressive strength. The influence of pre-wetting of dry masonry prisms, non-shrink grout, and grout strength on the axial compressive stress-strain response of half-scale and full-scale concrete masonry prisms was investigated. The influence of four different grout types (i.e., regular and non-shrink grouts) on the grout core shrinkage and the masonry prism compressive strengths and strains was investigated. Also, previously developed literature equations were examined against the test results to determine their capability of predicting the masonry prism compressive strength. This phase proposes recommendations to enhance the masonry compressive strength with alternative approaches to develop high-performance masonry for better sustainability of RMSW+BEs.

The experimental research work's second phase studied the axial compressive stress-strain behaviour of unreinforced unconfined MBEs and confined RMBEs. It aimed at examining different design parameters, namely, the vertical reinforcement ratio, the transverse steel

confinement ratio, the cross-section configuration, the construction pattern (i.e., stack pattern vs. running bond), and pre-wetting of dry masonry shell before grouting. Forty-three unreinforced MBEs and RMBEs were constructed and tested under concentric axial compression loading. This study evaluates the peak compressive stress and its corresponding strain, the strain at 25% strength degradation, the strain at 50% strength degradation, and the strain ductility. The test results were compared in terms of the stress-strain curves. Moreover, correlations of the test variables with the peak compressive stress and the strain ductility were established. This study sheds light on critical design parameters and construction procedures influencing the strength and ductility of confined RMBEs.

The third phase of the experimental work investigates the axial cyclic compressive behaviour of confined RMBEs. Twenty-six confined RMBEs were constructed and tested under axial cyclic compression loading. The influence of various parameters, namely, the grout compressive strength, the cross-section configuration, the vertical and transverse confinement steel configurations, and the pre-wetting of RMBEs, was studied. The results of this experimental phase and those reported in the second phase were utilized to examine if the monotonic stress-strain curves of the RMBEs form envelope curves to their counterparts, which were test under axial cyclic compression. This phase's results form a foundation and a step forward to further research efforts towards the axial cyclic behaviour of RMBEs.

Based on the experimental results of phase 2 and phase 3 and the available confined concrete models in the literature, axial and cyclic stress-strain models were developed to predict the full stress-strain curves of unconfined and confined RMBEs. The proposed stress-strain models can be integrated into numerical software packages to predict the lateral cyclic response of RMSW built with confined RMBEs.

This thesis also includes a numerical study focused on the sensitivity of the seismic response of RMSW+BEs to various wall configurations and critical design parameters. Three wall geometries, namely, the wall's aspect ratio, the RMBEs configurations, and the wall's length, were investigated. Moreover, the axial compressive stress level on the RMSW+BEs was examined. Four design parameters, namely, the vertical reinforcement ratio of the RMBEs, the masonry peak compressive stress, the masonry strain at peak stress, and the masonry modulus of elasticity, were studied. A 2D macro model was developed using displacement-based beam-column fiber elements

in the SeismoStruct software (2018). The numerical model was calibrated and validated to reliably predict the lateral nonlinear cyclic response of RMSW+BEs representing low, mid, and high-rise RCM structural wall buildings. This study's results present the sensitivity of the lateral yield capacity, the ultimate flexural capacity, the effective lateral stiffness, the lateral stiffness at 2.5% top drift, and the displacement ductility of RMSW+BEs to the studied parameters. These results facilitate the optimization of the seismic design of RMSW+BEs.

7.2 Conclusions

The seismic design of fully grouted RMSW+BEs necessitates reliable experimental and analytical investigations of their RMBEs. The RMBEs′ monotonic and cyclic behaviours are critical components in predicting the lateral cyclic response of RMSW+BEs. Therefore, this thesis investigated, experimentally and analytically, the axial monotonic and cyclic compressive stress-strain behaviour of RMBEs to develop axial and cyclic stress-strain models to predict the confined RMBEs stress-strain responses. This thesis also included a numerical study that focused on the influence of wall configurations and critical design parameters on the lateral nonlinear cyclic response of RMSWs built with confined RMBEs. These research efforts were performed to enhance the RMBEs′ compressive stress-strain response (i.e., strength and ductility) as well as contribute to the prediction of the seismic response and optimization of the seismic design of RMSW+BEs.

The findings of this research are divided into five sections. The first three sections provide the conclusions of the experimental results of the axial compressive behaviour of concrete-masonry prisms and RMBEs, whereas the fourth section presents the conclusions of the proposed models for the axial and cyclic stress-strain models for confined RMBEs. The fifth section concludes the findings of the numerical study that focused on the sensitivity of RMSW+BEs′ seismic response to the studied design parameters and walls′ configurations.

7.2.1 Conclusions of the fully grouted concrete-masonry prisms′ experimental results

- Increasing the grout compressive strength resulted in a non-proportional increase in the compressive strength of dry masonry prisms, and consistent results were recorded with different grout strengths. However, there was no obvious trend for the wet masonry prisms with increasing the grout strength.

- Masonry prisms constructed with non-shrink grout showed an increase in the compressive strength compared to masonry prisms with regular grout. Non-shrink grouted masonry prisms demonstrated a slightly higher initial modulus of elasticity, lesser strain corresponding to the peak stress, and similar post-peak behaviour compared to regular grouted masonry prisms.

- Pre-wetting of masonry prisms just before grouting was found to enhance their compressive strength.

- Wet masonry prisms were found to achieve the superposition of the grout core and the corresponding masonry shell strengths with different grout strengths.

- Clearly, wetting of dry masonry prisms is a promising construction procedure that significantly enhances grouted masonry's compressive strength. However, further research is required to determine the proper wetting procedure and ensure consistent results that can be adequately quantified.

- Half-scale masonry prisms showed a comparable modulus of elasticity and strain at peak stress to their full-scale counterparts. However, some discrepancies in the peak compressive stress and post-peak behaviour were observed.

Thus, enhancing the fully grouted concrete-masonry compressive strength can be achieved by combining non-shrink high-strength flowable grout with high-strength masonry blocks. Pre-wetting of dry masonry blocks is recommended for concrete-masonry columns and bearing walls (i.e., gravity walls) to enhance their axial load carrying capacity. However, pre-wetting's influence on the ductility of RMBEs and RMSW+BEs requires further experimental investigations to examine different pre-wetting approaches with different sectional confinement configurations (See conclusions of Sections 7.2.2 and 7.2.3).

7.2.2 Conclusions of the experimental results of RMBEs tested under axial monotonic compression

- The test results unveiled the most critical parameters affecting the peak compressive stress of RMBEs, which are the pre-wetting of dry masonry shells before grouting and increasing the vertical reinforcement ratio.

- Increasing the vertical reinforcement ratio enhanced the peak stress of RMBEs built with square or rectangular sections. However, RMBEs with higher reinforcement

ratios experienced the first hoop fracture sooner than those constructed with a lower ratio. Consequently, the former exhibited rapid deteriorating post-peak behaviour, lesser strain ductility, and earlier crushing of the grout core than the latter.

- The strain ductility of the tested RMBEs experienced a remarkable improvement as the volumetric ratio of the confinement reinforcement increased.

- Rectangular RMBEs showed enhanced performance than their square counterpart, especially the stress drop following the face shell spalling was significantly minimized.

- Unreinforced dry MBEs built with running-bond pattern showed less compressive strength than those laid in the stack pattern. Conversely, wet running-bond specimens had approximately similar strength as those with the stack pattern.

- Wet RMBEs built in the running-bond pattern had higher peak stress than those constructed in the stack pattern.

- Pre-wetting of dry unreinforced MBEs and confined RMBEs considerably enhanced their peak stress. However, the enhancement of the wet MBEs prisms' compressive strength adversely affected the strain ductility of their corresponding RMBEs.

- Based on the experimental results, it is recommended that upcoming versions of the CSA S304 shall correlate the design masonry ultimate compressive strain to the confinement configurations and cross-sectional shape of the RMBEs that are incorporated within the RMSW+BEs.

- It is recommended that increasing the vertical reinforcement ratio in RMBEs, especially when increasing the number of steel bars, to be associated with increasing the confinement ratio. This is to ensure that the additional bars are laterally restrained and alleviate their deterioration effect on the RMBEs' strain ductility.

Therefore, this study's findings suggest that the peak stress of confined RMBEs can be enhanced by increasing their vertical reinforcement ratio. This should be associated with adequate confinement to the grout core to further enhance the strain ductility, prevent premature buckling of vertical steel, and alleviate the grout core strength's rapid deterioration. The strain ductility of confined RMBEs can be further enhanced by reducing the confinement hoops' spacings rather than increasing their diameters.

7.2.3 Conclusions of the experimental results of RMBEs tested under axial cyclic compression loading

- Unlike RC members, RMBEs′ unconfined part accounts for ~45-60% of their overall cross-sectional area. However, the confined masonry core exhibited peak stress higher than that of the unconfined part due to the confinement hoops′ strength enhancement.

- The RMBEs′ cyclic response showed that increasing the unloading strain increased the residual strains, resulted in steeper unloading branches, reduced the reloading branches′ stiffness, and yielded bulgier cyclic loops.

- Reduction of confinement hoops′ spacing introduced more effective confinement to the tested RMBEs than increasing the confinement hoops size.

- Although RMBEs built with 20 MPa grout compressive strength showed higher peak stresses than those constructed with 50 MPa grout, they exhibited much lower strain ductility and steeper post-peak behaviour.

- Although pre-wetting of dry RMBEs significantly enhanced their peak compressive stress, the test results revealed that it negatively influenced their strain ductility.

Therefore, low grout compressive strengths are not recommended for confined RMBEs incorporated in RMSW+BEs when designed for high ductility demands. Also, due to its adverse effect on the strain ductility of the tested RMBEs, pre-wetting of ductile RMSW+BEs can not be suggested unless further detailed experimental evaluation of different pre-wetting schemes of RMBEs and RMSW+BEs with different sections and confinement configurations are conducted.

7.2.4 Conclusions of the proposed monotonic and cyclic stress-strain models of RMBEs

- Axial monotonic and cyclic stress-strain models were proposed for unconfined and confined concrete-masonry boundary elements subjected to concentric compression loading.

- The proposed monotonic model showed excellent conformity with the experimental rising branch of the stress-strain curves up to the peak stress and good agreement with the stress drop corresponding to the unconfined masonry's failure (i.e., at face shell spalling). Moreover, the model could predict the second peak stress observed in the experimental stress-strain curves due to the confinement hoops′ enhancement to the

confined masonry core; this observation was not captured by previous stress-strain models proposed for confined masonry.

- The proposed cyclic model was able to capture the unloading curves, the reloading branches, the new stress points due to cyclic degradation, and the softening of the unloading branches with increasing unloading strains. Besides, the plastic strains were captured within a very reasonable range, mostly when unloading occurs from the envelope curve after the confined masonry peak stress was attained.

7.2.5 Conclusions of the numerical work results

- The results showed that increasing the walls′ aspect ratio from 1.66 to 6.65 had a detrimental effect on the lateral ultimate capacity and the displacement ductility of the RMSW+BEs having different wall configurations.

- As the walls′ RMBEs size increased, both the lateral ultimate capacity and the displacement ductility significantly improved.

- Increasing the axial compressive stress level resulted in a slight increase in the lateral ultimate capacity and a significant reduction in the displacement ductility.

- Increasing the RMSW+BEs′ length by 60% had a noticeable enhancement on their seismic response in terms of the lateral flexural ultimate capacity and the displacement ductility.

- Changing the vertical reinforcement ratio by ±30% was found to have the most significant effect on the lateral yield and ultimate capacities of the RMSW+BEs; however, the influence of the masonry compressive strength, the masonry modulus of elasticity, and the masonry compressive strain at peak stress had an insignificant effect on them. The masonry compressive strength was found to have a more significant influence on the RMSW+BEs′ lateral ultimate capacity than the effect of the strain at peak stress and the modulus of elasticity.

- Decreasing the masonry strain at peak stress by 30% had a detrimental effect on the RMSW+BEs′ displacement ductility compared to the 30% increase of the same parameter.

- The RMSW+BEs′ displacement ductility is significantly affected by reducing the masonry strain at peak stress, the modulus of elasticity, and the masonry compressive strength, respectively.

- The lateral effective elastic stiffness of the RMSW+BEs was highly sensitive to changing the vertical steel ratio of the RMBEs and the masonry modulus of elasticity compared to the other design parameters.

- The RMSW+BEs′ secant stiffness at 2.5% drift was greatly influenced by reducing the masonry strain at peak stress and the modulus of elasticity rather than their increasing.

Based on this study's results, the seismic design of RMSW+BEs buildings can be optimized through careful choice of its design parameters. Enhancing the RMSW+BEs′ lateral yield capacity, ultimate capacity, and effective elastic stiffness can be achieved by increasing the vertical reinforcement ratio and masonry compressive strength. On the other hand, reducing the masonry strain at peak stress and/or the masonry modulus of elasticity greatly hinders the walls′ displacement ductility and the secant stiffness at 2.5% drift.

7.3 Limitations of This Thesis

It is noteworthy that the current research work has some limitations that can be summarized as follows:

- The first phase of the experimental research work investigated concrete-masonry prisms with a height-to-thickness ratio (h/t) of 2 according to the ASTM 1314-14 specifications. Therefore, further experimental research can be conducted on masonry prisms with different height-to-thickness ratios to enrich the state-of-the-art.

- All the RMBEs were constructed using C-shape concrete-masonry units. However, masonry stretcher units can also be investigated to quantify the influence of using different masonry units on the RMBEs′ behaviour.

- This thesis investigated limited prewetting schemes for the tested masonry prisms and the RMBEs. Therefore, further experimental research for various pre-wetting methods, including its application procedures and timing, are encouraged.

- This research focused on the axial monotonic and cyclic compressive behaviour of RMBEs. However, investigating the behaviour of confined RMBEs under fully-reversed cyclic loading is recommended.

- The numerical study focused on the sensitivity of the seismic response of RMSW+BEs to different design parameters and wall configurations. The developed numerical model was built based on the fiber modelling approach where the model cannot adequately capture the shear deformations. Therefore, the provided numerical model is most suitable for flexural-dominated RMSW+BEs.

7.4 Recommendations for Future Work

Based on this thesis's findings, the following recommendations are vital for the continuous research efforts towards enhancing the behaviour of RMBEs and RMSW+BEs. These recommendations are summarized as follows:

- Testing grouted concrete-masonry prisms with different height-to-thickness ratios, different pre-wetting schemes, and multiple masonry block compressive strengths.

- Investigating the behaviour of confined RMBEs under eccentric and/or fully reversed axial cyclic loading (i.e., including tension) to enhance the simulation of the RMSWs′ confined masonry boundary elements.

- Examining additional confinement configurations of RMBEs, especially those with increased vertical steel ratios.

- Further detailed experimental tests of different pre-wetting schemes of RMBEs and RMSW+BEs with different sections and confinement configurations are recommended to confirm its applicability.

- Quantifying and comparing the cyclic behaviour of RMBEs built with different masonry units (e.g., stretcher vs. C-shape) and different height-to-thickness ratios.

- The proposed monotonic and cyclic stress-strain models can be validated against additional experimental results of RMBEs, when available.

- The proposed stress-strain models can be integrated into numerical software tools to be further validated in predicting the lateral cyclic behaviour of RMSW+BEs

- Experimental investigations of the seismic response of RMSW+BEs with various constituent materials properties and different design parameters are recommended.

References

Abboud, B. E., Hamid, A. A., and Harris, H. G. (1990). "Small-scale modeling of concrete block masonry structures." *ACI Structural Journal*, 87(2), 145–155.

AbdelRahman, B., and Galal, K. (n.d.). "Experimental Investigation of Axial Compressive Behavior of Square and Rectangular Confined Concrete-Masonry Structural Wall Boundary Elements." *Engineering Structures*, Submitted.

AbdelRahman, B., and Galal, K. (2020). "Influence of pre-wetting, non-shrink grout, and scaling on the compressive strength of grouted concrete masonry prisms." *Construction and Building Materials*, 241.

Abo El Ezz, A., Seif Eldin, H. M., and Galal, K. (2015). "Influence of confinement reinforcement on the compression stress-strain of grouted reinforced concrete block masonry boundary elements." *Structures*, Elsevier B.V., 2, 32–43.

Albutainy, M., Ashour, A., and Galal, K. (2017). "Effect of Boundary Elements Confinement Level on the Behaviour of Reinforced Masonry Structural Walls with Boundary Elements." *13th Canadian Masonry Symposium*, Halifax, Nova Scotia, Canada.

Aly, N. E. (2019). "Seismic Performance and Building Height Limits of Ductile Reinforced Concrete Masonry Shear Walls with Boundary Elements." Concordia University, Montreal, Canada.

Aly, N., and Galal, K. (2019). "Seismic performance and height limits of ductile reinforced masonry shear wall buildings with boundary elements." *Engineering Structures*, Elsevier, 190(April), 171–188.

Aly, N., and Galal, K. (2020a). "In-plane cyclic response of high-rise reinforced concrete masonry structural walls with boundary elements." *Engineering Structures*, Elsevier, 219(August 2019).

Aly, N., and Galal, K. (2020b). "Experimental Investigation of Axial Load and Detailing Effects on the Inelastic Response of Reinforced-Concrete Masonry Structural Walls with Boundary Elements." *Journal of Structural Engineering*, 146(12), 04020259.

Aly, N., and Galal, K. (2020c). "Effect of Ductile Shear Wall Ratio and Cross-Section Configuration on Seismic Behavior of Reinforced Concrete Masonry Shear Wall Buildings." *Journal of Structural Engineering*, 146(4), 1–15.

American Society for Testing and Materials (ASTM). (2013). *Standard Test Method for Compressive Strength of Hydraulic Cement Mortars. C109/C109M-13*. West Conshohocken, PA, United States of America.

American Society for Testing and Materials (ASTM). (2014). *Standard Test Method for Compressive Strength of Masonry Prisms. C1314-14*. West Conshohocken, PA, United States of America.

American Society for Testing and Materials (ASTM). (2015a). *Standard Specification for Deformed and Plain Carbon-Steel Bars for Concrete Reinforcement. A615/A615M-15a*. West

Conshohocken, PA, United States of America.

American Society for Testing and Materials (ASTM). (2015b). *Standard Test Methods and Definitions for Mechanical Testing of Steel Products. ASTM A370-15*. West Conshohocken, PA, United States of America.

American Society for Testing and Materials (ASTM). (2015c). *Standard Test Methods for Sampling and Testing Concrete Masonry Units and Related Units. C140-15*. West Conshohocken, PA, United States of America.

American Society for Testing and Materials (ASTM). (2015d). *Compressive Strength of Cylindrical Concrete Specimens. C39/C39M-15a*. West Conshohocken, PA, United States of America.

American Society for Testing and Materials (ASTM). (2018). *Standard Specification for Steel Welded Wire Reinforcement, Plain, for Concrete. A1064/A1064M-18a*. West Conshohocken, PA, United States of America.

Baba, A., and Senbu, O. (1986). "Influencing Factors on Prism Strength of Grouted Masonry and Fracture Mechanism under Uniaxial Loading." Building Research Institute, Jaban.

Banting, B. (2013). "Seismic Performance Quantification Of Concrete Block Masonry Structural Walls With Confined Boundary Elements And Development Of The Normal Strain-Adjusted Shear Strength Expression (Nssse)." McMaster University.

Banting, B., and El-Dakhakhni, W. (2012). "Force- and Displacement-Based Seismic Performance Parameters for Reinforced Masonry Structural Walls with Boundary Elements." *Journal of Structural Engineering*, 138(12), 1477–1491.

Banting, B., and El-Dakhakhni, W. (2014). "Seismic Performance Quantification of Reinforced Masonry Structural Walls with Boundary Elements." *Journal of Structural Engineering*, 140(5), 1–15.

Blocfiller. (2015). "Concrete masonry unit grout, Technical data sheet, March 2015." <https://www.daubois.com/docs/blocfiller-en.pdf> (Apr. 6, 2018).

Bohl, A., and Adebar, P. (2011). "Plastic Hinge Lengths in High-Rise Concrete Shear Walls." ACI Structural Journal, 108(2), 148–157.

Boult, B. F. (1979). "Concrete Masonry Prism Testing." *Journal Proceedings*, 76(4), 513–536.

Calabrese, A., Almeida, J. P., and Pinho, R. (2010). "Numerical issues in distributed inelasticity modeling of RC frame elements for seismic analysis." *Journal of Earthquake Engineering*, Taylor & Francis Group, 14(SUPPL. 1), 38–68.

Canadian Standards Association (CSA). (2014a). *Design of masonry structures. S304-14*. Mississauga, Ontario, Canada.

Canadian Standards Association (CSA). (2014b). *Mortar and grout for unit masonry. A179-14*. National Standard of Canada CAN / CSA-A179-14, Mississauga, Ontario, Canada.

Cusson, D., and Paultre, P. (1994). "High-strength concrete columns confined by rectangular ties." *Journal of Structural Engineering*, 120(3), 783–804.

Cusson, D., and Paultre, P. (1995). "Stress-Strain Model for Confined High-Strength Concrete." *Journal of Structural Engineering*, 121(3), 468–477.

Dhanasekar, M., and Shrive, N. G. (2002). "Strength and deformation of confined and unconfined grouted concrete masonry." *ACI Structural Journal*, 99(6), 819–826.

Dodd, L. L., and Restrepo-Posada, J. I. (1995). "Model for Predicting Cyclic Behavior of Reinforcing Steel." *Journal of Structural Engineering*, 121(3), 433–445.

Drysdale, R. G., and Hamid, A. A. (1979). "Behavior of Concrete Block Masonry Under Axial Compression." *ACI Journal Proceedings*, 76(6), 707–721.

Drysdale, R. G., and Hamid, A. A. (2005). *Masonry Structures Behaviour and Design*. Canada Masonry Design Centre, Mississauga, ON, Canada.

El-Dakhakhni, W., and Ashour, A. (2017). "Seismic Response of Reinforced-Concrete Masonry Shear-Wall Components and Systems: State of the Art." *Journal of Structural Engineering (United States)*, 143(9), 1–25.

Enrique Martínez-Rueda, J., and Elnashai, A. S. (1997). "Confined concrete model under cyclic load." *Materials and Structures/Materiaux et Constructions*, 30(197), 139–147.

Ezzeldin, M., Wiebe, L., and El-Dakhakhni, W. (2016). "Seismic Collapse Risk Assessment of Reinforced Masonry Walls with Boundary Elements Using the FEMA P695 Methodology." *Journal of Structural Engineering*, 142(11), 04016108.

FEMA P695. (2009). *Quantification of Building Seismic Performance Factors*. *Fema P695*, Washington D.C.

Fortes, E. S., Parsekian, G. A., and Fonseca, F. S. (2014). "Relationship between the Compressive Strength of Concrete Masonry and the Compressive Strength of Concrete Masonry Units." *Journal of Materials in Civil Engineering*, 25(3), 403–410.

Gayed, M., and Korany, Y. (2011). "Concrete Masonry Compressive Strength Using the Unit Strength Method." *University of Alberta*, (102).

Giambanco, G., Rizzo, S., and Spallino, R. (2001). "Numerical analysis of masonry structures via interface models." *Computer Methods in Applied Mechanics and Engineering*, North-Holland, 190(49–50), 6493–6511.

Hamid, A. A., Drysdale, R. G., and Heidebrecht, A. C. (1978). "Effect of Grouting on the Strength Characteristics of Concrete Block Masonry." *Proceedings of the North American Masonry Conference*.

Hamzeh, L., Ashour, A., and Galal, K. (2018). "Development of Fragility Curves for Reinforced-Masonry Structural Walls with Boundary Elements." *Journal of Performance of Constructed Facilities*, 32(4), 04018034.

Hosseinzadeh, S., and Galal, K. (2020). "Seismic Fragility Assessment and Resilience of Reinforced Masonry Flanged Wall Systems." *Journal of Performance of Constructed Facilities*, 34(1).

Joyal, M. (2014). "Enhanced ductility of masonry shear walls using laterally confined (self-

reinforced) concrete block." McMaster University.

Karsan, I. ., and Jirsa, J. . (1969). "Behavior of Concrete Under Compressive Loadings." *Proceedings of the American Society of Civil Engineers*, 95(ST12), 2543–2562.

Kent, D. C., and Park, R. (1971). "Flexural members with confined concrete." *Journal of Structural Engineering*, 97(7), 1969–1990.

Khalaf, F. M., Hendry, A. W., and Fairbairn, D. R. (1994). "Study of the compressive strength of blockwork masonry." *ACI Structural Journal*, 91(4), 367–375.

Korany, Y. (2012). "Masonry Chair Report No . 105 ☐ 2012 Concrete masonry compressive strength using the unit strength method for grouted masonry." (May 2012).

Korany, Y., and Glanville, J. (2005). "Comparing Masonry Compressive Strength in Various Codes." *Concrete International*, 27(07), 35–40.

Long, L., Hamid, A. A., and Drysdale, R. G. (2005). "Small-scale modelling of concrete masonry using ½-scale units: A preliminary study." *10th Canadian Masonry Symposium, Banff, Alberta*, 1–10.

Lourenço, P. B., and Rots, J. G. (1997). "Multisurface Interface Model for Analysis of Masonry Structures." *Journal of Engineering Mechanics*, ASCE - American Society of Civil Engineers, 123(7), 660–668.

Mander, J. B., Priestley, M. J. N., and Park, R. (1988a). "Theoretical stress-strain model for confined concrete." *Journal of Structural Engineering*, 114(8), 1804–1826.

Mander, J. B., Priestley, M. J. N., and Park, R. (1988b). "Observed stress-strain behaviour of confined concrete." *Journal of Structural Engineering*, 114(8), 1827–1849.

Maurenbrecher, A. H. P. (1980). "Effect of the test procedures on compressive strength of masonry prisms." *Second Canadian Masonry Symposium*, Ottawa, 119–132.

McKenna, F., Fenves, G. L., and Scott, M. H. (2000). "Open system for earthquake engineering simulation." University of California, Berkeley, CA.

Menegotto, M., and Pinto, P. E. (1973). "Method of analysis for cyclically loaded R.C. plane frames including changes in geometry and non-elastic behaviour of elements under combined normal force and bending." *Symposium on the Resistance and Ultimate Deformability of Structures Acted on by Well Defined Repeated Loads, International Association for Bridge and Structural Engineering*, Zurich, Switzerland, 15–22.

Mohamed, M. (2018). "Compressive Stress-strain of Unreinforced Masonry Boundary Element Prisms." Concordia University, Montreal, Quebec, Canada.

NBCC, N. R. C. C. (2015). *National Building Code of Canada (NBCC)*. Ottawa, ON.

NCMA. (1994). *Research Evaluation of Flexural Tensile Strength of Concrete Masonry*.

Obaidat, A. T., Abo El Ezz, A., and Galal, K. (2017). "Compression behavior of confined concrete masonry boundary elements." *Engineering Structures*, Elsevier Ltd, 132, 562–575.

Obaidat, A. T., Ashour, A., and Galal, K. (2018). "Stress-Strain Behavior of C-Shaped Confined

Concrete Masonry Boundary Elements of Reinforced Masonry Shear Walls." *Journal of Structural Engineering*, 144(8), 04018119.

Obaidat, A. T., Ashour, A., and Galal, K. (2019). "Stress-strain model for C-shape confined concrete masonry boundary elements of RM shear walls." *Engineering Structures*, Elsevier, 183(August 2017), 1059–1071.

Paulay, T., and Priestly, M. J. N. (1992). *Seismic Design of Reinforced Concrete and Masonry Buildings*. *Seismic Design of Reinforced Concrete and Masonry Buildings*, John Wiley & Sons, Inc., Hoboken, NJ, USA.

Popovics, S. (1973). "A numerical approach to the complete Stress-strain curve of concrete." *Cement and Concrete Research*, 3(July), 583–599.

Priestley, M. J. N., and Elder, D. M. (1983). "Stress-Strain Curves for Unconfined and Confined Concrete Masonry." *ACI Journal*, 80(3).

Quikrete®non-shrink precision Grout. (2015). "Product No. 1585-00, Revised 28 August 2015." <https://www.quikrete.com/pdfs/data_sheet-non-shrink precision grout 1585-00.pdf> (Apr. 6, 2018).

Romagna, R. H., and Roman, H. R. (2002). "Compressive Strength of Grouted and Un-grouted Concrete Block Masonry." *Proceedings of the British Masonry Society*, 399–404.

Ross, M. D. (2013). "Recalibration of the Unit Strength Method for Determining the Compressive Strength of Grouted Concrete Masonry." University of Alberta.

Sajjad, N. (1990). "Confinement of Concrete Masonry." University of California - Los Angeles.

Scrivener, J. C., and Baker, L. R. (1988). "Factors Influencing Grouted Masonry Prism Compressive Strength." 874–883.

Seible, F., Hegemier, G. A., Igarashi, A., and Kingsley, G. R. (1994a). "Simulated Seismic-Load Tests on Full-Scale Five-Story Masonry Building." *Journal of Structural Engineering*.

Seible, F., Priestley, M. J. N., Kingsley, G. R., and Kürkchübasche, A. G. (1994b). "Seismic Response of Full-Scale Five-Story Reinforced-Masonry Building." *Journal of Structural Engineering*.

Seif ElDin, H. (2016). "In-Plane Shear Behaviour of Fully Grouted Reinforced Masonry Shear Walls." Concordia University.

SeismoSoft Inc. (2018). "SeismoStruct - Structural Assessment & Retrofitting - Seismosoft." https://seismosoft.com/products/seismostruct.

Shedid, M. T., El-Dakhakhni, W. W., and Drysdale, R. G. (2010). "Alternative Strategies to Enhance the Seismic Performance of Reinforced Concrete-Block Shear Wall Systems." *Journal of Structural Engineering*, 136(6), 676–689.

Shing, P. B., Carter, E. W., and Noland, J. L. (1993). "Influence of confining steel on flexural response of reinforced masonry shear walls." *The Masonry Society Journal*, 11(4), 72–85.

SikaGrout®-212. (2017). "Product Data Sheet Edition 12.2017/v1."

<https://can.sika.com/dms/getdocument.get/93842c32-adb3.../SikaGrout212_pds.pdf> (Feb. 8, 2018).

Sinha, B. P., Gerstle, K. H., and Tulin, L. G. (1964a). "Stress-Strain Relations for Concrete Under Cyclic Loading." *ACI Journal Proceedings*, 61, 195–211.

Sinha, B. P., Gerstle, K. H., and Tulin, L. G. (1964b). "Stress-Strain Relations for Concrete Under Cyclic Loading." *ACI Journal Proceedings*, 61(2), 195–211.

Steadman, M., Drysdale, R. G., and Khattab, M. M. (1995). "Influence of Block Geometry and Grout Type on Compressive Strength of Block Masonry.pdf." *Seventh Canadian Masonry Symposium*.

Sturgeon, G. R., Longworth, J., and Warwaruk, J. (1980). "An Investigation of Reinforced Concrete Block Masonry Columns." *University of Alberta Structural Engineering Report No. 91*, (91).

TMS 402/602-16. (2016). *Building Code Requirements and Specification for Masonry Structures*. The Masonry Society.

Tomaževič, M., and Weiss, P. (1994). "Seismic Behavior of Plain- and Reinforced-Masonry Buildings." *Journal of Structural Engineering*.

Yankelevsky, D. Z., and Reinhardt, H. W. (1987). "Model for cyclic compressive behavior of concrete." *Journal of Structural Engineering*, 113(2), 228–240.

Appendix A

Additional data to the experimental work (Chapters 3, 4, and 5)

A.1 General

This appendix provides supplemental information to the experimental research work presented in chapters 3, 4, and 5 of this thesis. Additional text, explanations (when needed), tables, and photos are presented. These supplemental data focused on each phase's construction procedures, testing setups, and failure modes of the tested specimens.

A.2 Construction, testing, and failure modes of concrete-masonry prisms

Figure A.1 Typical construction of half-scale and full-scale masonry prisms

Figure A.2 Typical grouting of masonry prisms and sampling of block moulded grout and cylinders

Figure A.3 Pre-wetted masonry prisms and masonry blocks before grouting

Figure A.4 Dry and wet grouted masonry prisms after hardening

(a)   (b)

Figure A.5 (a) regular grouted; and (b) non-shrink grouted masonry prisms after hardening
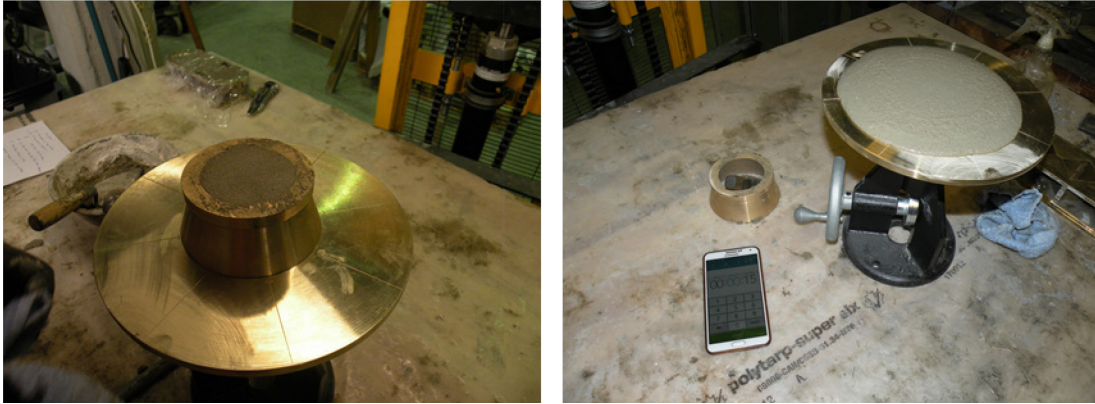
Figure A.6 Mortar flowability test

(a)

(b)

(c)

Figure A.7 Typical Failure of (a) grout cylinder; (b) block moulded grout prism; and (c) masonry stretcher block
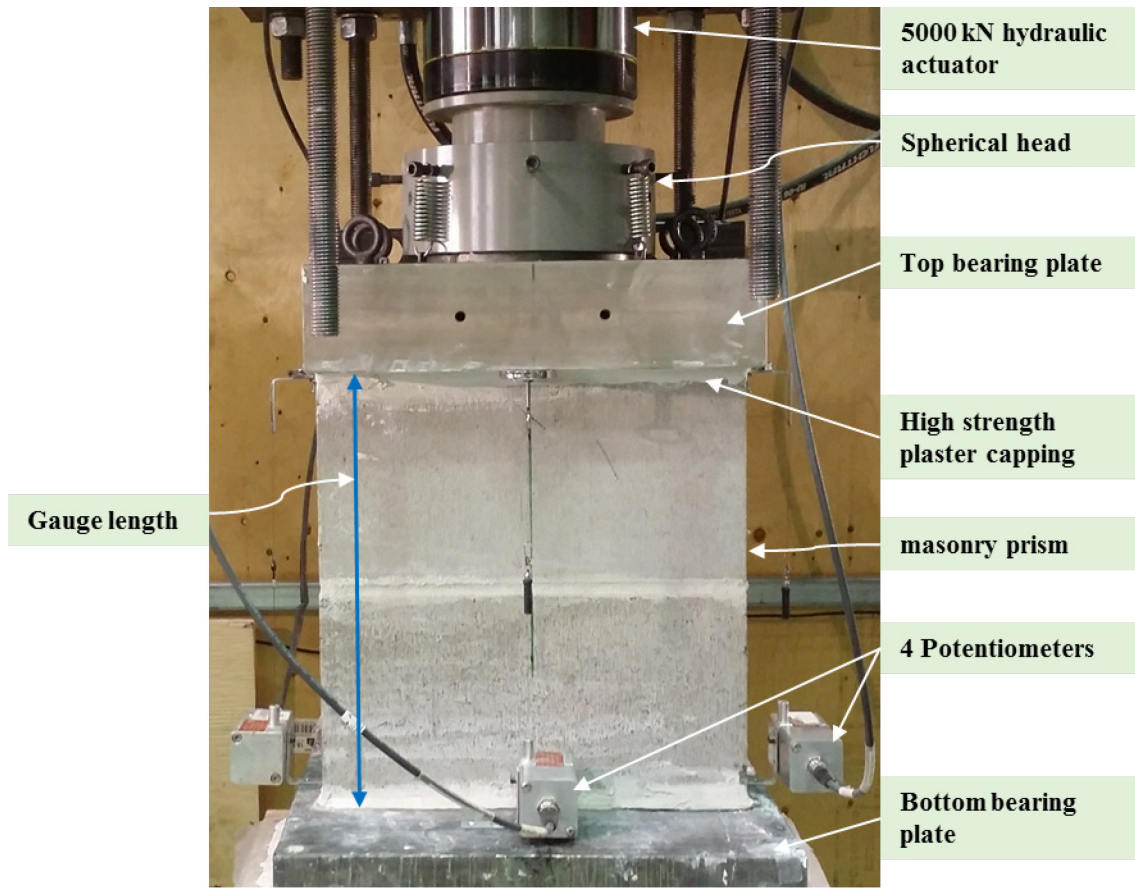
Figure A.8 Compression testing of full-scale masonry prism

A.3 Construction, testing, and failure modes of RMBEs

In this section, the construction procedures, the testing of constituent materials, as well as the failure modes of unreinforced and reinforced masonry boundary elements are presented. Moreover, the concrete top cap and bottom concrete footings mix proportions are reported.
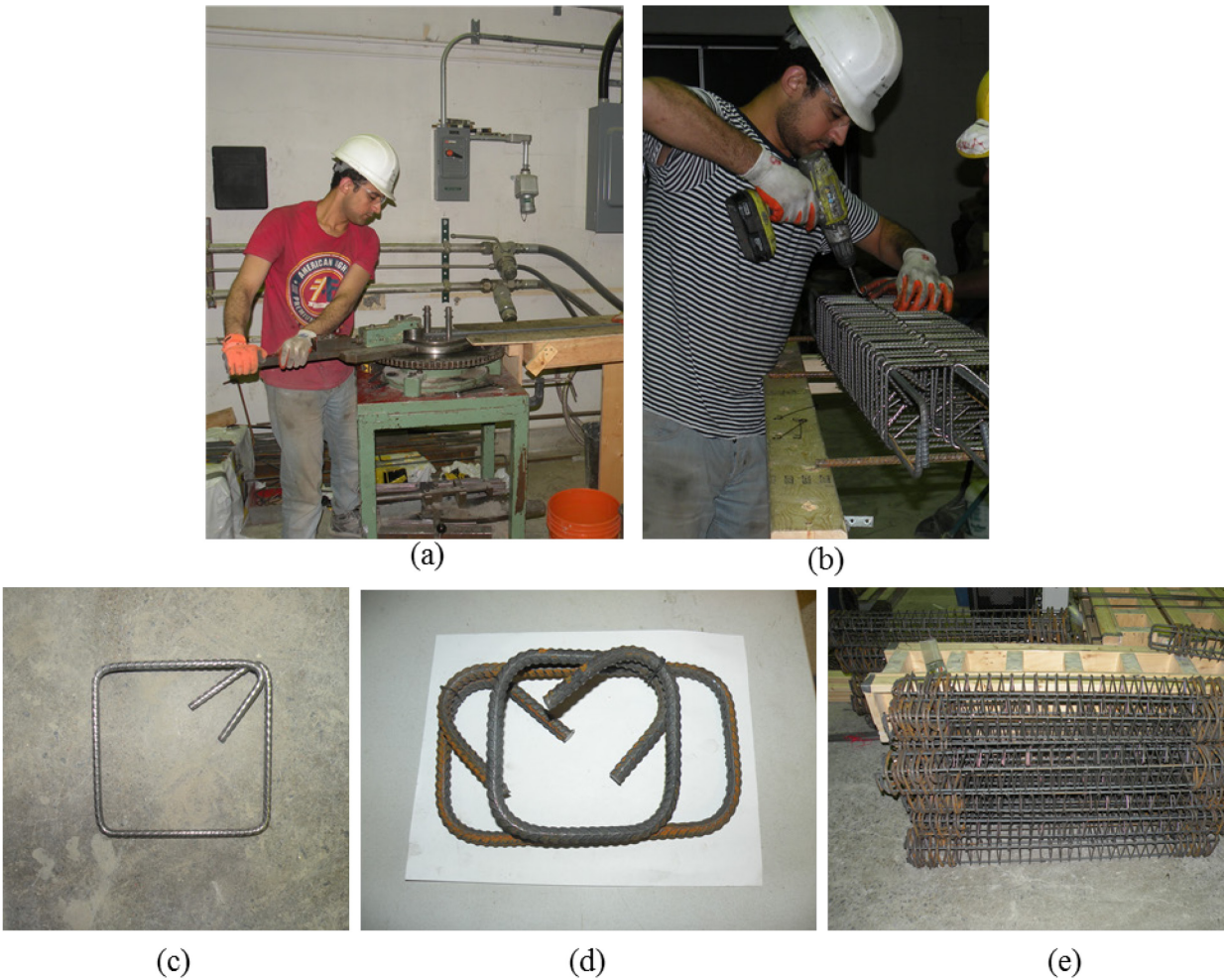
Figure A.9 Fabrication of steel cages: (a) bending vertical steel bars; (b) tying steel cages; (c) D4 confinement hoop; (d) 10M hoops for concrete footing; and (e) assembled steel cages
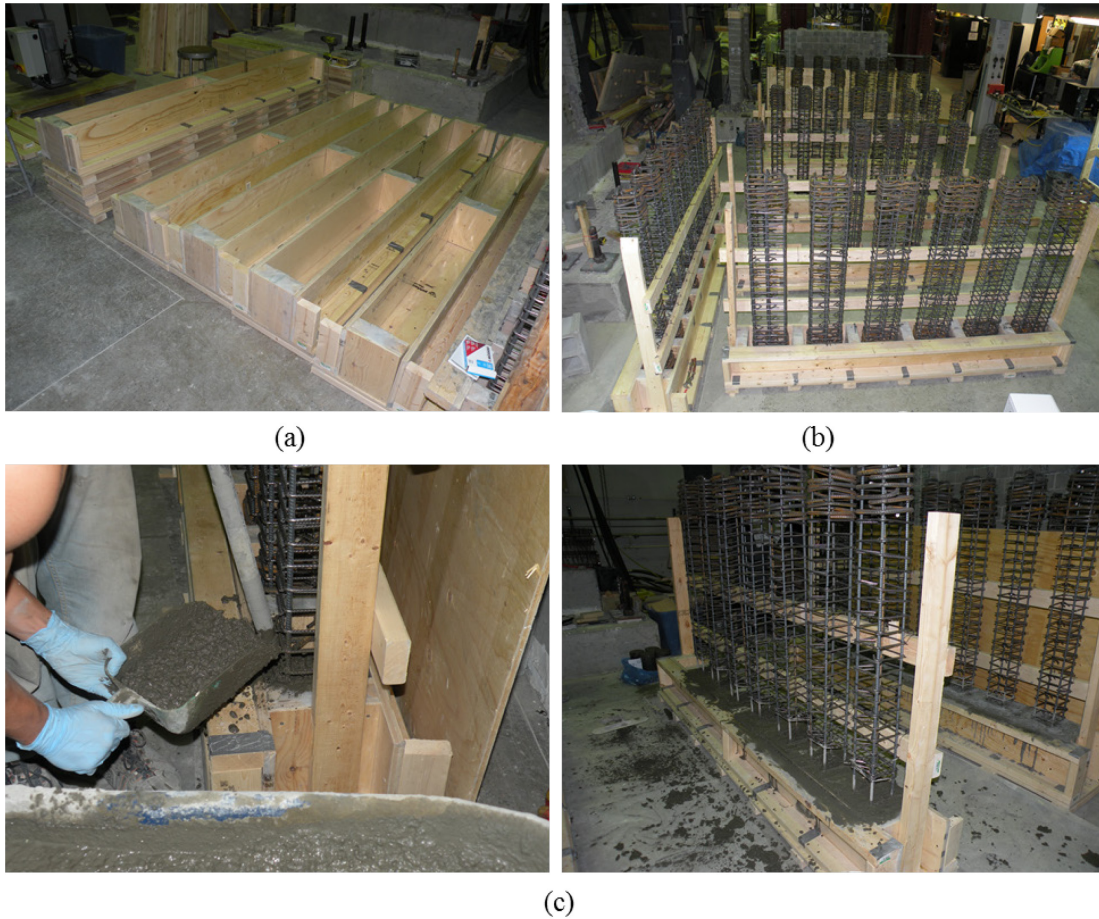
Figure A.10 Bottom concrete footing casting: (a) fabricated wooden forms for RMBEs; (b) Steel cages centered in wooden forms; (c) casting of concrete

Table A.1 Top concrete cap and bottom concrete footing's mix proportions

	Cement GUBSF*	Water	Sand	Coarse aggregate	Superplasticizer
% by weight	1.00	0.35	1.63	1.47	1140 ml/100 kg cement
Weights For 1 m3 (kg)	539.33	188.76	879.10	792.81	6.15 liters

* General use blended with 8% silica fume
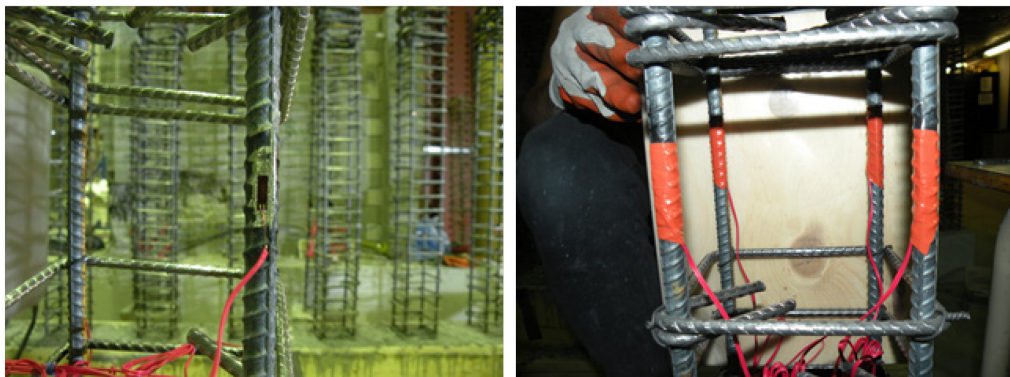
Figure A.11 Installation procedures of strain gauges: (a) grinding of steel bars; (b) installation kit of strain gauges; (c) attaching strain gauges; and (d) strain gauges′ final state

Figure A.12 Typical laying of masonry blocks: (a) laying of first Masonry course; (b) laying of second masonry course; (c) fully built square RMBEs; and (d) fully built rectangular RMBEs

Figure A.13 Dry and wet RMBEs before grouting

Figure A.14 Grouting of unreinforced MBE prisms and RMBEs

Figure A.15 Construction of top concrete caps: (a) RMBEs after grouting; (b) attaching wooden forms and casting of concrete; (c) curing of concrete
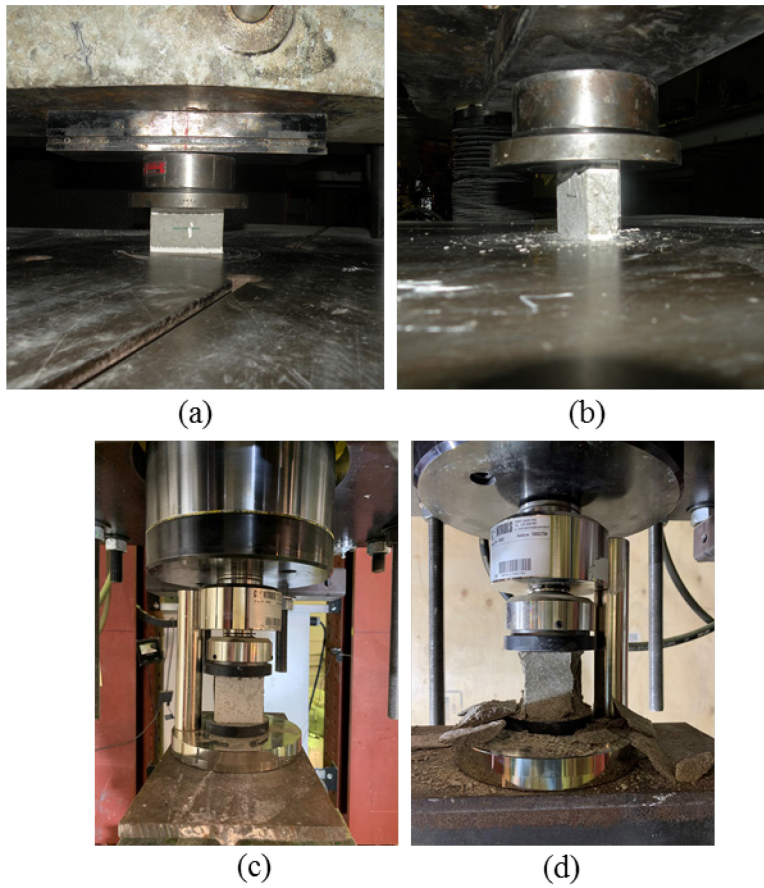
Figure A.16 Sampling of mortar cubes

Figure A.17 (a) Typical test of masonry coupon; (b) typical failure of masonry coupon under compression; (c) compression test of mortar cubes; and (d) failure of a mortar cube
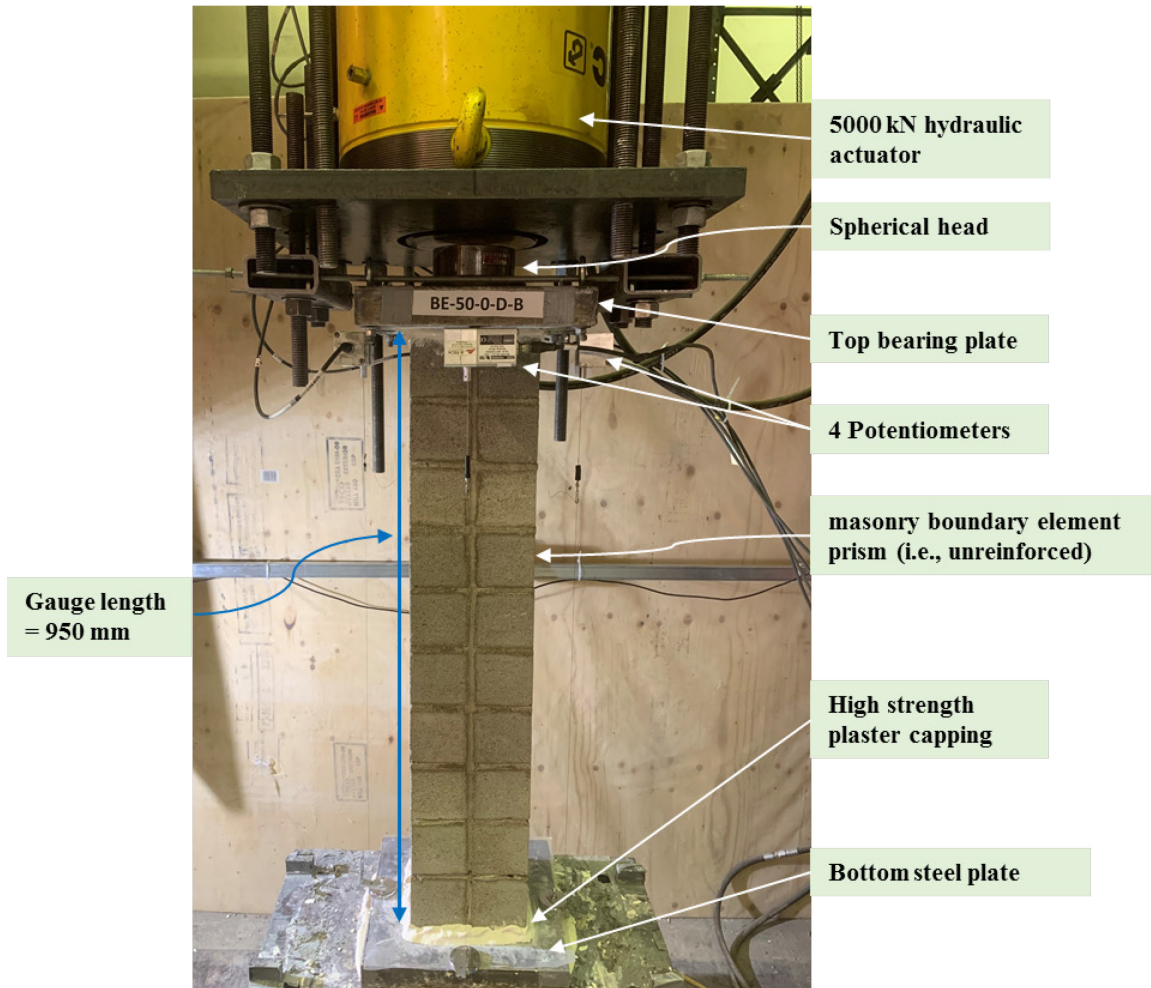
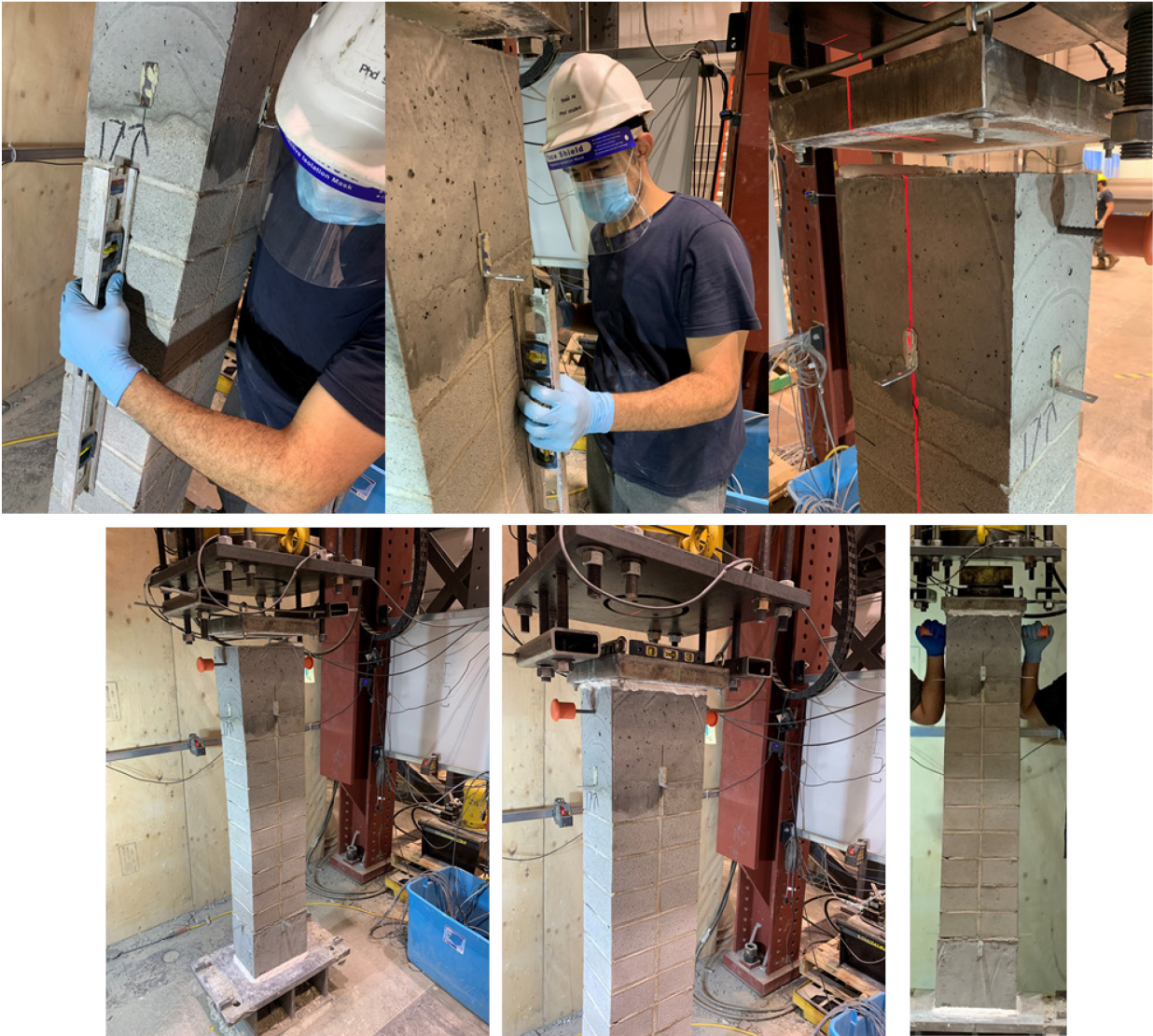**Figure A.18** Testing of square unreinforced masonry boundary element prism

Figure A.19 Levelling and aligning of rectangular RMBE specimen under the testing frame
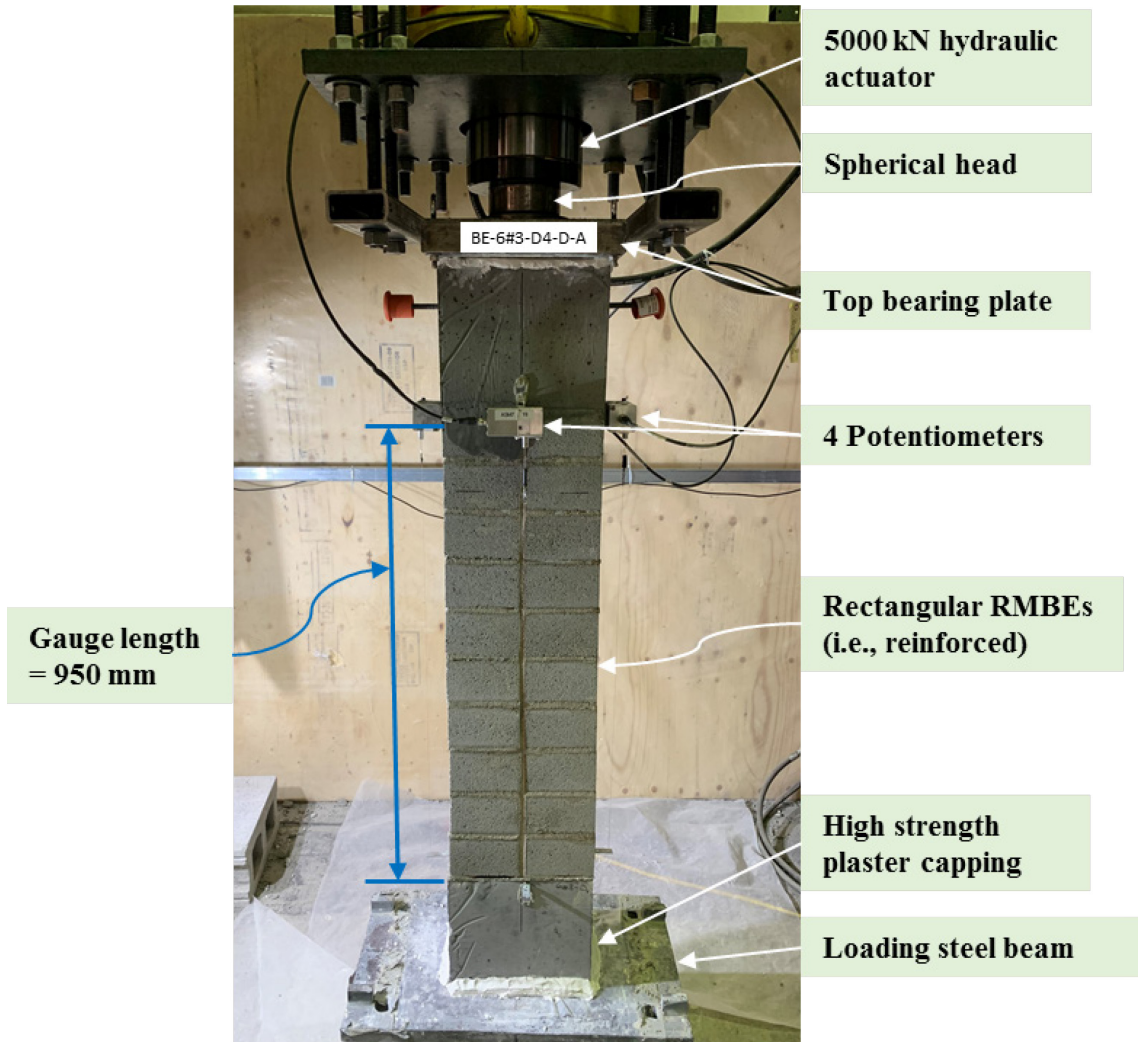
5000 kN hydraulic actuator

Spherical head

BE-6#3-D4-D-A

Top bearing plate

4 Potentiometers

Gauge length = 950 mm

Rectangular RMBEs (i.e., reinforced)

High strength plaster capping
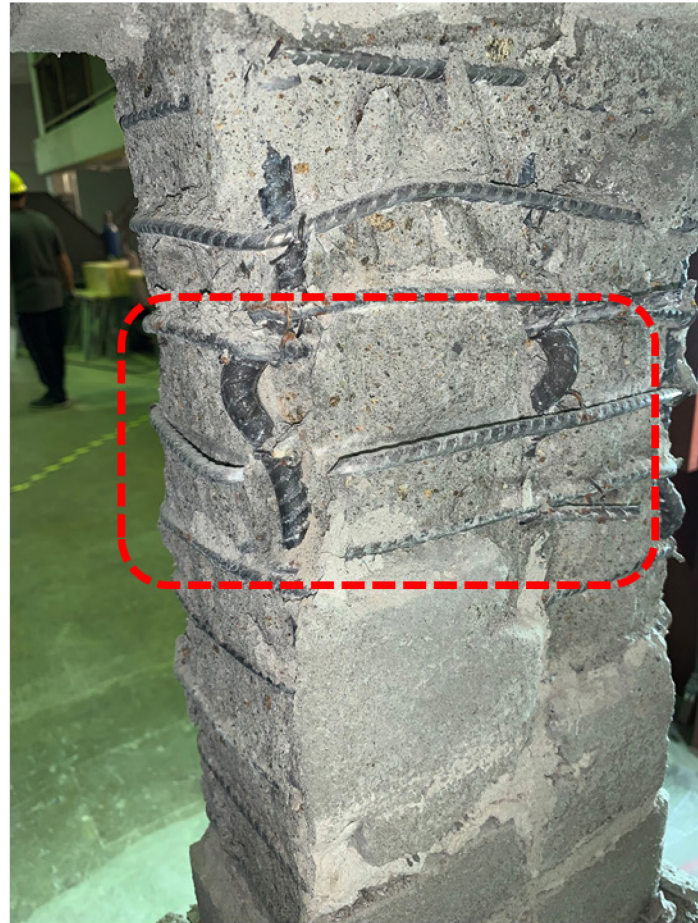
Loading steel beam

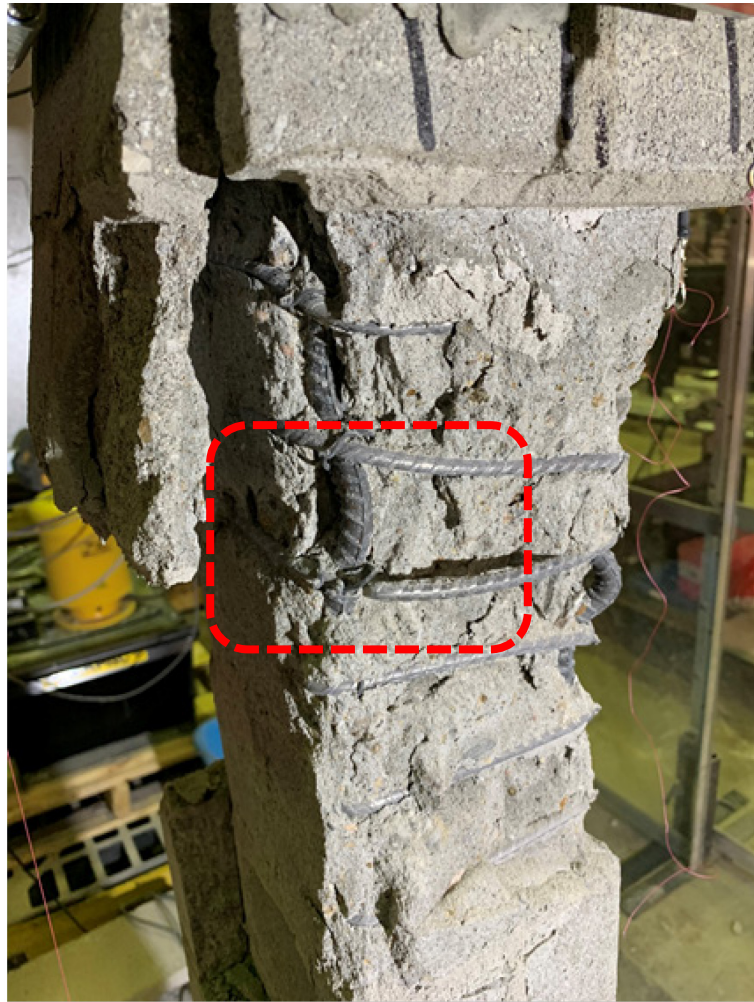**Figure A.20** Testing of RMBE specimen under the middle testing frame

@ 25% strength degradation @ 50% strength degradation @ 75% strength degradation

Figure A.21 Damage states of rectangular RMBE specimen with 6#3 steel bars

@ 25% strength degradation   **@ 75% strength degradation**

Figure A.22 Damage states of dry running-bond RMBE

Figure A.23 Typical final damage state at 75% strength degradation of rectangular RMBEs with 6#3 and 12#3 vertical steel bars

Figure A.24 Typical final damage state of square RMBEs